Refinamento e Otimização do Modelo de Treliça com Ângulo Variável –RASTM para Análise de Placas de Concreto Estrutural

Benedito Madian Viana de Carvalho Filho

Tese para obtenção do Grau de Doutor em
Engenharia Civil
(3° ciclo de estudos)

Orientador: Prof. Doutor Luís Filipe Almeida Bernardo
Coorientador: Prof. Doutor Bernardo Horowitz

novembro de 2021

Refinamento e Otimização do Modelo de Treliça com Ângulo Variável –RASTM para Análise de Placas de Concreto Estrutural

Benedito Madian Viana de Carvalho Filho

(Versão final após defesa)

Composição do Júri:

Prof. Doutor João Paulo de Castro Gomes (Presidente)
Prof. Doutor Sérgio Manuel Rodrigues Lopes (Arguente)
Prof. Doutor José Manuel de Matos Noronha da Câmara (Arguente)
Prof. Doutor Luiz Antônio Pereira de Oliveira (Vogal)
Prof. Doutor Luís Filipe Almeida Bernardo (Orientador)
Prof. Doutor Fernando Artur Nogueira Silva (Arguente)

Provas Públicas realizadas a 17 de novembro de 2021

Esta tese foi desenvolvida no *Centre of Materials and Building Technologies* (C-MADE), entre 2018 e 2021 com apoio financeiro e científico do Banco Santander Totta e da Universidade da Beira Interior, no âmbito da Bolsa de Incentivo a Doutoramento financiada pelo Contrato Plurianual de Mecenato UBI - Santander Totta, em particular através da referência identificativa (BID/FE/2019).

C MADE
CENTRE OF MATERIALS
& BUILDING TECHNOLOGIES

Santander Totta

UNIVERSIDADE
BEIRA INTERIOR

Dedicatória

Dedico esse trabalho a Deus, à verdade e à esperança.

Agradecimentos

Esse trabalho tornou-se realidade graças à interação, conhecimentos adivindos e disponibilidade irrestrita do orientador científico dessa tese, o Professor Doutor Luís Filipe Almeida Bernardo, e do Professor Doutor Bernardo Horowitz na qualidade de coorientador científico.

A consodolidação do percurso acadêmico percorrido até aqui não teria sido também possível sem o apoio dos estimados docentes, Professor Doutor Lúcio Antônio Alves Macêdo, Professor Doutor Luiz Antonio Pereira de Oliveira, Professor Doutor Fernando Artur Nogueira Silva, Professor Doutor António João Carvalho de Albuquerque (na qualidade de Diretor do Curso de 3° Ciclo de Engenharia Civil), Professor Doutor Fernando Manuel Leitão Diniz (na qualidade de Presidente do Departamento de Engenharia Civil e Arquitetura), Professor Doutor João Paulo de Castro Gomes (nas qualidades de Diretor do Curso de 3° Ciclo de Engenharia Civil e Coordenador do *Centre of Materials and Building Technologies* / C-MADE) e Professor Doutor Jorge Andrade.

O meu agradecimento especial à minha família, cada um com a sua singular e abissal importância, Marjolaine Lassé, Maëva Luzia Lassé Carvalho, Maria Mirtes Carvalho de Oliveira, Benedito Madian Viana de Carvalho, Zuleica Freire de Oliveira, Nilrene Freire de Oliveira, Artur Freire de Oliveira, Sergio Netto, Miguel Ahid, Érico Moura, Adelina Frazão, Anastácia Medeiros, Gabriel Henrique Bettencourt de Souza Gonçalves e Miriam Aparecida Bettencourt.

Resumo

O desenvolvimento de um modelo de análise de placas de concreto estrutural, que considere adicionalmente a influência do concreto a tração, como também outras tipologias de composição do concreto e técnicas de utilização de sistemas de reforço estrutural, ainda carece de melhor desenvolvimento e comprovação.

Este trabalho apresenta um modelo refinado de campos de tensões (Modelo de Treliça com Amolecimento e Ângulo Variável Eficiente - Eff. RA-STM) que considera esses fatores, os quais influenciam o comportamento das placas, de maneira que os resultados obtidos demonstram-se mais próximos aos obtidos por via experimental. Em adição, o trabalho também incorpora o objetivo de reformular o procedimento de solução do modelo predecessor ao aqui apresentado, com vista a aumentar a eficiência computacional e estabilidade numérica.

Para verificar a confiabilidade e a capacidade do modelo proposto, foram efetuadas comparações entre os resultados das previsões correspondentes ao modelo refinado de campo de tensões proposto neste trabalho e observações experimentais de testes relevantes encontrados na literatura. Esta abordagem levou a uma simulação mais realista e uma melhor compreensão do comportamento global das placas de concreto estrutural. O modelo proposto poderá ser útil para ajudar à verificação local de elementos estruturais de concreto com comportamento de placa.

Palavras-chave

RA-STM; Betão em tração; Procedimento de solução eficiente; Placas; Concreto estrutural.

Abstract

The development of a model to analyse structural concrete membranes, which additionally considers the influence of the tensile concrete, as well as other type of concretes and strengthening techniques, still needs better development and validation.

This work presents a refined stress field model (Efficient Rotating-Angle Softened Truss Model - Eff. RA-STM) considering the previous factors which influence the behavior of the plates, so that the predictions are closer to the results obtained experimentally. In addition, the work also incorporates the objective of reformulating the solution procedure of the previous version of the model to the one presented here, in view to increase the computational efficiency and numerical stability.

To check the reliability and capacity of the proposed model, comparisons were made between the predictions from the refined stress field model proposed in this work and the experimental results from relevant tests found in the literature. This approach led to a more realistic simulation and a better understanding of the overall behavior of structural concrete plates. The proposed model can be useful to help to check locally structural concrete plates.

Keywords

RA-STM; Tensile concrete; Efficient solution procedure; Plates; Structural concrete.

Lista de Publicações

Artigos incluídos nesta tese resultantes do programa de investigação doutoral

1. Softened Variable Truss Model (RA-STM): Model Description and Refinement/ Optimization Proposals.

Filho, B.; Bernardo, L.; Horowitz, B. 2020 “Softened Variable Angle Truss Model (RA-STM): Model Description and Refinement/ Optimization Proposals”, in STARTCON19 – International Doctorate Students + Lab Workshop in Civil Engineering, Kne Engineering, pages 36-48.
DOI: 10.18502/keg.v5i5.6909

2. Refinement of rotating-angle softened truss model with efficient solution procedure for RC membranes.

Bernardo, L.F.A.; Filho B.M.V.C.; Horowitz, B. 2020 “ Refinement of the rotating-angle softened truss model with efficient solution fo RC membranes”, Engineering Structures, Elsevier, ISSN: 0141-0296, Volume 213: 110552, pages 1 -12.
DOI: https://doi.org/10.1016/j.engstruct.2020.110552

3. Predicting the behavior of prestressed concrete membrane elements by refined rotating-angle softened-truss model with efficient solution procedure.

Bernardo, L.F.A.; Filho, B.M.V.C.; Horowitz, B. 2020 “ Predicting the behaviour of prestressed concrete membrane elements by refined rotating-angle softened-truss model with efficient solution procedure”, Structural Concrete, Journal of the fib, ISNN: 1751-7648, Volume 21: pp. 934-948.
DOI: https://doi.org/10.1002/suco.201900481

4. Predicting the behavior of FRP- strengthened RC membrane elements with efficient rotating-angle softened truss model procedure.

BERNARDO, L. F. A.; FILHO B. M. V. C.; HOROWITZ, B. 2021 "Predicting the behavior of FRP-strengthened RC membrane elements with efficient rotating-angle softened truss model procedure", Materials and Structures, RILEM, ISSN: 1359-5997, Volume 54, Article number: 42.
DOI: https://doi.org/10.1617/s11527-021-01631-y

5. Efficient Softened Truss Model for Prestressed Steel Fiber Concrete Membrane Elements.

BERNARDO, L. F. A.; FILHO B. M. V. C.; HOROWITZ, B. 2021 "Efficient Softened Truss Model for Prestressed Steel Fiber Concrete Membrane Elements", Journal of Building Engineering , Elsevier, ISSN: 2352-7120, Volume 40: 102363.
DOI: https://doi.org/10.1016/j.jobe.2021.102363

Índice

Dedicatória i
Agradecimentos iii
Resumo v
Palavras-chave v
Abstract vii
Keywords vii
Lista de Publicações ix
Índice xi
Lista de Figuras xvii
Lista de Tabelas xxi
Lista de Acrónimos xxiii
Simbologia xxv

Capítulo 1 1
Introdução 1
1. Enquadramento 1
2. Descrição do problema 2
3. Objetivos 5
4. Metodologia 6
5. Organização do documento 8
Referências Bibliográficas 9

Capítulo 2 12
Estado da arte 12
1. Introdução 12
2. Evolução dos modelos analíticos para placas de concreto estrutural 12
3. Modelo de treliça com amolecimento e ângulo variável 16
    3.1 Equilíbrio das tensões 16
    3.2 Compatibilidade das deformações 19
    3.3 Relações constitutivas dos materiais 19
        3.3.1 Concreto submetido à compressão 20

3.3.2 Armaduras submetidas à tração 21

3.4 Carregamento proporcional 22

3.5 Equações adicionais 25

3.6 Sistema de equações não lineares 25

3.7 Algoritmo de solução original 26

3.8 Algumas contribuições recentes ao RA-STM 27

Referências Bibliográficas 27

Capítulo 3 32

Modelo de Treliça com Amolecimento e Ângulo Varável (RA-STM): Descrição do Modelo e Propostas de Refinamento/Otimização. 32

Abstract 33

1.Introduction 33

2. Description of the RA-STM Model 34

2.1 Equations for RA-STM 34

2.2 Solution procedure 35

3. Comparative Analysis with Some Experimental Results 36

4. Future Developments for the Refined RA-STM 41

5. Conclusions 41

Notations 42

References 43

Capítulo 4 44

Refinamento do modelo de treliça com amolecimento e ângulo variável com procedimento de cálculo eficiente para membranas de concreto estrutural. 44

Abstract 45

Keywords 45

1. Introduction 45

Notation 46

2. Efficient RA-STM procedure with concrete in tension 47

2.1 Equations from equilibrium conditions 47

2.2 Equations from compatibility conditions 47

2.3 Smeared constitutive relationships for the materials 48

2.4 Equations for the loading condition 48
2.5 Additional equations 49
2.6 Equations for the residual functions 49
3. Algorithm for the refined efficient RA-STM procedure 50
4. Validation of the refined efficient RA-STM procedure 51
5. Conclusions 56
References 56

Capítulo 5 57
Prevendo o comportamento de elementos de membrana de concreto protendido pelo modelo refinado de treliça com amolecimento e ângulo variável com procedimento de solução eficiente. 57
Abstract 58
Keywords 58
1. Introduction 58
2. Refinement of efficient RA – STM procedure for PC membrane elements 60
2.1 Equilibrium and compatibility equations 60
2.2 Constitutive laws for the materials 61
2.3 Equations for proportional loading 64
3. Efficient solution procedure 65
3.1 Additional equations 65
3.2 Nonlinear equation for the initial estimates 65
3.3 Nonlinear equations for the refined efficient RA-STM procedure 66
3.4 Algorithm 66
4. Validation with experimental results 66
5. Conclusions 69
Notations 70
References 72

Capítulo 6 73
Prevendo o comportamento de elementos de membrana de concreto estrutural reforçados com FRP com procedimento do modelo de treliça com amolecimento e ângulo variável eficiente. 73
Abstract 74

Keywords 74
List of symbols 74
1. Introduction 75
2. Efficient RA-STM procedure for FRP strengthened RC membrane elements 77
    2.1 Equilibrium and compatibility equations 77
    2.2 Constitutive laws for the materials 78
        2.2.1 Constitutive laws for concrete 79
        2.2.2 Constitutive laws for reinforcement 79
    2.3 Equations for proportional loading 80
    2.4 Efficient solution procedure 81
        2.4.1 Additional equations 81
        2.4.2 Residual function for the initial estimates 81
        2.4.3 Residual function for the efficient RA-STM FRP procedure 82
        2.4.4 Calculation procedure and algorithm 82
3. Comparative analysis 82
4. Conclusions 87
References 88

Capítulo 7 90
Modelo eficiente de treliça com amolecimento para elementos de membrana de concreto protendido com fibras de aço. 90
Abstract 91
Keywords 91
1. Introduction 91
2. Efficient RA-STM procedure for PSFC membrane elements 92
    2.1 Basic equations for RA-STM 92
    2.2 Additional equations for the efficient RA-STM procedure 93
    2.3 Smeared constitutive relationships 94
        2.3.1 Steel fiber concrete in compression 94
        2.3.2 Steel fiber concrete in tension 95
        2.3.3 Mild steel bars in tension 95
    2.4 Algorithm to implement the efficient RA-STM procedure 96
3. Validation of the efficient RA-STM PSFC procedure 97
4. Conclusions 99

References 100
Notation 101

Capítulo 8 103
Conclusões e recomendações para trabalhos futuros. 103
1. Introdução 103
2. Conclusões 103
3. Recomendações para trabalhos futuros 105
Referências Bibliográficas 106

Anexos 109
    Anexo I. Código em MATLAB do RA-STM RC v2 110
    Anexo II. Previsões teóricas do RA-STM RC v2 123
    Anexo III. Código em MATLAB do RA-STM PC v2 145
    Anexo IV. Previsões teóricas do RA-STM PC v2 163
    Anexo V. Código em MATLAB do RA-STM FRP 170
    Anexo VI. Previsões teóricas do RA-STM FRP 182
    Anexo VII. Código em MATLAB do RA-STM PSFC 192
    Anexo VIII. Previsões teóricas do RA-STM PSFC 206

Lista de Figuras

Capítulo 1

Figura 1. Simplificação de estruturas de concreto armado em elementos do tipo placa 2
Figura 2. Esquema das forças locais para um estado plano de tensão 3

Capítulo 2

Figura 1. Placa de concreto estrural submetido a tensões gerais de membrana: (a) Concreto estrutural, (b) Concreto simples e (c) Malha ortogonal de aço 16
Figura 2. Elemento de concreto estrutural submetido a tensões principais de membrana: (a) Tensões principais aplicadas no concreto (R-D), (b) Eixos principais no concreto 17
Figura 3. Curva $\sigma - \varepsilon$ do concreto em compressão com amolecimento 20
Figura 4. Curva elasto-plástica perfeita para o aço 21
Figura 5. Relações entre as solicitações e a tensão principal de tração na placa: (a) Tensões gerais de membrana, (b) Relações de proporcionalidade e (c) Eixos ordenados 1-2 22
Figura 6. Fluxograma do procedimento original: análise de placa de concreto estrutural 26

Capítulo 3

Figure 1. Membrane elements to analyse concrete structures [5,6] 34
Figure 2. Flow Chart 38
Figure 3. Comparison between $\sigma_D - \varepsilon_D$ curves for panel VA1 [10] 40
Figure 4. Comparison between $\tau_{LT} - \gamma_{LT}$ curves for panel B2 [11] 40

Capítulo 4

Figure 1. 2D RC membrane element under in-plane stresses 47
Figure 2. Smeared constitutive relationships for the materials 48
Figure 3. Flowchart of the developed algorithm 49
Figure 4. Selected RC panels: direction of applied stresses and reinforcement direction 50
Figure 5. $\tau_{LT} - \gamma_{LT}$ curves for panels from VA - series [27] 51
Figure 6. $\tau_{LT} - \gamma_{LT}$ curves for panels from VB - series [27] 52
Figure 7. $\tau_{LT} - \gamma_{LT}$ curves for panels from A - series [18,21] 52
Figure 8. $\tau_{LT} - \gamma_{LT}$ curves for panels from B - series [18] 53
Figure 9. $\tau_{LT} - \gamma_{LT}$ curves for panels from F - series [31] 54
Figure 10. Examples of other curves for some panels 55

Capítulo 5

Figure 1. Two-dimensional (2D) PC member under in-plane stresses 60
Figure 2. Constitutive laws for the materials 62
Figure 3. Principal applied stresses in the two- dimensional (2D) PC member 64
Figure 4. Flowchart 67
Figure 5. Tested panels: loading condition and reinforcement direction 68
Figure 6. $\tau_{LT} - \gamma_{LT}$ curves for panels from TA - series 68
Figure 7. $\tau_{LT} - \gamma_{LT}$ curves for panels from PP- series 69
Figure 8. Other behavioral curves for selected panels 70

Capítulo 6

Figure 1. Stress diagrams for FRP-strengthened RC membrane element 78
Figure 2. Principal directions of stresses 78
Figure 3. Flowchart for the efficient RA-STM FRP procedure 83

Figure 4. Loading condition an reinforcement layout of reference test panels 84
Figure 5. $\tau_{LT} - \gamma_{LT}$ curves for reference FRP-strengthened RC panels 85

Capítulo 7

Figure 1. Stress components in PSFC membrane elements 93
Figure 2. Principal direction of stresses 93
Figure 3. Smeared constitutive laws for the materials 94
Figure 4. Flowchart of the algorithm 96
Figure 5. TAF panels [55]: loading condition and reinforcement 97
Figure 6. $\tau_{LT} - \gamma_{LT}$ curves for panels from series TAF 98
Figure 7. Comparison between similar PC and PSFC panels 99
Figure 8. Additional behavioral curves for Panel TAF-5 100

Lista de Tabelas

Capítulo 3

Table 1. Equilibrium and compatibility equations [2,3] 35

Table 2. Constitutive relationships for the materials [5,7] 36

Table 3. Set of equations for the refined RA-STM [5,7] 37

Table 4. Properties of tested RC panels under shear 39

Capítulo 4

Table 1. Properties of selected panels 50

Table 2. Comparative analysis between experimental and predicted key parameters 54

Capítulo 5

Table 1. Characteristics of the reference PC panels 61

Table 2. Comparative analysis 69

Capítulo 6

Table 1. Variables of reference panels and material properties [9,19] 78

Table 2. Comparative analysis 86

Capítulo 7

Table 1. Properties of PSFC panels from series TAF [55] 98

Table 2. Comparative analysis of key values 99

Lista de Acrónimos

BID	Bolsa de Incentivo a Doutoramento
CFT	*Compression Field Theory*
C-MADE	*Centre of Materials and Building Technologies*
CSMM	*Cyclic Softened Membrane Model*
DSFM	*Disturbed Stress Field Model*
Eff. RA-STM	*Efficient Rotating-Angle Softened Truss Model*
Eff. RA-STM FRP	*Efficient Rotating-Angle Softened Truss Model for Fiber Reinforced Polymer*
Eff.RA-STM PSFC	*Efficient Rotating-Angle Softened Truss Model for Prestressed Steel Fiber Concrete*
FA-STM	*Fixed-Angle Truss Model*
FRP	*Fiber Reinforced Polymer*
MCFT	*Modified Compression Field Theory*
MCTM	*Mohr Compatibility Truss Model*
PC	*Prestressed Concrete*
PSFC	*Prestressed Steel Fiber Concrete*
RA-STM	*Rotating-Angle Softened Truss Model*
RC	*Reinforced Concrete*
SF	*Steel Fiber*
SFC	*Steel Fiber Concrete*
SMM	*Softened Membrane Model*
SMM-FRP	*Softened Membrane Model for Fiber Reinforced Polymer*
SMM-PC	*Softened Membrane Model for Prestressed Concrete*
SMM-PSFC	*Softened Membrane Model for Prestressed Steel Fiber Concrete*
STM	*Softened Truss Model*
UBI	Universidade da Beira Interior
2D	*Two- Dimensional*

Simbologia

Alfabeto Latino

A', H	Coeficiente que relaciona as constantes de proporcionalidade
A_c	Área da secção de concreto ou Área da secção de concreto com adição de fibras de aço
A_{LP}	Área de armadura longitudinal protendida
A_{LS} , A_L	Área de armadura longitudinal ordinária
A_P	Área de armadura protendida
A_S	Área de armadura ordinária
A_{TP}	Área de armadura transversal protendida
A_{TS} , A_T	Área de armadura transversal ordinária
A_{Tf}	Área de reforço transversal com FRP
B', B	Coeficiente que relaciona as constantes de proporcionalidade, taxas de armadura e tensões nos aços
C', C	Coeficiente que relaciona as taxas de armadura e tensões nos aços
CF	Fator de correção para contabilizar o efeito de confinamento devido à armadura de protensão
D_f	Diâmetro das fibras de aço

cv	Coeficiente de variação
E_C	Módulo de Elasticidade do concreto ou Módulo de Elasticidade do concreto com adição de fibras de aço
E_{c1}	Módulo de Elasticidade do concreto com adição de fibras de aço antes da fissuração
E_{c2}	Módulo de Elasticidade do concreto com adição de fibras de aço imediatamente após a fissuração
E_{c3}	Módulo de Elasticidade extendido para o concreto com adição de fibras de aço
E_f	Módulo de Elasticidade do reforço de FRP
E_P	Módulo de Elasticidade da armadura de protensão
$E_P^{'}$	Módulo de Elasticidade de Ramberg- Osgood
E_S	Módulo de Elasticidade do aço
FF	Fator de fibra de aço
F_{MCTM}	Função resíduo do MCTM
F_{RA-STM}	Função resíduo do RA-STM
$F_{RA-STM}^{(i)}$	Função resíduo para o passo *i* do RA-STM
$F_{RA-STM}^{(1)}$	Primeira função resíduo para o procedimento do RA-STM FRP Eficiente ou Primeira função resíduo para o procedimento do RA-STM PSFC Eficiente

$F^{(2)}_{RA-STM}$	Segunda função resíduo para o procedimento do RA-STM FRP Eficiente ou Segunda função resíduo para o procedimento do RA-STM PSFC Eficiente
F_{START}	Função resíduo para as estimativas iniciais do RA-STM FRP Eficiente
f	Tensão normal nas armaduras
$f_c^{'}$, f_{cm}	Valor médio da resistência à compressão do concreto ou Resistência à compressão uniaxial do concreto com adição de fibras aço
f_{ck}	Tensão característica do concreto à compressão
$f_{cP,i}$	Tensão de compressão inicial no concreto devido à protensão ou Tensão de compressão inicial no concreto com adição de fibras de aço devido à protensão
f_{cpk}	Pico de tensão no concreto com adição de fibra de aço
f_{cr}	Tensão de fissuração do concreto à tração
f_{cy}	Tensão efetiva de escoamento para o concreto com adição de fibras de aço submetido ao carregamento proporcional
f_{fu}	Tensão última do reforço de FRP
f_L	Tensão na armadura longitudinal da placa
f_{Lf}	Tensão de tração no reforço longitudinal de FRP
f_{LP}	Tensão na armadura protendida longitudinal da placa
$f_{LP,i}$	Tensão inicial na armadura protendida longitudinal da placa

$f_{LP0,1\%}$	Tensão limite convencional de proporcionalidade da armadura protendida longitudinal
f_{Ly}	Tensão de escoamento da armadura longitudinal
f_{P}	Tensão na armadura de protensão
$f_{P,i}$	Tensão inicial na armadura de protensão
f_{Pu}	Tensão última da armadura de protensão
f_{S}	Tensão no aço das armaduras
f_{Sf}	Tensão de tração no reforço de FRP
f_{Sy} , $f_{y}^{'}$	Tensão de escoamento da armadura ordinária
f_{T}	Tensão na armadura transversal da placa
f_{Tf}	Tensão de tração no reforço transversal de FRP
f_{TP}	Tensão na armadura protendida transversal da placa
$f_{TP,i}$	Tensão inicial na armadura protendida transversal da placa
$f_{TP0,1\%}$	Tensão limite convencional de proporcionalidade da armadura protendida transversal
f_{Ty}	Tensão de escoamento da armadura transversal
$f_{y}^{'}$	Tensão de escoamento aparente das barras de aço embutidas
k	Índice identificador da iteração

$K_{f/s}$	Fator que relaciona as rigidezes do FRP e do aço
k_S	Rigidez ao cisalhamento no estado fissurado
$k_{S,\exp}$	Rigidez ao cisalhamento experimental no estado fissurado
$k_{S,th}^{eff.RA-STM}$	Rigidez ao cisalhamento teórica no estado fissurado do RA-STM Eficiente
$k_{S,th}^{eff.RA-STMFRP}$	Rigidez ao cisalhamento teórica no estado fissurado do RA-STM FRP Eficiente
K_W	Fator para o esquema de reforço
L_f	Comprimento da fibra de aço
m_L	Constantes de proporcionalidade longitudinal
m_{LT}	Constante de proporcionalidade ao cisalhamento
m_T	Constante de proporcionalidade transversal
$n_{\max}$	Número máximo de pontos da análise
$RF_{RA-STM}^{(1)}$	Primeira função resíduo para o procedimento do RA-STM Eficiente
$RF_{RA-STM}^{(2)}$	Segunda função resíduo para o procedimento do RA-STM Eficiente
RF_{START}	Função resíduo para as estimativas iniciais
s	Desvio padrão
V_f	Volume percentual de fibra de aço
W_f	Fator de correção para contabilizar o reforço de fibras de aço
$\bar{x}$	Média

Alfabeto Grego

α_D	Complemento do ângulo variável ou Ângulo das tensões compressivas principais na placa de concreto com adição de fibras de aço
α_R	Ângulo variável
α_1	Ângulo fixo
α_2	Complemento do ângulo fixo ou Ângulo das tensões compressivas principais na placa de concreto protendido com adição de fibras de aço
γ	Distorção na placa
γ_{LT}	Distorção média na placa segundo os eixos *L-T*
γ_u	Distorção última na placa
$\gamma_{u,\exp}$	Distorção última experimental na placa
$\gamma_{u,\mathrm{th}}$	Distorção última teórica na placa
$\gamma_{\mathrm{u},th}^{eff.RA-STM}$	Distorção última teórica na placa do RA-STM Eficiente
$\gamma_{\mathrm{u},th}^{eff.RA-STMFRP}$	Distorção última teórica na placa do RA-STM FRP Eficiente
$\gamma_{u,th}^{RA-STM}$	Distorção última teórica na placa do RA-STM PSFC Eficiente
$\gamma_{u,th}^{SMM}$	Distorção última teórica na placa do SMM
$\Delta\varepsilon_D$	Incremento entre as iterações
ε	Deformação

ε_{cpk}	Deformação correspondente à f_{cpk}
ε_{cr}	Deformação correspondente à tensão de fissuração do concreto
ε_{cu}	Deformação última do concreto à compressão
ε_{cu1}	Deformação última do concreto à compressão (análise não linear)
ε_{cy}	Deformação correspondente à f_{cy}
ε_{D}	Deformação principal de compressão na placa
ε_{dec}	Deformação na armadura de protensão após a descompressão do concreto
ε_{fu}	Deformação última do reforço de FRP
ε_{L}	Deformação na armadura longitudinal da placa
ε_{Lf}	Deformação no reforço de FRP longitudinal
ε_{Ly}	Deformação de escoamento na armadura longitudinal da placa
$\varepsilon_{\max}$	Deformação máxima do concreto com adição de fibras de aço
ε_{P}	Deformação na armadura de protensão
$\varepsilon_{P,i}$	Deformação de tração inicial na armadura protensão
$\varepsilon_{P0,7f_{Pu}}$	Deformação na armadura de protensão correspondente à $0,7f_{Pu}$
$\varepsilon^{L}_{P0,7f_{pu}}$	Deformação correspondente à $0,7f_{Pu}$ na parte linear (*L*) da curva $\sigma-\varepsilon$
ε_{R}	Deformação principal de tração na placa

ε_S	Deformação no aço das armaduras
ε_{Sf}	Deformação no reforço de FRP
$\varepsilon_{S,i}$	Deformação inicial de compressão nas armaduras ordinárias devido a aplicação da protensão
ε_{Sy}	Deformação de escoamento do aço das armaduras
ε_{su}	Deformação última do aço das armaduras
ε_T	Deformação na armadura transversal da placa
ε_{Tf}	Deformação no reforço de FRP transversal
ε_{Ty}	Deformação de escoamento na armadura transversal da placa
$\varepsilon_y^{'}$	Deformação correspondente à $f_y^{'}$
ε_0	Deformação correspondente ao pico de tensão no concreto ou Deformação correspondente ao pico de tensão no concreto com adição de fibras de aço
ζ	Coeficiente de amolecimento
ζ_{SFC}	Coeficiente de amolecimento para o concreto com adição de fibras de aço
ζ_{FRP}	Coeficiente de amolecimento que contabiliza o reforço de FRP
η	Relação entre as forças resistentes nas armaduras nas direções transversal e longitudinal
μ	Fator redutor de escala das tensões aplicadas na placa
ρ	Taxa de reforço

ρ_f	Taxa de reforço FRP na direção principal da tensão de tração
ρ_L	Taxa de armadura longitudinal
ρ_{Lf}	Taxa de reforço FRP longitudinal
ρ_{LP}	Taxa de armadura protendida longitudinal
ρ_S	Taxa de armadura
ρ_{Se}	Taxa de armadura que contabiliza o reforço de FRP
ρ_T	Taxa de armadura transversal
ρ_{Tf}	Taxa de reforço FRP transversal
ρ_{TP}	Taxa de armadura protendida transversal
σ	Tensão normal
σ_D	Tensão principal de compressão no elemento de concreto ou Tensão principal de compressão no elemento de concreto com adição de fibras de aço
σ_L	Tensão normal longitudinal aplicada na placa de concreto ou Tensão normal longitudinal aplicada na placa de concreto protendido com adição de fibras de aço
σ_L^c	Componente da tensão normal aplicada no concreto ou Tensão normal longitudinal aplicada na placa de concreto com adição de fibras de aço
σ_R	Tensão principal de tração na placa de concreto ou Tensão principal de tração na placa de concreto com adição de fibras de aço

σ_T	Tensão normal transversal aplicada na placa de concreto Tensão normal transversal aplicada na placa de concreto protendido com adição de fibras de aço
σ_T^c	Componente da tensão normal aplicada no concreto ou Tensão normal transversal aplicada na placa de concreto com adição de fibras de aço
σ_X	Tensão normal segundo o eixo x
σ_Y	Tensão normal segundo o eixo y
σ_1	Tensão principal de tração no elemento de concreto armado ou Tensão principal de tração no elemento de concreto protendido com adição de fibras de aço
σ_2	Tensão principal de compressão no elemento de concreto armado ou Tensão principal de compressão no elemento de concreto protendido com adição de fibras de aço
τ_{cr}	Tensão tangencial de fissuração
$\tau_{cr,\mathrm{exp}}$	Tensão tangencial de fissuração experimental
$\tau_{cr,\mathrm{th}}$	Tensão tangencial de fissuração teórica
$\tau_{cr,th}^{eff.RA-STM}$	Tensão tangencial de fissuração teórica do RA-STM Eficiente
$\tau_{cr,th}^{eff.RA-STMFRP}$	Tensão tangencial de fissuração teórica do RA-STM FRP Eficiente
$\tau_{cr,th}^{RA-STM}$	Tensão tangencial de fissuração teórica do RA-STM PSFC Eficiente
$\tau_{cr,th}^{SMM}$	Tensão tangencial de fissuração teórica do SMM
τ_{LT}	Tensão tangencial aplicada na placa de concreto ou Tensão tangencial aplicada na placa de concreto protendido com adição de fibras de aço

τ^{c}_{LT}	Componente da tensão tangencial aplicada no concreto ou Tensão tangencial aplicada na placa de concreto com adição de fibras de aço
τ_{u}	Tensão tangencial última
$\tau_{u,\exp}$	Tensão tangencial última experimental
$\tau_{u,\mathrm{th}}$	Tensão tangencial última teórica
$\tau^{eff.RA-STM}_{\mathrm{u},th}$	Tensão tangencial última teórica do RA-STM Eficiente
$\tau^{eff.RA-STMFRP}_{\mathrm{u},th}$	Tensão tangencial última teórica do RA-STM FRP Eficiente
$\tau^{RA-STM}_{u,th}$	Tensão tangencial última teórica do RA-STM PSFC Eficiente
$\tau^{SMM}_{u,th}$	Tensão tangencial última teórica do SMM
τ_{XY}	Tensão tangencial ortogonal aos eixos x
τ_{YX}	Tensão tangencial ortogonal aos eixo y

Capítulo 1

Introdução

1. Enquadramento

Este trabalho apresenta um modelo de análise estrutural baseado num modelo de campos de tensões. A análise do comportamento de um elemento bidimensional sujeito a esforços de membrana não é uma tarefa trivial. Na década de oitenta do século passado as previsões para o comportamento carga *versus* deformação de placas de concreto armado apresentavam margens de erro superiores a 15%, nesta altura, evidenciou-se que as previsões dependiam fortemente das relações tensão-deformação dos materiais [1].

Soma-se a esse fato, que as atuais demandas impostas aos projetistas estruturais condicionam o desenvolvimento de novos modelos analíticos, e a calibração dos atuais para que possam ser utilizados como ferramentas de auxílio para projetos estruturais no tocante à verificação da segurança de estruturas complexas. Para contornar esses problemas, têm sido desenvolvidos vários modelos analíticos para simular o comportamento de placas de concreto estrutural.

O Modelo de Treliça com Amolecimento e Ângulo Variável Eficiente (Eff. RA-STM) proposto neste trabalho, surge a partir do refinamento e otimização do Modelo de Treliça com Ângulo Variável (RA-STM – *Rotating Angle Softened Truss Model*) tendo por base o procedimento proposto por Silva e Horowitz em 2015 [2] e Silva et al. em 2017 [3].

O Eff. RA-STM é capaz de prever o comportamento de placas de concreto estrutural com armaduras ordinárias e/ou protendidas submetidas a esforços de membrana, em particular ao cisalhamento, assim como placas de concreto estrutural reforçadas com laminados de carbono, como também placas em concreto com adição de fibras de aço e armaduras de reforço ordinárias e/ou protendidas.

O presente trabalho integra-se, em parte, no âmbito da Bolsa de Incentivo a Doutoramento (BID), financiada pelo Contrato Programa Plurianual de Mecenato UBI-Santander Totta (BID/FE/2019).

2. Descrição do problema

Estruturas usuais de concreto armado têm o desafio de atender aos critérios de desempenho estrutural durante toda sua vida útil, designadamente de resistir aos esforços solicitantes que surgem a partir da sua construção e uso [4]. É uma prática comum na engenharia de estruturas a discretização de estruturas complexas, transformando a estrutura inicial numa combinação de elementos mais simples. Com base neste princípio vários modelos de análise estrutural têm sido desenvolvidos.

Em alguns casos, estruturas como plataformas marítimas, paredes resistentes em edifícios, estruturas de contenção nuclear, vigas caixão em pontes, coberturas em cascas de grandes vãos, entre outras, conforme ilustrado na Figura 1, podem ser simplificadas como uma associação de elementos laminares planos, caracterizados geometricamente por apresentar duas dimensões, largura e comprimento, consideravelmente superiores à terceira, espessura.

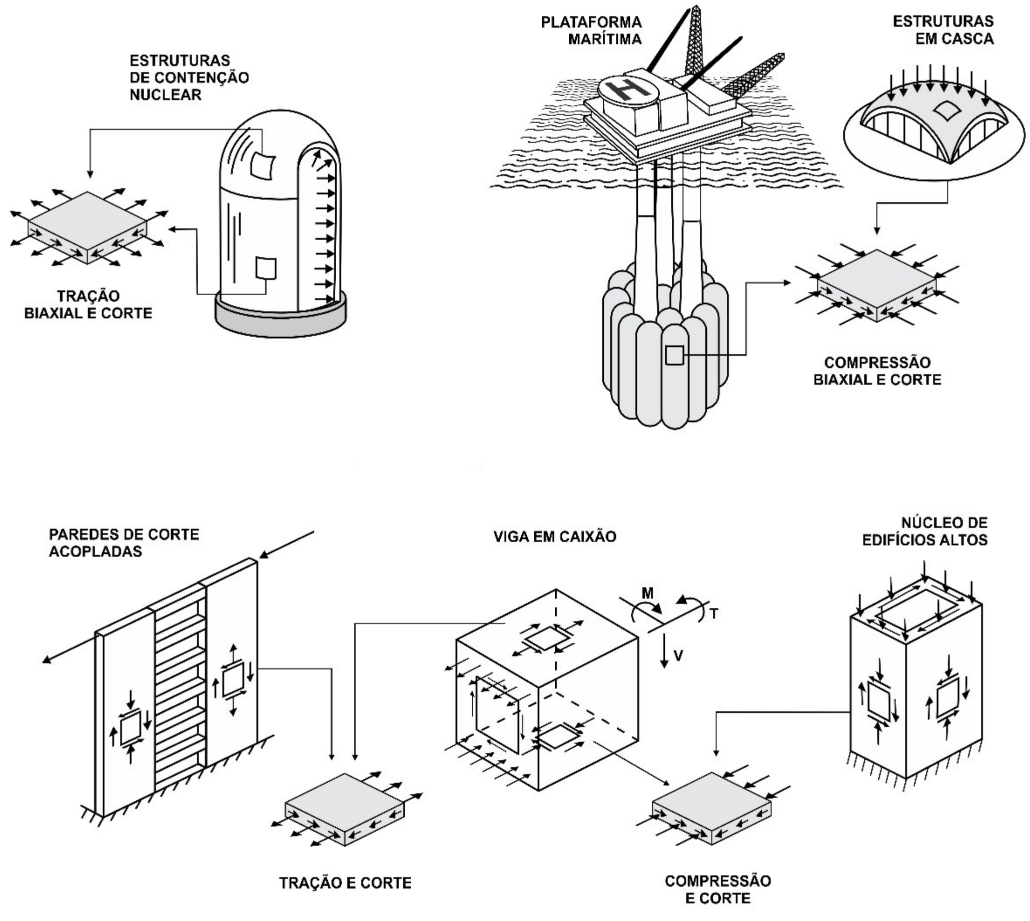

Figura 1 - Simplificação de estruturas de concreto armado em elementos do tipo placa.

Tais elementos constituídos de concreto armado e/ou protendido, com armaduras dispostas em sua generalidade em direções ortogonais, estão sujeitos apenas a tensões que atuam no seu próprio plano, os quais geram esforços de membrana. Devido a estas características, são denominados de placas ou painéis, e o seu comportamento pode ser determinado com métodos baseados em modelos de campos de tensões (ou de treliça).

Os fundamentos desse estudo têm alicerce no entendimento do mecanismo de transferência de tensões entre os materiais constituintes das placas de concreto estrutural no estado fissurado. O fenômeno da fissuração torna-se mais relevante quando a direção das armaduras não coincide com a direção da tensão principal de tração, responsável pela fissuração do concreto, esta condição é usual em placas de concreto estrutural submetidas predominantemente ao cisalhamento [5].

O modelo apresentado considera a fissuração das placas desde o início do carregamento, por considerar a problemática da fissuração e a baixa resistência do concreto à tração. Esta consideração é importante para o estudo do comportamento no estado pós-fissurado das placas.

A Figura 2 ilustra o esquema de carregamento em elementos estruturais do tipo placa, em que as grandezas empregadas para descrever o comportamento do elemento são as tensões normais orientadas segundo o eixo X, σ_X , e segundo o eixo Y, σ_Y , e as tensões de cisalhamento ortogonais aos eixos X e Y respectivamente, $\tau_{XY} = \tau_{YX}$, essa condição caracteriza o estado plano de tensões ou tensões de membrana.

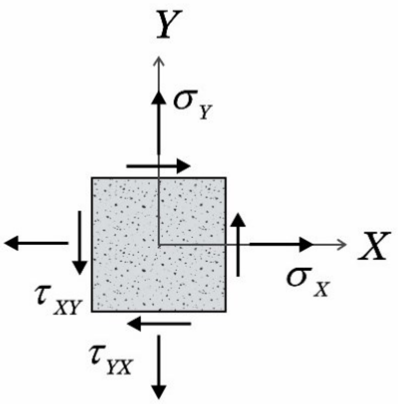

Figura 2 - Esquema das forças locais para um estado plano de tensão.

Atualmente, além da utilização das placas de concreto armado, amplamente utilizadas, a incorporação de técnicas de protensão em estruturas laminares é muito usual. A protensão tem a capacidade de otimizar o comportamento de serviço das estruturas, reduzir as dimensões dos elementos estruturais e incrementar a resistência última, quando aplicada de forma racional. A tensão inicial de compressão devido aos esforços axiais resultantes da protensão, combinada com a tensão tangencial induzida pelo cisalhamento, resulta num estado de tensão biaxial, como consequência, nota-se o retardamento da fissuração. Adicionalmente, a armadura de protensão contribui para o aumento da resistência última do elemento estrutural após a descompressão, por assumir a condição de armadura passiva e conter uma reserva de resistência.

A prática mais frequente da utilização da protensão é unidirecional, como por exemplo, em vigas contínuas. A aplicação bidirecional, apesar de menos frequente, pode ocorrer em situações específicas. As coberturas em cúpula de estruturas de contenção nuclear, para elevar a segurança à ação de acidentes correspondentes à explosão de reatores nucleares, e nas almas das vigas de seções em caixão em pontes nas zonas próximas aos apoios, devido ao elevado esforço cortante, são exemplos que podem ser citados. Por essas razões, o modelo considera além de placas de concreto dotado de armaduras ordinárias, o caso geral de placas de concreto com protensão bidirecional sujeito a ação de esforços de membrana.

Os sistemas de reforço em polímeros reforçados com fibra (FRP – *Fiber Reinforced Polymer*) ligados externamente, têm sido abrangentemente utilizados nos últimos trinta anos como técnica de reabilitação e fortalecimento de estruturas de concreto armado. Diversas vantagens podem ser apontados acerca do uso dos sistemas FRP, quando comparados a outros sistemas de reforço estrutural, como resistência à corrosão, facilidade de aplicação, alta resistência e alta rigidez [6,7].

Modelos analíticos bem estabelecidos estão disponíveis para projetar e analisar sistemas FRP em vigas e pilares sob ação de confinamento flexural e axial [6,7]. Porém para elementos de concreto estrutural reforçados com FRP onde o cisalhamento é a ação dominante, é reconhecido que o comportamento estrutural é mais complexo do que elementos não reforçados com FRP. Esse fato decorre da maior complexidade dos mecanismos e modos de falha associados a elementos com FRP [8].

Os modelos analíticos atuais, disponíveis para prever o comportamento de elementos de concreto estrutural reforçados com FRP submetidos ao cisalhamento como ação dominante, apresentam grandes dispersões quando comparados com resultados experimentais [9], por essa razão, consta na literatura recente que estudos analíticos e experimentais continuam a ser realizados [9-14], a exemplo desse trabalho, que apresenta um modelo fiável nesse sentido.

A adição de fibras de aço no concreto tem a capacidade de otimizar algumas propriedades do concreto. No estado pós-fissurado fica evidente o maior controle de a abertura de fendas, aumento da resistência à tração, ductilidade e tenacidade [15,16]. O concreto simples falha repentinamente ao atingir o pico de carga [17,18], enquanto o concreto com fibras de aço (SFC – *Steel Fiber Concrete*) suportam uma carga pós-pico significativa, por conta do efeito de ponte das fibras através da fissuração e do efeito de confinamento das fibras dentro do concreto.

Estruturas como, paredes de cisalhamento, vasos de contenção nuclear e vigas de seção em caixão utilizadas em pontes de grandes vãos podem se beneficiar além da protensão, com a utilização do SFC, pela sua capacidade de reduzir, e em alguns casos, eliminar, a necessidade de armaduras de cisalhamento convencionais. Este recurso tem o potencial de minimizar o tempo e a mão de obra associados à execução desses elementos estruturais.

Diante da descrição sumária das soluções estruturais de concreto mais comuns, e outra com imenso potencial de aplicação em grande escala, assim como o método de reforço estrutural referido, o Eff.RA-STM inclina-se na direção da ampla aplicabilidade e ser utilizada como ferramenta preditiva do comportamento local para o cálculo estrutural de estruturas complexas.

3. Objetivos

O modelo RA-STM modificado por Silva [2], Cerquido [19] e Lyrio [20], fornece boas previsões teóricas apenas para a fase última comportamental das placas. Além disso, o modelo foi validado somente para o caso de placas de concreto armado e concreto protendido sujeitas a cisalhamento puro com carregamento proporcional, sem considerar a influência do concreto à tração. Dessa forma, no âmbito deste doutoramento apresenta-se o refinamento e otimização do modelo RA-STM modificado, e avanços em vários aspectos que não foram abordados nos estudos anteriores, designadamente os estudos referidos anteriormente. Os principais objetivos aventados para esta investigação são os seguintes:

1. Implementar de forma numericamente eficiente os modelos de RA-STM modificado de Silva [2], Cerquido [19] e Lyrio [20] no MATLAB;

2. Incorporar a influência do concreto à tração no modelo RA-STM para capacitar o mesmo a prever adequadamente a transição do estado não fissurado para o estado fissurado e validar o novo modelo tendo por base resultados experimentais encontrados na literatura;

3. Generalizar o modelo para incorporar placas reforçadas com lâminas em FRP aderidas externamente. Validar o modelo tendo por base resultados experimentais encontrados na literatura;

4. Generalizar o modelo para incorporar placas que contenham SFC, ou seja fibras de aço em sua matriz de concreto, e que, em simultâneo, possam possuir armaduras protendidas. Validar o modelo tendo por base resultados experimentais obtidos na literatura.

Confome apresentado no Plano de Tese desse trabalho, no item Plano de Investigação e Metodologia, alguns objetivos foram ajustados por serem considerados necessários e adequados para o progresso desta investigação. O cumprimento dos objetivos anteriormente referidos requereu mais tempo do que o previsto no Plano de Tese, designadamente em resultado da implementação e calibração do modelo, bem como da necessária resolução de problemas de convergência. Por estes motivos, não foi possível, por exemplo, abordar até ao fim outros estados e tipos de carregamento (por exemplo, corte cíclico), assim como a utilização de critérios energéticos para reformular o modelo e tentar reduzir a complexidade do procedimento de cálculo.

Todavia, considera-se que importantes e atuais objetivos suplementares foram atingidos de modo a alargar as possibilidades de aplicação prática do modelo proposto. Nomeadamente, a generalização do novo modelo (Eff.RA-STM) para placas que contenham reforços em FRP aderidos externamente e para placas que contenham SFC em sua matriz de concreto, foram incorporadas à investigação e validadas com sucesso.

4. Metodologia

Primeiramente, desenvolveu-se uma pesquisa de propostas de modelos análiticos baseados em campos de tensões (modelos de treliça) para placas de concreto estrutural submetidas ao cisalhamento e suas aplicações. O próximo passo foi verificar como esses modelos contribuíram para o avanço da análise estrutural. Posteriormente, com base no conhecimento adquirido, foi refinado e otimizado um modelo anterior (RA-STM) de maneira que o alargamento da sua aplicabilidade, estabilidade numérica e aproximação a resultados experimentais fossem alcançados. O detalhamento das atividades executadas seguiram a sequência descrita.

Tarefa 1 – Pesquisa bibliográfica sobre o tema do trabalho, estudo dos elementos recolhidos, com interesse para o tema, elaboração do estado da arte sobre o tema, iniciação à programação em MATLAB. Essa tarefa possibilitou o entendimento do histórico e a visualização do atual estágio de avanço e aplicabilidade dos modelos analíticos baseados em treliças para placas de concreto estrutural, adicionalmente introduziu as ferramentas informáticas que viabilizaram esse trabalho.

Tarefa 2 – Implementação do modelo analítico no MATLAB com procedimento numérico eficiente. Nessa etapa do trabalho foi realizada a implementação do RA-STM, capaz de ser utilizada para análise de placas de concreto armado e concreto protendido. Adicionalmente, o modelo foi refinado com a incorporação da influência do concreto à tração, mediante a reformulação do procedimento solução com vista a incorporar esta contribuição. Os resultados obtidos foram validados tendo por base resultados experimentais encontrados na literatura.

Tarefa 3 – Reformulação do modelo e implementação no MATLAB por forma a incorporar a contribuição de reforços externos em FRP. Essa tarefa possibilitou a confirmação da versatilidade do modelo, nomeadamente quanto a sua capacidade de previsão do comportamento de placas de concreto estrutural reforçadas com FRP. Os resultados obtidos foram validados por resultados experimentais encontrados na literatura.

Tarefa 4 – Reformulação do modelo e implementação no MATLAB por forma a incorporar SFC. Nessa etapa o modelo foi novamente alargado e utilizado na previsão do comportamento de placas de concreto protendido, com adição de SFC na matriz de concreto. Os resultados obtidos foram validados por resultados experimentais encontrados na literatura.

Tarefa 5 – Organização das informações coletadas ao longo do trabalho e redação da tese. Recolhidas as informações, o passo seguinte foi a redação das conclusões de modo a dar suporte ao modelo análitico e suas aplicações apresentadas nesta tese.

5. Organização do documento

Nesta seção é apresentada a organização da tese, com uma descrição sumária do conteúdo de cada capítulo.

No capítulo 1, apresenta-se um panorama geral sobre o tema da tese e são salientados os aspectos que tornam essa investigação relevante e nescessária. Contém a introdução, incluindo o enquadramento, descrição do problema, objetivos, metodologia e também a organização do documento.

Consta no capítulo 2 a apresentação da revisão bibliográfica de alguns modelos analíticos, formulação e procedimento de cálculo do RA-STM original, incluindo os desenvolvimentos mais recentes.

O capítulo 3 é constituído por um artigo científico publicado num congresso internacional que resume os últimos desenvolvimentos do RA-STM e relata propostas de refinamento/otimização do modelo.

O capítulo 4 é composto por um artigo científico publicado em revista internacional que descreve e valida uma proposta do modelo RA-STM refinado e otimizado (Eff. RA-STM) para placas de concreto armado.

O capítulo 5 é formado por um artigo científico publicado em revista internacional que apresenta a extensão do Eff. RA-STM e sua validação para placas de concreto com armaduras protendidas.

O capítulo 6 é instituído por um artigo científico publicado em revista internacional, onde o Eff. RA-STM é modificado com vista a prever o comportamento de placas de concreto armado reforçadas externamente com FRP. É também apresentada a validação do modelo.

O capítulo 7 é concebido por um artigo científico publicado em revista internacional que propõe e valida a extensão do Eff. RA-STM para placas de concreto com adição de fibras de aço e armaduras protendidas.

Finalmente no capítulo 8 são apresentadas as conclusões do estudo realizado e as recomendações para futuros desenvolvimentos do trabalho.

Referências Bibliográficas

[1] Collins, M. P., Vecchio, F J., and Mehlhom, G. (1985),"An International Competition to Predict the Response of Reinforced Concrete Panels", Canadian Journal of Civil Engineering, Ottawa, Vol. 12, No. 3, pp. 626-644.

[2] Silva, J. R. B. e Horowitz, B. (2015), "Procedimento Eficiente Para Estimar o Comportamento Carga-Deformação de Painéis de Concreto Armado Submetidos a Esforços de Membrana Usando o Modelo de Treliça com Amolecimento e Ângulo Variável", CILAMCE 2015 – XXXVI Iberian Latin American Congresso on Computacional Methods in Engineering, Rio de Janeiro-RJ, Brasil.

[3] Silva, J. R. B, Horowitz, B., Bernardo, L. F A. (2017), "Efficient Procedure to Analyze RC Beam Sections using the Softened Truss Model", ACI Structural Journal, *American Concrete Institute*, Vol. 114, No. 3, May-June 2017, pp. 1-10.

[4] NP EN 1991-1-1 (2009) Eurocode 1: Acções em Estruturas - parte 1: acções gerais pesos volúmicos, pesos próprios, sobrecargas em edifícios.

[5] Bernardo, L. F. A. (2003), "Torção em Vigas em Caixão de Betão de Alta Resistência", Departamento de Engenharia Civil, Faculdade de Ciência e Tecnologia da Universidade de Coimbra.

[6] ACI Committee 440 (2017), "Guide for the design and construction of externally bonded FRP systems for strengthening concrete structures", ACI 440.2R-17. Farmington Hills (MI): *American Concrete Institute*.

[7] Task Group fib T5.1 (2019), "Externally applied FRP reinforcement for concrete structures". FIB BULLETIN No. 90. Lausanne, Switzerland: International Federation for Structural Concrete (fib).

[8] Belarbi A., Bae S. W., Ayoub,A., Kuchma, D., Mirmiran, A., Okeil A. (2011), "Design of FRP systems for strengthening concrete girders in shear", NCHRP Rep. No. 678, 2001, Transportation Research Board, Washington, DC.

[9] Zomorodian M., Belarbi A., Ayoub A. (2017), "Finite element model for predicting the shear behavior of FRP-strengthened RC members", *Engineering Structures*. 2017;153, pp. 239-253.

[10] He,R., Sneed, L.H., Belarbi. A. (2014), "Torsional repair of severely damaged column using carbon fiber-reinforced polymer", ACI Structural Journal, 2014;111(3), pp.705–716.

[11] Mofidi, A., Chaallal, O. (2014) , "Effect of steel stirrups on shear resistance gain due to externally bonded fiber-reinforced polymer strips and sheets", ACI Structural Journal, 2014;111, pp. 353–361.

[12] Ganganagoudar, A., Mondal, T.G., Prakash S.S. (2016), "Analytical and finite element studies on behavior of FRP strengthened RC beams under torsion", *Composite Structures*, 2016;153, pp. 876- 885.

[13] Baghi,H., Barros, J.A. (2016), " Shear strengthening of reinforced concrete T-beams with hybrid composite plate". *Journal of Composites for Construction*, 2016;20(6): 04016036.

[14] Zomorodian, M., Yang, G., Belarbi, A, Ayoub A. (2018), "Behavior of FRP-strengthened RC elements subjected to pure shear", Construction and Building Materials, 2018;170, pp. 378-391.

[15] ACI Committee 544. (1998), "Design Considerations for Steel Fiber Reinforced Concrete", ACI Structural Journal, 1998, 85(5), pp. 563-580.

[16] fib CEP-FIP. (2016), "Fibre-reinforced concrete: From design to structural applications", FRC 2014: ACI-fib International Workshop. FIB BULLETIN NO. 79. Lausanne, Switzerland: International Federation for Structural Concrete (fib).

[17] Traina L.A, Mansour S.A. (1991), "Biaxial Strength and Deformational Behavior of Plain and Steel", 498 Fiber Concrete, ACI Material Journal, 1991, 88(4),pp. 353-362.

[18] Thomas, J., Ramaswamy, A. (2007), "Mechanical Properties of Steel Fiber-Reinforced Concrete", 500 Journal of Materials in Civil Engineering, ASCE, 2007, 19(5).

[19] Bernardo, L.F.A, Cerquido, B.M.D, Silva, J.R.B and Horowitz, B. (2018), "Efficient refined rotating-angle softened truss model procedure to analyze reinforced concrete membrane elements", Structural Concrete, 2018, pp. 1971-1982 - Wiley Online Library

[20] Bernardo, L.F.A, Lyrio, A.R.B, Silva, J.R.B and Horowitz, B. (2018), “Refined softened truss model with efficient solution procedure for prestressed concrete membranes”, *Journal of Structural*, 2018 - ascelibrary.org

Capítulo 2

Estado da arte

1. Introdução

Nessa seção descreve-se, de maneira sucinta, alguns dos principais estudos realizados que possibilitaram o entendimento atual da modelação numérica de placas de concreto estrutural sujeitas ao cisalhamento, tendo por base o modelo de treliça plana.

2. Evolução dos modelos analíticos para placas de concreto estrutural

Os primeiros estudos relativos à modelos de treliça plana aplicados aos elementos de concreto estrutural submetidos a esforços de membrana, remontam à 1899 por iniciativa de Ritter [1], e posteriormente à Morsch , em 1902 [2]. Nesta fase primal dos estudos foi idealizado o modelo *45°Truss Model*, que trata a resistência ao cisalhamento de vigas de concreto como o mecanismo interno de uma treliça, onde as escoras diagonais de concreto são sujeitas à compressão axial e as armaduras sujeitas à tração.

Em 1968, Robinson e Demorieux , confirmaram o funcionamento do modelo *45° Truss Model*, e sob a ótica bidimensional, adicionaram o conceito do efeito de amolecimento (*softening effect*), onde a resistência à compressão nas escoras de concreto é reduzida pelo aparecimento de fissuras decorrentes de tensões de tração perpendiculares às tensões de compressão, quando comparada com a resistência obtida em ensaios de compressão uniaxial [3]. Com a aplicação desse novo conceito, eles foram capazes de explicar o equilíbrio das tensões em oito vigas de perfil I testadas experimentalmente, todavia não foram capazes de quantificar a redução de resistência nas escoras de concreto.

A quantificação do coeficiente de amolecimento para curva tensão-deformação compressiva do concreto foi objeto de estudo de Vecchio e Collins em 1981 [4], para alcançar esse objetivo foi construído um dispositivo específico para o ensaio ao cisalhamento. A partir dos resultados dos ensaios então realizados foi desenvolvida a Teoria do Campo de Compressões (*Compression Field Theory* - CFT), que satisfaz os

Princípios de Navier, e que representou um grande avanço no estudo da previsão do comportamento de elementos de concreto estrutural sob ação do cisalhamento [4] .

O CFT assume que a inclinação da tensão de compressão principal no concreto, coincide com a inclinação da deformação compressiva principal e das fissuras desenvolvidas perpendicularmente à direção principal de tração no concreto, essa suposição levou a imprecisões quanto à rigidez pós- fissuração do concreto.

Uma série de placas de concreto armado foram testadas experimentalmente na Universidade de Toronto em 1982 por Vecchio e Collins [5], e por Collins et al. [6] em 1985. No ano de 1986, Vecchio e Collins propuseram a Teoria Modificada do Campo de Compressões (*Modified Compression Field Theory* - MCFT), que assume o contributo da resistência do concreto à tração de modo a prever a rigidez do concreto pós-fissurado [7]. Meyboom relata em 1987, os resultados dos testes de uma série de três placas de concreto protendido, também realizados na Universidade de Toronto [8].

Em 1988, Balakrishinan e Murray definiram novas relações constitutivas dos materiais [9,10] e aplicaram os resultados em um modelo de fissura rotativa para prever o comportamento em placas submetidas ao cisalhamento [11], a validação ocorreu por comparação com resultados experimentais [5]. No mesmo ano, Hsu desenvolveu o modelo denominado de Modelo de Treliça com Amolecimento (*Softened Truss Model* - STM), que considera iguais a direção das fissuras e a direção das tensões principais no elemento de concreto [12].

Crisfield e Wills em 1989, demonstraram a diferença entre modelos de fissura fixa e modelos de fissura rotativa [13]. Para alcançar esse objetivo os resultados analíticos fornecido pelo modelo de fissura fixa, modelo de fissura rotativa e modelo de plasticidade simples foram comparados com resultados experimentais [5]. Nesse mesmo ano, Bhide e Vecchio analisaram novos painéis na Universidade de Toronto [14].

A década de noventa marca o início de uma fase de grande importância e volume de coleta de dados experimentais para os modelos analíticos, e também de avanços em novos modelos analíticos, a começar em 1990 quando Vecchio apresenta um modelo ortotrópico de fissura rotativa [15]. Dois anos depois, Marti e Meyboom testaram na Universidade de Toronto uma série de três placas reforçadas ortogonalmente, uma de concreto armado e duas de concreto protendido [16].

No ano de 1994 foi iniciado o desenvolvimento do Modelo de Treliça com Amolecimento e Ângulo Variável (*Rotating-Angle Softened Truss Model* - RA-STM) por Belarbi e Hsu , na Universidade de Houston. Nessa oportunidade foi proposta uma nova relação constitutiva para o aço em tração [17]. O modelo RA-STM foi finalizado em 1995 por Belarbi e Hsu [18], e por Pang e Hsu [19].

Nesse mesmo ano, Hsu, Belarbi e Pang iniciaram testes [20], em condições controladas [21], no *Universal Panel Tester* localizado na Universidade de Houston. Ao longo de vinte anos de atividade, Hsu e sua equipe, totalizaram testes experimentais em cerca de 130 placas com diversas características e configurações.

Em 1996, Pang e Hsu apresentaram o Modelo de Treliça com Ângulo Fixo (*Fixed-Angle Truss Model* - FA-STM), esse modelo inclue a resistência ao cisalhamento do concreto ao longo da direção da fissura inicial e requer quatro relações constitutivas dos materiais [22]. E em 1997, Hsu e Zhang confirmam a eficiência do FA-STM [23], através de uma análise comparativa entre as previsões fornecidas pelo modelo e resultados experimentais[20].

Hsu apontou dois erros conceituais do MCFT em 1998, um relacionado às tensões e outro relacionado ao ângulo de fissura, adicionalmente demonstrou a correta distribuição de tensões em um elemento de membrana submetido ao cisalhamento [24]. No mesmo ano, Zhang e Hsu testaram experimentalmente no *Universal Panel Tester* uma série de 14 placas de concreto de alta resistência de 100MPa submetidos à carregamentos biaxiais, os resultados experiementais foram comparados com sucesso com as previsões fornecidas pelos modelos RA-STM e FA-STM [25]. Ainda em 1998, Ayoub e Filippou apresentaram um modelo constitutivo de concreto ortotrópico [26], baseado em estudos anteriores [9,10,11,15], para a validação do modelo foram utlizados resultados experimentais [5].

Nos ano 2000 e 2001, Vecchio trabalhou no desenvolvimento de um modelo de campo de tensões perturbado (*Disturbed Stress Field Model* - DSFM), baseado no modelo de fissuras rotativas que incluia deslizamentos provocados pelo cisalhamento ao longo da fissura e exigia a verificação com utilização do MCFT. A validação do modelo foi feita à partir da comparação com resultados experimentais [5] e resultados fornecidos pelo MCFT [27].

Também em 2001, Mansour, Lee e Hsu realizaram testes em 6 placas de concreto armado submetidas à carregamentos cíclicos reversos [28]. O objetivo desse estudo foi obter as relações constitutivas cíclicas do concreto e do aço, para capacitar os modelos analíticos a prever o comportamento de estruturas de concreto armado submetidas ao cisalhamento cíclico.

No mesmo ano, Belletti et al. apresentaram um modelo de fissura fixa que incorporava o interbloqueamento dos agregados e o efeito ferrolho [29]. A validação do modelo foi realizada através da análise comparativa com resultados experimentais [5,6,14,18,19].

Ainda em 2001, Zhu, Hsu e Lee simplificaram o modelo FA-STM, que deixou de possuir um algoritmo de solução em duas etapas, e melhoraram a precisão do modelo com a adoção de uma nova relação tensão-deformação para o concreto em substituição a relação tensão-deformação anterior obtida empiricamente [30] .

O Modelo de Membrana com Amolecimento (*Softened Membrane Model* - SMM) apresentado por Hsu e Zhu em 2002, foi desenvolvido para prever todo o comportamento de placas submetidas ao cisalhamento monotônico, inclusive com maior rigor os ramos descendentes da curva cisalhamento – distorção pós-pico. Para alcançar este feito foi considerado o efeito de Poisson na fase fissurada, através da introdução dos designados racios Hsu/Zhu [31].

Em 2005, Mansour e Hsu apresentaram o Modelo de Membrana com Amolecimento Cíclico (*Cyclic Softened Membrane Model* - CSMM), utilizado para prever a rigidez, ductilidade e dissipação de energia de placas de concreto armado sujeitos a cisalhamento cíclico reverso [32]. A validação do modelo foi por análise comparativa com os resultados dos testes de 12 painéis de concreto armado submetidos a tensões de cisalhamento cíclicas reversas [33].

O RA-STM é o modelo eleito para este trabalho devido a sua simplicidade análitica e confiabilidade. A incomplexidade da formulação e procedimento de cálculo do RA-STM, destaca-se face a comparações com modelos posteriores mais avançados, como o FA-STM e o SMM. Desde os primeiros estudos, o RA-STM apresentou-se suficientemente confiável para prever o comportamento de placas de concreto estrutural pelo menos até o pico de carga [19].

3. Modelo de treliça com amolecimento e ângulo variável

A análise do comportamento pré-pico de elementos estruturais do tipo placa, submetidos a esforços de membrana pode ser realizada com a utilização do modelo de treliça com amolecimento e ângulo variável (*Rotating-Angle Truss Model*-RA-STM*)* [17,18,19]. O nome do modelo é justificado pelo mecanismo de resistência assemelhar-se a uma treliça, onde o concreto é responsável por resitir às tensões de compressão e as armaduras às tensões de tração. O modelo considera também o amolecimento do concreto devido a fissuração diagonal segundo a direção principal de compressão em elementos sob ação do cisalhamento, o comportamento não linear dos materiais e a redistribuição interna dos campos de tensões (ângulo variável nas escoras).

O RA-STM tem como fundamentos os três Princípios de Navier da mecânica dos materiais: equilíbrio das tensões, compatibilidade das deformações e as leis constitutivas dos materiais. As equações advindas do equilíbrio das tensões e de compatibilidade das deformações são obtidas através da análise do Círculo de Mohr, enquanto as leis constitutivas do concreto e do aço são embasadas nas relações médias tensão-deformação ($\sigma-\varepsilon$), calibradas experimentalmente.

3.1 Equilíbrio das tensões

A Figura 1 ilustra uma placa de concreto estrutural, submetido a tensões gerais de membrana, como a superposição de um elemento de concreto simples e uma malha ortogonal de aço. A orientação dos eixos *L-T* faz referência às armaduras longitudinal e transversal, respectivamente.

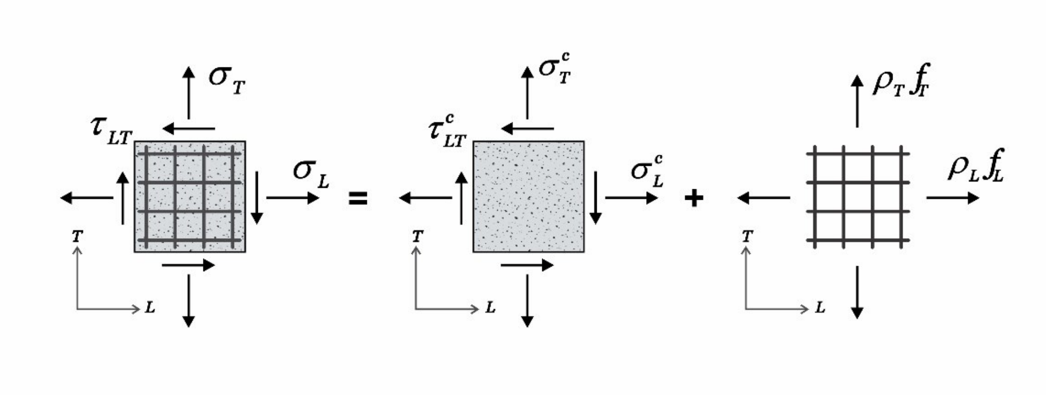

(a) (b) (c)

Figura 1 – Placa de concreto estrural submetido a tensões gerais de membrana:
(a) Concreto estrutural, (b) Concreto simples e (c) Malha ortogonal de aço.

As tensões gerais de membrana σ_L , σ_T , τ_{LT} podem ser separadas em componentes que atuam no concreto simples σ_L^c , σ_T^c , τ_{LT}^c e em componentes que atuam na malha de aço, $\rho_L f_L, \rho_T f_T$. O efeito ferrolho não é considerado, admite-se que as armaduras estão submetidas apenas a esforços axiais.

As tensões normais que atuam no elemento de concreto estrutural são representadas por σ_L e σ_T e a tensão de cisalhamento por τ_{LT}. No elemento de concreto simples, as tensões normais atuantes são representadas por σ_L^c e σ_T^c e a tensão de cisalhamento por τ_{LT}^c. As taxas de armadura são representadas por ρ_L e ρ_T , e as tensões atuantes nas armaduras são expressas por f_L e f_T.

A convenção de sinais adotada considera as tensões e deformações provenientes da solicitação de tração como positivas, e consequentemente as de compressão como negativas. Em adição, considera-se a perfeita aderência entre o aço e o concreto. Aplicando-se as condições de equilíbrio, obtem-se a Eq.1:

$$\begin{bmatrix} \sigma_L \\ \sigma_T \\ \tau_{LT} \end{bmatrix} = \begin{bmatrix} \sigma_L^c \\ \sigma_T^c \\ \tau_{LT}^c \end{bmatrix} + \begin{bmatrix} \rho_L f_L \\ \rho_T f_T \\ 0 \end{bmatrix} \tag{1}$$

A Figura 2 ilustra um elemento de concreto estrutural submetido a tensões principais de membrana, assumidas iguais à direção das fissuras, definida pelo sistema de coordenadas *R-D*. O ângulo variável α_R relaciona os sistemas de coordenadas *L-T* e *R-D*, a sua alteração ocorre consoante o aumento proporcional dos esforços de membrana, de modo que a resistência ao cisalhamento nessa orientação seja sempre nula, não é considerada a contribuição do concreto ao corte.

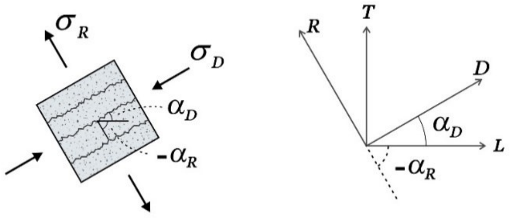

(a) (b)

Figura 2 - Elemento de concreto estrutural submetido a tensões principais de membrana: (a) Tensões principais aplicadas no concreto (R-D), (b) Eixos principais no concreto.

As tensões principais σ_D e σ_R podem ser definidas à partir das componentes das tensões aplicadas no concreto simples σ_L^c , σ_T^c , τ_{LT}^c e do ângulo α_R . Neste trabalho, optou-se pela utilização do ângulo α_D , complemento do ângulo α_R , essa modificação foi motivada pela igual possibilidade de utilização desse parâmetro para estimar a orientação das fissuras e pelo fato dos dois parâmetros conterem propriedades idênticas.

O RA-STM utilizada valores médios (*smeared*) para a tensão e deformação dos materiais ao longo de um comprimento suficiente para incluir várias fissuras, em detrimento da consideração de valores para pontos específicos. Dessa forma, evitava que a descontinuidade gerada pela fissuração interfirisse na avaliação dos resultados das previsões fornecidas pelo modelo.

A utilização do Círculo de Mohr das tensões na placa, permite a transformação de coordenadas entre *L-T* e *R-D*, para o elemento de concreto simples, conforme a Eq.2:

$$\begin{bmatrix} \varepsilon_L \\ \varepsilon_T \\ \gamma_{LT} \end{bmatrix} = \begin{bmatrix} \cos^2(\alpha_D) & sen^2(\alpha_D) & 2sen(\alpha_D)\cos(\alpha_D) \\ sen^2(\alpha_D) & \cos^2(\alpha_D) & -2sen(\alpha_D)\cos(\alpha_D) \\ -2sen(\alpha_D)\cos(\alpha_D) & 2sen(\alpha_D)\cos(\alpha_D) & 2\cos^2(\alpha_D)-2sen^2(\alpha_D) \end{bmatrix} \begin{bmatrix} \varepsilon_D \\ \varepsilon_R \\ 0 \end{bmatrix} \tag{2}$$

Aplicando a transformação de coordenadas segundo a Eq.2 na Eq.1, pode-se obter as equações de equilíbrio representadas na Eq.3:

$$\begin{bmatrix} \sigma_L \\ \sigma_T \\ \tau_{LT} \end{bmatrix} = \begin{bmatrix} \cos^2(\alpha_D) & sen^2(\alpha_D) & 2sen(\alpha_D)\cos(\alpha_D) \\ sen^2(\alpha_D) & \cos^2(\alpha_D) & -2sen(\alpha_D)\cos(\alpha_D) \\ -sen(\alpha_D)\cos(\alpha_D) & sen(\alpha_D)\cos(\alpha_D) & \cos^2(\alpha_D)-sen^2(\alpha_D) \end{bmatrix} \begin{bmatrix} \sigma_D \\ \sigma_R \\ 0 \end{bmatrix} + \begin{bmatrix} \rho_L f_L \\ \rho_T f_T \\ 0 \end{bmatrix} \tag{3}$$

Na versão original do RA-STM a contribuição da resistência do concreto à tração não era considerada, $\sigma_R = 0$. Dessa forma a Eq.3 pode ser descrita como as equações de equilíbrio Eqs.4–6:

$$\sigma_L = \sigma_D \cos^2(\alpha_D) + \rho_L f_L \tag{4}$$

$$\sigma_T = \sigma_D \operatorname{sen}^2(\alpha_D) + \rho_T f_T \tag{5}$$

$$\tau_{LT} = -\sigma_D \operatorname{sen}(\alpha_D)\cos(\alpha_D) \tag{6}$$

3.2 Compatibilidade das deformações

De modo análogo à seção anterior, a utilização do Círculo de Mohr das deformações pode relacionar os sistemas de coordenadas *L-T* e *R-D*, como mostra a Eq.7. Segundo o sistema de coordenadas *L-T*, as deformações médias nas direções longitudinal e transversal são representadas, respectivamente por ε_L e ε_T, enquanto γ_{LT} retrata a deformação devido ao cisalhamento. As deformações principais médias segundo os sistema de coordenadas *R-D* são representadas por ε_D e ε_R, respectivamente.

$$\begin{bmatrix} \varepsilon_L \\ \varepsilon_T \\ \gamma_{LT} \end{bmatrix} = \begin{bmatrix} \cos^2(\alpha_D) & sen^2(\alpha_D) & 2sen(\alpha_D)\cos(\alpha_D) \\ sen^2(\alpha_D) & \cos^2(\alpha_D) & -2sen(\alpha_D)\cos(\alpha_D) \\ -2sen(\alpha_D)\cos(\alpha_D) & 2sen(\alpha_D)\cos(\alpha_D) & 2\cos^2(\alpha_D)-2sen^2(\alpha_D) \end{bmatrix} \begin{bmatrix} \varepsilon_D \\ \varepsilon_R \\ 0 \end{bmatrix} \tag{7}$$

A combinação das duas primeiras linhas da Eq.7 e a utilização de algumas identidades trigonométricas possibilita a obtenção do 1° Princípio da Invariância das Deformações, de acordo com a Eq.8:

$$\varepsilon_L + \varepsilon_T = \varepsilon_D + \varepsilon_R \tag{8}$$

A deformação devido ao cisalhamento segundo o sistema de coordenadas *L-T*, calculada na última linha da Eq.7, pode ser representada de maneira simplificada conforme a Eq.9:

$$\gamma_{LT} = 2(\varepsilon_R - \varepsilon_D)sen(\alpha_D)\cos(\alpha_D) \tag{9}$$

3.3 Relações constitutivas dos materiais

O concreto sujeito à compressão, e as armaduras longitudinais e transversais sujeitas à tração, são os materiais considerados na versão original do modelo RA-STM. A incorporação dos referidos materiais, é realiza por intermédio de leis constitutivas médias.

3.3.1 *Concreto submetido à compressão*

Um corpo de prova cilíndrico de concreto sob ação de uma carga uniaxial de compressão pode ter a representação da curva $\sigma-\varepsilon$ expressa matematicamente pela parábola de Hognestad [34], apresentada na Eq.10:

$$\sigma_D = f_{ck}\left[2\left(\frac{\varepsilon_D}{\varepsilon_0}\right)-\left(\frac{\varepsilon_D}{\varepsilon_0}\right)^2\right] \tag{10}$$

A tensão de compressão resistente do concreto é representada por f_{ck}, enquanto a deformação correspondente a esta tensão é retratada por ε_0, correntemente admitida igual a 2×10^{-3} para betões de resistência normal . A curva $\sigma-\varepsilon$ da Eq.10 está representada na Figura 3.

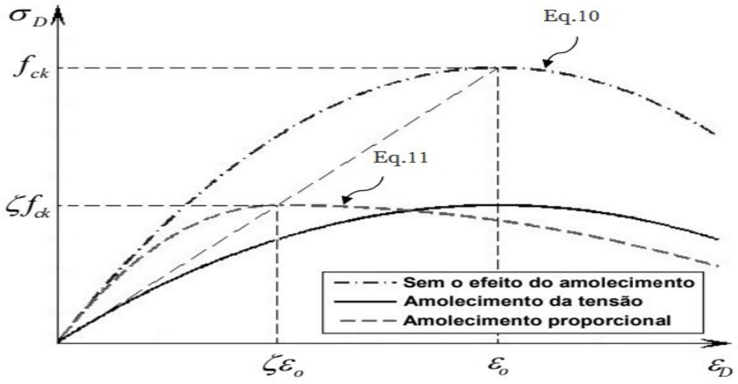

Figura 3 - Curva $\sigma-\varepsilon$ do concreto em compressão com amolecimento.

Para um estado biaxial de tração e compressão, não é coerente utilizar diretamente a curva da Eq.10, torna-se necessário ter em conta o efeito de amolecimento [3]. Alguns modelos consideram este efeito somente para a tensão, enquanto outros admitem o amolecimento proporcional, observado na tensão e na deformação.

A curva que representa a Eq.11, proposta por Hsu e Mo em 2010 [35], aproxima-se com mais realismo do comportamento em estudo, por considerar o amolecimento proporcional [36] e incorporar o coeficiente de amolecimento (ζ). Na versão original do RA-STM apenas era calculado o comportamento pré-pico da placa ($\varepsilon_D \leq \varepsilon_0$), correspondente à região ascendente da curva (Eq. 11), embora fosse possível calcular também o comportamento pós-pico ($\varepsilon_D > \zeta\varepsilon_0$). A curva $\sigma-\varepsilon$ da Eq.11 está também representada na Figura 3.

$$\sigma_D = \begin{cases} \zeta f_{ck}\left[2\left(\frac{\varepsilon_D}{\zeta\varepsilon_0}\right)-\left(\frac{\varepsilon_D}{\zeta\varepsilon_0}\right)^2\right], & \varepsilon_D \leq \zeta\varepsilon_0 \\ \zeta f_{ck}\left[1-\left(\frac{\frac{\varepsilon_D}{\xi\varepsilon_0}-1}{\frac{2}{\zeta}-1}\right)^2\right], & \varepsilon_D > \zeta\varepsilon_0 \end{cases} \tag{11}$$

Diversos autores dedicaram-se a equacionar o coeficiente de amolecimento. A partir de dados experimentais, Belarbi e Hsu [18] observaram que o referido coeficiente dependia das deformações decorrentes da tração principal no concreto (ε_R), expresso matematicamente conforme a Eq.12:

$$\zeta = \frac{0,9}{\sqrt{1+600\varepsilon_R}} \tag{12}$$

3.3.2 *Armaduras submetidas à tração*

Segundo Hsu e Mo [35], a curva elasto-plástica perfeita, apresentada na Figura 4, prevê de forma satisfatória a resistência ao cisalhamento de placas submetidas a esforços de membrana quando a resistência à tração é desprezada (σ_R), em adição representa bem comportamento à tração de uma barra de aço isolada.

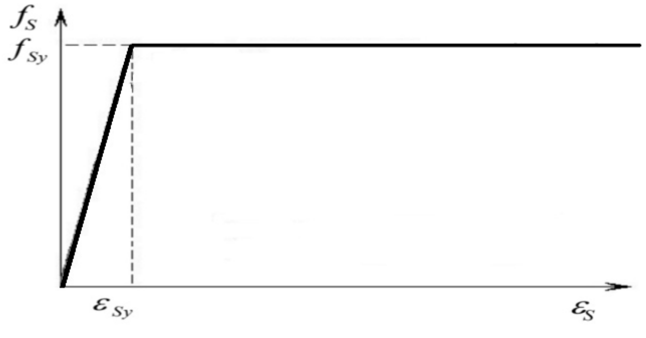

Figura 4 - Curva elasto-plástica perfeita para o aço.

A curva pode ser descrita conforme a Eq.13, onde o módulo de elasticidade do aço é expresso por E_S, enquanto ε_S representa a deformação no aço e ε_{Sy} a deformação de escoamento. A tensão no aço é representada por f_S, e a tensão de escoamento é representada por f_{Sy}.

$$f_S = \begin{cases} E_S \varepsilon_S \ , \ \varepsilon_s \leq \varepsilon_{Sy} = \dfrac{f_{Sy}}{E_S} \\ f_{Sy} \ , \ \varepsilon_S > \varepsilon_{Sy} \end{cases} \tag{13}$$

3.4 Carregamento proporcional

No carregamento proporcional a relação entre os esforços solicitantes se mantêm constantes, independente do estado de tensão que o elemento estrutural está submetido. As tensões gerais de membrana aplicadas no elemento podem ser relacionadas com a tensão principal de tração do elemento, através da utilização de constantes de proporcionalidade.

A Figura 5 ilustra uma placa de concreto estrutural, submetido a tensões gerais de membrana, segundo a orientação dos eixos *L-T*. Adicionalmente ilustra as relações de proporcionalidade entre as tensões gerais de membrana e a tensão principal de tração da placa. Ilustra também os eixos principais para as tensões solicitantes no elemento estrutural, representados pelo sistema de coordenadas 1-2.

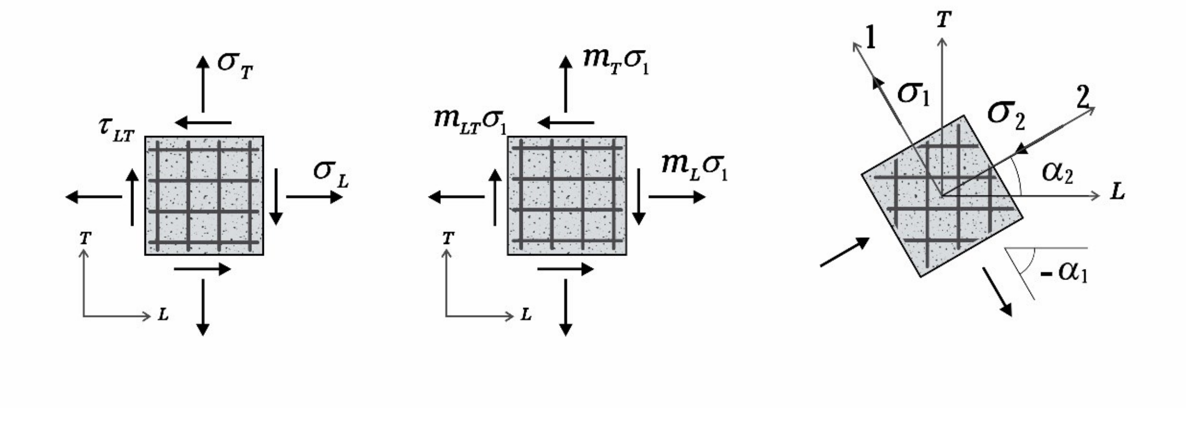

(a) (b) (c)

Figura 5 – Relações entre as solicitações e a tensão principal de tração na placa : (a) Tensões gerais de membrana, (b) Relações de proporcionalidade e (c) Eixos ordenados 1-2.

As tensões gerais de membrana são representadas pelos parâmetros σ_L , σ_T e τ_{LT} , enquanto a tensão principal de tração solicitante do elemento é descrita como σ_1 e a tensão principal de compressão solicitante por σ_2. As constantes de proporcionalidade são descritas por m_L , m_T e m_{LT} . O ângulo α_1 relaciona os sistemas de coordenadas *L-T* e 1-2, este ângulo é invariável diante do aumento proporcional das tensões solicitantes aplicados no elemento estrutural [35]. À semelhança da consideração feita anteriormente ao ângulo α_R , a orientação do sistema de coordenadas 1-2 pode ser definida pelo ângulo complementar α_2 .

Os coeficientes de proporcionalidade entre os esforços aplicados no elemento estrutural e a tensão principal de tração podem ser relacionados através das Eqs.14-16:

$$m_L = \frac{\sigma_L}{\sigma_1} \tag{14}$$

$$m_T = \frac{\sigma_T}{\sigma_1} \tag{15}$$

$$m_{LT} = \frac{\tau_{LT}}{\sigma_1} \tag{16}$$

A utilização do Círculo de Mohr possibilita o cálculo da tensão principal de tração solicitante conforme a Eq.17:

$$\sigma_1 = \frac{\sigma_L + \sigma_T}{2} + \sqrt{\left(\frac{\sigma_L - \sigma_T}{2}\right)^2 + \tau_{LT}{}^2} \tag{17}$$

Segundo Hsu e Mo [35], substituindo os coeficientes de proporcionalidade anteriormente calculados nas Eqs.4-6, pode-se encontrar:

$$m_L\sigma_1 - \rho_L f_L = \sigma_D \cos^2(\alpha_D) \tag{18}$$

$$m_T\sigma_1 - \rho_T f_T = \sigma_D sen^2(\alpha_D) \tag{19}$$

$$m_{LT}\sigma_1 = -\sigma_D \operatorname{sen}(\alpha_D)\cos(\alpha_D) \tag{20}$$

Multiplicando a Eq.18 pela Eq.19, elevando ao quadrado a Eq.20 e combinando os resultados, pode-se obter a Eq.21:

$$(m_L\sigma_1 - \rho_L f_L)(m_T\sigma_1 - \rho_T f_T) = (m_{LT}\sigma_1)^2 \tag{21}$$

A Eq.21 pode ser solucionada através da Eq.22, onde os coeficientes *H, B e C* são definidos nas Eqs.23-25:

$$\sigma_1 = \frac{1}{2H}\left(B \pm \sqrt{B^2 - 4HC}\right) \tag{22}$$

$$H = m_L m_T - m_{LT}{}^2 \tag{23}$$

$$B = m_L\rho_T f_T + m_T\rho_L f_L \tag{24}$$

$$C = \rho_T f_T \rho_L f_L \tag{25}$$

A Eq.22, apresentada por Hsu e Mo [35], tem grande relevância para o RA-STM por permitir o cálculo da tensão σ_1 em qualquer ponto estudado no comportamento carga-deformação da placa, somente com a utilização dos coeficientes de proporcionalidade, taxas de armadura e tensões nos aços.

3.5 Equações adicionais

Com recursos da trigonometria e das equações de compatibilidade (Eq.7), pode-se obter o ângulo α_D através das deformações nos sistemas de coordenadas *L-T* e *R-D*, conforme as Eqs.26-27:

$$sen^2\left(\alpha_D\right)=\frac{\varepsilon_L-\varepsilon_D}{\varepsilon_R-\varepsilon_D}=\frac{\varepsilon_R-\varepsilon_T}{\varepsilon_R-\varepsilon_D} \tag{26}$$

$$\cos^2\left(\alpha_D\right)=\frac{\varepsilon_R-\varepsilon_L}{\varepsilon_R-\varepsilon_D}=\frac{\varepsilon_T-\varepsilon_D}{\varepsilon_R-\varepsilon_D} \tag{27}$$

Estas equações são fundamentais para a estabilidade numérica do RA-STM, por possibilitarem a eliminação do ângulo α_D das equações de equilíbrio. Encontrada a solução, o ângulo α_D pode ser definido conforme a Eq.28:

$$\alpha_D=\arctan\left(\sqrt{\frac{\varepsilon_L-\varepsilon_D}{\varepsilon_T-\varepsilon_D}}\right) \tag{28}$$

3.6 Sistema de equações não lineares

Adicionando as Eqs.18 e 19 com as Eqs.27 e 28, respectivamente, e rearranjando as equações pode-se obter a função resíduo mostrada na Eq.29:

$$F_{RA-STM}=\begin{bmatrix}\sigma_D\dfrac{\varepsilon_T-\varepsilon_D}{\varepsilon_R-\varepsilon_D}-m_L\sigma_1+\rho_L f_L\\ \sigma_D\dfrac{\varepsilon_L-\varepsilon_D}{\varepsilon_R-\varepsilon_D}-m_T\sigma_1+\rho_T f_T\end{bmatrix}=\begin{bmatrix}0\\0\end{bmatrix} \tag{29}$$

As leis constitutivas dos materiais impõem a não linearidade das equações contidas na função resíduo F_{RA-STM} . As variáveis que atuam no procedimento de solução são as deformações nos aços ε_L e ε_T, definindo-se os seus valores por mil (10^{-3}), de modo a minimizar problemas de convergência.

3.7 Algoritmo de solução original

A Figura 6 ilustra o fluxograma do procedimento de solução original do RA-STM, o arranque do método interativo de cálculo depende que sejam arbitrados valores para ε_R e σ_1, posteriormente verificados. A estimativa desses valores é inerente ao usuário do algoritmo, com ausência de uma metodologia clara.

A utilização da curva elasto-plástica perfeita como relação constitutiva do aço, estabelece ao usuário que deseja calcular mais de um ponto da curva carga-deformação da placa, a necessidade de alterar o valor designado para ε_D, e de garantir que o limite estipulado por $\zeta\varepsilon_0$ não seja ultrapassado.

Esta técnica de tentativa e erro tende a encontrar a solução, porém quando existe a necessidade de demasiadas estimativas, o método perde eficiência e pode torna-se inviável.

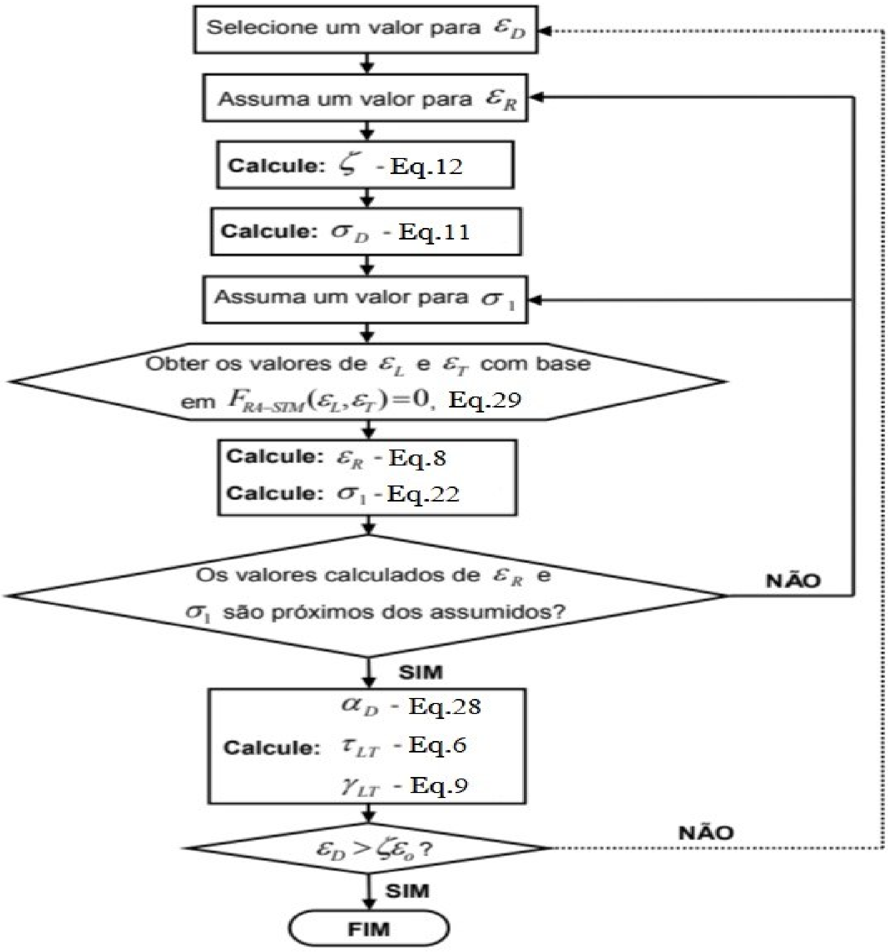

Figura 6 - Fluxograma do procedimento original: análise de placa de concreto estrutural.

3.8 Algumas contribuições recentes ao RA-STM.

Desde a sua concepção na década de noventa do século passado [17,18,19], o RA-STM vem sendo aprimorado por diversos autores, de modo a aproximar as previsões fornecidas pelo modelo ao comportamento real de placas de concreto estrutural sujeitas ao cisalhamento. De entre os avanços recentes podem-se citar os trabalhos desenvolvidos por Cerquido [39] e Lyrio [40] na Universidade da Beira Interior.

Baseado no procediemento proposto por Silva e Horowitz em 2015 [37] e Silva et al. em 2017 [38], Cerquido introduziu novas relações constitutivas para os materiais e alterou os critérios de paragem impostos anteriormente [37]. Desse modo, o modelo foi capaz de determinar o comportamento pós-pico das placas, sem a necessidade de considerar a resistência ao cisalhamento do betão e nem o efeito de Poisson no estado pós- fissurado [39].

Tendo também por base o algoritmo proposto por Siva e Horowitz em 2015 [37] e Silva et al. em 2017 [38], Lyrio reviu as equações de equilíbrio inicialmente estabelecidas para o RA-STM [35] e complementou as relações constitutivas do aço com a participação das armaduras protendidas. Por conseguinte extendeu o procedimento para incluir a análise de placas de concreto protendido [40].

Uma vez que os desenvolvimentos recentes anteriormente referidos servem de base para o presente trabalho, detalhes das formulações e procedimentos de cálculo são apresentados nos capítulos subsequentes, com as respetivas novas propostas de desenvolvimento e aplicação.

Referências Bibliográficas

[1] Ritter, W. (1899), “Die Bauweise Hennebique”, Schweizerische Bauzeitung, Vol.33, No.5, 6, and 7, Zurich, pp. 41-43, 49-52, and 59-61.

[2] Morsch, E. (1902), “Der Eisenbetonbau, seine Anwendung und Theorie”, Wayss and Freytag, A. G, Im Selbstverlag der Firma, Neustadt, A.D. Haardt, May 1902, pp. 118.[3]

Robinson, J. R. and Demorieux, J. M. (1968), “Essai de Traction-Compression sur Modeles d'Ames de Poutre en Beton Arme”, Compte Rendu PartielI, U.T.I., Institut de Recherches Appliquees du Beton Arme, Paris, France, pp. 43.

[4] Vecchio, F. and Collins, M.P. (1981), “Stress-strain Characteristic of Reinforced Concretein Pure Shear”, LABSE Colloquium, Advanced Mechanics of Reinforced Concrete, Delft, Final Report, International Association of Bridge and Structural Engineering, Zurich, Switzerland, pp. 221-225.

[5] Vecchio, F. J. and Collins, M. P. (1982), “Response of Reinforced Concrete to In Plane Shear and Normal Stresses”, Report No.82-03, University of Toronto, Toronto, Canada.

[6] Collins, M. P., Vecchio, F. J., and Mehlhom, G. (1985), “An International Competition to Predict the Response of Reinforced Concrete Panels”, Canadian Journal of Civil Engineering, Ottawa, Vol. 12, No. 3, pp. 626-644.

[7] Vecchio, F. J., and M. P. Collins (1986), “The Modified Compression Field Theory for Reinforced Concrete Elements Subjected to Shear”, ACI Journal, Vol. 83, No. 2, pp. 219-231.

[8] Meyboom, J. (1987), “An Experimental Investigation of Partially Presfressed, Orthogonally Reinforced Concrete Elements Subjected to Membrane Shear”, Masters Thesis, Department of Civil Engineering, University of Toronto, Toronto, Canada.

[9] Balakrishnan, S. and Murray, D. W. (1988), "Concrete Constitutive Model for NLFE Analysis of Structures," Journal of Structural Engineering, ASCE, Vol. 114, No. 7, July 1988, pp. 1449-1466.

[10] Balakrishnan, S. and Murray, D. W. (1988), “Strength of Reinforced Concrete Panels”, Canadian Journal of Civil Engineering, Vol. 15, No. 5, Oct. 1988, pp. 900-911.

[11] Balakrishnan, S. and Murray, D. W (1988), “Prediction of R/C Panels and Deep Beam Behavior by NLFEA”, Journal of Structural Engineering, ASCE, Vol. 114, No. 10, Oct. 1988, pp. 2323-2342.

[12] Hsu,T. T. C. (1988), “Softened Truss Model Theory for Shear and Torsion”, Structural Journal of the American Concrete Institute, 85(6), 1988, pp. 624-635.

[13] Crisfield, M. A. and Wills, J. (1989), "Analysis of R/C Panels Using Different Concrete Models", Journal of Engineering Mechanics, ASCE, Vol. 115, No. 3, Mar. 1989, pp. 578-597.

[14] Bhide, B. S. and Collins, M. P. (1989), "Influence of Axial Tension on Shear Capacity of Reinforced Concrete Members", ACI Structural Journal, Vol. 86, No. 5, pp. 570-580.

[15] Vecchio, F. J. (1990), "Reinforced Concrete Membrane Element Formulation", Journal of Structural Engineering, ASCE, Vol. 116, No. 3, pp. 730-750.

[16] Marti, P. and Meyboom, J. (1992), " Response of Prestressed Concrete Elements to In-Plane Shear Forces", J.Am. Concr.Inst., vol. 89, No. 5, 1992, pp. 503-514.

[17] Belarbi, A. and Hsu, T. T. C. (1994), "Constitutive Laws of Concrete in Tension and Reinforcing Bars Stiffened by Concrete", Structural Journal of the American Concrete Institute, Vol. 91, No. 4, pp. 465-474.

[18] Belarbi, A. and Hsu, T. T. C. (1995), "Constitutive Laws of Softened Concrete in Biaxial Tension-Compression", Structural Journal of the American Concrete Institute, Vol. 92, No. 5, pp. 562-573.

[19] Pang, X. B. and Hsu, T. T. C. (1995), "Behavior of Reinforced Concrete Membrane Elements in Shear", Structural Journal of the American Concrete Institute, Vol. 92, No. 6, pp. 665-679.

[20] Hsu, T. T. C, Belarbi, A., and Pang, X. B. (1995), "A Universal Panel Tester", Journal of Testing and Evaluations, ASTM, Vol. 23, No. 1, pp. 41-49.

[21] Hsu, T. T. C, Zhang, L. X., and Gomez, T. (1995), "A Servo-confrol System for Universal Panel Tester", Journal of Testing and Evaluations, ASTM, Vol. 23, No. 6, pp. 424-430.

[22] Pang, X. B. and Hsu, T. T. C. (1996), "Fixed-Angle Softened-Truss Model for Reinforced Concrete", Structural Journal of the American Concrete Institute, Vol. 93, No. 2, pp.197-207.

[23] Hsu, T. T. C. and Zhang, L. X. (1997), “Nonlinear Analysis of Membrane Elements by Fixed-Angle Softened-Truss Model”, Structural Journal of the American Concrete Institute, Vol. 94, No. 5, pp. 483-492.

[24] Hsu, T. T. C. (1998), “Stresses and Crack Angles in Concrete Membrane Elements”, Journal of Structural Engineering, ASCE, Vol. 124, No. 12, Dec. 1998, pp. 1476-1484.

[25] Zhang, L. X. and Hsu, T. T. C. (1998), “Behavior and Analysis of 100Mpa Concrete Membrane Elements”, Journal of Structural Engineering, ASCE, Vol. 124, No. 1, Jan. 1998, pp. 24-34.

[26] Ayoub, Amir and Filippou, Filip C. (1998), “Nonlinear Finite-Element Analysis of RC Shear Panels and Walls”, Journal of Structural Engineering, ASCE, Vol. 124, No. 3, Mar. 1998, pp. 298-308.

[27] Vecchio, F. J., Lai, D., Sim, W., and Ng, J. (2001), “Disturbed Stress Field Model for Reinforced Concrete: Validation”, Journal of Structural Engineering, ASCE, Vol. 127, No. 4, April 2001, pp. 350-358.

[28] Mansour, M.,Lee, J. Y., and Hsu, T. T. C. (2001), “Cyclic Stress-Strain Curves of Concrete and Steel Bars in Membrane Elements”, Journal of Structural Engineering, ASCE, V. 127, No. 12, 2001, pp. 1402-1411.

[29] Belletti, B., Cerioni, R., and Iori, I. (2001), “Physical Approach for Reinforced-Concrete (PARC) Membrane Elements”, Journal of Structural Engineering, ASCE, Vol. 127, No. 12, Dec. 2001, pp. 1412-1426.

[30] Zhu, R. H., Hsu, T. T. C, and Lee, J. Y. (2001), “Rational Shear Modulus for Smeared Crack Analysis of Reinforced Concrete”, Structural Journal of the American Concrete Institute, Vol. 98, No. 4, pp. 443-450.

[31] Hsu, T. T. C. and Zhu, R. R. H. (2002), “Softened Membrane Model for Reinforced Concrete Elements in Shear”, Structural Journal of American Concrete Institute, Vol. 99, No. 4, pp. 460-469.

[32] Mansour, M. and Hsu, T. T.C. (2005), “Behavior of Reinforced Concrete Elements under Cyclic Shear. II: Theoretical Model”, Journal of Structural Engineering-asce - J STRUCT ENG-ASCE. 131. 10.1061/(ASCE)0733-9445(2005)131:1(54).

[33] Mansour, M. and Hsu, T. T.C. (2005), “Behavior of Reinforced Concrete Elements under Cyclic Shear. I: Experiments”, Journal of Structural Engineering-asce - J STRUCT ENG-ASCE. 131. 10.1061/(ASCE)0733-9445(2005)131:1(44).

[34] Hognestad, E. (1952), “What Do We Know About Diagonal Tension and Web Reinforced in Concrete ?”, Circular S. No.64, 1952. University of Illinois.

[35]] Hsu, T. T. C, MO, Y. L. (2010), “Unified Theory of Concrete Structures”, Wiley.

[36] Bernardo, L. F. A, Andrade, J. M. A and Nunes, N. C. G. (2015), “ Generalized Softened Variable Angle Truss-Model for reinforced Concrete Beams under Torsion”, Materials and Structures, Vol.48.No 7, 2015, pp.2169-2193.

[37] Silva, J. R. B. e Horowitz, B. (2015), “Procedimento Eficiente Para Estimar o Comportamento Carga-Deformação de Painéis de Concreto Armado Submetidos a Esforços de Membrana Usando o Modelo de Treliça com Amolecimento e Ângulo Variável”, CILAMCE 2015 – XXXVI Iberian Latin American Congresso on Computacional Methods in Engineering, Rio de Janeiro-RJ, Brasil.

[38] Silva, J., Horowitz, B., Bernardo, L. (2017), “Efficient Procedure to Analyze RC Beam Sections using the Softened Truss Model”, ACI Structural Journal, American Concrete Institute, Vol. 114, No. 3, May-June 2017, pp. 1-10.

[39] Bernardo, L. F. A, Cerquido, B. M. D, Silva, J. R. B and Horowitz, B. (2018), “Efficient refined rotating-angle softened truss model procedure to analyze reinforced concrete membrane elements”, Structural Concrete, pp. 1971-1982, Wiley Online Library.

[40] Bernardo, L. F. A, Lyrio, A. R. B, Silva, J. R. B and Horowitz, B. (2018), “Refined softened truss model with efficient solution procedure for prestressed concrete membranes”, Journal of Structural, ascelibrary.org.

Capítulo 3

Modelo de Treliça com Amolecimento e Ângulo Varável (RA-STM): Descrição do Modelo e Propostas de Refinamento/Otimização.

Este capítulo consiste no artigo:

Softened Variable Truss Model (RA-STM): Model Description and Refinement/ Optimization Proposals.

Filho, B.; Bernardo, L.; Horowitz, B. 2020 “Softened Variable Angle Truss Model (RA-STM): Model Description and Refinement/ Optimization Proposals”, in STARTCON19 – International Doctorate Students + Lab Workshop in Civil Engineering, Kne Engineering, pages 36-48.
DOI: 10.18502/keg.v5i5.6909

KnE Engineering
STARTCON19
STARTCON19 - International Doctorate Students Conference +
Lab Workshop in Civil Engineering
Volume 2020

Conference Paper

Softened Variable Angle Truss Model (RA-STM): Model Description and Refinement/Optimization Proposals

Benedito Filho[1], Luís Bernardo[1], and Bernardo Horowitz[2]

[1]C-MADE - Centre of Materials and Building Technologies, University of Beira Interior, Covilhã, Portugal
[2]Department of Civil Engineering, Federal University of Pernambuco, Brazil

Abstract

This article presents a recent softened truss model with variable angle, namely the refined RA-STM (Rotating-Angle Softened Truss Model), to model the behaviour of structural concrete plates under pure shear. The equations of the model, as well as the solution procedure, are summarized. Some predictions from the RA-STM are also presented, discussed and compared with experimental results available in the literature. It is shown that the refined RA-STM still needs to be refined. In addition, the need to generalize the RA-STM for more general loading cases is also discussed as well as the need to optimize the solution procedure in order to facilitate its computational implementation.

Corresponding Author:
Benedito Filho
benedito.madian.filho@ubi.pt

Received: Month 2020
Accepted: Month 2020
Published: Month 2020

Publishing services provided by Knowledge E

Selection and Peer-review under the responsibility of the STARTCON19 Conference Committee.

1. Introduction

It is a common practice in structural engineering to discretize complex structures as a combination of simpler elements. As shown in Fig. 1 (a), some structures can be idealized as a set of two-dimensional structural concrete elements (panels, plates or membranes), with the reinforcement rebars usually arranged in orthogonal directions. Such elements are only subjected to in-plane stresses, which generate internal membrane forces. The full behaviour of such elements can be predicted with softened truss models (STM) considering rotating angles (RA) for the struts. Such models are called softened variable angle truss models or rotating angle – soft truss models (RA-STM).

Simple computational tools can be created from such models, which can be very useful to help for the design of structural concrete structures, namely to check the local safety of membrane elements.

The implementation of these nonlinear models is usually made in computers by using softwares with programming languages, such as MATLAB [1]. This allows to assess, calibrate and modify such models more easily.

How to cite this article: Benedito Filho, Luís Bernardo, and Bernardo Horowitz, (2020), “Softened Variable Angle Truss Model (RA-STM): Model Description and Refinement/Optimization Proposals” in *STARTCON19 - International Doctorate Students Conference + Lab Workshop in Civil Engineering*, KnE Engineering, pages 1–11. DOI 10.18502/4

2. Description of the RA-STM Model

The RA-STM model was proposed by Belarbi and Hsu in 1994 [2] and Pang and Hsu in 1995 [3]. Recently, this model has been refined by Silva and Horowitz in 2015 [4], Silva in 2016 [5], Cerquido in 2017 [6] and Bernardo *et al.* in 2018 [7, 8].

The resistance mechanism of RA-STM is assumed to be a plane truss, in which the concrete resists to compressive stresses and the reinforcement resists to tensile stresses (Fig. 1 (b)). The non-linear behaviour and the softening effect of concrete are key features of this model. This model is based on the three Navier's principles of material mechanics, namely: stresses equilibrium, strains compatibility and constitutive relationships for the materials.

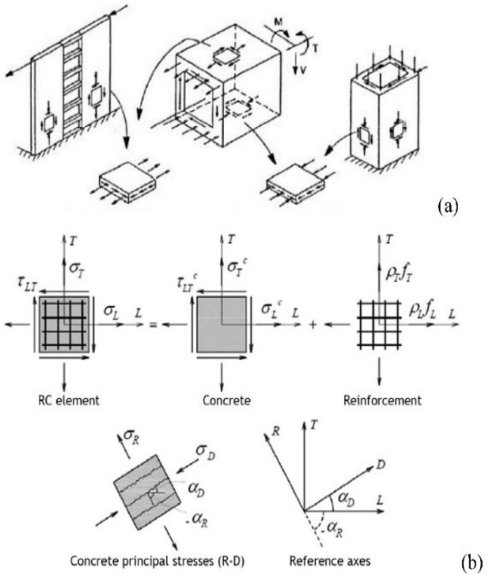

Figure 1: Membrane elements to analyse concrete structures [5, 6].

In the RA-STM, the equations derived from the stresses equilibrium and strains compatibility are obtained through the analysis of the Mohr´s circle for stresses (σ) and strains (ϵ), while the constitutive relationships for concrete and steel are assumed and based on average $\sigma - \epsilon$ relationships experimentally calibrated and found in the literature. For this reason, the relationship for concrete in compression ($\sigma_D - \epsilon_D$) in the principal direction of stresses has two main characteristics: a nonlinear relationship between stresses and strains and the influence of the softening effect in concrete due to transverse tensile stresses and diagonal cracking. For this latter, a softening coefficient ζ is incorporated to the constitutive relationship for concrete, which is experimentally calibrated and based on proposals that can be found in the literature.

2.1. Equations for RA-STM

Tables 1 to 3 summarize the set of equations of RA-STM. Details about the derivation of the presented equations for the original RA-STM and for reinforced concrete (RC) panels can be found in previous studies [2, 3, 5–7]. The meaning of all parameters can be found in the notation list at the end of this article. Some parameters can also be visualized in Fig. 1 (b).

TABLE 1: Equilibrium and compatibility equations [2, 3].

Equilibrium equations (stresses)	
$\begin{bmatrix}\sigma_L\\ \sigma_T\\ \tau_{LT}\end{bmatrix}=\begin{bmatrix}\sigma_L^c\\ \sigma_T^c\\ \sigma_{LT}^c\end{bmatrix}+\begin{bmatrix}\rho_L f_L\\ \rho_T f_T\\ 0\end{bmatrix}$	(1)
$\begin{bmatrix}\sigma_L^c\\ \sigma_T^c\\ \tau_{LT}^c\end{bmatrix}=\begin{bmatrix}\cos^2(\alpha_D) & \sin^2(\alpha_D) & 2\sin(\alpha_D)\cos(\alpha_D)\\ \sin^2(\alpha_D) & \cos^2(\alpha_D) & -2\sin(\alpha_D)\cos(\alpha_D)\\ -\sin(\alpha_D)\cos(\alpha_D) & \sin(\alpha_D)\cos(\alpha_D) & \cos^2(\alpha_D)-\sin^2(\alpha_D)\end{bmatrix}\begin{bmatrix}\sigma_D\\ \sigma_R\\ 0\end{bmatrix}$	(2)
$\begin{bmatrix}\sigma_L\\ \sigma_T\\ \tau_{LT}\end{bmatrix}=\begin{bmatrix}\cos^2(\alpha_D) & \sin^2(\alpha_D) & 2\sin(\alpha_D)\cos(\alpha_D)\\ \sin^2(\alpha_D) & \cos^2(\alpha_D) & -2\sin(\alpha_D)\cos(\alpha_D)\\ -\sin(\alpha_D)\cos(\alpha_D) & \sin(\alpha_D)\cos(\alpha_D) & \cos^2(\alpha_D)-\sin^2(\alpha_D)\end{bmatrix}\begin{bmatrix}\sigma_D\\ \sigma_R\\ 0\end{bmatrix}+\begin{bmatrix}\rho_L f_L\\ \rho_T f_T\\ 0\end{bmatrix}$	(3)
$\sigma_L=\sigma_D\cos^2(\alpha_D)+\rho_L f_L$	(4)
$\sigma_T=\sigma_D\sin^2(\alpha_D)+\rho_T f_T$	(5)
$\tau_{LT}=-\sigma_D\sin(\alpha_D)\cos(\alpha_D)$	(6)
Compatibility equations (strains)	
$\begin{bmatrix}\epsilon_L\\ \epsilon_T\\ \gamma_{LT}\end{bmatrix}=\begin{bmatrix}\cos^2(\alpha_D) & \sin^2(\alpha_D) & 2\sin(\alpha_D)\cos(\alpha_D)\\ \sin^2(\alpha_D) & \cos^2(\alpha_D) & -2\sin(\alpha_D)\cos(\alpha_D)\\ -2\sin(\alpha_D)\cos(\alpha_D) & 2\sin(\alpha_D)\cos(\alpha_D) & 2\cos^2(\alpha_D)-\sin^2(\alpha_D)\end{bmatrix}\begin{bmatrix}\epsilon_D\\ \epsilon_R\\ 0\end{bmatrix}$	(7)
$\epsilon_L+\epsilon_T=\epsilon_D+\epsilon_R$	(8)
$\gamma_{LT}=2(\epsilon_R-\epsilon_D)\sin(\alpha_D)\cos(\alpha_D)$	(9)

It should be noted that the initial estimates to initialize the solution procedure are computed using the Mohr compatibility truss model (MCTM) [9].

2.2. Solution procedure

Based on recent works, which aimed to refine the RA-STM, an efficient algorithm was successfully developed and proposed [4–7]. The associated flow chart is illustrated in Fig. 2. This algorithm needs to be implemented in a computer. In previous studies, MATLAB packages were used to implement the solution procedure [6, 7].

TABLE 2: Constitutive relationships for the materials [5–7].

Concrete in compression	
$\sigma_D = \begin{cases} \zeta f_C{}' \left[2\left(\frac{\epsilon_D}{\zeta\epsilon_0}\right) - \left(\frac{\epsilon_D}{\zeta\epsilon_0}\right)^2 \right], \text{ para } \epsilon_D \leq \zeta\epsilon_0 \\ \zeta f_C{}' \left[1 - \left(\frac{\frac{\epsilon_D}{\zeta\epsilon_0} - 1}{\frac{4}{\zeta} - 1} \right)^2 \right], \text{ para } \epsilon_D > \zeta\epsilon_0 \end{cases}$	(10)
$\zeta = \frac{R(f^{`})}{\sqrt{1 + \frac{400\epsilon_R}{\eta'}}}$	(11)
$\eta = \frac{\rho_T f_{Ty}}{\rho_L f_{Ly}}$	(12)
$\begin{cases} \eta \leq 1 \Rightarrow \eta' = \eta \\ \eta > 1 \Rightarrow \eta' = \frac{1}{\eta} \end{cases}$	(13)
$R(f_c') = \frac{5,8}{\sqrt{f_c'(\text{MPa})}} \leq 0,9$	(14)
Reinforcement in tension	
$f_S = \begin{cases} E_S \epsilon_S \text{ for } \epsilon_S \leq \epsilon_n \\ f_{Sy}[(0,91 - 2B) + (0,02 + 0,25B)\frac{\epsilon_S}{\epsilon_{Sy}}] \text{ for } \epsilon_S > \epsilon_n \end{cases}$	(15)
$\epsilon_n = (0,93 - 2B)\epsilon_{Sy}$	(16)
$B = \frac{1}{\rho}\left(\frac{f_{cr}}{f_{Sy}}\right)^{1,5}$	(17)
$f_{cr} = 0,311\sqrt{f_{cr}^{`}(\text{MPa})}$	(18)

3. Comparative Analysis with Some Experimental Results

Table 4 presents the main properties of two RC panels tested under shear and found in the literature [10, 11]. Some of the experimental results of these panels are compared below with those computed with the refined RA-STM [6, 7].

$$*\eta = \frac{\rho_T f_{Ty}}{\rho_L f_{Ly}}$$

Fig. 3 shows the $\sigma_D - \epsilon_D$ curves for concrete in compression (in the principal direction of compressive stresses) for panel VA1 [10]. Two curves are presented, the experimental one and the theoretical one computed from the refined RA-STM.

For the theoretical curve, a first stage with a quasi linear behaviour is observed. In this stage, as the compressive stress increases the corresponding strain also increases but at smaller rates. When the reinforcement yields, a strong nonlinear behaviour is observed until the peak stress is reached. After this, the strains highly increase with a small variation of the compressive stresses. The panel continues to behave in this

TABLE 3: Set of equations for the refined RA-STM [5–7]

Proportional loading	
$\sigma_L = m_L\sigma_1$ (19) $\sigma_T = m_T\sigma_1$	(20)
$\tau_{LT} = m_{LT}\sigma_1$	(21)
$\sigma_1 = \frac{\sigma_L + \sigma_T}{2} + \sqrt{\left(\frac{\sigma_L + \sigma_T}{2}\right)^2 + \tau_{LT}{}^2}$	(22)
$m_L\sigma_1 - \rho_L f_L = \sigma_D \cos^2\left(\alpha_D\right)$	(23)
$m_T\sigma_1 - \rho_T f_T = \sigma_D \sin^2\left(\alpha_D\right)$	(24)
$m_{LT}\sigma_1 = -\sigma_D \sin(\alpha_D)\cos(\alpha_D)$	(25)
$\sigma_1 = \frac{1}{2A'}\left(B' \pm \sqrt{B'^2 - 4A'C}'\right)$	(26)
$A' = m_L m_T - m_{LT}{}^2$	(27)
$B' = m_L\rho_T f_T - m_T\rho_L f_L$	(28)
$C' = \rho_T f_T \rho_L f_L$	(29)
Relations between stresses and strains	
$f_L = \frac{m_L + m_{LT}\cot(\alpha_D)}{\rho_L}\sigma_1$	(30)
$f_T = \frac{m_T + m_{LT}\tan(\alpha_D)}{\rho_T}\sigma_1$	(31)
$\sigma_D = \frac{-m_{LT}}{\sin(\alpha_D)\cos(\alpha_D)}\sigma_1$	(32)
$\epsilon_L = \frac{m_L + m_{LT}\cot(\alpha_D)}{E_S\rho_L}\sigma_1$	(33)
$\epsilon_T = \frac{m_T + m_{LT}\tan(\alpha_D)}{E_S\rho_T}\sigma_1$	(34)
$\epsilon_D = \frac{-m_{LT}}{E_c\sin(\alpha_D)\cos(\alpha_D)}\sigma_1$	(35)
Residual function for MCTM	
$F_{MCTM} = \frac{\epsilon_L - \epsilon_D}{\epsilon_T - \epsilon_D} - \tan^2(\alpha_D) = 0$	(36)
Residual function for RA-STM	
$F_{RA-STM} = \begin{bmatrix} \sigma_D\frac{\epsilon_T - \epsilon_D}{\epsilon_R - \epsilon_D} - m_L\sigma_1 + \rho_L f_L \\ \sigma_D\frac{\epsilon_L - \epsilon_D}{\epsilon_R - \epsilon_D} - m_T\sigma_1 + \rho_T f_T \end{bmatrix} = \begin{bmatrix} 0 \\ 0 \end{bmatrix}$	(37)

way until the criterion which define the theoretical failure is reached (at least one of the materials reach its conventional strain failure).

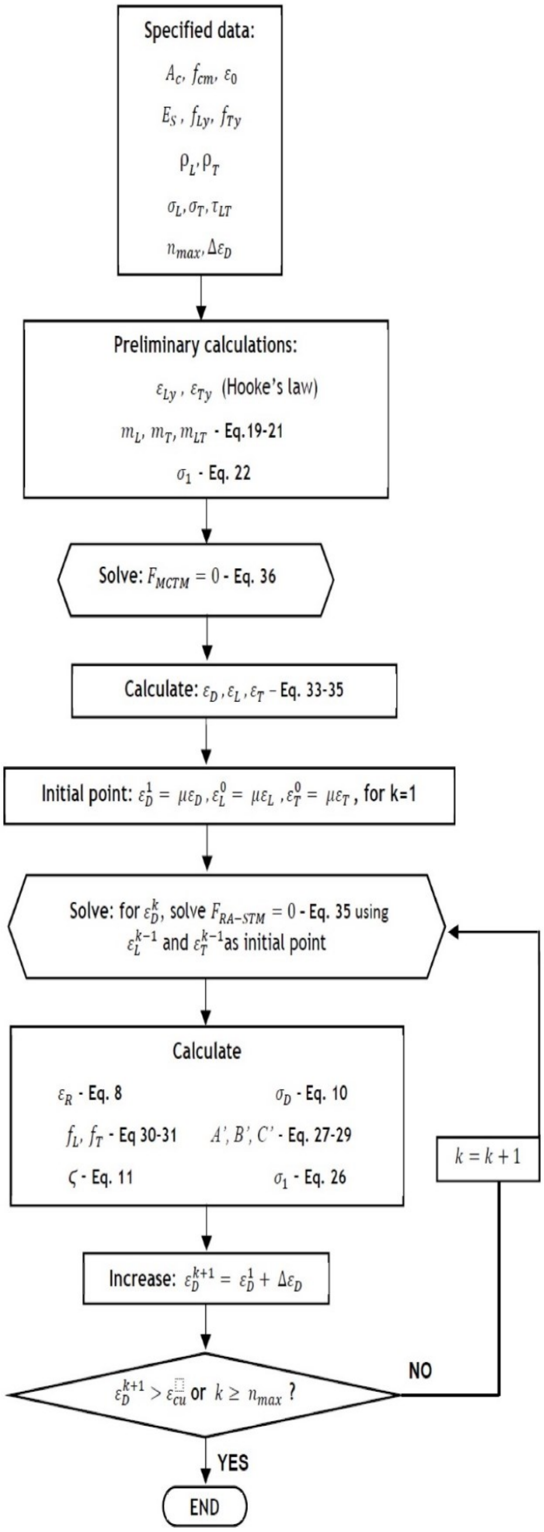

Figure 2: Flow Chart.

TABLE 4: Properties of tested RC panels under shear.

Panel	Concrete		Steel						η^*
			Longitudinal direction			Transverse direction			
	f_{cm} (MPA)	ε_0 (‰)	ρ_L	Reinforc.	f_{Ly} (MPA)	ρ_T	Reinforc.	f_{Ty} (MPA)	
VA1 [10]	95,1	2,45	0,012	10M@94 mm*	445	0,012	10M@94 mm*	445	1
B2 [11]	44,1	2,35	0,0179	-	446	0,0119	-	463	0,69

again at smaller rates, until the yielding of the reinforcement. In the third stage the strains highly increase and the compressive stress slowly decreases until failure is reached.

In general, the main features of the compressive concrete behaviour are well captured by the theoretical model, as well as the peak stress of concrete. However, the theoretical model is not able to predict the transition from the cracked stage to the uncracked stage. This is because the refined RA-STM neglects the influence of concrete in tension in the perpendicular direction to the principal compressive stresses ($\sigma_R = 0$, see Fig. 1 (b)), The previous results show that concrete in tension is important to be considered for low loading levels. In fact, the refined RA-STM considers that the plate is already fully cracked since the beginning of the loading. This simplification constitutes a drawback of the model, which needs to be solved because the transition from the cracked stage to the uncracked stage is important to be correctly predicted in order to assess the panel for loading services.

Fig. 4 shows the shear (τ_{LT}) versus shear strain (γ_{LT}) curves, both experimental and theoretical, for panel B2 [11]. The dashed curve corresponds to the prediction from the refined RA-STM, while the continuous curve corresponds to the original RA-STM from Pang and Hsu in 1995 [11]. This latter accounts for the tensile strength of concrete, in opposition to the refined RA-STM. Fig. 4 shows that the original RA-STM captures better the behaviour of the panel for low loading levels. This shows the importance for the model to include the influence of the concrete in tension. For the ultimate stage, the refined RA-STM shows better agreement with the experiment curve. In Fig. 4, both versions of the theoretical model capture well another feature of panel B2. This panel is not reinforced symmetrically (see parameter η in Table 3), its transverse reinforcement ratio is lesser that its longitudinal reinforcement ratio. For this reason, both reinforcements (longitudinal and transverse) didn´t yield for the same strain. This is shown in the graphs by two distinct points for which it is possible to observe two consecutive losses of stiffness, corresponding to the yielding of the transverse reinforcement (firstly) and longitudinal reinforcement (latter). This shows that RA-STM model is able to capture well the nonlinear behaviour under shear of asymmetrically reinforced panels.

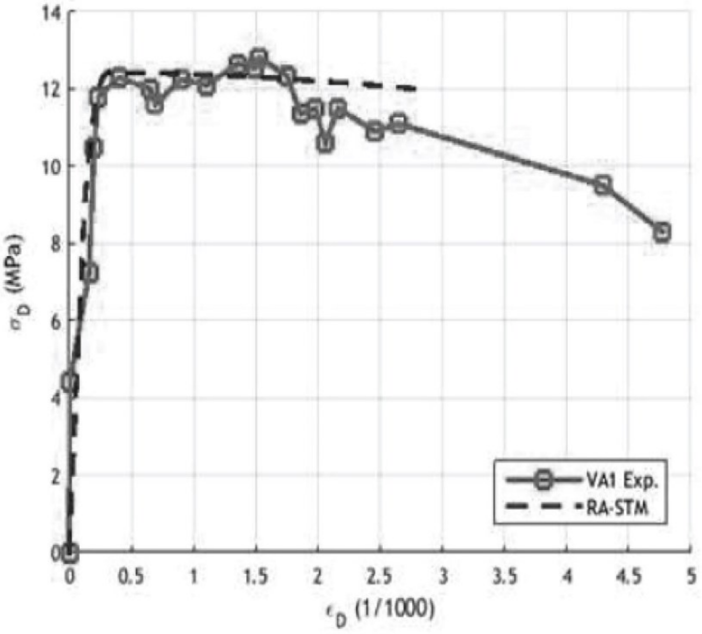

Figure 3: Comparison between $\sigma_D - \epsilon_D$ curves for panel VA1 [10].

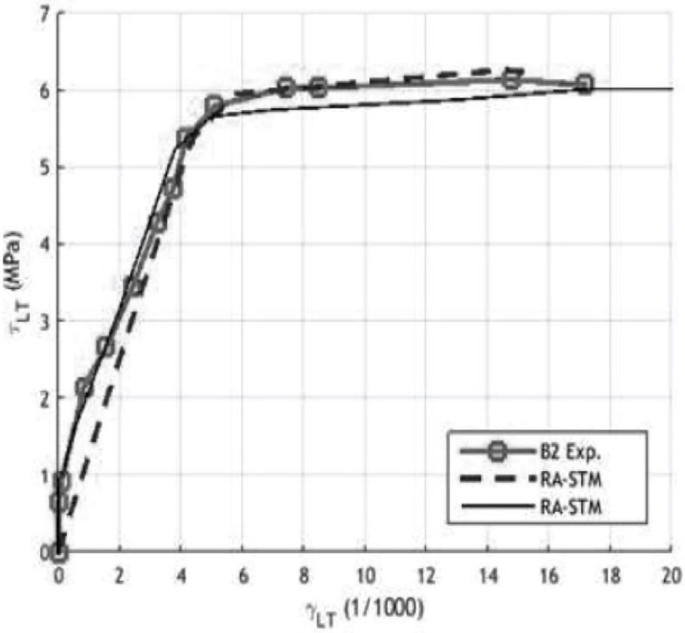

Figure 4: Comparison between $\tau_{LT} - \gamma_{LT}$ curves for panel B2 [11].

4. Future Developments for the Refined RA-STM

The previously presented results, related with panels VA1 and B2, generally show that the refined RA-STM is able to capture well the general features of panels under shear, namely for the ultimate stage. Additional examples with other panels under shear can be found in previous studies [6, 7], including for prestressed panels [8].

As referred before, the refined RA-STM neglects the influence of concrete in tension in the perpendicular direction to the principal compressive stresses. This drawback needs to be solved because the transition from the cracked stage to the uncracked stage needs to be correctly predicted. This is because current codes of practice impose to assess structural members for both the ultimate and service loading. For this latter, it is important to check the cracking load, as well as the stress state in the materials and the stiffness of the member after cracking.

The previous discussion only involved the behaviour of panels under shear. However, other loading conditions, such as axial stresses (combined or not with shear stresses) are common in structures (see Fig. 1 (a)). Few previous studies using RA-STM are focused on such condition loadings. Some of them show that RA-STM still do not capture the real behaviour of such panels and numerical problems are observed, which are mainly related with errors in the convergence criteria [6]. This shows that the RA-STM model still needs to be improved and generalized to other and more realistic loading conditions.

Finally, the intrinsic nonlinear feature of the RA-STM leads to a complex solution procedure, as previously shown. This problem can probably be minimized if the set of equations are rewritten using other criteria, such as the energetic ones. Many problems in physics are more easily formulated if they are based on energetic criteria, regardless of how they are applied (minimization of the potential energy or principle of virtual work for static or pseudo-static systems, least action principle for dynamics systems, etc.). The application of energetic criteria to establish the solution procedure for the RA-STM is still an open issue.

The previous discussion shows that the refined RA-STM still need further developments.

5. Conclusions

This article presented a recent softened truss model with variable angle, namely the refined RA-STM, to model the behaviour of structural concrete membranes under pure shear. The equations, as well as the solution procedure of the model, were summarily presented. Some predictions from the refined RA-STM, related to panels tested under shear, were also presented and compared with the corresponding experimental results which were found in the literature. From the comparative analysis, it was shown that the general features of RC panels under shear are well captured by the refined RA-STM, namely for the ultimate stage. For low loading conditions, the need to refine the model was also shown. In addition, some ideas were discussed in order to justify future developments for the refined RA-STM. Such developments constitute the main objectives for the Ph.D. project of the first author, which include specifically the following ones:

- to unify the refined RA-STM for reinforced concrete and prestressed concrete membranes;
- to consider the influence of concrete in tension in the refined RA-STM through the incorporation of an additional average constitutive relationship in the calculation procedure;
- to generalize the refined RA-STM to other loading conditions, including shear combined with axial forces and also cyclic loading;
- to optimize and simplify the calculation procedure of the refined RA-STM by using energetic criteria.

Finally, it should be referred that experimental data related with structural concrete membranes are still scarce and are not sufficient to fully assess the reliability of the refined RA-STM. For this reason, additional numerical results based on calibrated models using FEM will certainly be useful.

Notation

E_s = Young's modulus for steel

F_{MCTM} = residual function for MCTM

F_{RA-STM} = residual function for RA-STM

$f_c^{'};f_{cm}$ = uniaxial compressive strength of concrete

f_{cr} = tensile strength of concrete

f_L = tensile stress in the longitudinal reinforcement

f_{Ly} = yielding stress of the longitudinal reinforcement

f_S = average tensile stress in the steel bars

f_{sy}= yielding stress of the steel bars

f_T = tensile stress in the transverse reinforcement

f_{Ty} = yielding stress of the transverse reinforcement

k = umber of solution points

m_L = longitudinal proportionality coefficient

m_{LT} = shear proportionality coefficient

m_T = transverse proportionality coefficient

$n_{\max}$ = maximum number of solution points

α_D = angle of the principal compressive stresses in the concrete membrane element

α_R = angle of the principal tensile stresses in the concrete membrane element

ϵ_0 = strain correspondent to the peak stress

ϵ_{cu} = ultimate strain for concrete in compression

ϵ_s = average strain in the steel bars

ϵ_{sy} = yielding strain of the steel bars

ϵ_D = principal average compressive strain

ϵ_L = longitudinal average strain
ϵ_R = principal average tensile strain
ϵ_T = transversal average strain
γ_{LT}= average shear strain ζ = softening coefficient
ρ_L = longitudinal reinforcement ratio
ρ_T = transverse reinforcement ratio
σ_1 = principal tensile stress in the RC membrane element
σ_D = principal compressive strain in the concrete membrane element
σ_L = longitudinal normal stress in the RC membrane element
σ_L^c = longitudinal normal stress in the concrete membrane element
σ_R = principal tensile strain in the concrete membrane element
σ_T = transverse normal stress in the RC membrane element
σ_T^c = transverse normal stress in the concrete membrane element τ shear stress
τ_{LT} = shear stress in the RC membrane element
τ_{LT}^c = shear stress in the concrete membrane element

References

[1] MathWorks. (2017). "MATLAB - R2017". Academic license.
[2] Belarbi A, Hsu TTC. Constitutive laws of concrete in tension and reinforcing bars stiffened by concrete. Struct J Am Concr Inst. 1994;91(4): 465–474.
[3] Pang XB, Hsu TTC. Behavior of reinforced concrete membrane elements in shear. Struct J Am Concr Inst. 1995;92(6):665–679.
[4] Silva JRB, Horowitz B. Efficient procedure to estimate the load–deformation behavior of reinforced concrete panels under membrane forces [in Portuguese]. CILAMCE 2015: Iberian Latin American Congress on Computational Methods in Engineering; 2015; Rio de Janeiro-RJ, Brazil; vol. 36.
[5] Silva JRB. Efficient procedure for the analysis of reinforced concrete sections using the softened truss model [unpublished master's thesis]. Recife, Brazil: Department of Civil Engineering, Federal University of Pernambuco; 2016.
[6] Cerquido BMD. Analysis of reinforced concrete sections with the softened truss model [unpublished master's thesis]. Covilhã, Portugal: Department of Civil Engineering and Architecture, University of Beira Interior; 2017.
[7] Bernardo LFA, Cerquido BMD, Silva JRB, Horowitz B. Efficient Refined Rotating-Angle Softened Truss Model Procedure to Analyze Reinforced Concrete Membrane Elements. Struct Concr. fib 2018;19(6): 1971-1982.
[8] Bernardo L, Lyrio A, Silva J, Horowitz B. Refined Softened Truss Model with Efficient Solution Procedure for Prestressed Concrete Membranes. J Struct Eng ASCE. 2018;144(6): 04018045.
[9] Collins MP. Torque-twist characteristics of reinforced concrete beams. Inelasticity and non-linearity and non-linearity in structural concrete. Waterloo: University of Waterloo Press, 1973; p. 211–231.
[10] Zhang LX, Hsu TTC. Behavior and analysis of 100 MPa concrete membrane elements. J Struct Eng ASCE. 1998;124(1):24–34.
[11] Pang XB, Hsu TTC. Behavior of reinforced concrete membrane elements in shear. Struct J Am Concr Inst. 1995;92(6):665–679.

Capítulo 4

Refinamento do modelo de treliça com amolecimento e ângulo variável com procedimento de cálculo eficiente para membranas de concreto estrutural.

Este capítulo consiste no artigo:

Refinement of rotating-angle softened truss model with efficient solution procedure for RC membranes.

Bernardo, L.F.A.; Filho B.M.V.C.; Horowitz, B. 2020 “ Refinement of the rotating-angle softened truss model with efficient solution fo RC membranes”, Engineering Structures, Elsevier, ISSN: 0141-0296, Volume 213: 110552, pages 1-12.
DOI: https://doi.org/10.1016/j.engstruct.2020.110552

Engineering Structures 213 (2020) 110552

Contents lists available at ScienceDirect

Engineering Structures

journal homepage: www.elsevier.com/locate/engstruct

Refinement of the rotating-angle softened truss model with efficient solution procedure for RC membranes

L.F.A. Bernardo[a,*], B.M.V.C. Filho[a], B. Horowitz[b]

[a] University of Beira Interior, C-MADE – Centre of Materials and Building Technologies, Covilhã, Portugal
[b] Federal University of Pernambuco, Brazil

ARTICLE INFO

Keywords:
RA-STM
Efficient solution procedure
Membrane elements
Reinforced concrete
Tensile concrete

ABSTRACT

In a previous study, a new and numerically efficient solution procedure for the rotating-angle softened truss model (RA-STM) was proposed to compute the ultimate behavior or reinforced concrete (RC) membrane elements. In such new calculation procedure, the tensile stresses in concrete were neglected for simplicity. In this article, the efficient RA-STM procedure is refined in order to incorporate the contribution of the tensile stresses in concrete. The equations of the refined model are reformulated in order to incorporate this additional contribution and an appropriate smeared stress-strain relationship for tensile concrete is implemented. In addition, the new solution procedure is also presented. The refined efficient RA-STM procedure proposed in this study is able to predict the full behavior of RC membrane elements under in-plane stresses, including for both low and high loading stages, with high numerical efficiency and stability. The predictions obtained from the model are compared with the experimental results of tested RC panels found in the literature, where good agreement is observed, namely for the cracking load, stiffness after cracking and strength.

1. Introduction

Simpler analytical models are always desirable and can be very useful to analyze and understand the behavior of reinforced concrete (RC) structures. Among the several structural components, many of them (for instance, plates and shear walls) are mainly designed for in-plane stress states. For their analysis, these components can be considered as the union of small two-dimensional (2D) RC membrane elements. This simplification allows to use simpler models [1].

During the last decades, truss models have proven to be suitable to predict the behavior of RC members and understand the role of the different materials in the cracked stage. From the original simple truss models proposed in the very beginning of last century [2,3], several developments have been made to allow the truss models to predict even more accurately the behavior of RC members. Among such developments, some of the modern truss models treat the structural member as a continuous material, even in the cracked stage. By using appropriate smeared constitutive laws for the materials, which are calibrated along a sufficient length of the member to include several cracks, such truss models allow to compute average values for both the stresses and strains, instead of evaluating them locally. It should be noted that smeared analyses in concrete members have been successfully used in previous studies to approach in average the behavior of such members, including to develop reliable and efficient numerical methods for concrete members under shear and torsion [4–6].

Among several studies from different authors who proposed refined truss models in the second half of last century, some relevant contributions are worthy to be mentioned. In 1972, Elfgren [7] extended the first simpler truss models for RC members under shear and torsion for the case of more complex loadings. Few years later, Nielsen in 1967 [8] and Lampert and Thurlimann [9] in 1968 derived the fundamental equations from equilibrium by using the theory of plasticity for RC members under shear (called the plasticity truss model). Collins in 1973 [10] derived the fundamental equations from compatibility by using geometric relationships and Mohr's circle for strains for RC members under shear (called the Mohr Compatibility Truss Model - MCTM). In 1968 Robison and Demorieux [11] experimentally observed for the first time the so-called softening effect in the compressive concrete in the struts by testing RC panels under shear. Based on the previous experimental results, Vecchio and Collins in 1982 [12] proposed an equation to quantify a softening coefficient to correct the uniaxial stress (σ) – strain (ε) relationship for concrete in compression to be used in the truss models and developed the so-called Compression Field Theory (CFT). This model was refined in 1986 by Vecchio and Collins [13] by

---

[*] Corresponding author at: University of Beira Interior, Department of Civil Engineering and Architecture, Edifício II das Engenharias, Calçada Fonte do Lameiro, 6201-001 Covilhã, Portugal.

E-mail address: lfb@ubi.pt (L.F.A. Bernardo).

https://doi.org/10.1016/j.engstruct.2020.110552
Received 19 September 2019; Received in revised form 15 March 2020; Accepted 19 March 2020
0141-0296/

Notation

cv	coefficient of variation
E_c	Young's modulus for concrete
E_S	Young's modulus for steel
f'_c	uniaxial compressive strength of concrete
f_{cr}	tensile strength of concrete
f_L	tensile stress in the longitudinal reinforcement
f_{Ly}	uniaxial yielding stress of the longitudinal reinforcement
f_S	average tensile stress in the steel bars
f_{Sy}	uniaxial yielding stress for steel
f_T	tensile stress in the transverse reinforcement
f_{Ty}	uniaxial yielding stress of the transverse reinforcement
k	index of the step
k_S	shear stiffness in the cracked stage
$k_{S,exp}$	experimental shear stiffness in the cracked stage
$k_{S,th}$	theoretical shear stiffness in the cracked stage
m_L	longitudinal proportionality coefficient
m_{LT}	shear proportionality coefficient
m_T	transverse proportionality coefficient
$RF^{(1)}_{RA-STM}$	first residual function for the efficient RA-STM procedure
$RF^{(2)}_{RA-STM}$	second residual function for the efficient RA-STM procedure
RF_{START}	residual function for the initial estimates
s	standard deviation
$\bar{x}$	mean
α_2	angle of the principal compressive stresses in the RC membrane element
α_D	angle of the principal compressive stress in the concrete membrane element
$\Delta\varepsilon_D$	path increment forε_D
ε	strain
ε_0	strain corresponding to the concrete compressive peak stress
ε_{cr}	strain corresponding to the tensile strength of concrete
ε_{cu}	ultimate strain for concrete in compression
ε_D	principal average compressive strain
ε_L	longitudinal average strain
ε_{Ly}	yielding strain for the longitudinal reinforcement
ε_R	principal average tensile strain
ε_S	average strain in the steel bars
ε_{Sy}	yielding strain for steel
ε_T	transverse average strain
ε_{Ty}	yielding strain for the transverse reinforcement
γ	shear strain
γ_{LT}	average shear strain in the L-T coordinate system
γ_u	shear strain corresponding to the shear strength
$\gamma_{u,exp}$	experimental shear strain corresponding to the shear strength
$\gamma_{u,th}$	theoretical shear strain corresponding to the shear strength
ζ	softening coefficient
ρ_L	longitudinal reinforcement ratio
ρ_T	transverse reinforcement ratio
σ	stress
σ_1	principal tensile stress in the RC membrane element
σ_2	principal compressive stress in the RC membrane element
σ_D	principal compressive stress in the concrete membrane element
σ_L	longitudinal normal stress in the RC membrane element
σ_L^c	longitudinal normal stress in the concrete membrane element
σ_R	principal tensile stress in the concrete membrane element
σ_T	transverse normal stress in the RC membrane element
σ_T^c	transverse normal stress in the concrete membrane element
τ_{cr}	cracking shear stress
$\tau_{cr,exp}$	experimental cracking shear stress
$\tau_{cr,th}$	theoretical cracking shear stress
τ_{LT}	shear stress in the RC membrane element in the L-T coordinate system
τ_{LT}^c	shear stress in the concrete membrane element in the L-T coordinate system
τ_u	shear strength stress
$\tau_{u,exp}$	experimental shear strength stress
$\tau_{u,th}$	theoretical shear strength stress

incorporating the influence of the tensile stresses in concrete and also new $\sigma - \varepsilon$ relationships for the materials (called the Modified Compression-Field Theory - MCFT). Based on new experimental results for RC panels performed at the University of Houston, Hsu in 1988 [14] developed the Softened Truss Model (STM). Later, this model was modified and renamed as Rotating-Angle Softened Truss Model (RA-STM) [15] to account that, as a result of the internal redistribution of stresses and compatibility conditions after cracking, the direction of the principal compressive stresses in the concrete member rotates, being no longer equal to the direction of the first cracks. Further developments of the RA-STM include the incorporation of refined smeared $\sigma - \varepsilon$ relationships for compressive concrete [16] and for tensile steel reinforcing bars, including the stiffening effect [17] and also the dowel action [18]. Pang and Hsu in 1996 [19] and Hsu and Zhang in 1997 [20] considered the reference frame to write the equations at a fixed angle. This one was considered equal to the angle of the principal directions of the external stresses applied to the RC member, which is constant for proportional loading. This new approach allowed to incorporate the shear effect in the concrete member and a new shear (τ) – shear strain (γ) relationship for concrete was implemented. The new model was called Fixed-Angle Softened Truss Model (FA-STM). This model was refined by Hsu and Zhu in 2002 [21] in order to better predict the post-peak behavior of RC membranes. For this, the so-called Hsu/Zhu ratios where proposed to account for the Poisson's effect and incorporated in the model, which was renamed as Softened Membrane Model (SMM).

To compute the behavior of RC membrane elements under in-plane stresses, the calculation procedure of all the previous models is based on a trial-and-error technique and requires a large number of initial estimates. Such calculation procedures may require a large calculation effort and also can lose numerical efficiency, mainly for the truss models which are analytically more complicated.

When compared with the FA-STM and SMM, it is recognized that the RA-STM is a simpler model. For this reason, in recent studies an alternative and more efficient calculation procedure has been proposed for the RA-STM [22–25]. For this, the problem was formulated as a system of nonlinear equations with constraints. These equations are solved efficiently by using optimization algorithms which can be found in commercial software packages. This new calculation procedure, called here efficient RA-STM procedure, presents the following advantages: it avoids using a trial-and-error technique, it is numerically more efficient and it requires much less computational calculation effort. In addition, to improve the predictions from the efficient RA-STM procedure, Bernardo et al. in 2018 [25] also implemented a set of more appropriate smeared $\sigma - \varepsilon$ relationships for the materials.

In the previously referred studies [22–25], for simplicity the contribution of tensile stresses in concrete was neglected in the efficient RA-STM procedure. For this reason, when compared with experimental results related with RC membrane elements under in-plane stresses, the predictions from the efficient RA-STM procedure showed good agreement only for the ultimate stage, namely for the strength. The model is still not able to predict well the behavior of RC membrane elements for low loading stages. This constitutes a drawback because, as stated in the design codes, structural members must be checked for both the ultimate (high loading stages) and serviceability (low loading stages) limit states. Hence, theoretical models must also be reliable in predicting the behavior for low loading stages.

In this article, the efficient RA-STM procedure is refined in order to incorporate the contribution of the tensile stresses in concrete. For this, the refined model incorporates the tensile concrete in the perpendicular direction of the concrete struts. To model the behavior of the tensile concrete, an additional and appropriate smeared and non-linear $\sigma - \varepsilon$ relationship for concrete in tension is implemented, which was proposed in previous studies. The reformulation of the equations for the refined efficient RA-STM procedure and the new solution procedure are presented. The predictions obtained from the refined efficient RA-STM procedure are compared with the experimental results of tested RC panels found in the literature. It is showed that the proposed model is able to predict, with high numerical efficiency and stability, the full behavior of RC membrane elements under in-plane stresses, including for both low and high loading stages, namely the cracking load, stiffness after cracking and strength.

2. Efficient RA-STM procedure with concrete in tension

The efficient RA-STM procedure is refined in order to incorporate the contribution of concrete in tension. To present the refined model and the corresponding solution procedure, the presented steps follow the same general ones presented in previous studies where the RA-STM was the used model [15,25].

2.1. Equations from equilibrium conditions

Fig. 1. illustrates how a 2D RC membrane element under in-plane stresses (σ_L, σ_T and τ_{LT}) can be divided as the contribution of a concrete member under in-plane stresses (σ_L^c, σ_T^c and τ_{LT}^c) and steel reinforcing bars only under tensile stresses ($\rho_L f_L$ and $\rho_T f_T$) because the dowel action is neglected for simplicity [15]. In Fig. 1, ρ_L (ρ_T) is the longitudinal (transverse) reinforcement ratio, while f_L (f_T) is the tensile normal stress in the longitudinal (transverse) steel bars. The L-T coordinate system is defined from the direction of the longitudinal (L) and transverse (T) steel bars. As considered in the original version for the RA-STM, perfect bond is assumed between steel bars and concrete [15]. From Fig. 1, and based on the previous assumptions, the following 3 equilibrium equations can be stated:

$$\sigma_L = \sigma_L{}^c + \rho_L f_L \tag{1}$$

$$\sigma_T = \sigma_T{}^c + \rho_T f_T \tag{2}$$

$$\tau_{LT} = \tau_{LT}{}^c \tag{3}$$

The stress components in the concrete member (σ_L^c, σ_T^c and τ_{LT}^c) can be related with its principal stresses (σ_R and σ_D) and the variable angle α_D between the coordinate systems L-T and R-D (see Fig. 1) by using geometrical relations from the Mohr's circle for stresses [15,25]. Eq. (1) to (3) can be rewritten as:

$$\sigma_L = \cos^2(\alpha_D)\sigma_D + \sin^2(\alpha_D)\sigma_R + \rho_L f_L \tag{4}$$

$$\sigma_T = \sin^2(\alpha_D)\sigma_D + \cos^2(\alpha_D)\sigma_R + \rho_T f_T \tag{5}$$

$$\tau_{LT} = \sin(\alpha_D)cos(\alpha_D)(\sigma_R - \sigma_D) \tag{6}$$

In the previous equations, the principal tensile stress in concrete (σ_R) is no longer neglected, as it was previously assumed in previous studies [22–25].

2.2. Equations from compatibility conditions

As for the stresses, and by using the Mohr's circle for strains, the average strain components (ε_L, ε_T and γ_{LT}) can be related with the principal strains (ε_R and ε_D) and the variable angle α_D between the coordinate systems L-T and R-D [15,25]. This leads to the following 3 compatibility equations

$$\varepsilon_L = \cos^2(\alpha_D)\varepsilon_D + \sin^2(\alpha_D)\varepsilon_R \tag{7}$$

$$\varepsilon_T = \sin^2(\alpha_D)\varepsilon_D + \cos^2(\alpha_D)\varepsilon_R \tag{8}$$

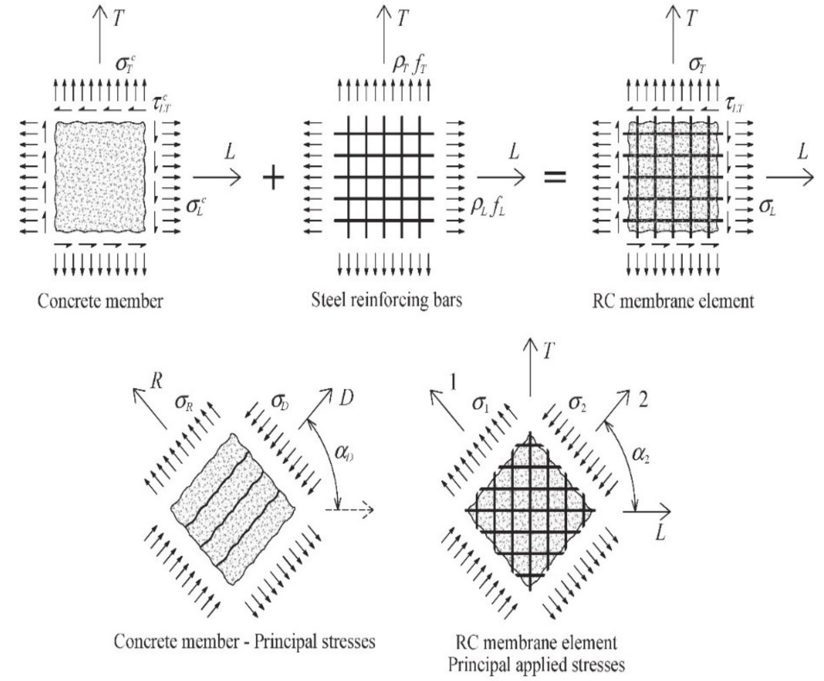

Fig. 1. 2D RC membrane element under in-plane stresses.

$$\gamma_{LT} = 2\sin(\alpha_D)\cos(\alpha_D)(\varepsilon_R - \varepsilon_D) \tag{9}$$

In addition, the trace of the strain tensors (also called the first invariant) in both L-T and R-D coordinate systems can be equalized to write the following invariant equation:

$$\varepsilon_L + \varepsilon_T = \varepsilon_D + \varepsilon_R \tag{10}$$

2.3. Smeared constitutive relationships for the materials

To model the behavior of concrete in compression in the struts, the same smeared and nonlinear $\sigma - \varepsilon$ softened relationship used and justified by Bernardo et al. in 2018 [25] and given by Eq. (11) was adopted for the refined efficient RA-STM procedure. This constitutive law (see Fig. 2) was proposed by Zhu et al. in 2001 [26] and calibrated from experimental tests with RC membranes under biaxial tensile-compressive stresses. In Eq. (11), f'_c is the uniaxial concrete compressive strength, ε_0 is the strain corresponding to the peak stress and ζ is a softening coefficient given in Eq. (12), which was proposed by Zhang and Hsu in 1998 [27]. This softening coefficient was calibrated to account for both the ratio of the transverse to the longitudinal reinforcement stresses (Eq. (13)) and for high-strength concretes (condition limit in Eq. (12)). In Eq. (13), f_{Ly} (f_{Ty}) is the yielding stress for the longitudinal (transverse) reinforcement.

$$\begin{cases} \sigma_D = \zeta f'_c\,[2(\varepsilon_D/\zeta\varepsilon_0) - (\varepsilon_D/\zeta\varepsilon_0)^2] & \text{if } \varepsilon_D/\zeta \leqslant \varepsilon_0 \\ \sigma_D = \zeta f'_c\left[1 - \left(\frac{\varepsilon_D/\zeta\varepsilon_0 - 1}{4/\zeta - 1}\right)^2\right] & \text{if } \varepsilon_D/\zeta > \varepsilon_0 \end{cases} \tag{11}$$

$$\zeta = \left(1 + \frac{400\varepsilon_R}{\eta'}\right)^{-1/2} \times \min\left\{\frac{5.8}{\sqrt{f'_c(\text{MPa})}}; 0.9\right\} \tag{12}$$

$$\eta = \frac{\rho_T f_{Ty} - \sigma_T}{\rho_L f_{Ly} - \sigma_L} \tag{13}$$

$$\begin{cases} \eta' = \eta & \text{if } \eta \leqslant 1 \\ \eta' = 1/\eta & \text{if } \eta > 1 \end{cases} \tag{14}$$

To model the behavior of steel bars in tension embedded in concrete, the same smeared and bilinear $\sigma - \varepsilon$ stiffened relationship used and justified by Bernardo et al. in 2018 [25] and given by Eq. (15) was adopted for the refined efficient RA-STM procedure. This constitutive law (see Fig. 2) was proposed by Jeng and Hsu in 2009 [28] as a simplification of the nonlinear relationship from Belarbi and Hsu in 1994 [17]. The used constitutive law neglects the dowel action in the steel bars for simplicity. This effect was found by Hsu and Zhu in 2002 [21] to be not so relevant.

$$\begin{cases} f_S = E_S\varepsilon_S & \text{if } \varepsilon_S \leqslant \varepsilon_n = (0.93 - 2B)\varepsilon_{Sy} \\ f_S = f_{Sy}\,[0.91 - 2B + (0.02 + 0.25B)\varepsilon_S/\varepsilon_{Sy}] & \text{if } \varepsilon_S > \varepsilon_n = (0.93 - 2B)\varepsilon_{Sy} \end{cases} \tag{15}$$

$$B = (1/\rho)(f_{cr}/f_{Sy})^{3/2} \tag{16}$$

In Eq. (15) and (16) the meaning of parameters are: f_S (ε_S) is the average tensile stress (strain) in the steel bars, f_{Sy} (ε_{Sy}) is the yielding stress (strain) for steel (subscript S is substituted by L and T for longitudinal and transverse reinforcement, respectively), E_S is the Young's Modulus for steel and f_{cr} is the tensile strength of concrete (see Eq. (19)).

In addition to the previous constitutive laws, an additional one needs to be incorporated to model the behavior of concrete in tension in the perpendicular direction to the struts. This is because the refined efficient RA-STM procedure proposed in this study includes the tensile stresses in concrete. In this study, the smeared and nonlinear $\sigma - \varepsilon$ relationship for tensile concrete proposed by Belarbi and Hsu in 1994 [17] for shear members was used (Eq. (17) to (19), see Fig. 2). This relationship was successfully used in previous models to compute the behavior of RC membrane elements under shear, accounting for the tensile concrete [18,21,27].

$$\begin{cases} \sigma_R = E_c\varepsilon_R & \text{if } \varepsilon_R \leqslant \varepsilon_{cr} = 0.00008 \\ \sigma_R = f_{cr}(\varepsilon_{cr}/\varepsilon_R)^{0.4} & \text{if } \varepsilon_R > \varepsilon_{cr} = 0.00008 \end{cases} \tag{17}$$

$$E_c = 3875\sqrt{f'_c(\text{MPa})} \tag{18}$$

$$f_{cr} = E_c\varepsilon_{cr} = 0.311\sqrt{f'_c(\text{MPa})} \tag{19}$$

In the previous equations, E_c is the Young's Modulus for concrete and ε_{cr} is the tensile strain corresponding to the peak stress (f_{cr}).

2.4. Equations for the loading condition

For a RC membrane element under in-plane stresses, the most common loading condition in practice and also in experiments is the one for which the ratio between the external stresses remains constant through all the loading history. Hence, only proportional loading condition was considered in this study. In this case, the applied (external) stresses in the RC membrane can be related to the principal tensile stress (σ_1) in the 1–2 coordinate system (direction of principal applied stresses, see Fig. 1 where α_2 is the angle between the L-T and 1–2 coordinate systems) through proportionality coefficients which remain constant, namely: longitudinal (m_L), transverse (m_T) and shear (m_{LT}) proportionality coefficients (Eq. (20) to (22)).

$$m_L = \sigma_L/\sigma_1 \tag{20}$$

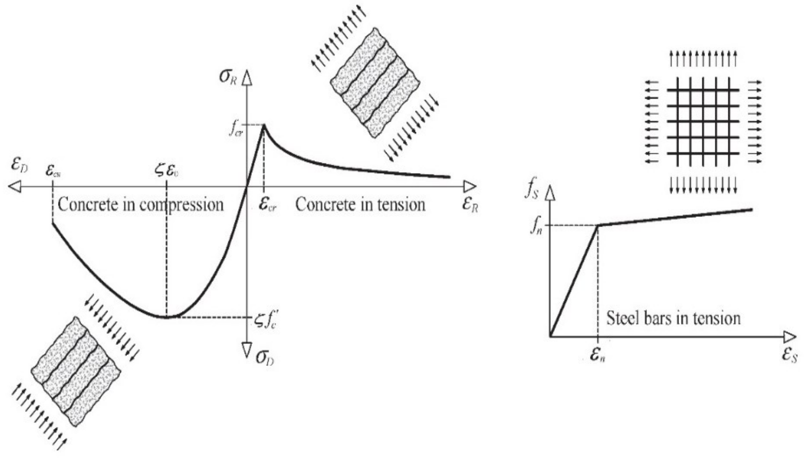

Fig. 2. Smeared constitutive relationships for the materials.

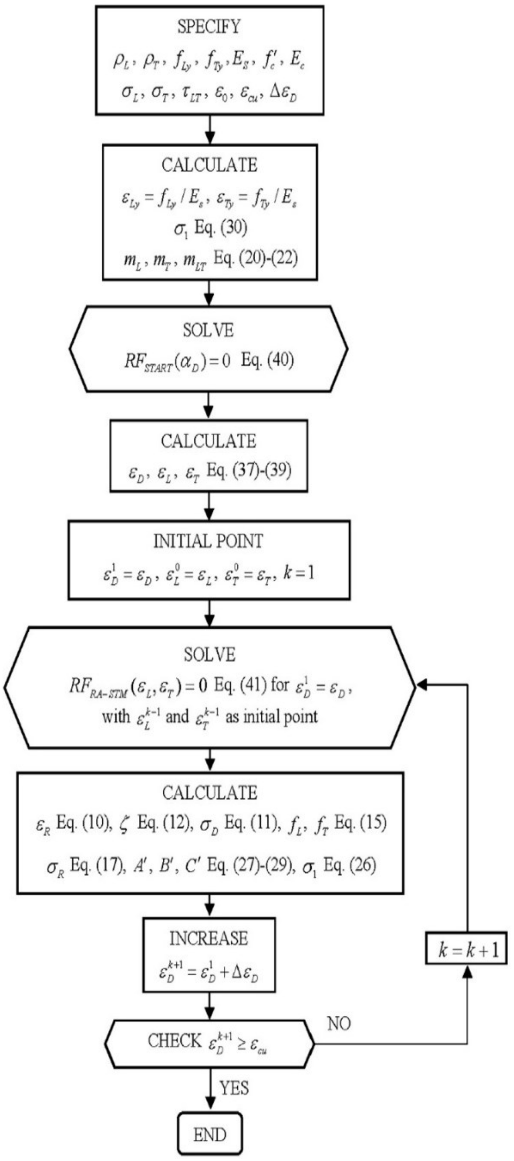

Fig. 3. Flowchart of the developed algorithm.

$$m_T = \sigma_T/\sigma_1 \tag{21}$$

$$m_{LT} = \tau_{LT}/\sigma_1 \tag{22}$$

Substituting σ_L, σ_T and τ_{LT} from Eq. (20) to (22) into Eq. (4) to (6) gives:

$$m_L\sigma_1 - \rho_L f_L = \cos^2(\alpha_D)\sigma_D + \sin^2(\alpha_D)\sigma_R \tag{23}$$

$$m_T\sigma_1 - \rho_T f_T = \sin^2(\alpha_D)\sigma_D + \cos^2(\alpha_D)\sigma_R \tag{24}$$

$$m_{LT}\sigma_1 = \sin(\alpha_D)cos(\alpha_D)(\sigma_R - \sigma_D) \tag{25}$$

Some auxiliary equations need to be derived. Using $\sin^2(\alpha_D) + cos^2(\alpha_D) = 1$, Eq. (23) and (24) can be rewritten as the auxiliary Eq. (*a*) and (*b*), respectively. Multiplying Eq. (*a*) and (*b*) member by member gives the auxiliary Eq. (*c*). Squaring both members of Eq. (25) gives the auxiliary Eq. (*d*). Eq. (23) to (25) can be combined by equating the left members of Eq. (*c*) and (*d*), which gives Eq. (e). After expanding Eq. (*e*) and rearranging terms, and considering σ_1 as the independent variable, a quadratic equation can be written (Eq. (*f*)):

$$- m_L\sigma_1 + \sigma_R + \rho_L f_L = \cos^2(\alpha_D)(\sigma_R - \sigma_D) \tag{a}$$

$$- m_T\sigma_1 + \sigma_R + \rho_T f_T = \sin^2(\alpha_D)(\sigma_R - \sigma_D) \tag{b}$$

$$(- m_L\sigma_1 + \sigma_R + \rho_L f_L)(- m_T\sigma_1 + \sigma_R + \rho_T f_T) = \cos^2(\alpha_D)\sin^2(\alpha_D)(\sigma_R - \sigma_D)^2 \tag{c}$$

$$(m_{LT}\sigma_1)^2 = \sin^2(\alpha_D)cos^2(\alpha_D)(\sigma_R - \sigma_D)^2 \tag{d}$$

$$(- m_L\sigma_1 + \sigma_R + \rho_L f_L)(- m_T\sigma_1 + \sigma_R + \rho_T f_T) = (m_{LT}\sigma_1)^2 \tag{e}$$

$$\begin{aligned}&(m_L m_T - m_{LT}{}^2)\sigma_1{}^2 + [- m_L(\sigma_R + \rho_T f_T) - m_T(\sigma_R + \rho_L f_L)]\sigma_1 + \\ &\quad(\sigma_R + \rho_T f_T)(\sigma_R + \rho_L f_L) = 0\end{aligned} \tag{f}$$

For the quadratic Eq. (*f*), a solution equation can be written for σ_1 as follows:

$$\sigma_1 = \frac{B' \pm \sqrt{B'^2 - 4A'C'}}{2A'} \tag{26}$$

$$A' = m_L m_T - m_{LT}{}^2 \tag{27}$$

$$B' = m_L(\sigma_R + \rho_T f_T) + m_T(\sigma_R + \rho_L f_L) \tag{28}$$

$$C' = (\sigma_R + \rho_T f_T)(\sigma_R + \rho_L f_L) \tag{29}$$

Finally, from Fig. 1 and from the Mohŕs circle for stresses, the principal tensile stress σ_1 in the RC membrane element can be easily related with the stresses in the L-T coordinate by the following useful equation:

$$\sigma_1 = 0.5(\sigma_L + \sigma_T) + \sqrt{(0.5(\sigma_L - \sigma_T))^2 + \tau_{LT}{}^2} \tag{30}$$

2.5. Additional equations

To compute the principal compressive stress in the concrete member (see Fig. 1), Eq.(25) is solved for σ_D, giving the following equation:

$$\sigma_D = \sigma_R - \frac{m_{LT}}{\sin(\alpha_D)\cos(\alpha_D)}\sigma_1 \tag{31}$$

Substituting Eq. (31) in to Eq. (23) and (24) and solving for the tensile stresses in the longitudinal (f_L) and transverse (f_T) reinforcement, respectively, gives Eq. (32) and (33):

$$f_L = \frac{m_L + m_{LT}\cot(\alpha_D)}{\rho_L}\sigma_1 - \frac{\sigma_R}{\rho_L} \tag{32}$$

$$f_T = \frac{m_T + m_{LT}tan(\alpha_D)}{\rho_T}\sigma_1 - \frac{\sigma_R}{\rho_T} \tag{33}$$

To write the variable angle α_D as function of the strains in the L-T and R-D coordinate systems, the trigonometric identity $\sin^2(\alpha_D) + cos^2(\alpha_D) = 1$ is firstly inserted in both Eq. (7) and (8), giving Eq. (34) and (35). The variable angle α_D is computed from Eq. (36), which is obtained dividing Eq. (34) by Eq. (35).

$$\sin(\alpha_D) = \sqrt{\frac{\varepsilon_L - \varepsilon_D}{\varepsilon_R - \varepsilon_D}} \tag{34}$$

$$\cos(\alpha_D) = \sqrt{\frac{\varepsilon_T - \varepsilon_D}{\varepsilon_R - \varepsilon_D}} \tag{35}$$

$$\tan(\alpha_D) = \sqrt{\frac{\varepsilon_L - \varepsilon_D}{\varepsilon_T - \varepsilon_D}} \tag{36}$$

2.6. Equations for the residual functions

The chosen initial estimates to start the calculation procedure are the strains ε_D, ε_L, and ε_T. To compute the initial estimates for these strains, a simple elastic truss model is idealized. For this, Hooké's laws for concrete ($\sigma_D = E_c\varepsilon_D$) and steel bars ($f_L = E_s\varepsilon_L$ and $f_T = E_s\varepsilon_T$) are substituted into Eq. (31) to (33) which are then solved for the strains. At this stage and for simplicity, the tensile stress in concrete is neglected

Table 1
Properties of selected panels.

Panel	f'_c MPa	f_{cr} MPa	E_c GPa	ε_0 $\times 10^{-3}$	ε_{cu} $\times 10^{-3}$	E_s GPa	ρ_L	f_{Ly} MPa	ε_{Ly} $\times 10^{-3}$	ρ_T	f_{Ty} MPa	ε_{Ty} $\times 10^{-3}$	α_2 °
VA0 [27]	98.8	3.1	38.5	2.40	2.8	200	0.006	445	2.23	0.006	445	2.23	45
VA1 [27]	95.1	3.0	37.8	2.45	2.8	200	0.0120	445	2.23	0.0120	445	2.23	45
VA2 [27]	98.2	3.1	38.4	2.50	2.8	200	0.0239	409	2.05	0.0239	409	2.05	45
VA3 [27]	94.6	3.0	37.7	2.45	2.8	200	0.0359	455	2.28	0.0359	455	2.28	45
VA4 [27]	103.1	3.2	39.3	2.35	2.8	200	0.0524	470	2.35	0.0524	470	2.35	45
VB1 [27]	98.2	3.1	38.4	2.50	2.8	200	0.0239	409	2.05	0.0120	445	2.23	45
VB2 [27]	97.6	3.1	38.3	2.45	2.8	200	0.0359	455	2.28	0.0120	445	2.23	45
VB3 [27]	102.3	3.1	39.2	2.35	2.8	200	0.0598	470	2.35	0.0120	445	2.23	45
VB4 [27]	96.9	3.1	38.1	2.30	2.8	200	0.0180	455	2.28	0.0060	445	2.23	45
A1R [21]	42.2	2.0	25.2	2.13	3.50	200	0.0077	445	2.23	0.0077	445	2.23	45
A2 [18]	41.2	2.0	24.9	2.10	3.50	200	0.0119	463	2.32	0.0119	463	2.32	45
A3 [18]	41.6	2.0	25.0	1.94	3.50	200	0.0179	446	2.23	0.0179	446	2.23	45
A4 [18]	42.5	2.0	25.3	2.20	3.50	200	0.0298	470	2.35	0.0298	470	2.35	45
B1 [18]	45.2	2.1	26.1	2.15	3.50	200	0.0119	463	2.32	0.0060	445	2.23	45
B2 [18]	44.1	2.1	25.7	2.35	3.50	200	0.0179	446	2.23	0.0119	463	2.32	45
B3 [18]	44.9	2.1	26.0	2.15	3.50	200	0.0179	446	2.23	0.0060	445	2.23	45
B4 [18]	44.7	2.1	25.9	2.05	3.50	200	0.0298	470	2.35	0.0060	445	2.23	45
B5 [18]	42.8	2.0	25.4	2.20	3.50	200	0.0298	470	2.35	0.0119	463	2.32	45
B6 [18]	43.0	2.0	25.4	2.20	3.50	200	0.0298	470	2.35	0.0179	446	2.23	45
F2 [31]	40.1	2.0	24.5	2.20	3.50	193	0.0127	446	2.31	0.0042	445	2.31	90
F3 [31]	42.6	2.0	25.3	2.00	3.50	193	0.0127	446	2.31	0.0042	445	2.31	90
F4 [31]	41.9	2.0	25.1	2.20	3.50	193	0.0127	446	2.31	0.0042	445	2.31	90

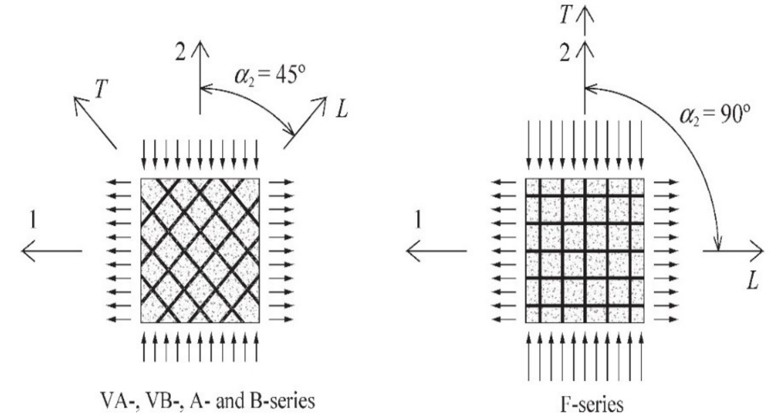

Fig. 4. Selected RC panels: direction of applied stresses and reinforcement direction.

($\sigma_R = 0$) to compute the initial estimates.

$$\varepsilon_D = \frac{-m_{LT}}{E_c \sin(\alpha_D)\cos(\alpha_D)}\sigma_1 \tag{37}$$

$$\varepsilon_T = \frac{(m_T + m_{LT}\cot(\alpha_D))\sigma_1}{E_S \rho_T} \tag{38}$$

$$\varepsilon_T = \frac{(m_T + m_{LT}\tan(\alpha_D))\sigma_1}{E_S \rho_T} \tag{39}$$

From Eq. (36), a nonlinear residual function (RF_{START}, Eq. (40)) can be written as function of the strains given by Eq. (37) to (39). The angle α_D which numerically minimizes this residual function, and the corresponding initial values for the strains, are used to start the calculations of the refined efficient RA-STM procedure.

$$RF_{START} = \frac{\varepsilon_L - \varepsilon_D}{\varepsilon_T - \varepsilon_D} - \tan^2(\alpha_D) = 0 \tag{40}$$

To derive two nonlinear residual functions for the refined efficient RA-STM procedure, the following steps are performed. Firstly, Eq. (23) and (35) are added. Then Eq. (34) and (35) are substituted in the resulting equation. After arranging terms, the first residual function for the efficient RA-STM procedure is obtained ($RF^{(1)}_{RA-STM}$). The second residual function ($RF^{(2)}_{RA-STM}$) is derived in a similar way by adding Eq. (25) and (34), substituting Eq. (34) and (35) and arranging terms.

$$\begin{cases} RF^{(1)}_{RA-STM} = \sigma_D \frac{\varepsilon_T - \varepsilon_D}{\varepsilon_R - \varepsilon_D} + \sigma_R \frac{\varepsilon_L - \varepsilon_D}{\varepsilon_R - \varepsilon_D} - m_L \sigma_1 + \rho_L f_L = 0 \\ RF^{(2)}_{RA-STM} = \sigma_D \frac{\varepsilon_L - \varepsilon_D}{\varepsilon_R - \varepsilon_D} + \sigma_R \frac{\varepsilon_T - \varepsilon_D}{\varepsilon_R - \varepsilon_D} - m_T \sigma_1 + \rho_T f_T = 0 \end{cases} \tag{41}$$

Eq. (41) is a system of two nonlinear equations which are numerically solved to compute the strains ε_L and ε_T which minimize both the residual functions.

3. Algorithm for the refined efficient RA-STM procedure

Based on the equations presented in the previous section, an algorithm to compute the numerical solution points for the refined efficient RA-STM procedure was developed and implemented in a computer. The flowchart for the developed algorithm is presented in Fig. 3. The calculation procedure starts with some data entry, namely the mechanical properties of the materials, the ratio of longitudinal and transverse reinforcement, the relative values for the loading stresses and the chosen path increment for the principal compressive strain ($\Delta\varepsilon_D$). Then, the initial estimates are computed by minimizing the residual function RF_{START} and the starting values for ε_D^1, ε_L^0 and ε_T^0 are obtained to compute

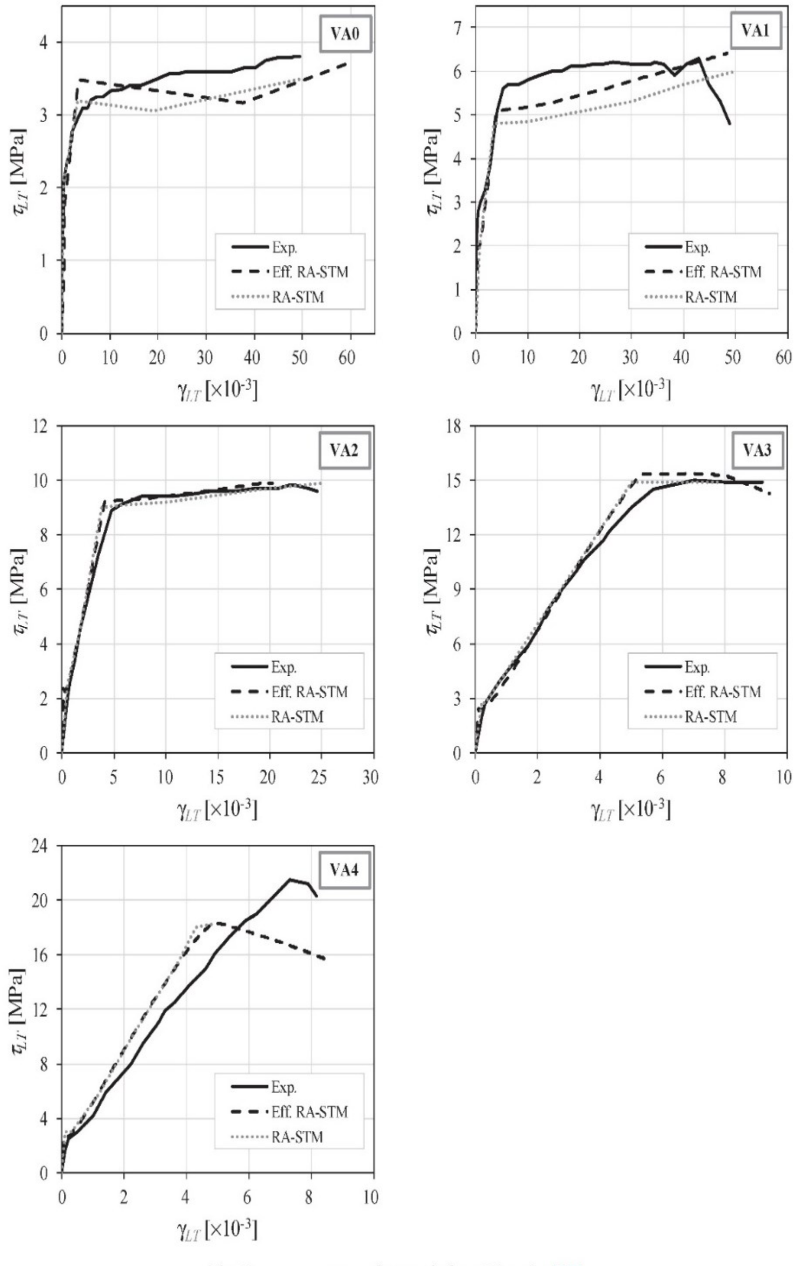

Fig. 5. $\tau_{LT} - \gamma_{LT}$ curves for panels from VA-series [27].

the first solution point (with index $k = 1$). After this, the strain ε_D is incremented by $\Delta\varepsilon_D$ in each step and the solution points are computed by minimizing both the residual functions $RF^{(1)}_{RA-STM}$ and $RF^{(2)}_{RA-STM}$. For each step, the initial point is considered to be the solution point from the previous step. This calculation procedure holds until the ultimate value specified for the concrete in compression (ε_{cu}, see Table 1), which was computed from Eurocode 2 procedures [29], is reached ($\varepsilon^{k+1}_D \geqslant \varepsilon_{cu}$).

The algorithm was implemented with MATLAB [30] and the least squares method was used to minimize the residual functions by using the function *lsqnonlin*.

4. Validation of the refined efficient RA-STM procedure

The predictions from the refined efficient RA-STM procedure are compared with the experimental results of 22 reference square RC panels (with dimensions 139.7 × 139.7 × 17.8 cm, except for panel VA4 with thickness 20.3 cm) tested under in-plane stresses and found in the literature. Table 1 summarizes the properties of the selected panels. It should be referred that the experimental database used in this study was expanded in comparison to the same one (with 18 selected panels) used by Bernardo et al. in 2018 [25] to validate the previous version of the efficient RA-STM procedure.

All panels from VA-, VB-, A- and B-series were tested under symmetrical biaxial stresses in the 1–2 coordinate system with steel bars oriented at 45° to the principal compressive stress ($\alpha_2 = 45°$, see Fig. 4). The ratios of the compressive stress to the tensile stress in the 1–2 coordinate system is (-1) for all panels. As a consequence, these panels were tested under pure shear in the L-T coordinate system ($\sigma_L = \sigma_T = 0$).

The panels from F-series were tested under asymmetrical biaxial stresses in the L-T coordinate system with steel bars oriented at 90° to the principal compressive stress ($\alpha_2 = 90°$, see Fig. 4). The ratio of the compressive stress to the tensile stress in the L-T coordinate system are (-2), (-3) and (-4) for panels F2, F3 and F4, respectively.

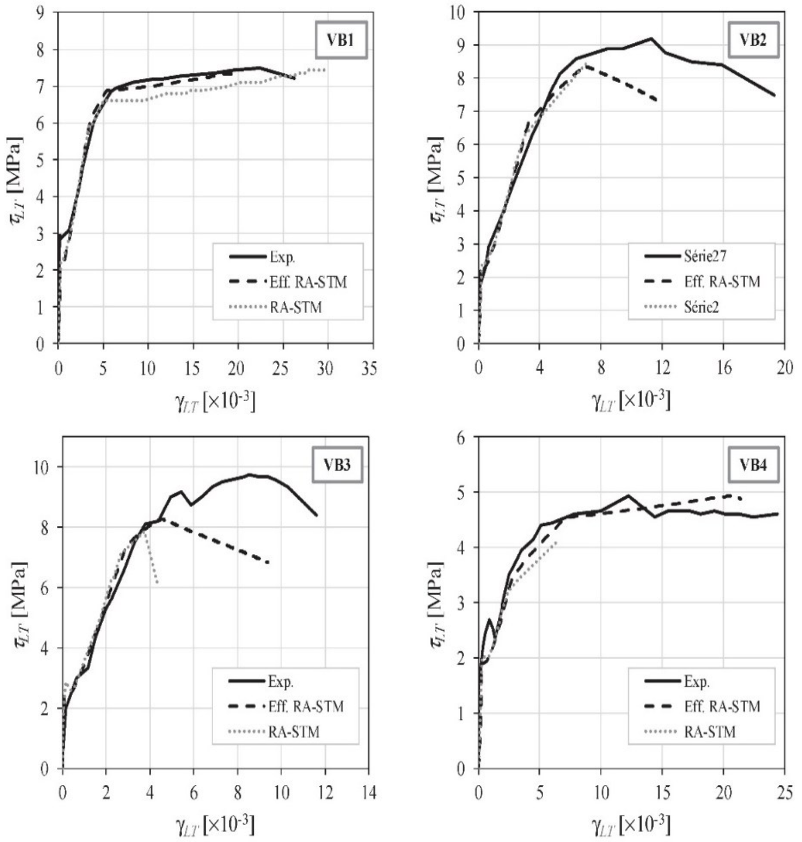

Fig. 6. $\tau_{LT} - \gamma_{LT}$ curves for panels from VB-series [27].

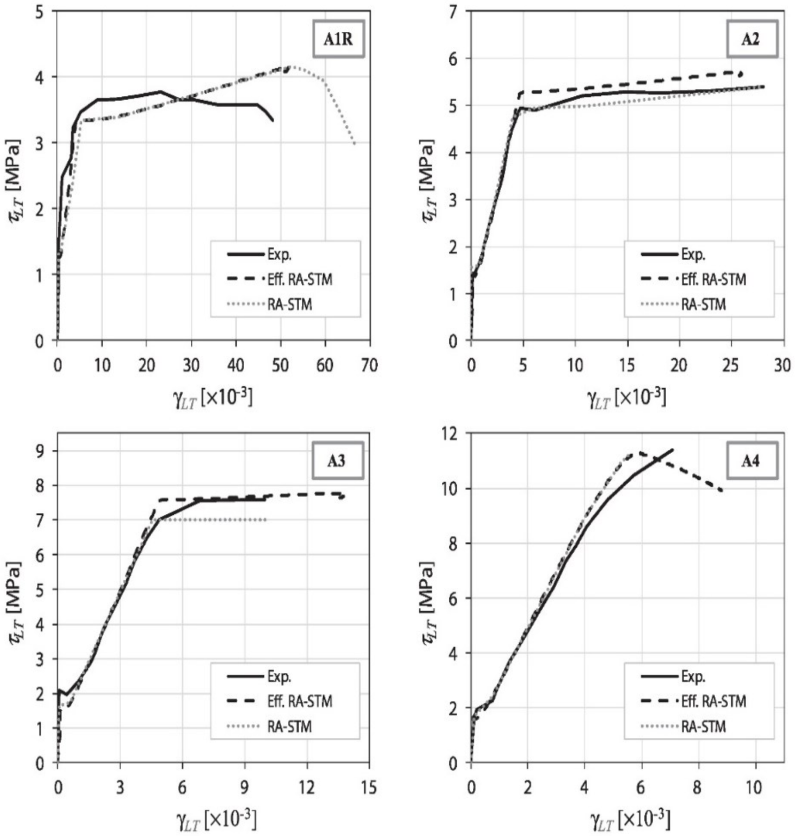

Fig. 7. $\tau_{LT} - \gamma_{LT}$ curves for panels from A-series [18,21].

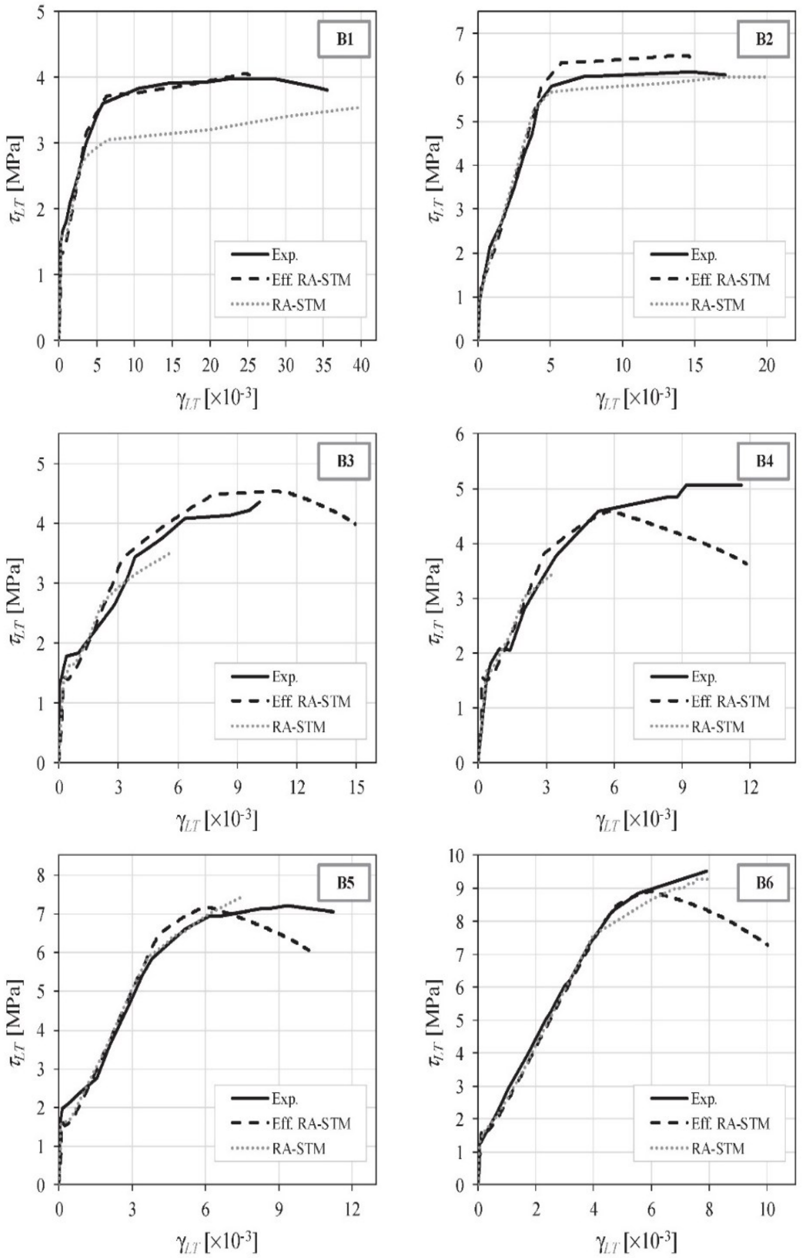

Fig. 8. $\tau_{LT} - \gamma_{LT}$ curves for panels from B-series [18].

The predicted full behavior of the selected panels was calculated with the refined efficient RA-STM procedure. Figs. 5 to 8 present graphs with the $\tau_{LT} - \gamma_{LT}$ curves of panels from VA-, VB-, A- and B-series, respectively. Each graph includes 3 curves: the experimental curve ("exp.") and two theoretical curves, one computed with the refined efficient RA-STM procedure ("Eff. RA_STM") proposed in this study and the other one from the RA-STM ("RA-STM") using the original calculation procedure with trial-and-error technique for comparison. Both experimental and theoretical curves from the original RA-STM were drawn from the graphs presented by the authors in their articles, namely: Zhang and Hsu in 1998 [27] for panels from VA- and VB-series, Hsu and Zhu in 2002 [21] for panel A1R and Pang and Hsu in 1995 [18] for panels from A- and B- series.

For panels from F-series, the presented experimental $\tau - \gamma$ curves by Hsu and Zhang in 1996 [31] were obtained for an inclined direction of 45° to the L-T coordinate system. The behavior of the referred panels must then be computed in such direction. For this, an equivalent applied stress state in the rotated direction was computed from Mohr's circle for stresses. The corresponding coordinate system is called Ĺ-Ť. In addition, equivalent reinforcement ratios were computed for the Ĺ-Ť coordinate system. Fig. 9 presents the $\tau_{L'T'}$ - $\gamma_{L'T'}$ curves of panels from F-series.

Figs. 5 to 9 show that, in general, the global behavior of the tested panels is well captured by the refined efficient RA-STM procedure, including the transition from the uncracked to the cracked stage (unlike the previous not refined model [22–25] which showed to capture well only the ultimate stage). Also, for most of the panels the predictions from the refined efficient RA-STM procedure are generally in good agreement with the same ones from the original RA-STM. Nevertheless, some differences can be observed, namely for the ultimate stage and mainly for panels with lower reinforcement ratios. This is probably because different constitutive laws where used in this study, namely for steel reinforcement. For some panels, such as panels VB2, VB3, VB4, B3, B4 and F3, the final part of the $\tau_{LT} - \gamma_{LT}$ curves from the refined

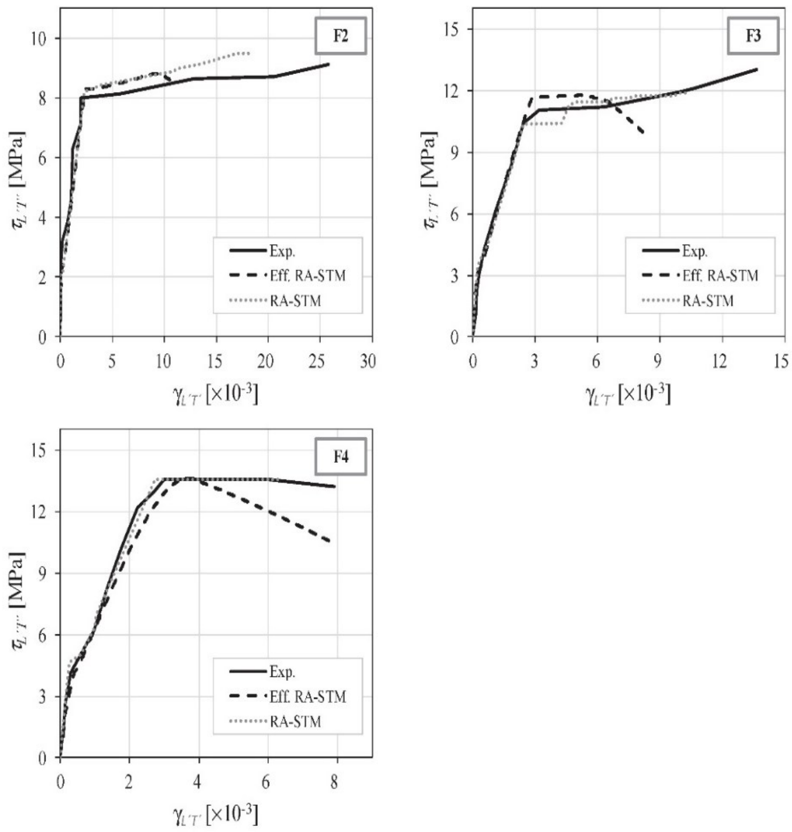

Fig. 9. $\tau_{LT} - \gamma_{LT}$ curves for panels from F-series [31].

Table 2
Comparative analysis between experimental and predicted key parameters.

Panel	$\tau_{cr,exp}$ MPa	$\tau_{cr,th}^{\text{eff. RA - STM}}$ MPa	$\frac{\tau_{cr,exp}}{\tau_{cr,th}^{\text{eff. RA - STM}}}$	$k_{S,exp}$ MPa	$k_{S,th}^{\text{eff. RA - STM}}$ MPa	$\frac{k_{S,exp}}{k_{S,th}^{\text{eff. RA - STM}}}$	$\tau_{u,exp}$ MPa	$\tau_{u,th}^{\text{eff. RA - STM}}$ MPa	$\frac{\tau_{u,exp}}{\tau_{u,th}^{\text{eff. RA - STM}}}$	$\gamma_{u,exp}$ $\times 10^{-3}$	$\gamma_{u,th}^{\text{eff. RA - STM}}$ $\times 10^{-3}$	$\frac{\gamma_{u,exp}}{\gamma_{u,th}^{\text{eff. RA - STM}}}$
VA0 [27]	2.05	1.72	1.19	0.409	0.590	0.69	3.80	3.70	1.03	49.50	59.33	0.83
VA1 [27]	2.00	1.98	1.01	0.770	0.993	0.78	6.30	6.41	0.98	42.90	48.34	0.89
VA2 [27]	2.60	2.35	1.10	1.586	1.925	0.82	9.80	9.91	0.99	21.80	19.77	1.10
VA3 [27]	2.70	2.45	1.10	2.568	2.715	0.95	15.00	15.36	0.98	7.00	6.96	1.01
VA4 [27]	2.50	2.69	0.93	3.221	3.732	0.86	21.50	18.33	1.17	7.30	4.97	1.47
VB1 [27]	2.95	2.11	1.40	1.075	1.343	0.80	7.50	7.33	1.02	22.43	18.81	1.19
VB2 [27]	1.70	2.35	0.72	1.184	1.659	0.71	9.18	8.35	1.10	11.28	7.08	1.59
VB3 [27]	2.00	2.44	0.82	1.722	2.032	0.85	9.76	8.27	1.18	8.51	4.58	1.86
VB4 [27]	1.66	1.89	0.88	0.834	0.781	1.07	4.94	4.94	1.00	12.27	20.54	0.60
A1R [21]	1.48	1.30	1.14	0.440	0.609	0.72	3.78	4.16	0.91	23.09	51.18	0.45
A2 [18]	1.34	1.44	0.93	0.842	0.963	0.87	5.39	5.71	0.94	28.00	25.36	1.10
A3 [18]	2.10	1.51	1.39	1.341	1.394	0.96	7.58	7.78	0.98	9.95	13.18	0.75
A4 [18]	1.69	1.69	1.00	1.838	2.017	0.91	11.38	11.28	1.01	7.07	5.86	1.21
B1 [18]	1.43	1.37	1.04	0.655	0.659	0.99	3.97	4.05	0.98	22.36	24.70	0.91
B2 [18]	0.92	1.31	0.70	0.956	1.136	0.84	6.14	6.51	0.94	14.76	14.05	1.05
B3 [18]	1.29	1.41	0.91	0.798	0.792	1.01	4.36	4.54	0.96	10.13	10.83	0.94
B4 [18]	1.52	1.52	1.00	0.989	0.990	1.00	5.07	4.60	1.10	9.18	5.89	1.56
B5 [18]	1.63	1.63	1.00	1.311	1.374	0.95	7.19	7.17	1.00	9.36	6.10	1.54
B6 [18]	1.27	1.66	0.77	1.642	1.640	1.00	9.51	8.90	1.07	7.93	5.96	1.33
F2 [31]	2.41	2.30	1.05	3.007	2.915	1.03	9.12	8.82	1.03	25.78	9.29	2.78
F3 [31]	2.21	3.10	0.71	3.177	3.520	0.90	13.03	11.77	1.11	13.56	5.16	2.63
F4 [31]	4.14	4.03	1.03	3.887	3.924	0.99	13.58	13.63	1.00	3.30	3.69	0.89
		$\bar{x}=$	0.993		$\bar{x}=$	0.896		$\bar{x}=$	1.022		$\bar{x}=$	1.258
		$s=$	0.191		$s=$	0.109		$s=$	0.072		$s=$	0.580
		$cv=$	19.22%		$cv=$	12.21%		$cv=$	7.05%		$cv=$	46.07%

efficient RA-STM procedure agree better with the experimental curves. This is probably due to the higher numerical efficiency and stability provided by the proposed new calculation procedure, allowing to compute more accurate solution points in the nonlinear stage. This also allows the efficient RA-STM procedure to predict better the failure mode of the panels. Several panels (for instance, panels VA1, VA2, VA3, VB1, VB4, A1R, A2, A3, B1, B2, B3, F2 and F3) clearly show a typical ductile failure. After the yielding of the reinforcement, the τ_{LT} - γ_{LT} (or $\tau_{L'T'}$ - $\gamma_{L'T'}$) curves show a plateau where the loading capacity is maintained with small variations over a large range of deformation until

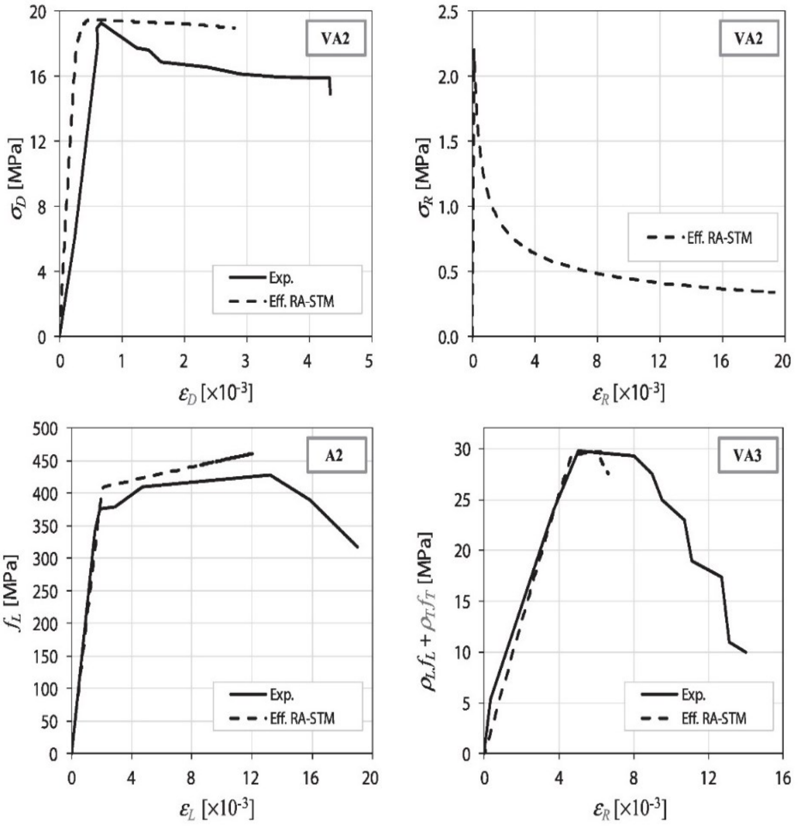

Fig. 10. Examples of other curves for some panels.

failure. For such panels, the predictions from the efficient RA-STM procedure for the final shape of the curves are good, although the model can predict a somewhat different length for the plateau (panels F2 and F3). Other panels show a somewhat less ductile behavior, with a clear reduction of the loading capacity after the peak stress (panels VB2 and VB3) or no apparent ductility (panels VA4, A4 and B6). For such panels, the efficient RA-STM procedure do not predict any horizontal plateau and the shear stress clearly decreases after the peak stress. Finally, for panel VA0 the theoretical $\tau_{LT} - \gamma_{LT}$ curves are atypical in comparison with the experimental one (Fig. 5). This is probably because panel VA0 does not meet the requirement for minimum reinforcement, as stated by Zhu et al. in 2001 [26]. The other panels selected for this study generally meet the necessary requirements for RC membranes to show an acceptable behavior (such requirements can be found in [1]).

For each panel, Table 2 presents both the experimental and theoretical (refined efficient RA-STM procedure) values for the following key parameters of the τ_{LT} - γ_{LT} (or $\tau_{L'T'}$ - $\gamma_{L'T'}$) curves: cracking shears $\tau_{cr,exp}$ and $\tau_{cr,th}^{\text{eff. RA-STM}}$, shear stiffnesses in the cracked stage $k_{S,exp}$ and $k_{S,th}^{\text{eff. RA-STM}}$, shear strengths $\tau_{u,exp}$ and $\tau_{u,th}^{\text{eff. RA-STM}}$ and the corresponding shear strains $\gamma_{u,exp}$ and $\gamma_{u,th}^{\text{eff. RA-STM}}$. The following ratios are also presented: $\tau_{cr,exp}/\tau_{cr,th}^{\text{eff. RA-STM}}$, $k_{S,exp}/k_{S,th}^{\text{eff. RA-STM}}$, $\tau_{u,exp}/\tau_{u,th}^{\text{eff. RA-STM}}$ and $\gamma_{u,exp}/\gamma_{u,th}^{\text{eff. RA-STM}}$. In addition, for each ratio the following statistical parameters were computed: mean ($\bar{x}$), standard deviation (s) and coefficient of variation (cv). It was not possible to obtain accurate values for the experimental shear strain corresponding to the cracking point, so this parameter was not included for the comparative analysis. To compute the shear stiffness in the cracked stage, the points of the τ_{LT} - γ_{LT} (or $\tau_{L'T'}$ - $\gamma_{L'T'}$) curves which lie in the approximately linear part of the ascending branch were selected. Then, a linear regression was performed in order to obtain the average slope, which corresponds to the shear stiffness.

Table 2 shows that the refined efficient RA-STM procedure predicts well both the cracking shear τ_{cr} ($\bar{x}$ = 0.993) and the shear stiffness in the cracked stage k_S ($\bar{x}$ = 0.896), although this last one is slightly overestimated. In addition, the degree of dispersion of the results is acceptable (cv = 19.22% and cv = 12.21%, respectively). For the cracking shear, the higher degree of dispersion can probably be due to the high variability of the tensile concrete strength, which highly influences the cracking point.

Table 2 also shows that the refined efficient RA-STM procedure predicts very well the ultimate shear stress τ_u ($\bar{x}$ = 1.022) and with a low degree of dispersion (cv = 7.05%). This result is in very good agreement with the results from Bernardo et al. in 2018 [25] obtained with the previous version of the efficient RA-STM procedure only reliable for the ultimate stage. In such study, the following statistical values were obtained for the shear strength without considering panel VA0 nor panels from F-series: $\bar{x}$ = 1.066 and cv = 8.635%. This shows that considering the contribution of concrete in tension in order to refine the efficient RA-STM procedure for low loading stages, as proposed in this study, does not affect negatively the prediction of the shear strength. As regards to the ultimate shear strain γ_u, Table 2 shows that, in general, the refined efficient RA-STM procedure seems to underestimate this parameter ($\bar{x}$ = 1.258) and with a high degree of dispersion (cv = 46.07%). This result is highly influenced by panels F2 and F3, for which the ultimate shear strain is highly underestimated (see Fig. 9). If such panels are disregarded, the following new values are obtained: $\bar{x}$ = 1.114 and cv = 32.28%. These values are much closer to the same ones obtained by Bernardo et al. in 2018 [25] ($\bar{x}$ = 1.129 and cv = 32.965%). In general, theoretical truss-based models present higher difficulty to predict well the deformation of the panels corresponding to the peak loads. However, such parameter is not very important for design.

Fig. 10 presents some examples of other behavioral curves, both theoretical and experimental (if exists), for selected panels, namely the $\sigma_D - \varepsilon_D$ and $\sigma_R - \varepsilon_R$ curves for panel VA2, the $f_L - \varepsilon_L$ curves for panel A2 and the $\rho_L f_L + \rho_T f_T - \varepsilon_R$ curves for panel VA3. Fig. 10 shows that the theoretical curves generally agree well with the experimental ones, including for the prediction of the peak stress for concrete, the yielding point and post-yielding behavior for the reinforcement.

5. Conclusions

In this article, the efficient RA-STM procedure proposed in a previous study was refined in order to incorporate the contribution of the tensile stresses in concrete. The equations of the refined model were reformulated in order to incorporate this additional contribution and an appropriate smeared constitutive law for tensile concrete was implemented. In addition, the new solution procedure was also presented. The predictions from the proposed refined efficient RA-STM procedure were compared with the experimental results of tested RC panels found in the literature. From the obtained results, the following main conclusions can be drawn:

- The refined efficient RA-STM procedure has proven to predict well the full response of RC membrane elements under in-plane stresses. Unlike the previous efficient RA-STM procedure, which showed to predict well only the shear strength, the refined efficient RA-STM procedure predicts also well the response of RC membrane elements for low loading stages, in particular the cracking point and the shear stiffness in the cracked stage;
- Unlike previous theoretical models which use a trial-and-error technique and a large number of initial estimates, the refined efficient RA-STM procedure allows to compute accurately the full behavior of RC membrane elements with high numerical efficiency and stability. It addition, the calculation procedure is easier to implement in a computer and require less calculation effort. The full response of the studied RC membrane elements was calculated in few seconds;
- The refined efficient RA-STM procedure showed to be a reliable and alternative theoretical model to other analytically more complicated truss models.

CRediT authorship contribution statement

L.F.A. Bernardo: Supervision, Conceptualization, Resources, Software, Writing - review & editing. **B.M.V.C. Filho:** Methodology, Investigation, Formal analysis, Validation, Writing - original draft. **B. Horowitz:** Supervision, Conceptualization, Writing - review & editing.

Declaration of Competing Interest

The authors declare that they have no known competing financial interests or personal relationships that could have appeared to influence the work reported in this paper.

References

[1] Hsu TTC, Mo YL (2010) Unified Theory of Concrete Structures. Wiley, 500 pp.

[2] Ritter W (1899) Die Bauweise Hennebique. Schweizerishe Bauzeitung, Zurich, 9 pp [in German].

[3] Mörsch E. Der Eisenbetonbau, seine Anwendung und Theorie. 1st ed. Wayss and Fretag, A. G., Im Selbstverlag der Firma, Neustadt a d. Haardt; 1902, 118 pp [in German].

[4] Karayannis CG. Smeared crack analysis for plain concrete in torsion. J Struct Eng 2000;126(6):638–45.

[5] Karayannis CG, Chalioris CE. Experimental validation of smeared analysis for plain concrete in torsion. J Struct Eng 2000;126(6):646–53.

[6] Yamamoto T, Vecchio FJ. Analysis of reinforced concrete shells for transverse shear and torsion. ACI Struct J 2001;98(2):191–200.

[7] Elfgren L. Reinforced Concrete Beams Loaded in Combined Torsion, Bending and Shear. Publication 71:3. Division of Concrete Structures, Chalmers University of Technology, Goteborg, Sweden; 1972. 249 pp.

[8] Nielsen MP. Om Forskydningsarmering i Jernbetonbjaelker. Bygningsstatiske Meddeleser 1967;38(2):33–58. (in German).

[9] Lampert P, Thürlimann B (1968) Torsionsversuche an Stahlbetonbalken. Institut für Baustatik, ETH Zürich, 101 pp [in German].

[10] Collins MP. Torque-twist characteristics of reinforced concrete beams. Inelasticity and Non-Linearity in Structural Concrete, Study No. 8, University of Waterloo Press; 1973. p. 211–231.

[11] Robinson JR, Demorieux JM (1968) Essais de Traction-Compression sur Modèles d'Âme de Poutre en Béton Armé. IRABA Report, Institut de Recherches Appliquées du Béton Armé, Part 1, June , 44 pp [in French].

[12] Vecchio FJ, Collins MP. The response of reinforced concrete to in-plane shear and normal stresses. Publication No. 82-03, Department of Civil Engineering, University of Toronto; 1982. 332 pp.

[13] Vecchio FJ, Collins MP. The modified compression-field theory for reinforced concrete elements subjected to shear. ACI J 1986;83(2):219–31.

[14] Hsu TTC. Softened Truss Model Theory for Shear and Torsion. Structural Journal of the American Concrete Institute 1988;85(6):624–35.

[15] Hsu TTC. Unified theory of reinforced concrete. Boca Raton, Florida: CRC Press Inc.; 1993. p. 313.

[16] Belarbi A, Hsu TTC. Constitutive laws of softened concrete in biaxial tension-compression. Struct J Am Concr Inst 1995;92(5):562–73.

[17] Belarbi A, Hsu TTC. Constitutive laws of concrete in tension and reinforcing bars stiffened by concrete. Struct J Am Concr Inst 1994;91(4):465–74.

[18] Pang XB, Hsu TTC. Behavior of reinforced concrete membrane elements in shear. Struct J Am Concr Inst 1995;92(6):665–79.

[19] Pang XB, Hsu TTC. Fixed-angle softened truss model of reinforced concrete. Struct J Am Concr Inst 1996;93(2):197–207.

[20] Hsu TTC, Zhang LX. Nonlinear analysis of membrane elements by fixed-angle softened-truss model. Struct J Am Concr Inst 1997;94(5):483–92.

[21] Hsu TTC, Zhu RRH. Softened membrane model for reinforced concrete elements in shear. Struct J Am Concr Inst 2002;99(4):460–9.

[22] Silva JRB, Horowitz B. Efficient procedure to estimate the load-deformation behavior of reinforced concrete panels under membrane forces. CILAMCE 2015 – XXXVI Iberian Latin American Congress on Computational Methods in Engineering, Rio de Janeiro-RJ, Brasil; 2015 [in Portuguese].

[23] Silva JRB. Efficient procedure for the analysis of reinforced concrete sections using the softened truss model, Master Thesis, Department of Civil Engineering, Federal University of Pernambuco, Recife, Brazil; 2016 [in Portuguese].

[24] Cerquido BMD. Analysis of reinforced concrete sections with the softened truss model. Master Thesis. Department of Civil Engineering and Architecture, University of Beira Interior, Covilhã, Portugal; 2017 [in Portuguese].

[25] Bernardo LFA, Cerquido BMD, Silva JRB, Horowitz B. Efficient Refined rotating-angle softened truss model procedure to analyze reinforced concrete membrane elements. Struct Concr J fib 2018;19(6):1971–82.

[26] Zhu RRH, Hsu TTC, Lee JY. Rational shear modulus for smeared-crack analysis of reinforced concrete. Struct J Am Concr Inst 2001;98(4):443–50.

[27] Zhang LX, Hsu TTC. Behavior and analysis of 100 MPa concrete membrane elements. J Struct Eng 1998;124(1):24–34.

[28] Jeng CH, Hsu TTC. A softened membrane model for torsion in reinforced concrete members. Eng Struct 2009;31(9):1944–54.

[29] NP EN 1992-1-1. Eurocode 2: Design of Concrete Structures - Part 1: General Rules and Rules for Buildings; March 2010.

[30] MathWorks (2018) MATLAB_R2018a.

[31] Hsu TTC, Zhang LX. Tension stiffening in reinforced concrete membrane elements. ACI Struct J 1996;93(1):108–15.

Capítulo 5

Prevendo o comportamento de elementos de membrana de concreto protendido pelo modelo refinado de treliça com amolecimento e ângulo variável com procedimento de solução eficiente.

Este capítulo consiste no artigo:

Predicting the behavior of prestressed concrete membrane elements by refined rotating-angle softened-truss model with efficient solution procedure.

Bernardo, L.F.A.; Filho, B.M.V.C.; Horowitz, B. 2020 “ Predicting the behaviour of prestressed concrete membrane elements by refined rotating-angle softened-truss model with efficient solution procedure”, Structural Concrete, Journal of the fib, ISNN: 1751-7648, Volume 21: pp. 934-948.
DOI: https://doi.org/10.1002/suco.201900481

Received: 11 November 2019 | Revised: 5 January 2020 | Accepted: 13 January 2020

DOI: 10.1002/suco.201900481

TECHNICAL PAPER

Predicting the behavior of prestressed concrete membrane elements by refined rotating-angle softened-truss model with efficient solution procedure

Luís F. A. Bernardo[1] | **Benedito M. V. C. Filho**[2] | **Bernardo Horowitz**[3]

[1]C-MADE - Centre of Materials and Building Technologies, University of Beira Interior, Covilhã, Portugal

[2]Department of Civil Engineering and Architecture, University of Beira Interior, Covilhã, Portugal

[3]Department of Civil Engineering, Federal University of Pernambuco, Recife, Brazil

Correspondence
Luís F. A. Bernardo, Department of Civil Engineering and Architecture, University of Beira Interior, Edifício II das Engenharias, Calçada Fonte do Lameiro, 6200-001 Covilhã, Portugal.
Email: lfb@ubi.pt

Abstract

This article presents a refined version of the rotating-angle softened truss model (RA-STM) with efficient solution procedure to predict the full behavior of prestressed concrete (PC) membrane elements under in-plane stresses. The refined model incorporates the concrete tensile strength in the perpendicular direction to the concrete struts and an additional smeared constitutive law for the tensile concrete. In order to avoid the classical trial and error solution procedure used in previous versions of the RA-STM, a new algorithm is presented which lead to a more efficient solution procedure with higher numerical stability. The reliability of the proposed model is verified with experimental data related with PC plates under in-plane stresses, where good agreement is observed.

KEYWORDS

efficient solution procedure, membrane elements, Prestressed concrete, rotating-angle softened truss model

1 | INTRODUCTION

In the last decades, truss models have been widely used to develop new analytical tools and have shown to be suitable to predict the behavior of several structural concrete members, or parts of them, under multiple loading conditions. When compared with other and more complex analytical models, truss models allow the users to easily understand the role of the materials (concrete and steel bars) and how the stress fields are distributed inside the structural member, namely in the cracked stage.

In order to simplify the problem, modern truss models treat the element under study as a continuous material even for the cracked stage. Instead of evaluating locally the stresses and strains, these ones are evaluated on average along a sufficient length to include several cracks. As a result, the mathematical formulation is easier to manipulate and, even in nonlinear problems, the algorithm for the solution procedure is also easier to implement with basic programming languages.

Among several applications, truss-based models have been developed to model two-dimensional (2D) elements under in-plane stress states, the so-called membrane elements. Reliable models for such elements are important because many structural concrete members, such as shells and shear walls, can be viewed as the union of small 2D membrane elements.[1]

The first so-called softened truss model (STM), accounting for the softening effect in the compressive concrete struts previously reported by Robinson and Demorieux,[2] was proposed by Hsu.[3] Unlike previous

---

Discussion on this paper must be submitted within two months of the print publication. The discussion will then be published in print, along with the authors' closure, if any, approximately nine months after the print publication.

refined truss models proposed by other authors at that time, such as the so-called modified compression-field theory from Vecchio and Collins,[4,5] the STM was the first model to incorporate a smeared and softened constitutive law for the concrete in compression instead of the usual uniaxial stress (σ)–strain (ε), relationship.

Since the 1990s of the last century, and based on new experimental data from controlled tests with RC and prestressed concrete (PC) panels, the STM has been refined over the years and new models were proposed.

Experiments showed that, after cracking, the direction of principal stresses rotates as a result of the stress redistribution and deformation compatibility.[6] For this reason, the SMT was modified in order to allow the direction of the principal compressive stresses in the concrete member to rotate. The model was renamed Rotating-Angle STM (RA-STM).[7] At that time, several refinements of the RA-STM were proposed, including refined smeared σ–ε relationships calibrated with new experimental data, namely, for normal- and high-strength concrete in compression,[8,9] and for steel reinforcing bars in tension including the stiffening effect and the dowel action.[7,10] In addition, the contribution of the tensile concrete in the perpendicular direction to the struts, neglected in the first version of the model, was also implemented in order to refine the STA for the early loading stages. This was achieved by incorporating a new smeared σ–ε relationship for concrete in tension.[7,8,10] At that time, the RA-STM was already able to predict the behavior of both reinforced concrete (RC) and PC membrane elements under in-plane stresses, despite very few experiments with PC panels existed in the literature for comparison at that time.[11]

In order to neglect the contribution of concrete in shear, the equilibrium and compatibility equations of RA-STM are written with respect to a fixed Cartesian reference frame which coincides with the rotating principal directions of internal stresses in the concrete member. Although small, the referred contribution exists due to interlocking of the aggregates along the cracks and also because the direction of cracks tends to deviate from the direction of the principal compressive stresses.[12] To consider this new contribution, Pang and Hsu[13] and Hsu and Zhang[14] considered a new reference frame at a fixed angle to write the equations and incorporated a new shear stress (τ)–shear strain (γ) relationship for concrete in shear. This angle was considered to be equal to the angle of the principal directions of the external stresses applied to the RC member. The new model was called fixed-angle STM (FA-STM).

In order to refine the model for the postpeak loading stage, Zhu and Hsu[15] incorporated the so-called Hsu/Zhu ratios to account for the Poisson's effect and called the new model softened membrane model (SMM). Later, based on new experiments with PC panels, Laskar et al.[16] extended the SMM for PC membrane elements and proposed the so-called SMM-PC. As expected, it was found that prestress delays the cracking of concrete and increases the resistance of the tested panels, as the result of the biaxial stress state induced by the prestress compressive stresses and the applied in-plane stresses.

For all the versions of the aforementioned truss models, the calculation procedures are based on trial-and-error techniques which may require a large calculation effort. In addition, they can lead to the loss of numerical efficiency and stability due to the intrinsic nonlinear characteristic of the equations to be solved and also due to the large number of estimated parameters which are needed to start the calculations. For these reasons, alternative and efficient solution procedures are always desirable.

Due to its analytical simplicity when compared to the FA-STM or SMM, in recent studies, the RA-STM has continued to be used and extended to other structural members.[17] In particular, some attempts have been made to propose new algorithms in order to increase the numerical efficiency and stability of the calculation procedure for RC and PC membrane elements.[18–21] Bernardo et al.[20,21] reformulated the RA-STM as a system of nonlinear equations with constraints. These equations were then solved efficiently by using an optimization algorithm. This new calculation procedure, called here efficient RA-STM procedure, avoids the need to use trial-and-error techniques, and shown to be numerically very efficient and stable, and also to require much less computational calculation effort. In addition to this improvement, the referred authors also refined the model by using a set of appropriated smeared constitutive laws for the materials to improve the precision of the model. Based on comparative analyses with experimental data, the authors found that the efficient RA-STM procedure captures well the ultimate behavior of RC panels under in-plane stresses. For PC panels, the results were considered to be acceptable. Since the concrete tensile strength was neglected in the model for simplicity, this one was not able to predict the transition from the uncracked to the cracked stage of the studied panels.

In this article, the efficient RA-STM procedure is refined for PC membrane elements in order to incorporate the influence of the concrete tensile stresses in the perpendicular direction to the concrete struts. The equations and the new solution procedure are presented. The predictions obtained from the new model are compared with the experimental results of some PC panels tested under in-plane stresses which are available in the literature. It is shown that the refined efficient RA-STM procedure provides good results for the ultimate state and, in addition, is also able to predict well the behavior for low loading stages, namely the cracking point and the stiffness in the cracked stage.

2 | REFINEMENT OF EFFICIENT RA-STM PROCEDURE FOR PC MEMBRANE ELEMENTS

In this section, the efficient RA-STM procedure for PC membrane elements is modified to incorporate the concrete tensile strength. The new refined and efficient solution procedure is also described. The followed steps to present the model are similar to the same ones presented by Hsu[6] and Pang and Hsu[7] for the original RA-STM and also by Bernardo et al.[20,21] for the previous versions of the efficient RA-STM procedure.

In both the RA-STM and efficient RA-STM procedure, a nonlinear plain truss model is idealized as the resistance mechanism, where concrete resists to compressive stresses and reinforcement (steel bars) resists to axial tensile stresses. The equations follow the three Navier's principles of mechanics: equilibrium of stresses, compatibility of strains, and constitutive laws for the materials.

2.1 | Equilibrium and compatibility equations

Figure 1 illustrates a 2D PC membrane element under in-plane normal (σ_L and σ_T) and shear (τ_{LT}) stresses in the longitudinal (L)–transverse (T) coordinate system, corresponding to the direction of longitudinal and transverse reinforcement. Perfect bond is assumed between steel bars and concrete, and dowel action is neglected. Using the principle of superposition, the in-plane stresses in the PC membrane element are broken into three components: the in-plane stresses in the concrete membrane element (σ_L^c, σ_T^c, and τ_{LT}^c), and the normal stresses in the non-prestress steel bars ($\rho_L f_L$ and $\rho_T f_T$) and prestress steel bars ($\rho_{LP} f_{LP}$ and $\rho_{TP} f_{TP}$). In Figure 1, ρ stands for the reinforcement ratio (see footnotes in Table 1) and f stands for the normal stress in the steel bars. From Figure 1, the following three equilibrium equations for stresses are written in matricial form:

$$\begin{bmatrix} \sigma_L \\ \sigma_T \\ \tau_{LT} \end{bmatrix} = \begin{bmatrix} \sigma_L{}^c \\ \sigma_T{}^c \\ \tau_{LT}{}^c \end{bmatrix} + \begin{bmatrix} \rho_L f_L \\ \rho_T f_T \\ 0 \end{bmatrix} + \begin{bmatrix} \rho_{LP} f_{LP} \\ \rho_{TP} f_{TP} \\ 0 \end{bmatrix} \tag{1}$$

From Mohr's circle for stresses, the stress components in concrete can be related with the principal stresses (σ_R

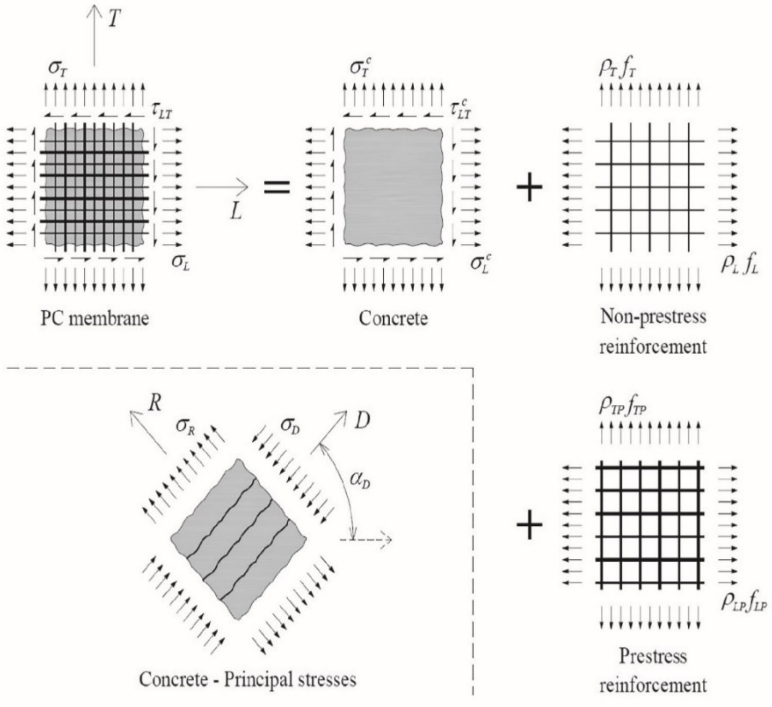

FIGURE 1 Two-dimensional (2D) PC member under in-plane stresses

TABLE 1 Characteristics of the reference PC panels

PC panel	f'_c MPa	ε_0 %	$\rho_{LP}{}^{a}$ %	$\rho_L{}^{a}$%	$f_{cP,\,i}$ MPa	f_{Pu} MPa	f_{Ly} MPa	E_P GPa	E'_P GPa	E_S GPa	$\rho_T{}^{a}$ %	f_{Ty} MPa	E_S GPa
TA-1[16]	41.5	0.21	0.84	—	8.3	1,793	—	200	209	—	0.42	414	197
TA-2[16]	41.3	0.19	0.84	—	8.3	1,793	—	200	209	—	0.77	415	192
TA-3[16]	42.2	0.19	0.84	—	8.3	1,793	—	200	209	—	1.54	415	192
TA-4[16]	42.5	0.21	0.59	—	5.8	1,793	—	200	209	—	0.77	415	192
TA-5[16]	41.1	0.21	0.42	—	4.1	1,793	—	200	209	—	0.77	415	192
PP2[11]	28.1	0.21	0.29	1.30	2.1	1,793	486	200	200	200	0.65	480	200
PP3[11]	27.7	0.21	0.59	0.65	4.4	1,793	480	200	200	200	0.65	480	200

[a] $\rho_{LP} = A_{LP}/A_c$; $\rho_T = A_{TS}/A_c$; $\rho_L = A_{LS}/A_c$.

and σ_D) and the variable angle α_D between the coordinate systems L-T and R-D (see Figure 1). Equation (1) can be rewritten as follows:

$$\begin{bmatrix} \sigma_L \\ \sigma_T \\ \tau_{LT} \end{bmatrix} = \begin{bmatrix} \cos^2(\alpha_D) & \sin^2(\alpha_D) & 2\sin(\alpha_D)\cos(\alpha_D) \\ \sin^2(\alpha_D) & \cos^2(\alpha_D) & -2\sin(\alpha_D)\cos(\alpha_D) \\ -\sin(\alpha_D)\cos(\alpha_D) & \sin(\alpha_D)\cos(\alpha_D) & \cos^2(\alpha_D)-\sin^2(\alpha_D) \end{bmatrix} \begin{bmatrix} \sigma_D \\ \sigma_R \\ 0 \end{bmatrix} + \begin{bmatrix} \rho_L f_L \\ \rho_T f_T \\ 0 \end{bmatrix} + \begin{bmatrix} \rho_{LP} f_{LP} \\ \rho_{TP} f_{TP} \\ 0 \end{bmatrix} \tag{2}$$

Unlike the previous versions of the efficient RA-STM procedure,[20,21] concrete tensile strength is no longer neglected ($\sigma_R \neq 0$). For convenience, the matricial Equation (2) is rewritten as the following system of three equilibrium equations:

$$\sigma_L = \sigma_D \cos^2(\alpha_D) + \sigma_R \sin^2(\alpha_D) + \rho_L f_L + \rho_{LP} f_{LP} \tag{3}$$

$$\sigma_T = \sigma_D \sin^2(\alpha_D) + \sigma_R \cos^2(\alpha_D) + \rho_T f_T + \rho_{TP} f_{TP} \tag{4}$$

$$\tau_{LT} = (-\sigma_D + \sigma_R)\sin(\alpha_D)\cos(\alpha_D) \tag{5}$$

From Mohr's circle for strains, the average strain components (ε_L, ε_T, and γ_{LT}) can be related with the principal strains (ε_R and ε_D) and the variable angle α_D as follows:

$$\begin{bmatrix} \varepsilon_L \\ \varepsilon_T \\ \gamma_{LT} \end{bmatrix} = \begin{bmatrix} \cos^2(\alpha_D) & \sin^2(\alpha_D) & 2\sin(\alpha_D)\cos(\alpha_D) \\ \sin^2(\alpha_D) & \cos^2(\alpha_D) & -2\sin(\alpha_D)\cos(\alpha_D) \\ -2\sin(\alpha_D)\cos(\alpha_D) & 2\sin(\alpha_D)\cos(\alpha_D) & 2\cos^2(\alpha_D)-2\sin^2(\alpha_D) \end{bmatrix} \begin{bmatrix} \varepsilon_D \\ \varepsilon_R \\ 0 \end{bmatrix} \tag{6}$$

In addition, the following invariant equation can be written from the first invariant (trace) of the strain tensor for both L-T and R-D coordinate systems:

$$\varepsilon_L + \varepsilon_T = \varepsilon_D + \varepsilon_R \Leftrightarrow \varepsilon_R = \varepsilon_L + \varepsilon_T - \varepsilon_D \tag{7}$$

For convenience, the third compatibility equation is isolated from the matricial Equation (6),

$$\gamma_{LT} = 2(\varepsilon_R - \varepsilon_D)\sin(\alpha_D)\cos(\alpha_D) \tag{8}$$

2.2 | Constitutive laws for the materials

For concrete in compression, the same smeared softened σ–ε relationship, used and justified by Bernardo et al.,[21] was adopted in this study. This relationship was firstly proposed by Belarbi and Hsu[8] and refined latter by Zhu et al.[22] (Equation (9), see Figure 2). The meaning of

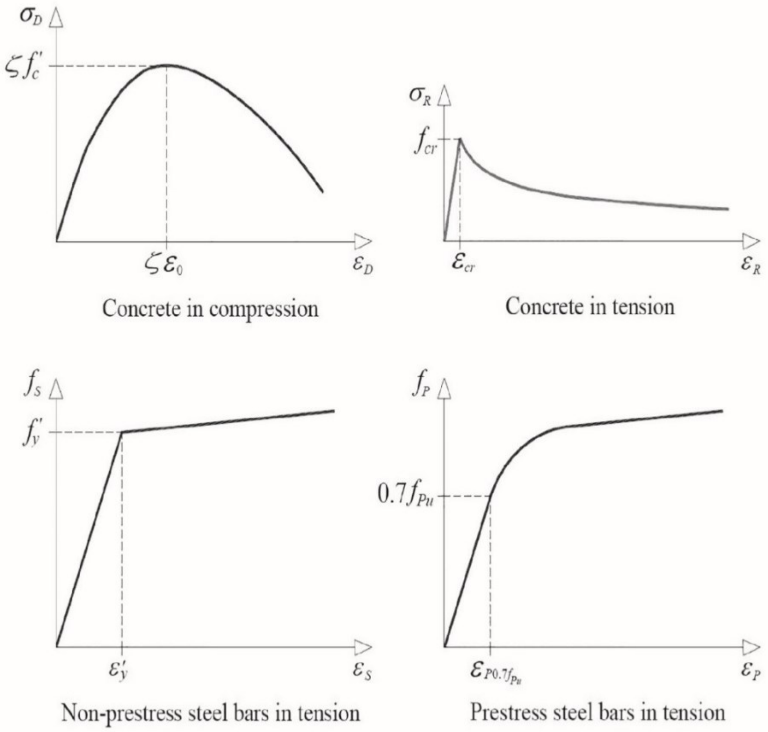

FIGURE 2 Constitutive laws for the materials

parameters in Equation (9) is the following ones: f_c' is the uniaxial compressive strength of concrete, ε_0 is the strain corresponding to the peak stress (f_c') and ζ is the softening coefficient. This last one is computed from Equations (10)–(12) and was proposed by Zhang and Hsu[9] and refined by Zhu et al.[22] This softening coefficient accounts for the ratio of the transverse to the longitudinal tensile strength of reinforcements (Equations (11) and (12)) through parameter η' and must account for the prestress reinforcement. The additional validity condition $0.4 < \eta < 2.5$ (equivalent to $0.4 < \eta' < 1.0$) from Pang and Hsu[7] and Zhang and Hsu[9] was also adopted in this study.

$$\sigma_D = \zeta f_c'\left[2\left(\frac{\varepsilon_D}{\zeta\varepsilon_0}\right) - \left(\frac{\varepsilon_D}{\zeta\varepsilon_0}\right)^2\right] \quad \text{if } \varepsilon_D \le \zeta\varepsilon_0 \qquad (9a)$$

$$\sigma_D = \zeta f_c'\left[1 - \left(\frac{(\varepsilon_D/\zeta\varepsilon_0) - 1}{(4/\zeta) - 1}\right)^2\right] \quad \text{if } \varepsilon_D > \zeta\varepsilon_0 \qquad (9b)$$

$$\zeta = \left(\frac{5.8}{\sqrt{f_c'(\text{MPa})}} \le 0.9\right) \cdot \frac{1}{\sqrt{1 + \frac{400\varepsilon_R}{\eta'}}} \qquad (10)$$

$$\eta = \frac{\rho_T f_{Ty} + \rho_{TP} f_{TP0.1\%} - \sigma_T}{\rho_L f_{Ly} + \rho_{LP} f_{LP0.1\%} - \sigma_L} \qquad (11)$$

$$\begin{cases} \eta' = \eta \ \text{ if } \ \eta \le 1 \\ \eta' = \dfrac{1}{\eta} \ \text{ if } \ \eta > 1 \end{cases} \quad (0.4 < \eta' < 1.0) \qquad (12)$$

Since the concrete tensile strength is not neglected in this study, an additional σ–ε relationship for tensile concrete needs to be incorporated in the efficient RA-STM procedure. The smeared σ–ε relationship for tensile concrete proposed by Belarbi and Hsu[10] for shear elements (Equations (13)–(16) see Figure 2) was also used in this study. This relationship was successfully used in truss-based models to compute the behavior of RC members under shear, accounting for the concrete tensile strength.[7,9,15] In Equations (13)–(16), the meaning of the parameters are: E_c is the Young's modulus for concrete and ε_{cr} is the tensile strain corresponding to the peak stress f_{cr} (concrete tensile strength).

$$\sigma_R = E_c\varepsilon_R \quad \text{if } \varepsilon_R \le \varepsilon_{cr} \qquad (13a)$$

$$\sigma_R = f_{cr}\left(\frac{\varepsilon_{cr}}{\varepsilon_R}\right)^{0.4} \quad \text{if } \varepsilon_R > \varepsilon_{cr} \qquad (13b)$$

$$E_c = 3875\sqrt{f_c'(\text{MPa})} \qquad (14)$$

$$\varepsilon_{cr} = 0.00008 \tag{15}$$

$$f_{cr} = E_c \varepsilon_{cr} = 0.311\sqrt{f'_c(\text{MPa})} \tag{16}$$

For nonprestress steel bars in tension embedded in concrete, the same smeared σ–ε relationship used and justified by Bernardo et al.[21] was also adopted in this study. This relationship is the simplified bilinear σ–ε relationship proposed by Pang and Hsu[7] (see Equations (17)–(20) and Figure 2).

$$f_S = E_S \varepsilon_S \text{ if } \varepsilon_S \leq \varepsilon'_y \tag{17a}$$

$$f_S = (0.91 - 2BN) f_{Sy} + (0.02 + 0.25BN) E_S \varepsilon_S \text{ if } \varepsilon_S > \varepsilon'_y \tag{17b}$$

$$\varepsilon'_y = \frac{f'_y}{E_S} \tag{18}$$

$$f'_y = (0.93 - 2BN) f_{Sy} \tag{19}$$

$$BN = \frac{1}{\rho}\left(\frac{f_{cr}}{f_{Sy}}\right)^{1.5} \quad (\rho \geq 0.15\%) \tag{20}$$

In Equations (17)–(20), f_S and ε_S are the average tensile stress and strain in the nonprestress steel bars, respectively, f_{Sy} is the yielding stress and E_S is the Young's modulus for steel.

For prestress steel bars, some considerations need to be discussed before the chosen smeared σ–ε relationship is presented. Before concrete decompression, the behavior of PC membrane elements lies entirely in the elastic domain because at this stage the strains in the materials are very small. For this reason, as assumed in previous studies where authors worked STMs for prestress members,[21,23] the calculation procedure of the refined efficient RA-STM procedure starts after concrete decompression. Hence, the strain in the prestress reinforcement, ε_P, is computed as follows,

$$\varepsilon_P = \varepsilon_{dec} + \varepsilon_S \tag{21}$$

where ε_{dec} is the strain at decompression and ε_S is the strain in non-prestress reinforcement (at decompression $\varepsilon_S = 0$). The strain ε_{dec} is computed from Equation (22), where $\varepsilon_{P,i}$ ($\varepsilon_{S,i}$) is the initial tensile (compressive) strain in the prestress (nonprestress) reinforcement due to prestress and which can be computed from Equation (23) (Equation (24)).

$$\varepsilon_{dec} = \varepsilon_{P,i} + \varepsilon_{S,i} \tag{22}$$

$$\varepsilon_{P,i} = \frac{f_{P,i}}{E_P} \tag{23}$$

$$\varepsilon_{S,i} = \frac{A_P f_{P,i}}{A_S(E_S - E_c) + E_c(A_c - A_P)} \tag{24}$$

In Equations (23) and (24), E_P is the Young's modulus for prestress steel, A_P and A_S are the total area of prestress and nonprestress steel, respectively, and A_c is the area of the concrete cross section.

To compute the stress in the prestress reinforcement, f_P, from the strain ε_P, the same uniaxial σ–ε relationship used and justified by Bernardo et al.[21] was also adopted in this study. The used σ–ε relationship, defined in Equation (25), is a corrected version of the one proposed by Hsu[24] (see Figure 2), which was based on the Ramberg–Osgood's curve.

$$f_P = E_P(\varepsilon_{dec} + \varepsilon_S) \text{ if } \varepsilon_P \leq \varepsilon_{P0.7f_{Pu}} \tag{25a}$$

$$f_P = \frac{E'_P(\varepsilon_{dec} + \varepsilon_S - \Delta\varepsilon_P)}{\left[1 + \left(\frac{E'_P(\varepsilon_{dec} + \varepsilon_S - \Delta\varepsilon_P)}{f_{Pu}}\right)^R\right]^{1/R}} \text{ if } \varepsilon_P > \varepsilon_{P0.7f_{Pu}} \tag{25b}$$

In the previous equations, E'_P is the Young's modulus of Ramberg–Osgood and R is a geometrical parameter to adjust the shape of the curve. Such parameters need to be evaluated experimentally from uniaxial tensile tests. For this study, the following values from Laskar et al.[16] were considered: $E'_P = 209$ GPa and $R = 5$. Also in the previous equations, f_{Pu} is the tensile strength of the prestress steel and $\varepsilon_{P0.7f_{Pu}}$ is the strain of prestress steel corresponding to $0.7f_{Pu}$. The variation strain $\Delta\varepsilon_P$ aims to translate, by a very small amount, the nonlinear curve from the original one (with $\Delta\varepsilon_P = 0$) to impose the continuity between the linear and nonlinear part of the $\sigma - \varepsilon$ curve. As explained by Bernardo et al.,[21] this correction is needed to avoid convergence problems when the solution points are computed at the transition between the referred parts of the σ–ε curve. As also justified in the referred study, $\Delta\varepsilon_P$ is computed as follows:

$$\Delta\varepsilon_P = \varepsilon^L_{P0.7f_{Pu}} - \varepsilon^{NL}_{P0.7f_{Pu}} \tag{26}$$

$$\varepsilon^L_{P0.7f_{Pu}} = \frac{0.7f_{Pu}}{E_P} \tag{27}$$

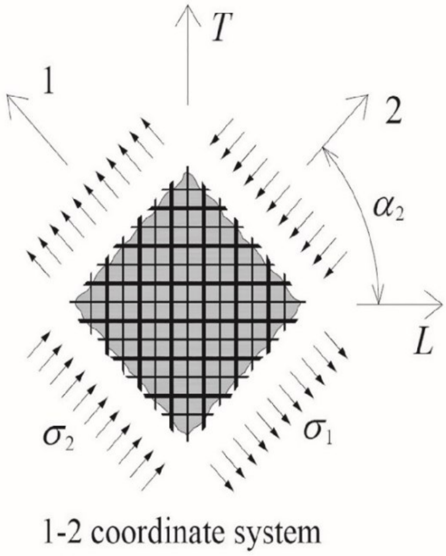

FIGURE 3 Principal applied stresses in the two-dimensional (2D) PC member

$$0.7f_{Pu} = \frac{E'_P \varepsilon^{NL}_{P0.7f_{Pu}}}{\left[1 + \left(\frac{E'_P \varepsilon^{NL}_{P0.7f_{Pu}}}{f_{Pu}}\right)^R\right]^{1/R}} \rightarrow \varepsilon^{NL}_{P0.7f_{Pu}} \tag{28}$$

In the previous equations, $\varepsilon^{L}_{P0.7f_{Pu}}$ and $\varepsilon^{NL}_{P0.7f_{Pu}}$ are the strains corresponding to $0.7f_{Pu}$ computed from the linear (L) and nonlinear (NL) part of the $\sigma - \varepsilon$ relationship, respectively. The strain $\varepsilon^{NL}_{P0.7f_{Pu}}$ is computed by solving a nonlinear equation (Equation (28)).

2.3 | Equations for proportional loading

In this study, proportional loading is assumed, that is, the ratios between the in-plane applied stresses in the PC membrane element remains constant. For this loading condition, it is possible to relate the in-plane applied stresses in the L–T coordinate system (σ_L, σ_T, and τ_{LT}) with the principal tensile stress in the PC membrane element in the 1–2 coordinate system, which coincides with the direction of principal applied stresses (σ_1 and σ_2) (Figure 3). For this, three proportionality coefficients are defined, namely longitudinal (m_L), transverse (m_T), and shear (m_{LT}) proportionality coefficients, according to Equation (29)–(31).

$$m_L = \frac{\sigma_L}{\sigma_1} \tag{29}$$

$$m_T = \frac{\sigma_T}{\sigma_1} \tag{30}$$

$$m_{LT} = \frac{\tau_{LT}}{\sigma_1} \tag{31}$$

From Mohr's circle for stresses, Equation (32) can be established to relates σ_1 with σ_L, σ_T, and τ_{LT}.

$$\sigma_1 = \frac{\sigma_L + \sigma_T}{2} + \sqrt{\left(\frac{\sigma_L - \sigma_T}{2}\right)^2 + \tau_{LT}{}^2} \tag{32}$$

Substituting m_L, m_T, and m_{LT} from Equations (29)–(31) into Equations (3)–(5), gives:

$$m_L\sigma_1 - \rho_L f_L - \rho_{LP} f_{LP} = \sigma_D \cos^2(\alpha_D) + \sigma_R \sin^2(\alpha_D) \tag{33}$$

$$m_T\sigma_1 - \rho_T f_T - \rho_{TP} f_{TP} = \sigma_D \sin^2(\alpha_D) + \sigma_R \cos^2(\alpha_D) \tag{34}$$

$$m_{LT}\sigma_1 = (-\sigma_D + \sigma_R)\sin(\alpha_D)\cos(\alpha_D) \tag{35}$$

Using the trigonometric identity $\sin^2(\alpha_D) + \cos^2(\alpha_D) = 1$, Equations (33) and (34) can be rewritten as follows:

$$m_L\sigma_1 - \rho_L f_L - \rho_{LP} f_{LP} = \sigma_D \cos^2(\alpha_D) + \sigma_R\left[1 - \cos^2(\alpha_D)\right]$$

$$\ldots \Leftrightarrow \text{-}m_L\sigma_1 + \sigma_R + \rho_L f_L + \rho_{LP} f_{LP} = (\sigma_R - \sigma_D)\cos^2(\alpha_D) \tag{a}$$

$$m_T\sigma_1 - \rho_T f_T - \rho_{TP} f_{TP} = \sigma_D \sin^2(\alpha_D) + \sigma_R\left[1 - \sin^2(\alpha_D)\right]$$

$$\ldots \Leftrightarrow \text{-}m_T\sigma_1 + \sigma_R + \rho_T f_T + \rho_{TP} f_{TP} = (\sigma_R - \sigma_D)\sin^2(\alpha_D) \tag{b}$$

Multiplying Equations (a) and (b) gives:

$$\begin{aligned}(\text{-}m_L\sigma_1 + \sigma_R + \rho_L f_L + \rho_{LP} f_{LP})(\text{-}m_T\sigma_1 + \sigma_R + \rho_T f_T + \rho_{TP} f_{TP}) \\ = (\sigma_R - \sigma_D)^2\cos^2(\alpha_D)\sin^2(\alpha_D)\end{aligned} \tag{c}$$

Squaring Equation (35) gives:

$$(m_{LT}\sigma_1)^2 = (-\sigma_D + \sigma_R)^2\sin^2(\alpha_D)\cos^2(\alpha_D) \tag{d}$$

Equating the left members of Equations (c) and (d) gives Equation (36), which combines Equations (33)–(35).

$$\begin{aligned}(\text{-}m_L\sigma_1 + \sigma_R + \rho_L f_L + \rho_{LP} f_{LP})(\text{-}m_T\sigma_1 + \sigma_R + \rho_T f_T + \rho_{TP} f_{TP}) \\ = (m_{LT}\sigma_1)^2\end{aligned} \tag{36}$$

Expanding Equation (36) and rearranging terms, the following quadratic polynomial equation can be written:

$$
\begin{aligned}
&m_L m_T - m_{LT}{}^2 \sigma_1{}^2 + [-m_L \sigma_R + \rho_T f_T + \rho_{TP} f_{TP} \\
&\quad - m_T \sigma_R + \rho_L f_L + \rho_{LP} f_{LP}] \sigma_1 + \ldots\ldots + \sigma_R + \rho_L f_L \\
&\quad + \rho_{LP} f_{LP} . (\sigma_R + \rho_T f_T + \rho_{TP} f_{TP}) = 0 \Leftrightarrow A' \sigma_1{}^2 \\
&\quad + -B' \sigma_1 + C' = 0
\end{aligned} \tag{37}
$$

with:

$$A' = m_L m_T - m_{LT}{}^2 \tag{38}$$

$$B' = m_L(\sigma_R + \rho_T f_T + \rho_{TP} f_{TP}) + m_T(\sigma_R + \rho_L f_L + \rho_{LP} f_{LP}) \tag{39}$$

$$C' = (\sigma_R + \rho_L f_L + \rho_{LP} f_{LP})(\sigma_R + \rho_T f_T + \rho_{TP} f_{TP}) \tag{40}$$

The quadratic formula for σ_1 gives:

$$\sigma_1 = \frac{B' \pm \sqrt{B'^2 - 4A'C'}}{2A'} \tag{41}$$

3 | EFFICIENT SOLUTION PROCEDURE

3.1 | Additional equations

By incorporating the trigonometric identity $\sin^2(\alpha_D) + \cos^2(\alpha_D) = 1$ in both the first two equations from the matricial compatibility equations (Equation (6)), the angle α_D (Figure 1) can be written as function of the strains in the L–T and R–D coordinate systems (Equations (42) and (43)).

$$\sin^2(\alpha_D) = \frac{\varepsilon_L - \varepsilon_D}{\varepsilon_R - \varepsilon_D} \tag{42}$$

$$\cos^2(\alpha_D) = \frac{\varepsilon_T - \varepsilon_D}{\varepsilon_R - \varepsilon_D} \tag{43}$$

The angle α_D can be computed from dividing Equation (42) by Equation (43):

$$\alpha_D = \arctan\left(\sqrt{\frac{\varepsilon_L - \varepsilon_D}{\varepsilon_T - \varepsilon_D}}\right) \tag{44}$$

Solving Equation (35) for σ_D gives the following equation:

$$\sigma_D = \frac{-m_{LT}\sigma_1}{\sin(\alpha_D)\cos(\alpha_D)} + \sigma_R \tag{45}$$

Solving Equations (33) and (34) for f_L and f_T, gives Equations (46) and (47), respectively:

$$f_L = \frac{-\sigma_D \cos^2(\alpha_D) - \sigma_R \sin^2(\alpha_D) + m_L \sigma_1 - \rho_{LP} f_{LP}}{\rho_L} \tag{46}$$

$$f_T = \frac{-\sigma_D \sin^2(\alpha_D) - \sigma_R \cos^2(\alpha_D) + m_T \sigma_1 - \rho_{TP} f_{TP}}{\rho_T} \tag{47}$$

3.2 | Nonlinear equation for the initial estimates

The efficient solution procedure requires initial estimates for the strains ε_D, ε_L, and ε_T. Instead of assuming arbitrary values, the initial estimates are computed by using the Mohr compatibility truss model (MCTM), which assumes elastic and linear constitutive laws for the materials[1] (Hooke's law is valid).

Substituting Hooke's laws for concrete ($\sigma_D = E_c \varepsilon_D$) into Equation (45), and solving for ε_D gives:

$$\varepsilon_D = \frac{-m_{LT}\sigma_1}{E_c \sin(\alpha_D)\cos(\alpha_D)} + \frac{\sigma_R}{E_c} \tag{48}$$

Substituting Hooke's laws for longitudinal and transverse nonprestress steel bars ($f_L = E_s \varepsilon_L$ and $f_T = E_s \varepsilon_T$) into Equations (46) and (47), respectively, and solving for the strains ε_L and ε_T, gives the following equations:

$$\varepsilon_L = \frac{(m_L + m_{LT}\cot(\alpha_D))\sigma_1 - \sigma_R - \rho_{LP} f_{LP,i}}{E_S \rho_L} \tag{49}$$

$$\varepsilon_T = \frac{(m_T + m_{LT}\tan(\alpha_D))\sigma_1 - \sigma_R - \rho_{TP} f_{TP,i}}{E_S \rho_T} \tag{50}$$

In the previous equations, f_{LP} (f_{TP}) is substituted by $f_{LP,\,i}$ ($f_{TP,\,i}$) which represents the initial stress in the longitudinal (transverse) reinforcement, in order to account for the initial stress due to prestress to compute the initial estimates.

To calculate the initial estimates, the tensile stress σ_R can be neglected in Equation (48)–(50) because at this stage the strains are very low.

From Equation (44), the nonlinear Equation (51) can be written, in which the strains are computed from Equations (48)–(50) (with $\sigma_R = 0$).

$$F_{\text{MCTM}} = \frac{\varepsilon_L - \varepsilon_D}{\varepsilon_T - \varepsilon_D} - \tan^2(\alpha_D) = 0 \tag{51}$$

Equation (51) is solved to estimate the angle α_D which minimizes the so-called residual function for MCTM

(F_{MCTM}). Once α_D is estimated, the strains are recalculated from Equations (48)–(50) (again with $\sigma_R = 0$) and used as the initial estimates to start the refined efficient RA-STM procedure, as explained below.

3.3 | Nonlinear equations for the refined efficient RA-STM procedure

Adding Equations (33) and (43), substituting Equations (42) and (43), and arranging terms, gives the first residual function for the refined efficient RA-STM procedure, $F^{(1)}_{\text{RA-STM}}$. Similarly, adding Equations (34) and (42), substituting Equations (42) and (43) and arranging terms, gives the second residual function, $F^{(2)}_{\text{RA-STM}}$.

$$\begin{bmatrix} F^{(1)}_{\text{RA-STM}} \\ F^{(2)}_{\text{RA-STM}} \end{bmatrix} = \begin{bmatrix} \sigma_D \dfrac{\varepsilon_T - \varepsilon_D}{\varepsilon_R - \varepsilon_D} + \sigma_R \dfrac{\varepsilon_L - \varepsilon_D}{\varepsilon_R - \varepsilon_D} - m_L \sigma_1 + \rho_L f_L + \rho_{LP} f_{LP} \\ \sigma_D \dfrac{\varepsilon_L - \varepsilon_D}{\varepsilon_R - \varepsilon_D} + \sigma_R \dfrac{\varepsilon_T - \varepsilon_D}{\varepsilon_R - \varepsilon_D} - m_T \sigma_1 + \rho_T f_T + \rho_{TP} f_{TP} \end{bmatrix} = \begin{bmatrix} 0 \\ 0 \end{bmatrix} \tag{52}$$

The matricial Equation (52) is equivalent to a system of two nonlinear equations which are solved to compute the strains ε_L and ε_T as the values which minimize both the residual functions $F^{(1)}_{\text{RA-STM}}$ and $F^{(2)}_{\text{RA-STM}}$.

3.4 | Algorithm

Figure 4 presents the flowchart for the algorithm used to implement the refined efficient RA-STM procedure for PC membrane elements. Some initial data must be given to start the calculation procedure. These data are related with material properties and loading condition. In addition, the chosen path's increment $\Delta\varepsilon_D$ for the strain ε_D must also be given. Next, the initial stress and deformation state for the first imposed valued ε_D^0 are estimated from the MCTM, which requires solving Equation (51) for α_D. From this first calculation, the initial estimates ε_D^1, ε_L^0, and ε_T^0 are obtained to compute the first solution point with index $k = 1$. After this, all the remaining solution points are computed from the refined efficient RA-STM procedure. For this, the strain ε_D is incremented by $\Delta\varepsilon_D$ for each step ($\varepsilon_D^{k+1} = \varepsilon_D^k + \Delta\varepsilon_D$), and the new stress and deformation state is successively estimated by solving Equation (52) for ε_L and ε_T. For each step, the initial point is defined as the solution point from the previous one. The calculation procedure holds until the conventional ultimate (failure) value specified for concrete in compression (ε_{cu}) is reached ($\varepsilon_D^{k+1} \geq \varepsilon_{cu}$). Eurocode 2[25] was used to define ε_{cu}.

In this study, the algorithm for the refined efficient RA-STM procedure was implemented in MATLAB[26] and nonlinear Equations (51) and (52) were solved with the least squares method by using the function *lsqnonlin*.

4 | VALIDATION WITH EXPERIMENTAL RESULTS

To validate the refined efficient RA-STM procedure for PC membrane elements presented in the previous sections, the theoretical predictions are compared with the same experimental results used by Bernardo et al.[21] to validate the previous version of the model only for the ultimate stage, namely for the shear strength. The experimental results came from only two studies found in the literature, where PC panels were tested under in-plane stresses (with proportional loading) until failure.

Laskar et al.[16] tested some PC panels at the Universal Panel Tester in the University of Houston. Among the reported tests, five PC panels (TA series) were tested under proportional loading and symmetrical biaxial stresses in the 1–2 coordinate system ($\sigma_2 = -\sigma_1$), with steel bars oriented at 45° (Figure 5). As a consequence, the referred PC panels were tested under pure shear in the L-T coordinate system ($\sigma_L = \sigma_T = 0$, see Figure 1). All PC panels have sizes $139.8 \times 139.8 \times 17.8$ cm^3 and prestress was only applied in the longitudinal direction of the L-T coordinate system (no longitudinal nonprestress reinforcement exists). The main variable study was the reinforcement ratio in each direction. It should be referred that Laskar et al.[16] also reported the experimental results of five additional PC panels (TE-series) tested under sequential loading. The aim of these tests was to study the constitutive laws for the materials. These additional experimental results were not used in this study because of their different loading condition.

Marti and Meyboom[11] tested two PC panels (PP-series) on the shell element tester at the University of

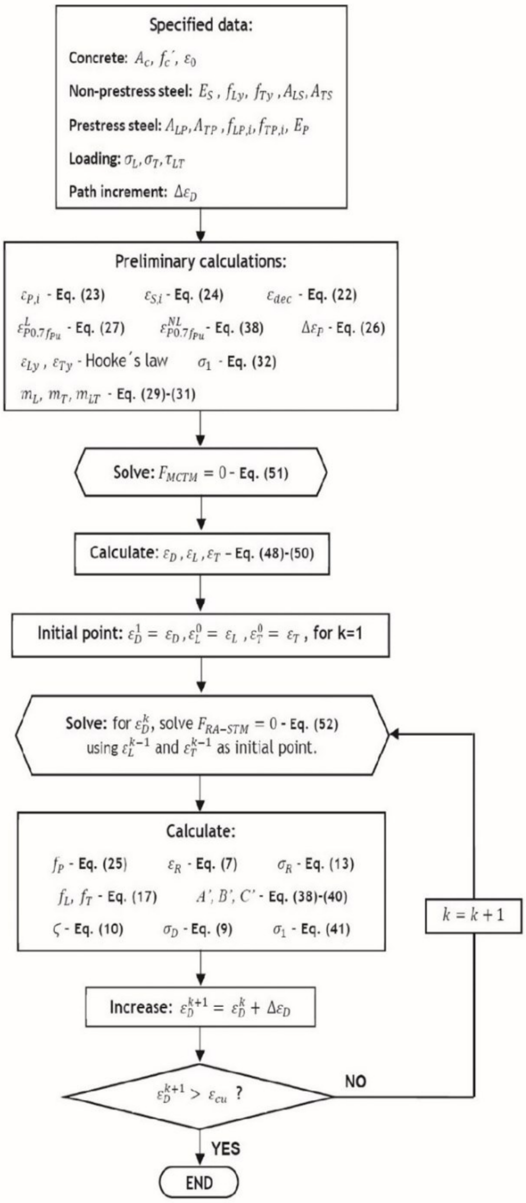

FIGURE 4 Flowchart

Toronto, with similar loading condition and prestress direction as previously described for the PC panels (TA-series) from Laskar et al.[16] Both panels have sizes $162.6 \times 162.6 \times 28.7$ cm^3 and the variable study was the amount of prestressing. Although Laskar et al.[16] reported some deficiencies in the study from Marti and Meyboom,[11] the experimental results of these additional two PC panels were also considered for this study.

Table 1 summarizes the properties of the seven tested PC panels used to validate the refined efficient RA-STM procedure. Most of the presented parameters were already defined in the previous sections. In addition, parameter $f_{cP,\ i}$ is the initial concrete compressive stress due to prestress in the longitudinal direction.

The theoretical behavior of each of the seven PC panels from Table 1 was computed using the refined efficient RA-STM procedure presented in the previous sections. Such results are compared with the experimental ones reported by Laskar et al. in 2007[16] and Marti and Meyboom.[11]

Figures 6 and 7 present the experimental and theoretical shear stress (τ_{LT})–shear strain (γ_{LT}) curves for the PC panels from TA-series and PP-series, respectively. Two theoretical curves are presented for the five PC panels from TA-series, one computed from the refined efficient RA-STM procedure proposed in this study (eff. RA-STM) and another one drawn from the theoretical curve presented by Laskar et al.[16] Such theoretical curve was computed by the referred authors from the SMM-PC and is also presented here for comparison. For the two PC panels from PP-series, Marti and Meyboom[11] only presented some experimental $\tau_{LT} - \gamma_{LT}$ points with error bars.

Figures 6 and 7 show that, in general, the global behavior of the tested panels is well captured by the refined efficient RA-STM procedure, including the transition from the uncracked to the cracked stage (unlike the previously proposed efficient RA-STM procedure[21]), and the theoretical curves are in good agreement with the experimental ones. Some numerical difficulties reported with the previous model for some of the panels[21] were also solved with the refined efficient RA-STM procedure.

Figure 6 also shows that, for the five PC panels from TA-series, the predictions from the refined efficient RA-STM procedure are generally also in good agreement with the same ones from the SMM-PC, which is a more complex analytical model as referred in the introduction section. However, the descending branch of the theoretical $\tau_{LT} - \gamma_{LT}$ curves from SMM-PC seems to agree better with the experimental curves. This is because the SMM-PC incorporates the so-called Hsu/Zhu ratios to account for the Poisson's effect. As explained by Zhu and Hsu,[15] this allows the model to predict better the postpeak behavior of the membrane elements under shear.

In order to validate better the refined efficient RA-STM procedure in a quantitative way, Table 2 presents, for each reference PC panel, the experimental and theoretical values for some key values and properties of the $\tau_{LT} - \gamma_{LT}$ curves. These are the following ones: cracking shear stresses $\tau_{cr,exp}$ and $\tau_{cr,th}^{\text{eff.RA-STM}}$, shear stiffnesses in the cracked stage $k_{S,\ exp}$ and $k_{S,th}^{\text{eff.RA-STM}}$, shear strengths stresses (ultimate values) $\tau_{u,exp}$ and $\tau_{u,th}^{\text{eff.RA-STM}}$, and the corresponding shear strains $\gamma_{u,\ exp}$ and $\gamma_{u,th}^{\text{eff.RA-STM}}$. The ratios of the experimental to the theoretical values are also presented ($\tau_{cr,exp}/\tau_{cr,th}^{\text{eff.RA-STM}}$, $k_{S,exp}/k_{S,th}^{\text{eff.RA-STM}}$, $\tau_{u,exp}/\tau_{u,th}^{\text{eff.RA-STM}}$ and $\gamma_{u,exp}/\gamma_{u,th}^{\text{eff.RA-STM}}$). Although only seven panels were studied, Table 2 also presents the

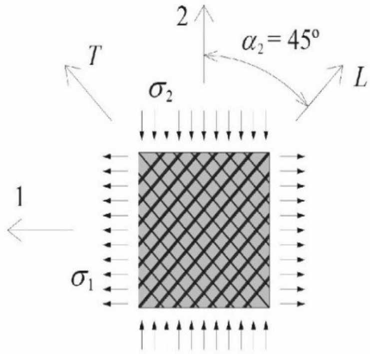

FIGURE 5 Tested panels: loading condition and reinforcement direction

values for the mean ($\bar{x}$), *SD* (s), and coefficient of variation (cv) corresponding to the presented ratios. The shear strain corresponding to the cracking shear stress was not included as a key value because it was not possible to obtain accurate values from the experimental $\tau_{LT} - \gamma_{LT}$ curves drawn in the consulted studies. This is because at this early stage, the shear strains are very small. The shear stiffness in the cracked stage was estimated as the slope of a straight line obtained from a linear regression of the points of the $\tau_{LT} - \gamma_{LT}$ curves which lies on the approximately linear part of the ascending branch after the cracking point. For the PC panels from PP-series, the average values of each error bar were considered as the representative values.

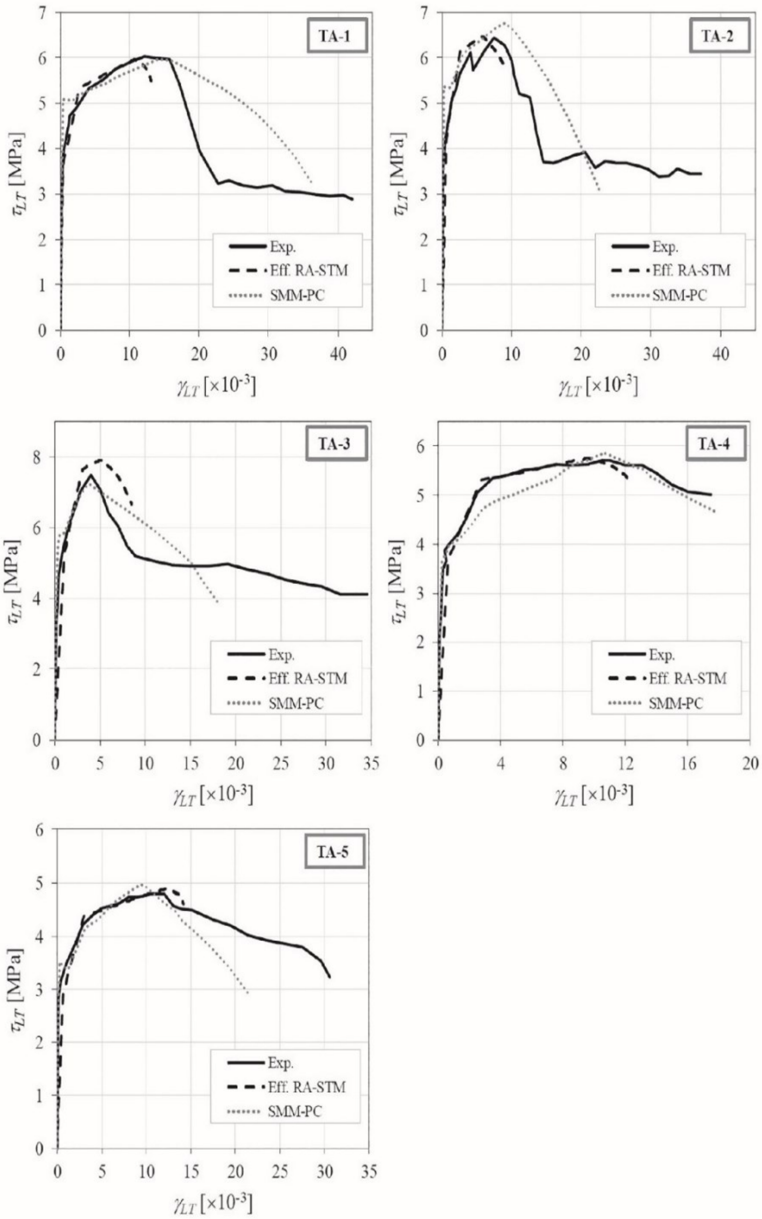

FIGURE 6 $\tau_{LT} - \gamma_{LT}$ curves for panels from TA-series

FIGURE 7 $\tau_{LT} - \gamma_{LT}$ curves for panels from PP-series

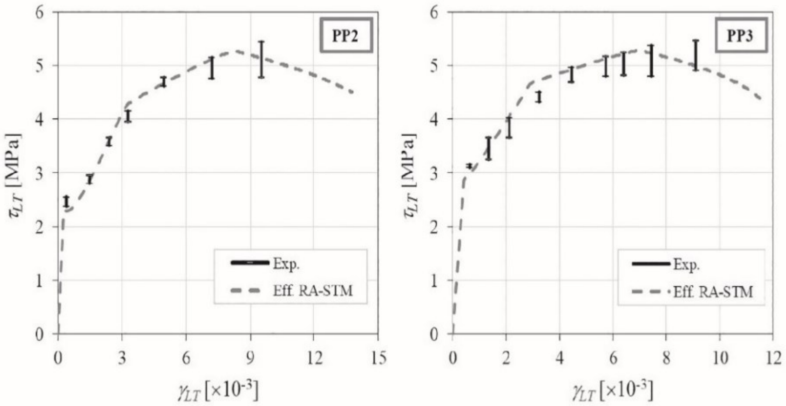

TABLE 2 Comparative analysis

Panel	$\tau_{cr,\,exp}$ MPa	$\tau_{cr,th}^{\text{eff.RA-STM}}$ MPa	$\frac{\tau_{cr,exp}}{\tau_{cr,th}^{\text{eff RA-STM}}}$	$k_{S,\,exp}$ MPa	$k_{S,th}^{\text{eff.RA-STM}}$ MPa	$\frac{k_{S,exp}}{k_{S,th}^{\text{eff RA-STM}}}$	$\tau_{u,\,exp}$ MPa	$\tau_{u,th}^{\text{eff.RA-STM}}$ MPa	$\frac{\tau_{u,exp}}{\tau_{u,th}^{\text{eff RA-STM}}}$	$\gamma_{u,\,exp}$ ×10^{-3}	$\gamma_{u,th}^{\text{eff.RA-STM}}$ ×10^{-3}	$\frac{\gamma_{u,exp}}{\gamma_{u,th}^{\text{eff RA-STM}}}$
TA-1[16]	3.82	3.75	1.02	0.091	0.080	1.13	6.03	5.96	1.01	12.20	10.72	1.14
TA-2[16]	4.22	4.31	0.98	0.097	0.091	1.06	6.44	6.46	1.00	7.50	5.89	1.27
TA-3[16]	4.71	5.08	0.93	0.964	1.113	0.87	7.49	7.91	0.95	4.00	5.07	0.79
TA-4[16]	3.87	3.69	1.05	0.659	0.763	0.86	5.71	5.75	0.99	11.00	9.60	1.15
TA-5[16]	2.83	2.89	0.98	0.453	0.632	0.72	4.79	4.88	0.98	10.50	12.29	0.85
PP2[11]	2.46	2.31	1.06	0.745	0.798	0.93	5.11	5.26	0.97	9.55	8.31	1.15
PP3[11]	3.12	2.86	1.09	0.500	0.732	0.68	5.19	5.28	0.98	9.11	6.99	1.30
		$\bar{x}=$	1.015		$\bar{x}=$	0.892		$\bar{x}=$	0.983		$\bar{x}=$	1.093
		$s=$	0.057		$s=$	0.163		$s=$	0.021		$s=$	0.198
		$cv=$	5.64%		$cv=$	18.27%		$cv=$	2.09%		$cv=$	18.10%

From Table 2, it can be stated that the refined efficient RA-STM procedure predicts very well the cracking shear stress τ_{cr} ($\bar{x} = 1.015$) with a very low degree of dispersion (cv = 5.64%). For the shear stiffness in the cracked stage k_S, the proposed model predicts well its value ($\bar{x} = 0.892$), although this last one seems to be slightly overestimated, and with an acceptable degree of dispersion (cv = 18.27%).

From Table 2, it can also be stated that the refined efficient RA-STM procedure predicts very well the ultimate shear stress τ_u ($\bar{x} = 0.983$) with a very low degree of dispersion (cv = 2.09%). This result is slightly better when compared with the results from Bernardo et al.,[21] which used the previous version of the efficient RA-STM procedure for the same reference PC panels, and for which the following statistical values were obtained: $\bar{x} = 1.11$ and cv = 8.86%. This shows that the refinement of the model in order to include the concrete tensile strength also affected slightly and positively the prediction of the ultimate shear strength.

For the ultimate shear strain γ_u, Table 2 shows that the refined efficient RA-STM procedure also predict well the values ($\bar{x} = 1.093$), although it seems to be slightly underestimated, and with an acceptable degree of dispersion (cv = 18.10%).

Finally, Figure 8 presents some examples of other behavioral curves for selected panels, both theoretically and experimentally (if exists), namely: the $\sigma_D - \varepsilon_D$ and $\sigma_R - \varepsilon_R$ curves for panel TA-5, and the $\tau_{LT} - \varepsilon_R$ and $\tau_{LT} - \varepsilon_D$ curves for panel TA-2. In general, the theoretical curves show expected shapes and agree well when compared with the experimental ones.

The foregoing shows that the refined efficient RA-STM procedure constitutes a reliable model to predict well the full behavior of PC membrane elements.

5 | CONCLUSIONS

In this article, a previous version of the efficient RA-STM procedure to model the behavior of PC membrane elements under in-plane stresses was refined in order to include the concrete tensile strength and also an appropriate smeared nonlinear $\sigma - \varepsilon$ relationships for concrete

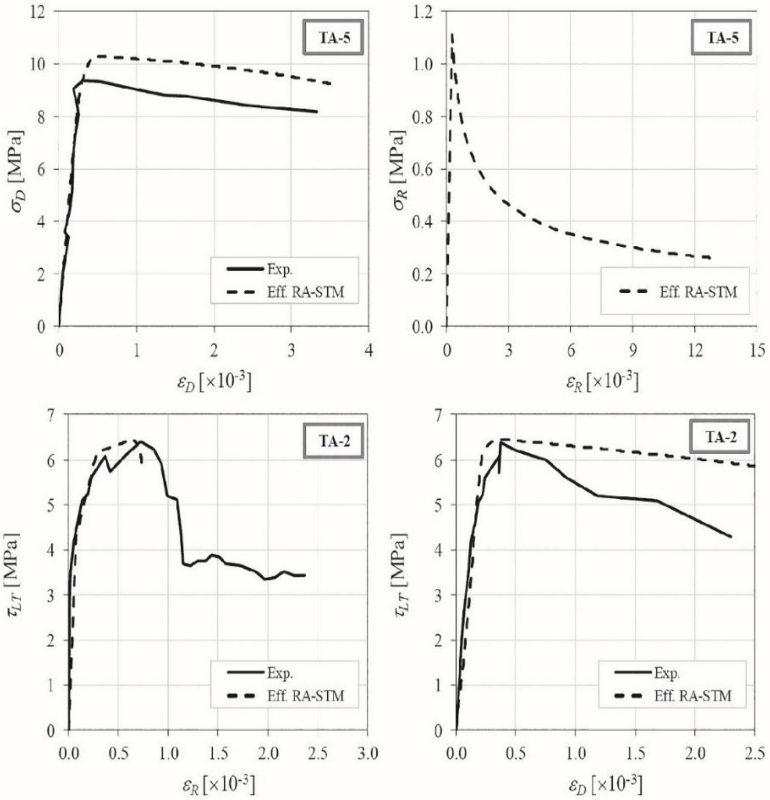

FIGURE 8 Other behavioral curves for selected panels

in tension. The aim was to refine the model in order to predict the full behavior of PC membranes under in-plane stresses, including the transition between the uncracked and the cracked stages. From the results obtained through this study, the following conclusions can be drawn:

1. When compared with experimental results, the refined efficient RA-STM procedure has proven to provide good predictions for the full response of PC membrane elements under in-plane stresses, including the behavior for low loading stages.
2. In particular, the refined efficient RA-STM procedure provided good predictions for the cracking shear stress, the shear stiffness in the cracked stage, and also the shear strength stress and corresponding shear strain for the studied PC membrane elements.
3. The efficient solution procedure shown to be accurate and provided high numerical efficiency and stability. The numerical results were obtained in few seconds (average processing time approximately equal to 8–12 s with Intel(R) Core(TM) i7-4700MQ CPU @ 2.40 GHz);
4. The refined efficient RA-STM procedure shown to be a simple a reliable truss-based model for PC membrane elements under in-plane stresses, and constitutes a good and alternative analytical model to more complicated ones.

It should be noted that the STM constitutes a simplified model to describe the behavior of concrete structural elements and structures. It cannot model realistically the localized failure. This one is a direct consequence of a postpeak softening, which is the major manifestation of failure. Such behavior cannot be objectively modeled by $\sigma - \varepsilon$ relationships alone. Instead, a more detailed analysis can be obtained with the help of models based on continuum mechanic, for example, models based on the fracture mechanics. Nevertheless, by incorporating smeared $\sigma - \varepsilon$ relationships for the materials, the refined efficient RA-STM procedure used in this study was able to model well the average full response of the studied PC membrane elements under in-plane stresses.

Finally, it should also be noted that the refined efficient RA-STM procedure was validated with the experimental results related with only seven PC panels. For this reason, additional experimental results with PC panels, including panels under more general in-plane stresses in the L–T coordinate system, are still needed.

NOTATION

A_c	Area of concrete cross section
A_{LP}	Area of longitudinal prestress reinforcement
A_{LS}	Area of longitudinal nonprestress reinforcement
A_P	Area of prestress reinforcement

A_S	Area of nonprestress reinforcement
A_{TP}	Area of transverse prestress reinforcement
A_{TS}	Area of transverse nonprestress reinforcement
E_c	Young's modulus for concrete
E_P	Young's modulus for prestress steel
E_S	Young's modulus for nonprestress steel
f'_c	Uniaxial compressive strength of concrete
$f_{cP,i}$	Initial compressive stress in concrete due to prestress
f_{cr}	Tensile strength of concrete
f_L	Tensile stress in the longitudinal nonprestress reinforcement
f_{LP}	Tensile stress in the longitudinal prestress reinforcement
$f_{LP,i}$	Initial tensile stress in the longitudinal prestress reinforcement due to prestress
$f_{LP0.1\%}$	Proportional conventional limit stress to 0.1% for the longitudinal prestress steel
f_{Ly}	Yielding stress of the longitudinal nonprestress reinforcement
f_P	Tensile stress in the prestress reinforcement
$f_{P,\,i}$	Initial tensile stress in the prestress reinforcement due to prestress
f_{Pu}	Tensile strength of the prestress steel
f_S	Average tensile stress in the nonprestress steel bars
f_{Sy}	Uniaxial yielding stress of the nonprestress steel bars
f_T	Tensile stress in the transverse nonprestress reinforcement
f_{TP}	Tensile stress in the transverse prestress reinforcement
$f_{TP,\,i}$	Initial tensile stress in the transverse prestress reinforcement due to prestress
$f_{TP0.1\%}$	Proportional conventional limit stress to 0.1% for the transverse prestress steel
f_{Ty}	Yielding stress of the transverse nonprestress reinforcement
f'_y	Yielding stress of the embedded nonprestress bars
k_S	Shear stiffness in the cracked stage
m_L	Longitudinal proportionality coefficient
m_{LT}	Shear proportionality coefficient
m_T	Transverse proportionality coefficient
α_1	Angle of the principal tensile stresses in the PC membrane element
α_2	Angle of the principal compressive stresses in the PC membrane element
α_D	Angle of the principal compressive stress in the concrete membrane element
α_R	Angle of the principal tensile stresses in the concrete membrane element
ε_0	Strain corresponding to the concrete compressive peak stress
ε_{cr}	Tensile strain corresponding to the tensile strength of concrete
ε_{cu}	Ultimate strain for concrete in compression
ε_D	Principal average compressive strain
ε_{dec}	Decompression strain
ε_P	Strain in the prestress steel bars
$\varepsilon_{P0.7f_{Pu}}$	strain in the prestress steel corresponding to $0.7f_{Pu}$.
$\varepsilon_{P,\,i}$	Initial tensile strain in the prestress steel bars due to prestress
ε_L	Longitudinal average strain
ε_{Ly}	Yielding strain of the longitudinal nonprestress steel bars
ε_R	Principal average tensile strain
ε_S	Average strain in the nonprestress steel bars
$\varepsilon_{S,\,i}$	Initial compressive strain in the nonprestress steel bars due to prestress
ε_T	Transverse average strain
ε_{Ty}	Yielding strain of the transverse nonprestress steel bars
γ_{LT}	Average shear strain in the PC membrane element
γ_u	Shear strain corresponding to the shear strength
ζ	Softening coefficient
ρ_L	Longitudinal nonprestress reinforcement ratio
ρ_{LP}	Longitudinal prestress reinforcement ratio
ρ_T	Transverse nonprestress reinforcement ratio
ρ_{TP}	Transverse prestress reinforcement ratio
σ_1	Principal tensile stress in the PC membrane element
σ_2	Principal compressive stress in the PC membrane element
σ_D	Principal compressive stress in the concrete membrane element
σ_L	Longitudinal normal stress in the PC membrane element
σ_L^c	Longitudinal normal stress in the concrete membrane element
σ_R	Principal tensile strain in the concrete membrane element
σ_T	Transverse normal stress in the PC membrane element
σ_T^c	Transverse normal stress in the concrete membrane element
τ_{cr}	Cracking shear stress
τ_{LT}	Shear stress in the PC membrane element
τ_{LT}^c	Shear stress in the concrete membrane element
τ_u	Shear strength stress

ORCID

Luís F. A. Bernardo https://orcid.org/0000-0003-0484-350X

REFERENCES

1. Hsu TTC, Mo YL. Unified theory of concrete structures. Chichester, UK: John Wiley & Sons Ltd., 2010;p. 500.
2. Robinson JR, Demorieux JM. Essais de traction-compression sur modèles d'âme de poutre en béton armé. IRABA Report, Institut de Recherches Appliquées du Béton Armé, Part 1. 1968;1:44 (in French).
3. Hsu TTC. Softened truss model theory for shear and torsion. Struct J Am Concr Inst. 1988;85(6):624–635.
4. Vecchio FJ, Collins MP. The response of reinforced concrete to in-plane shear and normal stresses. Toronto: University of Toronto, 1982;p. 332.
5. Vecchio FJ, Collins MP. The modified compression-field theory for reinforced concrete elements subjected to shear. ACI J. 1986;83(2):219–231.
6. Hsu TTC. Unified theory of reinforced concrete. Boca Raton, FL: CRC Press Inc., 1993;p. 313.
7. Pang XB, Hsu TTC. Behavior of reinforced concrete membrane elements in shear. Struct J Am Concr Inst. 1995;92(6):665–679.
8. Belarbi A, Hsu TTC. Constitutive Laws of softened concrete in biaxial tension-compression. Struct J Am Concr Inst. 1995;92(5):562–573.
9. Zhang LX, Hsu TTC. Behavior and analysis of 100 MPa concrete membrane elements. J Struct Eng. 1998;124(1):24–34.
10. Belarbi A, Hsu TTC. Constitutive Laws of concrete in tension and reinforcing bars stiffened by concrete. Struct J Am Concr Inst. 1994;91(4):465–474.
11. Marti P, Meyboom J. Response of Prestressed concrete elements to in-plane shear forces. ACI Struct J. 1992;89(5):503–514.
12. Pang XB, Hsu TTC (1992) Constitutive laws of reinforced concrete in shear. Research Report UHCEE 92-1, Department of Civil and Environmental Engineering, University of Houston, 187.
13. Pang XB, Hsu TTC. Fixed-angle softened truss model of reinforced concrete. Struct J Am Concr Inst. 1996;93(2):197–207.
14. Hsu TTC, Zhang LX. Nonlinear analysis of membrane elements by fixed-angle softened-truss model. Struct J Am Concr Inst. 1997;94(5):483–492.
15. Hsu TTC, Zhu RRH. Softened membrane model for reinforced concrete elements in shear. Struct J Am Concr Inst. 2002;99(4):460–469.
16. Laskar A, Wang J, Hsu TTC, Mo YL (2007) Rational shear provisions for AASHTO LRFD specifications. Technical Report, University of Houston, 192.
17. Wong HF, Kuang JS. Predicting shear strength of RC interior beam-column joints by modified rotating-angle softened-truss model. Comput Struct. 2014;133:12–17.
18. Ji T. A new algorithm for the rotating-angle, softened-truss model of reinforced concrete elements. Mag Concr Res. 2005;57(6):353–360.
19. Silva JRB, Horowitz B (2015) Efficient procedure to estimate the load-deformation behavior of reinforced concrete panels under membrane forces. CILAMCE 2015 – XXXVI Iberian Latin American Congress on Computational Methods in Engineering, Rio de Janeiro-RJ, Brasil (in Portuguese).
20. Bernardo LFA, Cerquido BMD, Silva JRB, Horowitz B. Efficient refined rotating-angle softened truss model procedure to analyze reinforced concrete membrane elements. Struct Concr. 2018;19(6):1971–1982.
21. Bernardo LFA, Lyrio ARB, Silva JRB, Horowitz B. Refined softened truss model with efficient solution procedure for prestressed concrete membranes. J Struct Eng. 2018;144(6):04018045.
22. Zhu RRH, Hsu TTC, Lee JY. Rational shear Modulus for smeared-crack analysis of reinforced concrete. Struct J Am Concr Inst. 2001;98(4):443–450.
23. Hsu TTC, Mo YL. Softening of concrete in torsional members—prestressed concrete. Struct J Am Concr Inst. 1985;82(5):603–615.
24. Hsu TTC. Nonlinear analysis of membrane elements. Struct J Am Concr Inst. 1991;88(5):552–561.
25. NP EN 1992-1-1, Eurocode 2: Design of Concrete Structures - Part 1: General Rules and Rules for Buildings, March 2010.
26. MathWorks (2018) MATLAB_R2018a.

AUTHOR BIOGRAPHIES

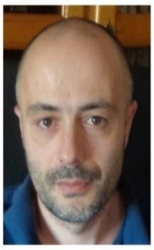

Luís F. A. Bernardo
C-MADE - Centre of Materials and Building Technologies
University of Beira Interior
Covilhã, Portugal
lfb@ubi.pt

Benedito M. V. C. Filho
Department of Civil Engineering and Architecture
University of Beira Interior
Covilhã, Portugal
madianvfilho@gmail.com

Bernardo Horowitz
Department of Civil Engineering
Federal University of Pernambuco
Recife, Brazil
horowitz@ufpe.br

How to cite this article: Bernardo LFA, Filho BMVC, Horowitz B. Predicting the behavior of prestressed concrete membrane elements by refined rotating-angle softened-truss model with efficient solution procedure. *Structural Concrete*. 2020;21:934–948. https://doi.org/10.1002/suco.201900481

Capítulo 6

Prevendo o comportamento de elementos de membrana de concreto estrutural reforçados com FRP com procedimento do modelo de treliça com amolecimento e ângulo variável eficiente.

Este capítulo consiste no artigo:

Predicting the behavior of FRP- strengthened RC membrane elements with efficient rotating-angle softened truss model procedure.

BERNARDO, L. F. A.; FILHO B. M. V. C.; HOROWITZ, B. 2021 “Predicting the behavior of FRP-strengthened RC membrane elements with efficient rotating-angle softened truss model procedure”, Materials and Structures, RILEM, ISSN: 1359-5997, Volume 54, Article number: 42.

DOI: https://doi.org/10.1617/s11527-021-01631-y

Materials and Structures (2021)54:42
https://doi.org/10.1617/s11527-021-01631-y

ORIGINAL ARTICLE

Predicting the behavior of FRP-strengthened RC membrane elements with efficient rotating-angle softened truss model procedure

Luís Filipe Almeida Bernardo · Benedito Madian Viana de Carvalho Filho · Bernardo Horowitz

Received: 18 April 2020 / Accepted: 13 January 2021

Abstract This article presents an analytical model, based on a refinement of the rotating-angle softened truss model (RA-STM) with efficient solution procedure, to predict the full response of reinforced concrete (RC) membrane elements strengthened with fiber reinforced polymers (FRP). To extend the RA-STM, equations from equilibrium conditions and smeared constitutive relationships for the materials are modified in order to account for the tensile FRP reinforcement and its interactions with the other material components. In addition, an efficient algorithm is proposed for the calculation procedure to avoid using the classical trial and error technique to compute the solution points. This new algorithm provides higher numerical efficiency and stability. The reliability of the efficient RA-STM FRP solution procedure is checked against some experimental data related with FRP-strengthened RC panels tested under in-plane shear and found in the literature, and also with the predictions from the softened membrane model (SMM-FRP) for comparison. In general, reasonably good agreement is observed between the efficient RA-STM FRP procedure and the SMM-FRP, and also with the experimental response of the reference test panels.

Keywords Rotating-angle softened truss model · Efficient solution procedure · FRP-strengthened RC membranes · Shear behavior

List of symbols

A_c	Area of concrete cross section
A_{Tf}	Area of transverse FRP reinforcement
A_L	Area of longitudinal steel reinforcement
A_T	Area of transverse steel reinforcement
E_c	Young's modulus of concrete
E_f	Tensile Young's modulus of FRP reinforcement
E_S	Young's modulus of steel reinforcement
f'_c	Uniaxial compressive strength of concrete
f_{cr}	Tensile strength of concrete
f_{Lf}	Tensile stress in the longitudinal FRP reinforcement
f_{Sf}	Tensile stress in the FRP reinforcement
f_{Tf}	Tensile stress in the transverse FRP reinforcement
f_{fu}	Ultimate tensile strength of the FRP reinforcement

L. F. A. Bernardo (✉) · B. M. V. de Carvalho Filho
Department of Civil Engineering and Architecture, C-MADE—Centre of Materials and Building Technologies, University of Beira Interior, Edifício II das Engenharias, Calçada Fonte do Lameiro, 6200-001 Covilhã, Portugal
e-mail: lfb@ubi.pt

B. M. V. de Carvalho Filho
e-mail: madianvfilho@gmail.com

B. Horowitz
Department of Civil Engineering, Federal University, Pernambuco, Brazil
e-mail: horowitz@ufpe.br

f_L	Tensile stress in the longitudinal steel reinforcement
f_{Ly}	Yielding stress of the longitudinal steel reinforcement
f_S	Tensile stress of steel reinforcement
f_{Sy}	Uniaxial yielding stress of steel reinforcement
f_T	Tensile stress in the transverse steel reinforcement
f_{Ty}	Yielding stress of the transverse steel reinforcement
f_y'	Apparent yielding stress of the embedded steel rebars
$K_{f/s}$	Factor for FRP/steel stiffness ratio
K_w	Factor for FRP wrapping scheme
k	Index for the step of the calculation procedure
k_S	Shear stiffness in the cracked stage
m_L	Longitudinal proportionality coefficient
m_{LT}	Shear proportionality coefficient
m_T	Transverse proportionality coefficient
α_2	Angle of the principal compressive stresses in the FRP-strengthened RC membrane element
α_D	Angle between the L–T and R–D coordinate systems
$\Delta\varepsilon_D$	Path increment for ε_D
ε_0	Strain corresponding to f_c'
ε_{cr}	Tensile strain corresponding to the tensile strength of concrete
ε_{cu}	Ultimate strain for concrete in compression
ε_D	Principal compressive strain
ε_{Lf}	Strain in the longitudinal FRP reinforcement
ε_{Sf}	Strain in the FRP reinforcement
ε_{su}	Ultimate strain for steel reinforcement
ε_{Tf}	Strain in the transverse FRP reinforcement
ε_{fu}	Ultimate strain for FRP reinforcement
ε_L	Longitudinal strain
ε_{Ly}	Yielding strain of the longitudinal steel reinforcement
ε_R	Principal tensile strain
ε_S	Strain in the steel reinforcement
ε_T	Transverse strain
ε_{Ty}	Yielding strain of the transverse steel reinforcement
ε_y'	Strain corresponding to f_y'
γ_{LT}	Shear strain
γ_u	Shear strain corresponding to τ_u
ζ	Softening coefficient
ζ_{FRP}	Softening coefficient accounting for the FRP reinforcement
ρ_f	FRP reinforcement ratio in the principal direction of tensile stresses
ρ_L	Longitudinal steel reinforcement ratio
ρ_{Lf}	Longitudinal FRP reinforcement ratio
ρ_S	Steel reinforcement ratio
ρ_{Se}	Steel reinforcement ratio accounting for the FRP reinforcement
ρ_T	Transverse steel reinforcement ratio
ρ_{Tf}	Transverse FRP reinforcement ratio
σ_1	Principal tensile stress in the FRP-strengthened RC membrane element
σ_2	Principal compressive stress in the FRP-strengthened RC membrane element
σ_D	Principal compressive stress in the concrete membrane element
σ_L	Longitudinal normal stress in the FRP-strengthened RC membrane element
σ_L^c	Longitudinal normal stress in the concrete membrane element
σ_R	Principal tensile strain in the concrete membrane element
σ_T	Transverse normal stress in the FRP-strengthened RC membrane element
σ_T^c	Transverse normal stress in the concrete membrane element
τ_{cr}	Cracking shear stress
τ_{LT}	Shear stress in the FRP-strengthened RC membrane element
τ_{LT}^c	Shear stress in the concrete membrane element
τ_u	Shear strength stress (ultimate)

1 Introduction

In the last 3 decades, externally bonded fiber reinforced polymers (FRP) systems have been widely used as a rehabilitation and strengthening technique for existing reinforced concrete (RC) structures. When compared with other strengthening systems, FRP systems show several advantages, such as resistance to corrosion, ease of application, high strength and high stiffness [1, 2].

Well-established analytical models are already available to analyze and design FRP-strengthened beams and columns under flexural and axial-confinement actions [1, 2]. For FRP-strengthened RC members with predominant shear behavior it is recognized that the behavior is far more complex than unstrengthened RC members. This is because of the higher complexity of the failure mechanisms and failures modes that are associated with the behavior of such members [3]. Available analytical models for predicting the behavior of FRP-strengthened RC members under predominant shear still present large scatters when compared with experimental results [4]. Because of this, experimental and analytical studies on the behavior of FRP-strengthened RC members under predominant shear are still reported in the recent literature [4–9].

Among the analytical models used to predict the behavior of structural concrete members, the truss approach has been widely used. Such models allow to easily identify the contribution of each material component constituting the member and also how the stress fields develop and evolve in the cracked stage. In addition, recent truss models evaluate the stresses and strains on the member on average along a sufficient length to include several cracks, instead of evaluating them locally. This is achieved by using smeared relationships for the materials, calibrated experimentally, which account for multiaxial stress states, damage and also the interaction between the material components. Because of this, such truss models provide simpler formulations, even for nonlinear problems, which are easier to implement in a computer with basic programming languages.

Two dimensional (2D) concrete members are widely used in practice. In many applications, such as shear walls and shells, such members are mainly under in-plane stresses and behave as membrane elements. To model their behavior, such members can be viewed as the union of small 2D membranes [10]. In previous studies, such small members have been successfully modeled with reliable softened truss models, which account for the softening effect in the compressive concrete struts due to the biaxial tension–compression stress state.

Based on several experimental data from controlled tests performed with the Universal Panel Tester [11] on representative RC and prestressed concrete (PC) panels at the university of Houston, three analytical models were successively developed and refined. The first one is the so-called Rotating-Angle Softened Truss Model (RA-STM) [12]. This model idealizes the resistance mechanism of membrane elements as a nonlinear plain truss model, where steel bars resist to axial tensile stresses and concrete resists to compressive stresses. The equations are derived following the three Navier's principles of mechanics: equilibrium, compatibility and constitutive laws (stress (σ)–strain (ε) relationships). The RA-STM allows the direction of the principal compressive stresses in the concrete member to rotate. This is because experiments showed that after cracking the direction of principal stresses rotates as a result of the internal stress redistribution and deformation compatibility. From that time, the RA-STM was being refined to incorporate refined and smeared σ–ε relationships for the materials [13–15]. The RA-STM neglects the contribution of concrete in shear because both equilibrium and compatibility equations are written with respect to a rotating reference frame which coincides with the principal directions of internal stresses in the concrete member. To include this contribution, the equations were rewritten with respect to a fixed reference frame which coincides to the principal directions of the external stresses applied to the RC member. A new smeared shear stress (τ)–shear strain (γ) relationship for concrete in shear was calibrated from experimental results and incorporated into the model [16, 17]. The new model was called fixed-angle softened truss model (FA-STM). Latter, the Poisson's effect in the cracking stage was incorporated through the so-called Hsu/Zhu ratios, which where calibrated from experimental results [18]. This allowed the new model, called softened membrane model (SMM), to predict much better the post-peak response stage for both RC and PC membrane elements.

Recently, the SMM was extended to FRP-strengthened RC membrane elements [4, 19]. For this, specific sets of experimental tests were performed with FRP-strengthened members. From the obtained results, the smeared constitutive relationships for the materials and the Hsu/Zhu ratios were corrected to properly account for the interaction between the materials components, including the FRP reinforcement [19–21]. In addition, the equilibrium equations were modified to also incorporate the contribution of the FRP reinforcement. The new model was called SMM-FRP and it was validated against some experimental results with FRP-strengthened RC panels under shear [4, 9].

The formulation and the calculation procedure of the RA-STM is simpler when compared with the other referred models. In addition, the model showed to be sufficiently reliable to predict the full response of RC membrane elements [12, 14]. For these reasons, the RA-STM still continue to be used by other authors as based-model, including for other structural members [22–25]. In addition, in previous studies the RA-STM has also been successfully refined in order to provide better predictions and also increase the numerical efficiency and stability of the calculation procedure for both RC and PC membrane elements [26–28]. The calculation procedure of the original versions of the RA-STM, as well as for the other referred models, is based on a trial and error technique, which may require a large calculation effort and lose numerical efficiency. In addition, such calculation procedure may require a large number of required estimated parameters to start the calculations. To solve these drawbacks, recently the RA-STM was reformulated as a system of nonlinear equations with constraints, which can be solved using an optimization algorithm instead of using the trial and error technique [27, 28]. The new version of the RA-STM, called "efficient RA-STM procedure" showed to be numerically very efficient and stable. The model also showed to predict well the full response of both RC and PC membrane elements.

In this article, the RA-STM is extended to FRP-strengthened RC membrane elements. For this, the smeared constitutive relationships for the materials are modified according to the proposals of previous studies [20, 21], in order to account for the interaction between the FRP reinforcement and the other material components (concrete and steel reinforcement). The equilibrium equations are also modified to include the contribution of the FRP reinforcement. In addition, an efficient calculation procedure is proposed which allows to avoid using the classical trial and error technique to compute the solution points. The new model, called "efficient RA-STM FRP procedure" is checked against some experimental results available in the literature, related with FRP-strengthened panels under shear, and also against the predictions from the SMM-FRP for comparison. In general, reasonably good agreement is observed between the predictions from the efficient RA-STM FRP procedure and the SMM-FRP, and also with the experimental results from FRP-strengthened RC panels under shear.

2 Efficient RA-STM procedure for FRP-strengthened RC membrane elements

In this section, the efficient RA-STM procedure for RC membrane elements is extended for FRP-strengthened RC membrane elements. The modification of the equations and the efficient calculation procedure are presented with some details. More information about the derivation of some fundamental equations from the RA-STM can be found in previous studies [10, 12]. As for the previous versions of the model, in this study it is also assumed that perfect bond exists between steel / FRP reinforcement and concrete, and dowel action in the steel rebars is neglected.

2.1 Equilibrium and compatibility equations

Figure 1 illustrates a FRP-strengthened RC membrane element under in-plane stresses (normal stresses σ_L, σ_T and shear stress τ_{LT}). The longitudinal (L)–transverse (T) coordinate system corresponds to the direction of longitudinal and transverse reinforcement. Both the FRP-strengthened RC membrane element and the in-plane stresses (σ_L, σ_T and τ_{LT}) in Fig. 1 can be viewed as the superposition of the following components: concrete element with in-plane stresses (σ_L^c, σ_T^c and τ_{LT}^c), steel grid element with in-plane normal stresses ($\rho_L f_L$ and $\rho_T f_T$) and FRP strip element with in-plane normal stresses ($\rho_{Lf} f_{Lf}$ and $\rho_{Tf} f_{Tf}$). In Fig. 1, ρ stands for the reinforcement ratio (see footnotes in Table 1) and f stands for the normal stress in both steel and FRP reinforcement. From Fig. 1, three equilibrium equations for stresses can be written in the L–T coordinate system as follows:

$$\begin{bmatrix} \sigma_L \\ \sigma_T \\ \tau_{LT} \end{bmatrix} = \begin{bmatrix} \sigma_L^c \\ \sigma_T^c \\ \tau_{LT}^c \end{bmatrix} + \begin{bmatrix} \rho_L f_L \\ \rho_T f_T \\ 0 \end{bmatrix} + \begin{bmatrix} \rho_{Lf} f_{Lf} \\ \rho_{Tf} f_{Tf} \\ 0 \end{bmatrix} \tag{1}$$

For the concrete element, the in-plane stresses in the L–T coordinate system can be related with the principal stresses (σ_R and σ_D) and the variable angle α_D between the L–T and R–D coordinate systems (see Fig. 2) as follows:

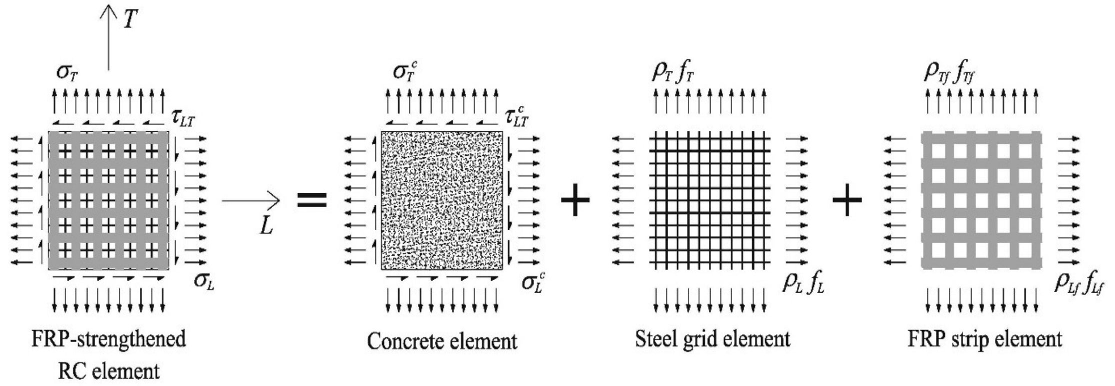

Fig. 1 Stress diagrams for FRP-strengthened RC membrane element

Table 1 Variables of reference panels and material properties [9, 19]

Panel name	f_c' (MPa)	$\varepsilon_{0(1)}$ (%)	$\varepsilon_{cu(1)}$ (%)	$\rho_{L(2)}$ (%)	f_{Ly} (MPa)	$\rho_{T(2)}$ (%)	f_{Ty} (MPa)	E_S (GPa)	$\rho_{Tf(2)}$ (%)	f_{fu} (MPa)	E_f (GPa)
P3-025-FW	51	0.24	0.35	0.76	462	0.43	459	190	0.54	827	82.7
P3-040-FW	50	0.24	0.35	0.76	462	0.43	459	190	0.87	876	72.4
P4-025-FW	45	0.23	0.35	0.76	462	0.76	462	190	0.54	827	82.7
P4-040-FW	52	0.24	0.35	0.76	462	0.76	462	190	0.87	876	72.4
P4-080-FW	54	0.24	0.35	0.76	462	0.76	462	190	1.74	876	72.4
P4-040-SB	44	0.23	0.35	0.76	462	0.76	462	190	0.87	876	72.4
P4-025-FA	52	0.24	0.35	0.76	462	0.76	462	190	0.54	827	82.7
P4-040-FA	52	0.24	0.35	0.76	462	0.76	462	190	0.87	876	72.4

(1) Computed from Eurocode 2 [30]; (2) $\rho_L = A_L/A_c$; $\rho_T = A_T/A_c$; $\rho_{Tf} = A_{Tf}/A_c$

$$\begin{bmatrix} \sigma_L^c \\ \sigma_T^c \\ \tau_{LT}^c \end{bmatrix} = \begin{bmatrix} \cos^2(\alpha_D) & \sin^2(\alpha_D) & 2\sin(\alpha_D)\cos(\alpha_D) \\ \sin^2(\alpha_D) & \cos^2(\alpha_D) & -2\sin(\alpha_D)\cos(\alpha_D) \\ -\sin(\alpha_D)\cos(\alpha_D) & \sin(\alpha_D)\cos(\alpha_D) & \cos^2(\alpha_D) - sin^2(\alpha_D) \end{bmatrix} \begin{bmatrix} \sigma_D \\ \sigma_R \\ 0 \end{bmatrix} \tag{2}$$

As for the stresses, the average strain components in the L–T coordinate system (ε_L, ε_T and γ_{LT}) can be related with the principal strains (ε_R and ε_D) and the variable angle α_D as follows:

$$\begin{bmatrix} \varepsilon_L \\ \varepsilon_T \\ \gamma_{LT} \end{bmatrix} = \begin{bmatrix} \cos^2(\alpha_D) & \sin^2(\alpha_D) & 2\sin(\alpha_D)\cos(\alpha_D) \\ \sin^2(\alpha_D) & \cos^2(\alpha_D) & -2\sin(\alpha_D)\cos(\alpha_D) \\ -2\sin(\alpha_D)\cos(\alpha_D) & 2\sin(\alpha_D)\cos(\alpha_D) & 2\cos^2(\alpha_D) - 2sin^2(\alpha_D) \end{bmatrix} \begin{bmatrix} \varepsilon_D \\ \varepsilon_R \\ 0 \end{bmatrix} \tag{3}$$

In addition, from Mohr's circle for strains, the following invariant equation can be stated:

$$\varepsilon_R = \varepsilon_L + \varepsilon_T - \varepsilon_D \tag{4}$$

Equations (3) and (4) represent the four compatibility equations of the RA-STM.

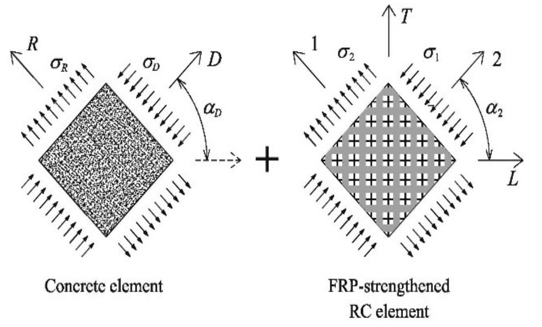

Fig. 2 Principal directions of stresses

2.2 Constitutive laws for the materials

In this study, the same smeared constitutive laws previously used and justified for the efficient RA-STM procedure for RC and PC membrane elements are used [27, 28], namely for concrete in compression, concrete in tension and steel rebars in tension. Based on the proposals from previous studies [20, 21], these smeared constitutive laws are modified for this study to account for the interaction between the tensile FRP reinforcement and the other material components. In addition, a new constitutive law for the tensile FRP reinforcement needs to be incorporated to compute the stresses from the strains.

2.2.1 Constitutive laws for concrete

For concrete in compression, the smeared softened σ–ε relationship firstly proposed by Belarbi and Hsu in 1995 [13] and refined latter by Zhu et al. in 2001 [29] (Eqs. 5a–5b) is used. The softening coefficient ζ from Zhang and Hsu in 1998 [14] and refined by Zhu et al. in 2001 [29] (Eq. 6) was modified with the correction factor $f(\mathrm{FRP})$ proposed by Yang et al. in 2017 [21] (Eq. 9) to account for the influence of the FRP reinforcement. In addition, the ratio η of the transverse to the longitudinal tensile strength of reinforcements (Eqs. 7–8) must also be modified to account for the tensile strength of the FRP reinforcement.

$$\sigma_{\mathrm{D}} = \zeta_{\mathrm{FRP}} f'_{\mathrm{c}}\left[2\left(\frac{\varepsilon_{\mathrm{D}}}{\zeta_{\mathrm{FRP}}\varepsilon_0}\right) - \left(\frac{\varepsilon_{\mathrm{D}}}{\zeta_{\mathrm{FRP}}\varepsilon_0}\right)^2\right] \quad \text{if } \varepsilon_D \leq \zeta_{\mathrm{FRP}}\varepsilon_0 \tag{5a}$$

$$\sigma_{\mathrm{D}} = \zeta_{\mathrm{FRP}} f'_{\mathrm{c}}\left[1 - \left(\frac{(\varepsilon_{\mathrm{D}}/\zeta_{\mathrm{FRP}}\varepsilon_0) - 1}{(4/\zeta_{\mathrm{FRP}}) - 1}\right)^2\right] \quad \text{if } \varepsilon_{\mathrm{D}} > \zeta_{\mathrm{FRP}}\varepsilon_0 \tag{5b}$$

$$\begin{aligned}\zeta_{\mathrm{FRP}} &= \zeta \cdot f(\mathrm{FRP}) \\ &= \left(\frac{5.8}{\sqrt{f'_{\mathrm{c}}\ (\mathrm{MPa})}} \leq 0.9\right) \cdot \frac{1}{\sqrt{1 + \frac{400\varepsilon_{\mathrm{R}}}{\eta'}}} \cdot f(\mathrm{FRP})\end{aligned} \tag{6}$$

$$\eta = \frac{\rho_{\mathrm{T}} f_{\mathrm{Ty}} + \rho_{\mathrm{Tf}} f_{\mathrm{fu}} - \sigma_{\mathrm{T}}}{\rho_{\mathrm{L}} f_{\mathrm{Ly}} + \rho_{\mathrm{Lf}} f_{\mathrm{fu}} - \sigma_{\mathrm{L}}} \tag{7}$$

$$\begin{cases} \eta' = \eta & \text{if } \eta \leq 1 \\ \eta' = \dfrac{1}{\eta} & \text{if } \eta > 1 \end{cases} \tag{8}$$

$$f(\mathrm{FRP}) = 1 + 0.0076\sqrt{\rho_{\mathrm{f}} E_{\mathrm{f}}\ (\mathrm{MPa})} \tag{9}$$

The meaning of the new parameters included in the previous equations are the following ones: f'_{c} is the uniaxial compressive strength of concrete, ε_0 is the strain corresponding to the peak stress (f'_{c}), f_{fu} is the tensile failure stress of FRP reinforcement, ρ_{f} is the FRP reinforcement ratio and E_{f} is the tensile Young's Modulus of FRP reinforcement.

For concrete in tension, the smeared softened σ–ε relationship proposed by Belarbi and Hsu in 1994 [15] (Eqs. 10–13) was also used for this study. This relationship proved to be adequate to be used in truss models for RC members under shear, in order to account for the contribution of the tensile concrete [12, 14, 18]. In the original relationship, the exponent c in Eq. (10b) was equal to 0.4. For this study, this parameter was modified according to Yang et al. in 2015 [20] to account for the influence of the FRP reinforcement and is given by Eq. (14). Factor K_w (Eq. 15) accounts for the effects of wrapping scheme, while factor $K_{\mathrm{f/s}}$ (Eq. 16) accounts for the FRP to steel stiffness ratio.

$$\sigma_{\mathrm{R}} = E_{\mathrm{c}}\varepsilon_{\mathrm{R}} \quad \text{if } \varepsilon_{\mathrm{R}} \leq \varepsilon_{\mathrm{cr}} \tag{10a}$$

$$\sigma_{\mathrm{R}} = f_{\mathrm{cr}}\left(\frac{\varepsilon_{\mathrm{cr}}}{\varepsilon_{\mathrm{R}}}\right)^{\mathrm{c}} \quad \text{if } \varepsilon_{\mathrm{R}} > \varepsilon_{\mathrm{cr}} \tag{10b}$$

$$E_{\mathrm{c}} = 3875\sqrt{f'_{\mathrm{c}}\ (\mathrm{MPa})} \tag{11}$$

$$\varepsilon_{\mathrm{cr}} = 0.00008 \tag{12}$$

$$f_{\mathrm{cr}} = E_{\mathrm{c}}\varepsilon_{\mathrm{cr}} = 0.311\sqrt{f'_{\mathrm{c}}(\mathrm{MPa})} \tag{13}$$

$$c = K_{\mathrm{w}} K_{\mathrm{f/s}} \tag{14}$$

$$K_{\mathrm{w}} = 1\,(\text{fully wrap or U-wrap with anchors}) \tag{15a}$$

$$K_{\mathrm{w}} = 1.6\,(\text{Side bond or U-wrap}) \tag{15b}$$

$$K_{\mathrm{f/s}} = 0.25\left(\frac{\rho_{\mathrm{f}} E_{\mathrm{f}}}{\rho_{\mathrm{S}} E_{\mathrm{S}}}\right) + 0.15 \tag{16}$$

In the previous equations, the new parameters are: E_{c} is the Young's Modulus for concrete, $\varepsilon_{\mathrm{cr}}$ is the tensile strain corresponding to the peak stress f_{cr} (concrete tensile strength) and ρ_{S} is the steel reinforcement ratio.

2.2.2 Constitutive laws for reinforcement

For steel rebars in tension embedded in concrete, the simplified smeared bilinear σ–ε relationship proposed by Pang and Hsu in 1995 [12] (Eqs. 17–20) is used. To account for the influence of the FRP reinforcement on the increase of the apparent yielding stress f'_{y}, which represents the observed reduced yielding stress due to the stiffening effect, Yang et al. in 2015 [20] proposed to substitute the steel reinforcement ratio (ρ_S) in Eq. (20) by a new ratio, the so-called reinforcement ratio ρ_{Se} (Eqs. 21–22).

$$f_S = E_S\varepsilon_S \quad \text{if} \quad \varepsilon_S \le \varepsilon'_y \tag{17a}$$

$$f_S = (0.91 - 2\mathrm{BN})f_{Sy} + (0.02 + 0.25BN)E_S\varepsilon_S \quad \text{if} \quad \varepsilon_S > \varepsilon'_y \tag{17b}$$

$$\varepsilon'_y = \frac{f'_y}{E_S} \tag{18}$$

$$f'_y = (0.93 - 2BN)f_{Sy} \tag{19}$$

$$\mathrm{BN} = \frac{1}{\rho_{Se}}\left(\frac{f_{cr}}{f_{Sy}}\right)^{1.5} \tag{20}$$

$$\rho_{Se} = \rho_S + n_{f/s}\rho_f \tag{21}$$

$$n_{f/s} = \frac{E_f}{E_S} \tag{22}$$

In Eqs. (17)–(22), f_S and ε_S are the average tensile stress and strain of the steel reinforcement, respectively, f_{Sy} is the yielding stress and E_S is the Young's modulus for steel. Subscript "S" is replaced by "L" and "T" for longitudinal and transverse steel reinforcement, respectively.

For FRP reinforcement a smeared linear σ–ε relationship is used, as proposed by Yang et al. in 2015 [20] (Eq. 23).

$$f_{Sf} = E_f\varepsilon_{Sf} \quad \text{if} \quad \varepsilon_{Sf} < \varepsilon_{fu} \tag{23a}$$

$$f_{Sf} = 0 \quad \text{if} \quad \varepsilon_{Sf} \ge \varepsilon_{fu} \tag{23b}$$

In the previous equations, f_{Sf} and ε_{Sf} are the average tensile stress and strain of the FRP reinforcement, respectively, ε_{fu} is the ultimate strain corresponding to f_{fu} from Hooke's law. As for the steel reinforcement, subscript "S" is replaced by "L" and "T" for longitudinal and transverse FRP reinforcement, respectively.

2.3 Equations for proportional loading

For this study it is assumed that the ratios between the applied in-plane stresses are constant throughout the loading history. This loading condition is known as proportional loading. The following three proportionality coefficients are defined: longitudinal (m_L), transverse (m_T) and shear (m_{LT}) proportionality coefficients (Eqs. 24–26). These coefficients relate the applied in-plane stresses in the L–T coordinate system (σ_L, σ_T and τ_{LT}) with the principal tensile stress (σ_1) in the FRP-strengthened RC membrane element in the 1–2 coordinate system (direction of principal applied stresses, see Fig. 2).

$$m_L = \frac{\sigma_L}{\sigma_1} \tag{24}$$

$$m_T = \frac{\sigma_T}{\sigma_1} \tag{25}$$

$$m_{LT} = \frac{\tau_{LT}}{\sigma_1} \tag{26}$$

Substituting the applied in-plane stresses in the L–T coordinate system (σ_L, σ_T and τ_{LT}) from Eqs. (24)–(26) into the equilibrium equations (Eqs. 1–2), gives:

$$m_L\sigma_1 - \rho_L f_L - \rho_{Lf} f_{Lf} = \sigma_D\cos^2(\alpha_D) + \sigma_R\sin^2(\alpha_D) \tag{27}$$

$$m_T\sigma_1 - \rho_T f_T - \rho_{Tf} f_{Tf} = \sigma_D\sin^2(\alpha_D) + \sigma_R\cos^2(\alpha_D) \tag{28}$$

$$m_{LT}\sigma_1 = (-\sigma_D + \sigma_R)\sin(\alpha_D)cos(\alpha_D) \tag{29}$$

Equations (27) and (28) can be combined into one single equation (Eq. 30) as follows: rewrite Eqs. (27) and (28) using the trigonometric identity $\sin^2(\alpha_D) + cos^2(\alpha_D) = 1$ and multiply both equations member by member.

$$\begin{aligned} &(-m_L\sigma_1 + \sigma_R + \rho_L f_L + \rho_{Lf} f_{Lf}) \\ &(-m_T\sigma_1 + \sigma_R + \rho_T f_T + \rho_{Tf} f_{Tf}) \\ &= (\sigma_R - \sigma_D)^2\cos^2(\alpha_D)\sin^2(\alpha_D) \end{aligned} \tag{30}$$

Next, Eqs. (29) and (30) can be combined into one single quadratic equation, Eq. (31), with coefficients given by Eqs. (32)–(34) as follows: square both members of Eq. (29) and equate the left member with the left member of Eq. (30), expand the resulting equation and rearrange terms considering the principal tensile stress σ_1 in the FRP-strengthened RC membrane element as the independent variable.

$$A'\sigma_1^2 - B'\sigma_1 + C' = 0 \tag{31}$$

$$A' = m_L m_T - m_{LT}^2 \tag{32}$$

$$\begin{aligned} B' &= m_L(\sigma_R + \rho_T f_T + \rho_{Tf} f_{Tf}) \\ &\quad + m_T(\sigma_R + \rho_L f_L + \rho_{Lf} f_{Lf}) \end{aligned} \tag{33}$$

$$C' = (\sigma_R + \rho_L f_L + \rho_{Lf} f_{Lf})(\sigma_R + \rho_T f_T + \rho_{Tf} f_{Tf}) \tag{34}$$

The solution equation for Eq. (31) is:

$$\sigma_1 = \frac{B' \pm \sqrt{B'^2 - 4A'C'}}{2A'} \tag{35}$$

From Mohr's circle for stresses, the principal tensile stress σ_1 in the FRP-strengthened RC membrane element (Fig. 2) can easily be related with the stresses in the L–T coordinate system (Fig. 1) as follows:

$$\sigma_1 = \frac{\sigma_L + \sigma_T}{2} + \sqrt{\left(\frac{\sigma_L - \sigma_T}{2}\right)^2 + \tau_{LT}^2} \tag{36}$$

2.4 Efficient solution procedure

2.4.1 Additional equations

Solving Eq. (29) for the principal compressive stress σ_D in the concrete membrane element (Fig. 2) gives Eq. (37). Substituting σ_D from Eq. (37) into Eqs. (27) and (28), and solving for the stresses in the longitudinal (f_L) and transverse (f_T) steel reinforcement, respectively, gives Eqs. (38) and (39).

$$\sigma_D = \frac{-m_{LT}\sigma_1}{\sin(\alpha_D)\cos(\alpha_D)} + \sigma_R \tag{37}$$

$$f_L = \frac{-\sigma_D \cos^2(\alpha_D) - \sigma_R \sin^2(\alpha_D) + m_L\sigma_1 - \rho_{Lf} f_{Lf}}{\rho_L} \tag{38}$$

$$f_T = \frac{-\sigma_D \sin^2(\alpha_D) - \sigma_R \cos^2(\alpha_D) + m_T\sigma_1 - \rho_{Tf} f_{Tf}}{\rho_T} \tag{39}$$

Using the trigonometric identity $\sin^2(\alpha_D) + cos^2(\alpha_D) = 1$ in the two first compatibility equations (Eq. 3) allows to write the variable angle α_D (Fig. 2) as function of the strains in both L–T and R–D coordinate systems with Eqs. (40) or (41). The principal tensile strain ε_R can be eliminated to calculate the variable angle α_D by dividing Eq. (40) by Eq. (41), giving Eq. (42).

$$\sin^2(\alpha_D) = \frac{\varepsilon_L - \varepsilon_D}{\varepsilon_R - \varepsilon_D} \tag{40}$$

$$\cos^2(\alpha_D) = \frac{\varepsilon_T - \varepsilon_D}{\varepsilon_R - \varepsilon_D} \tag{41}$$

$$\tan^2(\alpha_D) = \sqrt{\frac{\varepsilon_L - \varepsilon_D}{\varepsilon_T - \varepsilon_D}} \tag{42}$$

2.4.2 Residual function for the initial estimates

As for the previous versions of the model [27, 28], average strains ε_D, ε_L, and ε_T are chosen to be the initial estimates to start the efficient RA-STM FRP procedure. Usually, the initial estimates are assumed with arbitrary values. In this study, they are computed by using the Mohr compatibility truss model (MCTM), which apply to a RC membrane element with elastic and linear materials [10].

For simplicity, both the tensile concrete and FRP reinforcement are neglected at this initial stage. Using Hooke's laws for the remaining material components ($\sigma_D = E_c\varepsilon_D$, $f_L = E_s\varepsilon_L$ and $f_T = E_s\varepsilon_T$) in Eqs. (37)–(39) and solving for the average strains, the following equations for the initial estimates can be written:

$$\varepsilon_D = \frac{-m_{LT}\sigma_1}{E_c \sin(\alpha_D)\cos(\alpha_D)} \tag{43}$$

$$\varepsilon_L = \frac{(m_L + m_{LT}\cot(\alpha_D))\sigma_1}{E_S\rho_L} \tag{44}$$

$$\varepsilon_T = \frac{(m_T + m_{LT}\tan(\alpha_D))\sigma_1}{E_S\rho_T} \tag{45}$$

From Eq. (42), after rearranging terms, a nonlinear residual function ($F_{START}(\alpha_D)$) can be defined (Eq. 46), where the strains are defined from the previous equations. This residual function is set to zero and the resulting equation (Eq. 41) is numerically solved for the angle α_D which minimizes F_{START}. This initial angle is then used to compute the initial estimates ε_D, ε_L, and ε_T using again Eqs. (43)–(45), which are used to start the efficient RA-STM FRP procedure, as explained bellow.

$$F_{\mathrm{START}}(\alpha_{\mathrm{D}}) = \frac{\varepsilon_{\mathrm{L}} - \varepsilon_{\mathrm{D}}}{\varepsilon_{\mathrm{T}} - \varepsilon_{\mathrm{D}}} - \tan^2(\alpha_{\mathrm{D}}) \tag{46}$$

$$F_{\mathrm{START}}(\alpha_{\mathrm{D}}) = 0 \tag{47}$$

2.4.3 *Residual functions for the efficient RA-STM FRP procedure*

Following the previous versions of the model [27, 28], the average strains ε_{L} and ε_{T} are chosen to be the primary variables. For this, two nonlinear residual functions are needed to be set. For the first one ($F^{(1)}_{\mathrm{RA-STM}}(\varepsilon_{\mathrm{L}}, \varepsilon_{\mathrm{T}})$, Eq. 48), the following steps are performed: Eqs. (27) and (41) are added to form a new equation, then Eqs. (40) and (41) are substituted in the new equation and terms are rearranged. Similarly, for the second nonlinear residual function ($F^{(2)}_{\mathrm{RA-STM}}(\varepsilon_{\mathrm{L}}, \varepsilon_{\mathrm{T}})$, Eq. 49): Eqs. (28) and (40) are added to form a new equation, then Eqs. (40) and (41) are substituted in the new equation and terms are rearranged. Both nonlinear residual functions are set to zero to form a system of two nonlinear equations (Eq. 49) which are solved to compute the average strains ε_{L} and ε_{T} as the values which minimize both $F^{(1)}_{\mathrm{RA-STM}}(\varepsilon_{\mathrm{L}}, \varepsilon_{\mathrm{T}})$ and $F^{(2)}_{\mathrm{RA-STM}}(\varepsilon_{\mathrm{L}}, \varepsilon_{\mathrm{T}})$.

$$\begin{bmatrix} F^{(1)}_{\mathrm{RA-STM}}(\varepsilon_{\mathrm{L}}, \varepsilon_{\mathrm{T}}) \\ F^{(2)}_{\mathrm{RA-STM}}(\varepsilon_{\mathrm{L}}, \varepsilon_{\mathrm{T}}) \end{bmatrix} = \begin{bmatrix} \sigma_{\mathrm{D}} \dfrac{\varepsilon_{\mathrm{T}} - \varepsilon_{\mathrm{D}}}{\varepsilon_{\mathrm{R}} - \varepsilon_{\mathrm{D}}} + \sigma_{\mathrm{R}} \dfrac{\varepsilon_{\mathrm{L}} - \varepsilon_{\mathrm{D}}}{\varepsilon_{\mathrm{R}} - \varepsilon_{\mathrm{D}}} - m_{\mathrm{L}}\sigma_{\mathrm{l}} + \rho_{\mathrm{L}} f_{\mathrm{L}} + \rho_{\mathrm{Lf}} f_{\mathrm{Lf}} \\ \sigma_{\mathrm{D}} \dfrac{\varepsilon_{\mathrm{L}} - \varepsilon_{\mathrm{D}}}{\varepsilon_{\mathrm{R}} - \varepsilon_{\mathrm{D}}} + \sigma_{\mathrm{R}} \dfrac{\varepsilon_{\mathrm{T}} - \varepsilon_{\mathrm{D}}}{\varepsilon_{\mathrm{R}} - \varepsilon_{\mathrm{D}}} - m_{\mathrm{T}}\sigma_{\mathrm{l}} + \rho_{\mathrm{T}} f_{\mathrm{T}} + \rho_{\mathrm{Tf}} f_{\mathrm{Tf}} \end{bmatrix} \tag{48}$$

$$\begin{bmatrix} F^{(1)}_{\mathrm{RA-STM}}(\varepsilon_{\mathrm{L}}, \varepsilon_{\mathrm{T}}) \\ F^{(2)}_{\mathrm{RA-STM}}(\varepsilon_{\mathrm{L}}, \varepsilon_{\mathrm{T}}) \end{bmatrix} = \begin{bmatrix} 0 \\ 0 \end{bmatrix} \tag{49}$$

2.4.4 *Calculation procedure and algorithm*

Figure 3 illustrates the flowchart for the efficient RA-STM FRP procedure. To start the calculations, some initial data must be specified by the user, including the path's increment $\Delta\varepsilon_{\mathrm{D}}$ for the strain ε_{D}. Next, after defining the loading condition, for $\varepsilon^0_{\mathrm{D}} = \Delta\varepsilon_{\mathrm{D}}$ (with superscript $k = 0$ representing the number of the step) the initial estimates ($\varepsilon^1_{\mathrm{D}}$, $\varepsilon^0_{\mathrm{L}}$ and $\varepsilon^0_{\mathrm{T}}$), are computed from the solution parameter α_{D} (Eq. 47). These initial estimates allow to compute the first solution point. Then, the efficient RA-STM FRP procedure is started. For each step and for each incremented strain $\varepsilon^{k+1}_{\mathrm{D}} = \varepsilon^k_{\mathrm{D}} + \Delta\varepsilon_{\mathrm{D}}$, the primary variables ε_{L} and ε_{T} are computed as the solutions parameters of Eq. (49). For each step, the initial point is defined as the solution point from the previous one.

The calculation procedure stops when one of the following failure criteria for the materials is reached: for concrete in compression when the strain ε_{D} is higher than the ultimate value ($\varepsilon^{k+1}_{\mathrm{D}} \geq \varepsilon_{\mathrm{cu}}$); for FRP in tension when the strain ε_{f} is higher than the ultimate value ($\varepsilon^{k+1}_{\mathrm{f}} \geq \varepsilon_{\mathrm{fu}}$); for steel reinforcement in tension when the strain ε_{S} is higher than the ultimate value ($\varepsilon^{k+1}_{\mathrm{S}} \geq \varepsilon_{\mathrm{su}}$). For $\varepsilon_{\mathrm{cu}}$ and $\varepsilon_{\mathrm{su}}$ conventional values were defined from Eurocode 2 [30]. The value for $\varepsilon_{\mathrm{fu}}$ was computed from Hooke's law as stated in Sect. 2.2.2. Since the efficient RA-STM FRP is a smeared model, as for the SMM-FRP, the local failure of the FRP reinforcement, other than the uniaxial tensile failure (for instance, FRP debonding of FRP anchorage failure), is not captured. Hence, such failure mode was not considered in the proposed model.

In this study, a code in MATLAB [31] was implemented to compute the solutions points with the efficient calculation procedure. Equations (47) and (49) were solved with the least squares method using the MATLAB function *lsqnonlin*.

3 Comparative analysis

In this section, the predictions from the refined efficient RA-STM FRP procedure for the response of FRP-strengthened RC membrane elements are compared with some experimental results found in the literature and also with the predictions from the SMM-FRP for comparison. The experimental results came from 8 FRP-strengthened RC panels tested under pure shear with the Universal Panel Tester at the University of Houston [9, 19]. These experimental results were the only ones found in the literature and related with the testing of FRP-strengthened RC membrane elements under controlled proportional loading until failure.

It should be referred that experimental results of some FRP-strengthened RC panels tested under

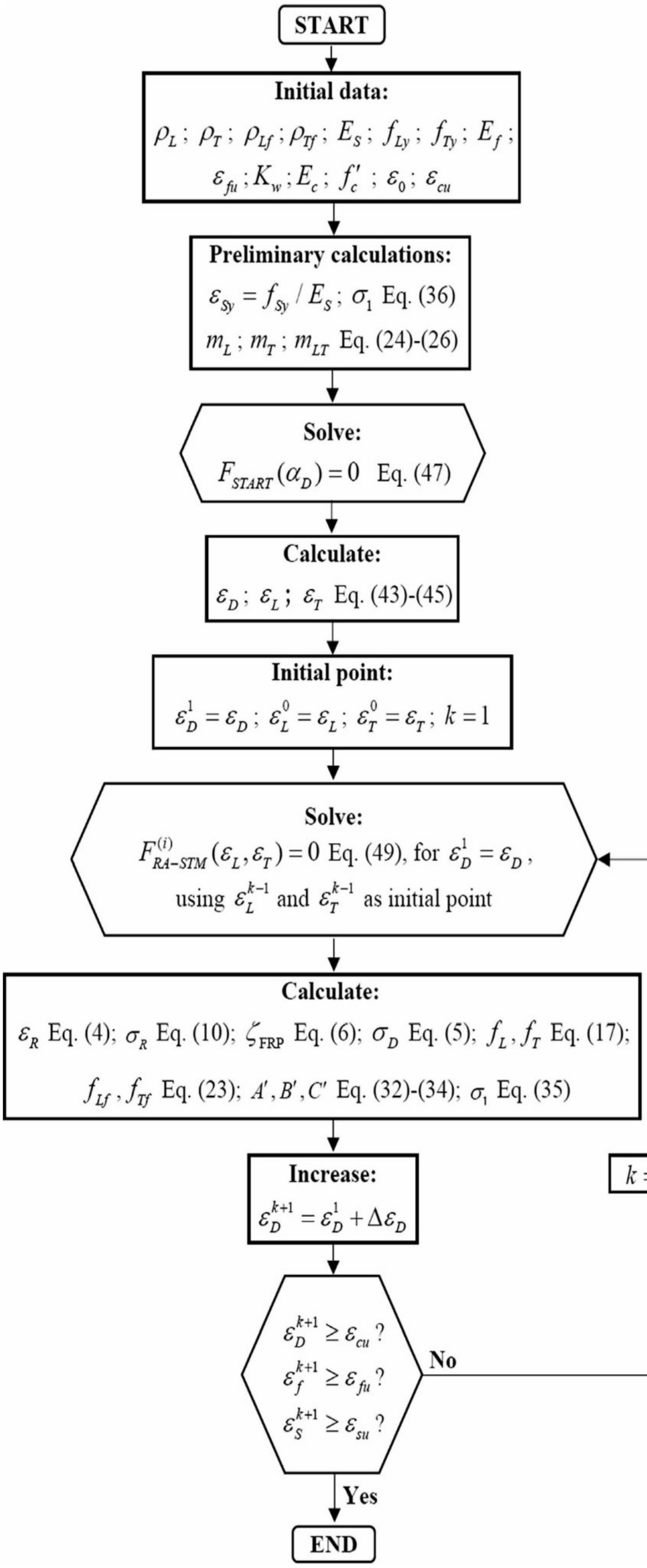

Fig. 3 Flowchart for the efficient RA-STM FRP procedure

sequential loading can also be found in the literature [21]. These experimental tests aimed to calibrate the constitutive laws for the materials. These experimental results were not used in this study because the panels were not tested under proportional loading.

The experimental results from the tests under proportional loading were also used by Zomorodian et al. in 2017 [4] to check the SMM-FRP. As illustrated in Fig. 4, the panels were tested under symmetrical biaxial stresses in the 1–2 coordinate system ($\sigma_2 = -\sigma_1$), with steel and FRP reinforcements oriented at 45°. As a consequence, all panels were tested under pure shear in the L–T coordinate system ($\sigma_L = \sigma_T = 0$, see Fig. 1). All panels have sizes 1398 × 1398 × 178 mm and FRP reinforcement was only applied in the transverse direction of the L–T coordinate system. FRP reinforcement consisted of external FRP sheets composed of unidirectional carbon fibers attached on the two opposite surfaces of the panel specimens (Fig. 4). The FRP strips had a width of 144 mm and were spaced 188 mm between center to center. Two internal layers of steel reinforcement were used. The steel reinforcement consisted of grade 60 deformed bars with cross-sectional areas of 71 mm^2 (#3 rebar) and 129 mm^2 (#4 rebar) spaced at 188 mm in both L and T directions (Fig. 4). The studied variables were the FRP reinforcement ratio, the FRP wrapping scheme and the transverse steel reinforcement ratio.

Table 1 summarizes the main variables of the reference panels and material properties which are needed for the efficient RA-STM FRP procedure. All presented parameters were already defined in the previous sections. The panels were identified according to their original name PX–Y–Z, in which P stands for Panel, X stands for the transverse rebar size (Nos. 3 and 4), Y stands for the FRP thickness (0.025, 0.040 and 0.080 in., with 1 in. = 25.4 mm) and Z stands for the FRP wrapping scheme (fully wrap—FW, side bond—SB and U-wrap with FRP anchors—FA).

The response of each reference FRP-strengthened RC panel from Table 1 was computed using the efficient RA-STM FRP procedure presented in the previous section. Such results are compared with the experimental curves reported in [9, 19] and also with the theoretical predictions from the SMM-FRP reported in [4, 19].

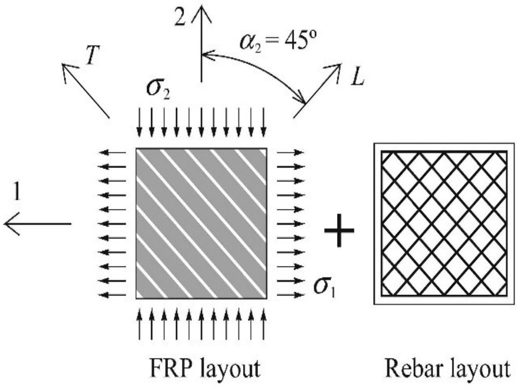

Fig. 4 Loading condition and reinforcement layout of reference test panels

Figure 5 presents the experimental and theoretical shear stress (τ_{LT})–shear strain (γ_{LT}) curves for the reference FRP-strengthened RC panels from Table 1. Two theoretical curves are presented for each panel for comparison. The first one was computed with the efficient RA-STM FRP procedure presented in this study (Eff. RA-STM FRP). The second one was computed with the SMM-FRP and drawn from the theoretical curves presented in [4, 19].

Figure 5 shows that, in general, the theoretical $\tau_{LT} - \gamma_{LT}$ curves from the efficient RA-STM FRP procedure are in good agreement with the same ones from the SMM-FRP up to the maximum shear stress. For the SMM-FRP, the descending branch of the curves is generally much longer and, for some panels, follows better the experimental curves. This is because the SMM-FRP, as for the original SMM and unlike the RA-STM, incorporates the so-called Hsu/Zhu ratios to account for the Poisson's effect after cracking. As explained by Hsu and Zhu in 2002 [18], this refinement allows the model to predict better the post-peak behavior of RC and PC membrane elements under shear. However, for design this feature is not so important and, for this reason, the efficient RA-STM FRP procedure can be also considered a reliable model, despite to being simpler.

Figure 5 also shows that the efficient RA-STM FRP, as for the SMM-FRP, captures well the global response of the reference panels, including the transition from the uncracked to the cracked stage. For some panels, the most striking observed differences between the theoretical and experimental curves, namely at the ultimate stage, were previously explained by Zomorodian et al. in 2017 [4] for the SMM-FRP. Such explanations are also valid for the efficient RA-STM FRP.

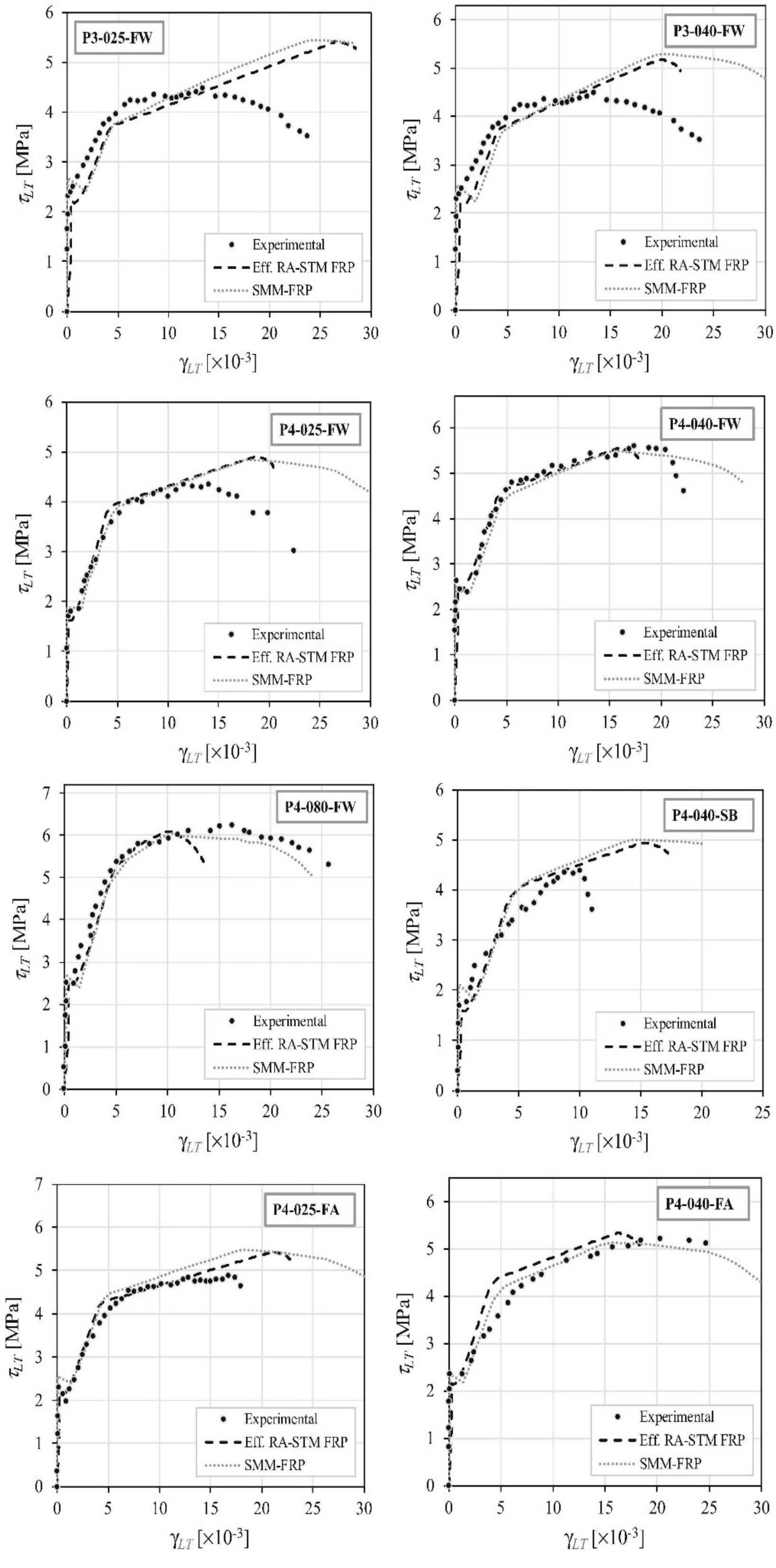

Fig. 5 $\tau_{LT} - \gamma_{LT}$ curves for reference FRP-strengthened RC panels

Table 2 Comparative analysis

Panel	$\tau_{\mathrm{cr,exp}}$ MPa	$\tau_{\mathrm{cr,th}}^{\mathrm{eff.RA-STM}}$ MPa	$\frac{\tau_{\mathrm{cr,exp}}}{\tau_{\mathrm{cr,th}}^{\mathrm{eff.RA-STM}}}$	$k_{\mathrm{S,exp}}$ MPa	$k_{\mathrm{S,th}}^{\mathrm{eff.RA-STM}}$ MPa	$\frac{k_{\mathrm{S,exp}}}{k_{\mathrm{S,th}}^{\mathrm{eff.RA-STM}}}$	$\tau_{\mathrm{u,exp}}$ MPa	$\tau_{\mathrm{u,th}}^{\mathrm{eff.RA-STM}}$ MPa	$\frac{\tau_{\mathrm{u,exp}}}{\tau_{\mathrm{u,th}}^{\mathrm{eff.RA-STM}}}$	$\gamma_{\mathrm{u,exp}} \times 10^{-3}$	$\gamma_{u,th}^{\mathrm{eff.RA-STM}} \times 10^{-3}$	$\frac{\gamma_{\mathrm{u,exp}}}{\gamma_{\mathrm{u,th}}^{\mathrm{eff.RA-STM}}}$
P3-025-FW	2.31	2.23	1.04	0.413	0.490	0.84	4.48	5.42	0.83	13.39	26.58	0.50
P3-040-FW	2.31	2.21	1.04	0.412	0.497	0.83	4.49	5.17	0.87	13.37	19.89	0.67
P4-025-FW	1.71	1.61	1.06	0.423	0.624	0.68	4.36	4.91	0.89	14.00	18.74	0.75
P4-040-FW	2.62	2.48	1.05	0.604	0.633	0.95	5.59	5.55	1.01	17.38	15.95	1.09
P4-080-FW	2.51	2.51	1.00	0.712	0.733	0.97	6.22	6.10	1.02	16.30	10.14	1.61
P4-040-SB	1.69	1.60	1.06	0.978	0.689	1.42	4.38	4.94	0.89	10.01	15.31	0.65
P4-025-FA	2.30	2.14	1.07	0.656	0.637	1.03	4.89	5.43	0.90	16.70	21.15	0.79
P4-040-FA	2.35	2.36	1.00	0.345	0.637	0.54	5.20	5.33	0.98	20.28	16.25	1.25
		$\bar{x}$	1.041		$\bar{x}$	0.908		$\bar{x}$	0.921		$\bar{x}$	0.914
		s	0.028		s	0.262		s	0.071		s	0.371
		cv	2.66%		Cv	28.81%		Cv	7.67%		cv	40.55%

Panels P3-025-FW and P3-040-FW have the smaller steel reinforcement ratio in the transverse direction ($\rho_{\mathrm{T}} = 0.43\%$). The maximum shear stresses for these panels were predicted to be higher that the experimental ones. This occurred because, for simplicity, the effect of very different steel ratios in both L and T directions was neglected to establish the correction factor $f(\mathrm{FRP})$ (Eq. 9) used to compute the softening coefficient ζ_{FRP} (Eq. 6) in order to account for the interaction with the FRP reinforcement. When the steel reinforcement ratio decreases, the compressive concrete in the struts sustain less stress and suffer less damages. As a consequence, the concrete contribution increases [18]. This explains the differences between the theoretical an experimental maximum shear stresses for panels P3-025-FW and P3-040-FW. For the majority of the other panels, with equilibrated steel reinforcement ratio in both longitudinal and transverse directions ($\rho_{\mathrm{L}} = \rho_{\mathrm{T}} = 0.76\%$), the predictions of the maximum shear stresses agree better with the experimental ones.

As stated in Sect. 2.4.4, as for the SMM-FRP, the efficient RA-STM FRP is a smeared model. Therefore, the local failure of the FRP reinforcement, other than the uniaxial tensile failure, is not captured. Panels P4-040-SB and P4-025-FA suffered a premature debonding and anchorage failure of the FRP reinforcement, respectively [9, 19]. For these reasons, the maximum shear stresses of these panels were predicted to be also higher that the experimental ones.

Table 2 presents, for each reference panel, the experimental and theoretical values for some key values and properties of the $\tau_{\mathrm{LT}} - \gamma_{\mathrm{LT}}$ curves considered important for design, namely: the cracking shear stresses $\tau_{\mathrm{cr,exp}}$ and $\tau_{\mathrm{cr,th}}^{\mathrm{eff.RA-STMFRP}}$, shear stiffnesses in the cracked stage $k_{\mathrm{S,exp}}$ and $k_{\mathrm{S,th}}^{\mathrm{eff.RA-STMFRP}}$, peak shear stresses (ultimate values) $\tau_{\mathrm{u,exp}}$ and $\tau_{\mathrm{u,th}}^{\mathrm{eff.RA-STMFRP}}$, and the corresponding shear strains $\gamma_{\mathrm{u,exp}}$ and $\gamma_{\mathrm{u,th}}^{\mathrm{eff.RA-STMFRP}}$. The ratios of the experimental to the theoretical values are also presented ($\tau_{\mathrm{cr,exp}}/\tau_{\mathrm{cr,th}}^{\mathrm{eff.RA-STM}}$, $k_{\mathrm{S,exp}}/k_{\mathrm{S,th}}^{\mathrm{eff.RA-STM}}$, $\tau_{\mathrm{u,exp}}/\tau_{\mathrm{u,th}}^{\mathrm{eff.RA-STM}}$ and $\gamma_{\mathrm{u,exp}}/\gamma_{\mathrm{u,th}}^{\mathrm{eff.RA-STM}}$). Although a limited number of panels was studied, Table 2 also presents, for each ratio, the mean ($\bar{x}$), standard deviation (s) and coefficient of variation (cv). The very small shear strains corresponding to the cracking shear stresses were not included in Table 2 because it was not possible to obtain accurate values from the experimental $\tau_{LT}-\gamma_{LT}$ curves. The shear stiffness in the cracked stage was estimated as follows. Firstly, the points of the $\tau_{LT}-\gamma_{LT}$ curves lying on the approximately linear part of the ascending branch after cracking were retained. Then, a straight line from a linear regression of the referred points was computed. The slope of this straight line represents the shear stiffness in the cracked stage.

The results from Table 2 show that the efficient RA-STM FRP procedure is able to predict very well the cracking shear stress τ_{cr} ($\bar{x} = 1.041$) and with a very low degree of dispersion ($cv = 2.66\%$). For the shear stiffness in the cracked stage k_S, the predictions of the model seems to be slightly overestimated ($\bar{x} = 0.908$) and the degree of dispersion is somewhat high ($cv = 28.81\%$). This last result is in agreement with previous studies on RC and PC membrane elements [27, 28].

Also from Table 2, it can be observed that the efficient RA-STM FRP procedure predicts well the ultimate shear stress τ_u ($\bar{x} = 0.921$), although it seems to be slightly overestimated, and with a low degree of dispersion ($cv = 7.67\%$). For the ultimate shear strain γ_u, the predictions seem to be also slightly overestimated ($\bar{x} = 0.914$). However, as for the shear stiffness in the cracked stage, the degree of dispersion is high ($cv = 40.55\%$). This last result is also in agreement with previous studies [27, 28].

The previous results are somewhat affected by Panels P3-025-FW, P3-040-FW, P4-040-SB and P4-025-FA, as previously discussed, namely as far as the ultimate shear stresses and the ultimate shear strains are concerned. If such panels are disregarded, the following statistical parameters are obtained for the ultimate parameters: $\bar{x} = 0.973$ and $cv = 6.13\%$ for the ultimate shear stress (τ_u), $\bar{x} = 1.173$ and $cv = 30.45\%$ for the ultimate shear strain (γ_u). While for the ultimate shear stress the predictions are improved, as expected, for the ultimate shear strain no substantial improvement is observed. In general, smeared truss models show difficulties to predict well the deformations at the ultimate stage, however such drawback is not very important for design.

4 Conclusions

In this article, the RA-STM was extended to FRP-strengthened RC membrane elements. The new model was called efficient RA-STM FRP procedure. For this, both the equilibrium equations and the smeared constitutive relationships for the materials were modified to account for the contribution of the FRP reinforcement. In addition, an efficient calculation procedure was implemented in order to avoid using the classical trial and error technique to compute the solution points. The predictions from the efficient RA-STM FRP procedure where compared with some experimental results and also with the predictions from another theoretical model. From the obtained results, the following conclusions can be drawn:

- The predictions from the efficient RA-STM FRP procedure showed to be in good agreement with the same ones from the SMM-FRP up to the maximum shear stress. This show that, is spite being a simpler model, the efficient RA-STM FRP procedure captures well the most important features of the response of FRP-strengthened RC membrane elements under shear;
- As for the SMM-FRP, the efficient RA-STM FRP procedure showed to predict reasonably well the experimental response of FRP-strengthened RC panels under shear for all loading stages, namely the maximum shear and the transition between the uncracked to the cracked stage. This is particularly true for FRP-strengthened RC panels with equilibrated longitudinal to transverse steel reinforcement ratios and also for panels without local failure of the FRP reinforcement.
- Unlike previous theoretical models, such as the SMM-FRP, which incorporates a trial and error technique and a large number of initial estimates, the efficient RA-STM FRP procedure allows to compute the full response of FRP-strengthened RC membrane elements with high numerical efficiency and stability. In addition, the calculation procedure is easier to implement and require less calculation effort.

Finally, it should be referred that the previous conclusions were based on a limited number of comparative analyses with experimental results, and only for FRP-strengthened RC panels under shear. In addition, the results in this study help to support the need to calibrate better the constitutive material's laws to be used in smeared truss models to simulate such structural members. For this reason, additional studies on this subject and also additional experimental results are still needed, including with FRP-strengthened RC panels under more general in-plane stresses.

It should be also referred that, in the present form, the efficient RA-STM FRP procedure is limited to the study of the local behavior of RC membrane-type or wall-type structures/members externally bonded with FRP sheets, such as local parts of webs in shear beam or shear walls with uniform in-plane loading and reinforcement layout. However, the equations for the efficient RA-STM FRP procedure can also be used to implement the model into a non-linear finite element program, which can be used to study the global response of RC membrane-type or wall-type structures. For instance, such a development of a smeared truss model was successfully performed with the SMM [10].

References

1. ACI Committee 440 (2017) Guide for the design and construction of externally bonded FRP systems for strengthening concrete structures. ACI 440.2R-17. American Concrete Institute, Farmington Hills (MI)
2. Task Group *fib* T5.1 (2019) Externally applied FRP reinforcement for concrete structures. *FIB* BULLETIN NO. 90. International Federation for Structural Concrete (*fib*), Lausanne, Switzerland
3. Belarbi A, Bae SW, Ayoub A, Kuchma D, Mirmiran A, Okeil A (2011) Design of FRP systems for strengthening concrete girders in shear. NCHRP Rep. No. 678, Transportation Research Board, Washington, DC
4. Zomorodian M, Belarbi A, Ayoub A (2017) Finite element model for predicting the shear behavior of FRP-strengthened RC members. Eng Struct 153:239–253
5. He R, Sneed LH, Belarbi A (2014) Torsional repair of severely damaged column using carbon fiber-reinforced polymer. ACI Struct J 111(3):705–716
6. Mofidi A, Chaallal O (2014) Effect of steel stirrups on shear resistance gain due to externally bonded fiber-reinforced polymer strips and sheets. ACI Struct J 111:353–361
7. Ganganagoudar A, Mondal TG, Prakash SS (2016) Analytical and finite element studies on behavior of FRP strengthened RC beams under torsion. Compos Struct 153:876–885
8. Baghi H, Barros JA (2016) Shear strengthening of reinforced concrete T-beams with hybrid composite plate. J Compos Constr 20(6):04016036
9. Zomorodian M, Yang G, Belarbi A, Ayoub A (2018) Behavior of FRP-strengthened RC elements subjected to pure shear. Constr Build Mater 170:378–391
10. Hsu TTC, Mo YL (2010) Unified theory of concrete structures. Wiley, London
11. Hsu TTC, Zhang LX, Gomez T (1995) A servo-control system for universal panel tester. J Test Eval 23:424–430
12. Pang XB, Hsu TTC (1995) Behavior of reinforced concrete membrane elements in shear. Struct J Am Concr Insti 92(6):665–679
13. Belarbi A, Hsu TTC (1995) Constitutive laws of softened concrete in biaxial tension-compression. Struct J Am Concr Inst 92(5):562–573
14. Zhang LX, Hsu TTC (1998) Behavior and analysis of 100 MPa concrete membrane elements. J Struct Eng 124(1):24–34
15. Belarbi A, Hsu TTC (1994) Constitutive laws of concrete in tension and reinforcing bars stiffened by concrete. Struct J Am Concr Inst 91(4):465–474
16. Pang XB, Hsu TTC (1996) Fixed-Angle softened truss model of reinforced concrete. Struct J Am Concr Inst 93(2):197–207
17. Hsu TTC, Zhang LX (1997) Nonlinear analysis of membrane elements by fixed-angle softened-truss model. Struct J Am Concr Inst 94(5):483–492
18. Hsu TTC, Zhu RRH (2002) Softened membrane model for reinforced concrete elements in shear. Struct J Am Concr Inst 99(4):460–469
19. Zomorodian M (2015) Behavior of FRP strengthened concrete panel elements subjected to pure shear. Ph.D. Thesis. Faculty of the Department of Civil and Environmental Engineering, University of Houston
20. Yang G, Zomorodian M, Belarbi A, Ayoub A (2015) Uniaxial tensile stress–strain relationships of RC elements strengthened with FRP sheets. J Compos Constr 04015075
21. Yang G, Zomorodian M, Belarbi A (2017) Material laws of FRP-strengthened RC element in biaxial tension–compression. J Compos Constr 04017030
22. Greene GG, Belarbi A (2009) Model for reinforced concrete members under torsion, bending, and shear. I: theory. J Eng Mech 135(9):961–969
23. Silva J, Horowitz B, Bernardo L (2017) Efficient analysis of beam sections using softened truss model. ACI Struct J 114(3):765–774
24. Wong HF, Kuang JS (2014) Predicting shear strength of RC interior beam-column joints by modified rotating-angle softened-truss model. Comput Struct 133:12–17
25. Bernardo LFA, Andrade JMA, Nunes NCG (2015) Generalized softened variable angle truss-model for reinforcement concrete beams under torsion. Mater Struct 48(7):2169–2193
26. Ji T (2005) A new algorithm for the rotating-angle, softened-truss model of reinforced concrete elements. Mag Concr Res 57(6):353–360
27. Bernardo LFA, Filho BMVC, Horowitz B (2020) Predicting the behavior of prestressed concrete membrane elements by refined rotating-angle softened-truss model with efficient solution procedure. Struct Concr. https://doi.org/10.1002/suco.201900481
28. Bernardo LFA, Filho BMVC, Horowitz B (2020) Refined efficient RA-STM procedure for RC membrane elements.

Eng Struct. https://doi.org/10.1016/j.engstruct.2020.110552

29. Zhu RRH, Hsu TTC, Lee JY (2001) Rational shear modulus for smeared-crack analysis of reinforced concrete. Struct J Am Concr Inst 98(4):443–450
30. NP EN 1992-1-1 (2010) Eurocode 2: design of concrete structures—part 1: general rules and rules for buildings
31. MathWorks (2018) MATLAB_R2018a

Capítulo 7

Modelo eficiente de treliça com amolecimento para elementos de membrana de concreto protendido com fibras de aço.

Este capítulo consiste no artigo:

Efficient Softened Truss Model for Prestressed Steel Fiber Concrete Membrane Elements.

BERNARDO, L. F. A.; FILHO B. M. V. C.; HOROWITZ, B. 2021 "Efficient Softened Truss Model for Prestressed Steel Fiber Concrete Membrane Elements", Journal of Building Engineering, Elsevier, ISSN: 2352-7102, Volume 40: 102363.

DOI: https://doi.org/10.1016/j.jobe.2021.102363

Journal of Building Engineering 40 (2021) 102363

Contents lists available at ScienceDirect

Journal of Building Engineering

journal homepage: http://www.elsevier.com/locate/jobe

Efficient softened truss model for prestressed steel fiber concrete membrane elements

L.F.A. Bernardo [a,*], B.M.V.C. Filho [a], B. Horowitz [b]

[a] *University of Beira Interior, C-MADE - Centre of Materials and Building Technologies, Covilhã, Portugal*
[b] *Federal University of Pernambuco, Brazil*

ARTICLE INFO

Keywords:
Rotating-angle softened truss model
Efficient solution procedure
Membrane elements
Prestressed steel fiber concrete

ABSTRACT

In this article, a recent version of the rotating-angle softened truss model proposed by the authors, to compute the full behavior of prestressed concrete membrane elements under in-plane stresses, is extended to prestressed steel fiber concrete membrane elements. For this, the smeared constitutive relationships for the component materials are modified to include the influence of the steel fiber reinforcement. In particular, a new smeared constitutive relationship for steel fiber concrete in tension is incorporated in the model. The extended model, called efficient rotating-angle softened truss model for prestressed steel fiber concrete, is checked against some experimental results found in the literature and related with prestressed steel fiber concrete panels tested under shear up to failure. It is shown that the proposed model is able to predict well the full behavior of prestressed steel fiber concrete membrane elements for all loading ranges, including the influence after cracking of the steel fiber reinforcement.

1. Introduction

Nowadays, it is well known that the addition of steel fibers highly improves some mechanical key properties of concrete, namely the post-cracking tensile performance, such as: tensile strength, ductility, toughness and higher crack control [1,2]. Due to the bridging effect of the fibers across the tensile cracks and to the confinement effect of the fibers within the concrete matrix, steel fiber concrete (SFC) specimens sustain significant post-peak load and deformation, while plain concrete fails suddenly upon reaching the peak load [3,4]. Several recent studies on the constitutive modeling of SFC have demonstrated the physical mechanisms which explain the positive interaction between steel fibers and concrete mainly in the cracked stage [5–7], including when conventional reinforcement also exists [8]. It has also been reported that SFC display good behavior in reinforced concrete members primary under high shear loads [3,9–15], in particular both the shear strength and ductility increase. This is important for many prestressed concrete structures, such as: shear walls, box beams for girders in long span bridges and nuclear containment vessels.

In addition to the benefits of prestressing, steel fiber (SF) reinforcement has the potential to reduce or, in some cases, eliminate the need for the conventional shear reinforcements (stirrups). This possibility allows to reduce the time and labor cost associated with the fabrication and placement of such reinforcement [16–18]. As example, this feature is important for prestressed bridge girders with thin webs which carry high shear loads. It was reported that, by using SFC, the shear capacity of prestressed bridge girders with stirrups was increased, allowing to reduce or replace conventional shear reinforcement [19,20]. In previous studies, models have already been proposed to compute the shear strength of beams accounting for the SF reinforcement, namely by using softened truss model approaches [12,17,21,22] and nonlinear finite element analysis [16,23,24].

For the referred structural members, many of their parts are mainly under in-plane stresses and can be viewed as prestressed membrane elements. Hence, such structural members can be viewed as the union of smaller 2D membranes [25].

Among the analytical models used to predict the behavior of concrete 2D membranes, rational mechanic models based on the smeared-crack concept (in contrast to the discrete-crack concept where the cracks are evaluated locally), in the form of smeared truss approaches, have been widely used. In such models, which satisfy Navier's three principles of mechanics of materials (stress equilibrium, strain compatibility and

---

* Corresponding author. University of Beira Interior, Department of Civil Engineering and Architecture, Edifício II das Engenharias, Calçada Fonte do Lameiro, 6201-001 Covilhã, Portugal.

E-mail address: lfb@ubi.pt (L.F.A. Bernardo).

https://doi.org/10.1016/j.jobe.2021.102363
Received 16 September 2020; Received in revised form 28 January 2021; Accepted 28 February 2021

constitutive laws), the stresses and strains in the member are evaluated along a sufficient length to include several cracks. Hence, smeared relationships for the materials (experimentally calibrated) are used to account for the effects due to the evolving biaxial stress state, namely the damages and interaction between the material components. Such models allow to easily account for the contribution and nonlinear behavior of each material component, allowing to predict how the stress and strain fields evolve after cracking. Rational models based on the smeared-crack concept have been proposed by several authors during the last decades. A review of some developments which leaded to some smeared truss models is briefly presented below.

The first experiments on reinforced concrete (RC) panels under shear showed that the compressive strength of concrete was reduced due the existing biaxial compression-tension stress state, namely in the cracking stage [26]. In order to quantify this "softening effect", additional experiments were performed by Vecchio and Collins in 1981 [27] and 1982 [28] in the so-called "shear rig" device. The obtained results allowed the authors to quantify a softening coefficient to be incorporated in the compressive stress (σ) – strain (ε) relationship of concrete and to develop the so-called compression field theory (CFT) for cracked RC panels, which assumes that the direction of the principal compressive stress rotates after cracking (rotating-crack model). Later, the CFT was refined by the same authors to incorporate the concrete tensile stresses in order to predict correctly the post-cracking stiffness. The new model was called modified compression field theory (MCFT) [29]. Variants of rotating crack models were also developed and proposed by other authors [30–34].

Starting at the end of the nineties, several additional tests on RC and PC panels were performed in the Universal Panel Tester at the University of Houston. Based on the obtained experimental results, and in order to correct some inconsistencies of the MCFT [35], Thomas Hsu and collaborators successively developed three smeared truss models.

The first model, called rotating-angle softened truss model (RA-STM) [36–38], incorporated a new smeared $\sigma - \varepsilon$ relationship for steel bars embedded in concrete. Such as for the MCFT, both equilibrium and compatibility equations were written with respect to a rotating reference frame which coincides with the principal directions of stresses in concrete. Hence, the resistance of concrete to shear was neglected. To correct this issue, the second model called fixed-angle softened truss model (FA-STM) was proposed in 1996 and developed further [39–41]. In this model, the equations were written with respect to a fixed reference frame which coincides to the principal directions of the external stresses applied to the RC member at initial cracking (fixed crack model). A new smeared shear stress (τ) – shear strain (γ) relationship for concrete in shear was defined and incorporated. Variants of fixed crack models were also developed and proposed by other authors [31,42]. Finally, a third model was proposed with the aim to better predict the post-peak response of the panels, the so-called softened membrane model (SMM) [43–45]. In this model, the Poisson's effect (mutual influence of the two normal principal strains) was defined and incorporated in the cracking stage. All three models showed good agreement with experimental results, although the SMM was the one who gave the best predictions for RC panels under shear, including the post-peak response. They were also successively extended to PC membrane elements [46,47].

Among the referred models, the RA-STM is the one with the simpler formulation and calculation procedure. It also shows good agreement with experimental results, at least until the peak load is reached [38]. For these reasons, the RA-STM still continues to be used as a physically based-model and has been extended to other structural members [48–51]. The RA-STM has also been successfully refined to provide better predictions and also to increase the numerical efficiency and stability of the calculation procedure [52–54]. For this, instead of using a classical trial-and-error technique to compute the solution points, the authors reformulated the RA-STM as a system of nonlinear equations with constraints, which are solved using an optimization algorithm. This recent version of the model, called "efficient RA-STM procedure", was successfully applied to RC and PC membrane elements [53,54].

In this work, the efficient RA-STM procedure is extended to prestressed steel fiber concrete (PSFC) membrane elements. For this, the smeared constitutive relationships for the materials are modified to account for the influence of the SF reinforcement, according to the proposals of a previous experimental study [55]. Also, a new smeared constitutive relationship for SFC in tension is incorporated in the model. The extended model, called "efficient RA-STM PSFC procedure", is checked against some experimental results available in the literature and related with PSFC plates tested under shear up to failure. The predictions of the proposed model are also compared with the ones from the SMM extended for PSFC membrane elements [55]. In general, it is showed that the efficient RA-STM PSFC procedure is a reliable model to predict the full behavior of PSFC membrane elements under shear.

2. Efficient RA-STM procedure for PSFC membrane elements

In this section, the efficient RA-STM procedure for PC membrane elements is extended for PSFC membrane elements. As for the previous versions of the model, it is assumed that perfect bond exists between steel bars and the fiber reinforced concrete. In addition, the dowel action in the steel bars is neglected. Equations which remain unchanged (basic equations from the RA-STM and additional equations for the efficient RA-STM procedure for PC membrane elements) are summarized. Details about the derivation/justification of such equations can be found in previous studies [25,38,53,54]. The modification of the constitutive relationships of the materials, to account for the influence of the SF reinforcement, are presented and justified. The new smeared constitutive relationship for SFC under tension is also presented.

2.1. Basic equations for the RA-STM

A PSFC membrane element is illustrated in Fig. 1 (left side) and subjected to an in-plane stress state, with applied normal (σ_L) and transversal (σ_T) stresses, and also shear stress (τ_{LT}) in the Longitudinal (L) – Transverse (T) coordinate system (direction of the longitudinal and transverse reinforcement). As also illustrated in Fig. 1, the in-plane stress state in the PSFC membrane element can be considered as the superposition of three in-plane stress states, each of them applied in a particular element, namely: in the SFC element (σ_L^c,σ_T^c and τ_{LT}^c), in the mild steel grid element ($\rho_L f_L$ and $\rho_T f_T$) and in the prestress steel grid element ($\rho_{LP} f_{LP}$ and $\rho_{TP} f_{TP}$). In Fig. 1, ρ stands for the reinforcement ratio (see definition in footnote in Table 1) and f stands for the normal stress in the steel bars. Based on the previous decomposition, and by using the Mohr's circle for stresses and strains, a set of equilibrium and compatibility equations (Eqs. (1)–(3)) can be derived [25,38].

$$\begin{bmatrix}\sigma_L\\ \sigma_T\\ \tau_{LT}\end{bmatrix}=\begin{bmatrix}\cos^2(\alpha_D) & \sin^2(\alpha_D) & 2\sin(\alpha_D)\cos(\alpha_D)\\ \sin^2(\alpha_D) & \cos^2(\alpha_D) & -2\sin(\alpha_D)\cos(\alpha_D)\\ -\sin(\alpha_D)\cos(\alpha_D) & \sin(\alpha_D)\cos(\alpha_D) & \cos^2(\alpha_D)-\sin^2(\alpha_D)\end{bmatrix}\begin{bmatrix}\sigma_D\\ \sigma_R\\ 0\end{bmatrix}+\begin{bmatrix}\rho_L f_L\\ \rho_T f_T\\ 0\end{bmatrix}+\begin{bmatrix}\rho_{LP} f_{LP}\\ \rho_{TP} f_{TP}\\ 0\end{bmatrix} \tag{1}$$

$$\begin{bmatrix}\varepsilon_L\\ \varepsilon_T\\ \gamma_{LT}\end{bmatrix}=\begin{bmatrix}\cos^2(\alpha_D) & \sin^2(\alpha_D) & 2\sin(\alpha_D)\cos(\alpha_D)\\ \sin^2(\alpha_D) & \cos^2(\alpha_D) & -2\sin(\alpha_D)\cos(\alpha_D)\\ -2\sin(\alpha_D)\cos(\alpha_D) & 2\sin(\alpha_D)\cos(\alpha_D) & 2\cos^2(\alpha_D)-2\sin^2(\alpha_D)\end{bmatrix}\begin{bmatrix}\varepsilon_D\\ \varepsilon_R\\ 0\end{bmatrix} \tag{2}$$

$$\varepsilon_R=\varepsilon_L+\varepsilon_T-\varepsilon_D \tag{3}$$

In the previous equations, σ_R and σ_D are the principal stresses (tensile and compressive, respectively) in the SFC element, and α_D is the variable angle between the coordinate systems L-T and R-D (Fig. 2). Also, ε_L, ε_T and γ_{LT} are the average strains components corresponding to the stresses (normal and shear strains, respectively), while ε_R and ε_D are the average

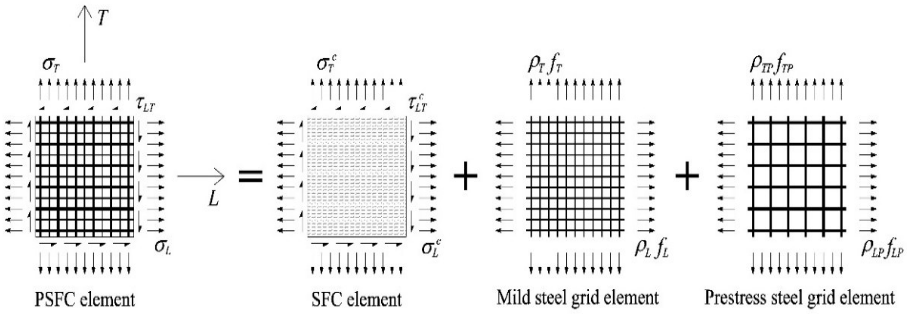

Fig. 1. Stress components in PSFC membrane elements.

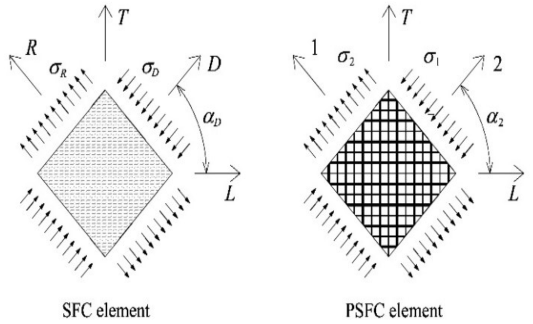

Fig. 2. Principal direction of stresses.

principal strains (tensile and compressive, respectively).

2.2. Additional equations for the efficient RA-STM procedure

In order to reformulate the RA-STM as a system of nonlinear equations with constraints, the authors have previously justified/derived a set of additional equations to build an optimized algorithm to compute the solution points for both RC and PC membrane elements [53,54]. Such equations are summarized below.

For a RC membrane element under in-plane stresses, the most common loading condition in real situations and also in experiments on membrane elements is the one for which the ratio between the external stresses remains constant through all the loading history [54]. For this reason, this loading condition was assumed for this study, as for the previous versions of the proposed model for RC and PC panels [53,54].

Proportional loading is characterized by a constant ratio between the in-plane applied stresses through the entire loading history. For such loading, the following three constant proportionality coefficients are defined: longitudinal (m_L, Eq. (4)), transverse (m_T, Eq. (5)) and shear (m_{LT}, Eq. (6)) proportionality coefficients. Parameter σ_1 is the applied principal tensile stress in the PSFC membrane element.

$$m_L = \frac{\sigma_L}{\sigma_1} \tag{4}$$

$$m_T = \frac{\sigma_T}{\sigma_1} \tag{5}$$

$$m_{LT} = \frac{\tau_{LT}}{\sigma_1} \tag{6}$$

From Mohr's circle for stresses, Eq. (7) relates the in-plane applied stresses in the L-T coordinate system (σ_L, σ_T and τ_{LT}) with the applied principal tensile stress in the PSFC membrane element in the 1–2 coordinate system (σ_1), which coincides with the direction of the principal applied stresses (σ_1 and σ_2) (see Fig. 2).

$$\sigma_1 = \frac{\sigma_L + \sigma_T}{2} + \sqrt{\left(\frac{\sigma_L - \sigma_T}{2}\right)^2 + \tau_{LT}^2} \tag{7}$$

Substituting Eqs. (4)–(6) into the equilibrium equations (Eq. (1)) and developing, an additional quadratic formula (Eqs. (8)–(11)) can be written with the principal tensile stress σ_1 as variable. The solution is given by Eq. (12).

$$A' \sigma_1^2 + (-B')\sigma_1 + C' = 0 \tag{8}$$

$$A' = m_L m_T - m_{LT}^2 \tag{9}$$

$$B' = m_L(\sigma_R + \rho_T f_T + \rho_{TP} f_{TP}) + m_T(\sigma_R + \rho_L f_L + \rho_{LP} f_{LP}) \tag{10}$$

$$C' = (\sigma_R + \rho_L f_L + \rho_{LP} f_{LP})(\sigma_R + \rho_T f_T + \rho_{TP} f_{TP}) \tag{11}$$

$$\sigma_1 = \frac{B' \pm \sqrt{B'^2 - 4A'C'}}{2A'} \tag{12}$$

The compatibility equations (Eq. (2)) can be manipulated to derive the following two equations to compute the angle α_D:

$$\sin^2(\alpha_D) = \frac{\varepsilon_L - \varepsilon_D}{\varepsilon_R - \varepsilon_D} \tag{13}$$

$$\cos^2(\alpha_D) = \frac{\varepsilon_T - \varepsilon_D}{\varepsilon_R - \varepsilon_D} \tag{14}$$

Combining the previous equations with the equations which resulted from the substitution of Eqs. (4)–(6) into Eq. (1), the following set of two nonlinear equations can be written.

$$\begin{bmatrix} F_{RA-STM}^{(1)} \\ F_{RA-STM}^{(2)} \end{bmatrix} = \begin{bmatrix} \sigma_D \frac{\varepsilon_T - \varepsilon_D}{\varepsilon_R - \varepsilon_D} + \sigma_R \frac{\varepsilon_L - \varepsilon_D}{\varepsilon_R - \varepsilon_D} - m_L \sigma_1 + \rho_L f_L + \rho_{LP} f_{LP} \\ \sigma_D \frac{\varepsilon_L - \varepsilon_D}{\varepsilon_R - \varepsilon_D} + \sigma_R \frac{\varepsilon_T - \varepsilon_D}{\varepsilon_R - \varepsilon_D} - m_T \sigma_1 + \rho_T f_T + \rho_{TP} f_{TP} \end{bmatrix} = \begin{bmatrix} 0 \\ 0 \end{bmatrix} \tag{15}$$

$F_{RA\ STM}^{(1)}$ and $F_{RA\ STM}^{(2)}$ are called the residual functions (or simply residuals) for the RA-STM and represent the residual (a kind of error) of the desired result. In the efficient RA-STM procedure, the two nonlinear equations stated in Eq. (15) are solved for the strains ε_L and ε_T, given initial estimates for the strains and limit values for the residuals. This is done numerically by minimizing both residual functions $F_{RA-STM}^{(1)}$ and $F_{RA-STM}^{(2)}$.

To compute the solution points from the efficient RA-STM procedure, the following strains need to be estimated: ε_D, ε_L, and ε_T. For the first solution point, the initial estimates are computed using the Mohr compatibility truss model (MCTM), which constitutes a simplified elastic linear model for membrane elements [25].

From Eq. (13)-(14), the following nonlinear equation can be written:

$$F_{MCTM} = \frac{\varepsilon_L - \varepsilon_D}{\varepsilon_T - \varepsilon_D} - \tan^2(\alpha_D) = 0 \tag{16}$$

F_{MCTM} is called the residual function for the MCTM and has the same meaning stated before for Eq. (15). The strains ε_D, ε_L and ε_T can be estimated from Eq. (17)-(19), which result from substituting Hooke's law in some of the equations previously obtained and solving them for the strains. In addition, for this initial stage and for simplicity, the tensile stress σ_R is neglected.

$$\varepsilon_D = \frac{-m_{LT}\sigma_1}{E_c \sin(\alpha_D)\cos(\alpha_D)} \tag{17}$$

$$\varepsilon_L = \frac{\left(m_L + m_{LT}\cot(\alpha_D)\right)\sigma_1 - \rho_{LP} f_{LP,i}}{E_S \rho_L} \tag{18}$$

$$\varepsilon_T = \frac{\left(m_T + m_{LT}\tan(\alpha_D)\right)\sigma_1 - \rho_{TP} f_{TP,i}}{E_S \rho_T} \tag{19}$$

In Eq. (18)-(19), $f_{LP,i}$ and $f_{TP,i}$ represent the initial stress in the longitudinal and transverse prestress reinforcement, respectively, while E_c and E_S are the Young's modulus for SF concrete and mild steel, respectively.

Eq. (16) is numerically solved for the angle α_D by minimizing the residual function F_{MCTM}. After this, the strains are reestimated from Eq. (17)-(19) and used as the initial estimates to start the efficient RA-STM procedure, as explained in Section 2.4.

2.3. Smeared constitutive relationships

To extend the efficient RA-STM procedure previously proposed by the authors for PC membrane elements [53] to PSFC membrane elements, the smeared constitutive relationships for the materials under biaxial stress state are modified according to the proposals from Hoffman in 2010 [55]. To the best of the authors knowledge, the work from this author is the only one found in the literature who aimed to study the smeared σ - ε relationships for the materials for PSFC membrane elements. Based on previous experimental results on SFC panels under shear conducted at the University of Houston, with the aim to obtain smeared σ - ε relationships for SFC, Hoffman in 2010 [55] extended such relationships for PSFC. For this, he conducted an experimental program with PSFC panels (TEF panels) under sequential loading to investigate the effect of both prestress and SF reinforcement on the smeared σ - ε relationships of the component materials. As a result, a set of empirical correction factors were calibrated and proposed to correct both the smeared σ - ε relationships for SF concrete in compression and steel bars in tension. In addition, a new smeared σ - ε relationship for SF concrete in tension was also proposed. Such proposals are used in this study to modify the previously used smeared σ - ε relationships for the materials and to incorporate the smeared σ - ε relationship for SF concrete in tension.

It should be referred that, as also assumed in the previous study from the authors [53], the calculation procedure of the efficient RA-STM procedure starts after concrete decompression. Before concrete decompression the behavior of PC membrane elements lies entirely in the elastic domain (the strains in the materials are very small). This simplification avoids to model the stress and strain evolution in the pre-decompression stage.

2.3.1. Steel fiber concrete in compression

For concrete in compression, the smeared σ - ε relationship proposed by Belarbi and Hsu in 1995 [37] and refined latter by Zhu et al., in 2001 [45] (Eq. (20)-(24), see Fig. 3) is adopted and modified. This smeared relationship for plain concrete was used and justified by the authors in previous studies [53,54]. In order to account for the SF reinforcement, the softening coefficient for plain concrete ζ in Eq. (21) is modified by

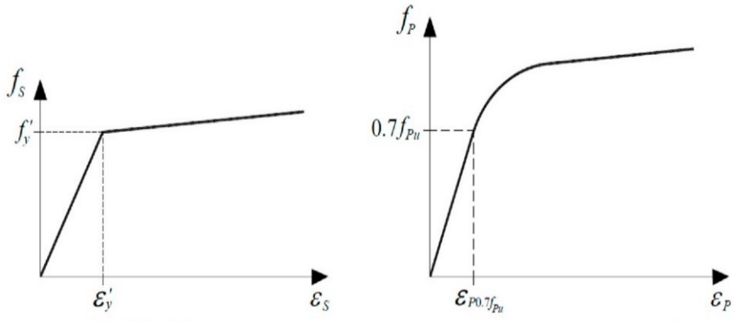

Mild steel bars in tension

Prestress steel bars in tension

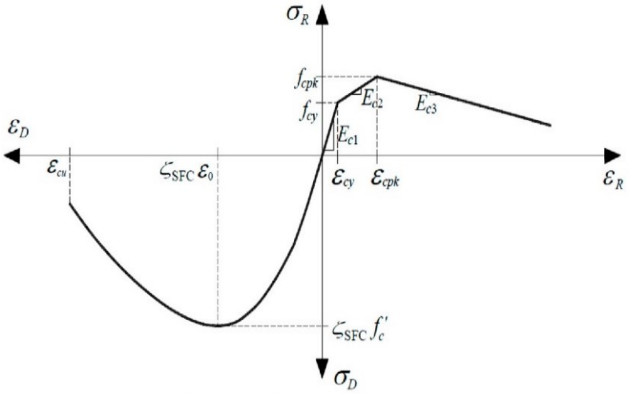

SF concrete in compression / tension

Fig. 3. Smeared constitutive laws for the materials.

the correction factor W_f (Eq. (22)) and an additional upper limit of 0.9 is imposed [55].

$$\sigma_D = \zeta_{SFC} f_c^{'} \left[2\left(\frac{\varepsilon_D}{\zeta_{SFC}\varepsilon_0}\right) - \left(\frac{\varepsilon_D}{\zeta_{SFC}\varepsilon_0}\right)^2 \right] \text{ if } \varepsilon_D \le \zeta_{SFC}\varepsilon_0 \tag{20a}$$

$$\sigma_D = \zeta_{SFC} f_c^{'} \left[1 - \left(\frac{\frac{\varepsilon_D}{\zeta_{SFC}\cdot\varepsilon_0} - 1}{\frac{4}{\zeta_{SFC}} - 1} \right)^2 \right] \text{ if } \varepsilon_D > \zeta_{SFC}\varepsilon_0 \tag{20b}$$

$$\zeta_{SFC} = \zeta \cdot W_f = \left(\frac{5.8}{\sqrt{f_c^{'}(\text{MPa})}} \le 0.9 \right) \cdot \frac{1}{\sqrt{1 + \frac{400\varepsilon_R}{\eta^{'}}}} \cdot W_f \le 0.9 \tag{21}$$

$$W_f = 1 + 0.5FF \tag{22}$$

$$\eta = \frac{\rho_T f_{Ty} + \rho_{TR} f_{TP0.1\%} - \sigma_T}{\rho_L f_{Ly} + \rho_{LR} f_{LP0.1\%} - \sigma_L} \tag{23}$$

$$\begin{cases} \eta^{'} = \eta \text{ if } \eta \le 1 \\ \eta^{'} = \frac{1}{\eta} \text{ if } \eta > 1 \end{cases} \quad (0.4 < \eta^{'} < 1.0) \tag{24}$$

In Eq. (20), $f_c^{'}$ is the uniaxial compressive strength of SFC, ε_0 is the strain corresponding to the peak stress $(f_c^{'})$ and ζ_{SFC} is the softening coefficient for SFC. Eq. (21) for the softening coefficient ζ without corrections was proposed by Zhang and Hsu in 1998 [41] and refined by Zhu et al., in 2001 [45]. This equation accounts for the ratio of the transverse to the longitudinal tensile strength of reinforcements (Eq. (23)-(24)) through parameter $\eta^{'}$. The additional condition $0.4 < \eta < 2.5$ from Pang and Hsu in 1995 [38] and Zhang and Hsu in 1998 [41] was imposed. In Eq. (22), FF stands for fiber factor, which is computed from Eq. (25), where L_f and D_f are the length and diameter of the steel fiber, respectively, and V_f is the percentual volume of steel fiber.

$$FF = \frac{L_f}{D_f} V_f \tag{25}$$

Eq. (25) to compute the fiber factor was proposed by Hoffman in 2010 [55] based on the type of steel fibers used in PSFC panels tested under shear in the University of Houston (Dramix-Bekaert steel fibers with hooked ends). As referred in Section 3, the experimental results from Hoffman in 2010 [55] will be used to check the efficient RA-STM PSFC procedure. For this reason, the same fiber factor proposed by the referred author was used in this work. However, fibers with different shape will certainly play a key role of defining the bond between fiber and concrete. In such case, appropriate fiber factors should be used. Formulations for the fiber factor are available in the literature (see for instance Ref. [13]).

2.3.2 Steel fiber concrete in tension

Based on the proposals from Hoffman in 2010 [55], a simplified trilinear smeared σ - ε relationship for SF tensile concrete in tension was used (Eq. (26)-(34), see Fig. 3).

$$\sigma_R = E_{c1}\varepsilon_R \text{ if } \varepsilon_R \le \varepsilon_{cy} \tag{26a}$$

$$\sigma_R = f_{cy} + E_{c2}(\varepsilon_R - \varepsilon_{cy}) \text{ if } \varepsilon_{cy} < \varepsilon_R \le \varepsilon_{cpk} \tag{26b}$$

$$\sigma_R = f_{cpk} + E_{c3}(\varepsilon_R - \varepsilon_{cpk}) \text{ if } \varepsilon_R > \varepsilon_{cpk} \tag{26c}$$

$$\varepsilon_{cy} = 0.0005 \tag{27}$$

$$f_{cy} = 0.4FF \cdot CF\sqrt{f_c^{'}(\text{MPa})} \tag{28}$$

$$\varepsilon_{cpk} = 0.01 - \varepsilon_{P,i} \tag{29}$$

$$f_{cpk} = (0.2FF + 12\rho_l)\sqrt{f_c^{'}(\text{MPa})} \tag{30}$$

$$E_{c1} = \frac{f_{cy}}{\varepsilon_{cy}} \tag{31}$$

$$E_{c2} = \frac{f_{cpk} - f_{cy}}{\varepsilon_{cpk} - \varepsilon_{cy}} \tag{32}$$

$$E_{c3} = \frac{-f_{cpk}}{\varepsilon_{\max} - \varepsilon_{cpk}} \tag{33}$$

$$\varepsilon_{\max} = 0.04 - \varepsilon_{P,i} \tag{34}$$

In the previous equations, the meaning of the parameters are the following ones: f_{cy} is the effective "yield" stress of SFC for proportional loading, ε_{cy} is the yield strain corresponding to f_{cy}, CF is an additional correction factor to account for the confinement effect due to prestress tendons ($CF = 1$ for tensile SFC volume confined or sandwiched by two or more layers of tendons; $CF = 0.5$ for tensile SFC volume unconfined by tendons - only one layer of tendons exists), f_{cpk} is the peak stress of SFC, ε_{cpk} is the strain corresponding to f_{cpk}, $\varepsilon_{\max}$ is the maximum strain of SFC, $\varepsilon_{P,i}$ is initial tensile strain in the prestress reinforcement (see Eq. (41)), ρ_l is the longitudinal steel ratio (see footnote in Table 1), E_{c1} is the Young's modulus of SFC before cracking, E_{c2} is the modulus of SFC just after cracking and E_{c3} is the extended modulus of SFC.

2.3.3. Mild steel bars in tension

For mild steel bars in tension embedded in concrete, the same smeared σ - ε relationship used and justified by the authors in previous studies [53,54] was also adopted here. This smeared bilinear σ - ε relationship was proposed by Pang and Hsu in 1995 [38] (see Eq. (35)-(38) and Fig. 3). In order to account for the SF reinforcement, the tensile stress after yielding is modified trough correction factors incorporating the fiber factor FF from Eq. (25). In addition, in Eq. (38) the tensile strength f_{cr} for plain concrete in the original equations is substituted by the effective "yield" stress (Eq. (28)) for SFC.

$$f_S = E_S\varepsilon_S \text{ if } \varepsilon_S \le \varepsilon_y^{'} \tag{35a}$$

$$f_S = (1 - 0.096FF)(0.91 - 2BN)f_{Sy} + (0.2FF + 1)(0.02 + 0.25BN)E_S\varepsilon_S \text{ if } \varepsilon_S > \varepsilon_y^{'} \tag{35b}$$

$$\varepsilon_y^{'} = \frac{f_y^{'}}{E_S} \tag{36}$$

$$f_y^{'} = (0.93 - 2BN)f_{Sy} \tag{37}$$

$$BN = \frac{1}{\rho}\left(\frac{f_{cy}}{f_{Sy}}\right)^{1.5} \quad (\rho \ge 0.15\%) \tag{38}$$

In Eq. (35)-(38), f_S and ε_S are the average tensile stress and strain in the mild steel bars, respectively, f_{Sy} is the yielding stress and E_S is the Young's modulus for mild steel.

2.3.4. Prestress steel bars in tension

As previously referred, the efficient RA-STM procedure starts after concrete decompression. Hence, as for the previous version of the model for PC membrane elements [53], the strain in the prestress reinforcement, ε_P, is computed as follows,

$$\varepsilon_P = \varepsilon_{dec} + \varepsilon_S \tag{39}$$

$$\varepsilon_{dec} = \varepsilon_{P,i} + \varepsilon_{S,i} \tag{40}$$

$$\varepsilon_{P,i} = \frac{f_{P,i}}{E_P} \tag{41}$$

$$\varepsilon_{S,i} = \frac{A_P f_{P,i}}{A_S(E_S - E_c) + E_c(A_c - A_P)} \tag{42}$$

In the previous equations, ε_{dec} is the strain at decompression, ε_S is the strain in the mild steel reinforcement (at decompression $\varepsilon_S = 0$), $\varepsilon_{P,i}$ is the initial tensile strain in the prestress steel bars due to prestress, $\varepsilon_{S,i}$ is the initial compressive strain in the mild steel reinforcement due to prestress, E_P is the Young's modulus for prestress steel, A_P and A_S are the total area of prestress and mild steel, respectively, and A_c is the area of the SF concrete cross section.

For prestress steel bars in tension embedded in concrete, the same smeared σ - ε relationship used and justified by the authors in a previous study [53] was also adopted here. The used σ - ε relationship is a corrected version of the one proposed by Hsu in 1991 [56] (see Fig. 3), which was based on the Ramberg-Osgood's curve. According to Hoffman in 2010 [55], there is no need to modify this relationship in order to account for the influence of the steel fiber reinforcement.

$$f_P = E_P(\varepsilon_{dec} + \varepsilon_S) \;\text{ if }\; \varepsilon_P \leq \varepsilon_{P0.7f_{Pu}} \tag{43a}$$

$$f_P = \frac{E_p^{'}(\varepsilon_{dec} + \varepsilon_S - \Delta\varepsilon_P)}{\left[1 + \left(\frac{E_p^{'}(\varepsilon_{dec} + \varepsilon_S - \Delta\varepsilon_P)}{f_{Pu}}\right)^R\right]^{1/R}} \;\text{ if }\; \varepsilon_P > \varepsilon_{P0.7f_{Pu}} \tag{43b}$$

In Eq. (43), $E_p^{'}$ is the Young's modulus of Ramberg-Osgood, R is a geometrical parameter to adjust the shape of the curve, f_{Pu} is the tensile strength of the prestress steel and $\varepsilon_{P0.7f_{Pu}}$ is the strain of prestress steel corresponding to $0.7f_{Pu}$. Both parameters $E_p^{'}$ and R need to be evaluated experimentally from uniaxial tensile tests. The adopted values in this study were obtained by Laskar et al., in 2007 [47] for PC membrane elements with similar tendons: $E_p^{'} = 209$ GPa and $R = 5$.

As explained by the authors in a previous study [53], the strain variation $\Delta\varepsilon_P$ aims to translate horizontally by a very small amount the original nonlinear curve to impose the continuity with the initial linear curve (see Fig. 3). This correction showed to be necessary to avoid convergence problems at the transition zone. The strain variation $\Delta\varepsilon_P$ is computed as follows:

$$\Delta\varepsilon_P = \varepsilon^{L}_{P0.7f_{Pu}} - \varepsilon^{NL}_{P0.7f_{Pu}} \tag{44}$$

$$\varepsilon^{L}_{P0.7f_{Pu}} = \frac{0.7f_{Pu}}{E_P} \tag{45}$$

$$0.7f_{Pu} = \frac{E_P^{'}\,\varepsilon^{NL}_{P0.7f_{Pu}}}{\left[1 + \left(\frac{E_P^{'}\,\varepsilon^{NL}_{P0.7f_{Pu}}}{f_{Pu}}\right)^R\right]^{1/R}} \rightarrow \varepsilon^{NL}_{P0.7f_{Pu}} \tag{46}$$

In the previous equations, $\varepsilon^{L}_{P0.7f_{Pu}}$ and $\varepsilon^{NL}_{P0.7f_{Pu}}$ are the strains corresponding to $0.7f_{Pu}$ computed from the linear (L) and nonlinear (NL) part of the $\sigma - \varepsilon$ relationship, respectively. The strain $\varepsilon^{NL}_{P0.7f_{Pu}}$ is computed by solving a nonlinear equation (Eq. (46)).

2.4. *Algorithm to implement the efficient RA-STM procedure*

The flowchart with the used algorithm to implement the efficient RA-STM procedure for PSFC membrane elements (or "efficient RA-STM PSFC procedure") is presented in Fig. 4. The structure of the algorithm is similar to the one presented by the authors for RC and PC membrane elements [53,54].

The calculation procedure can be described as follows. First, some initial data related with the material properties, the loading condition and the path's increment $\Delta\varepsilon_D$ for the strain ε_D must be introduced by the user to start the calculation procedure. Next, for the first introduced value ε_D^0 and by solving Eq. (16) for α_D, the initial stress and deformation state of the membrane element is estimated. Then, the initial estimates for the strains ε_D^1, ε_L^0 and ε_T^0 are computed and the first solution point is obtained (corresponding to index $k = 1$).

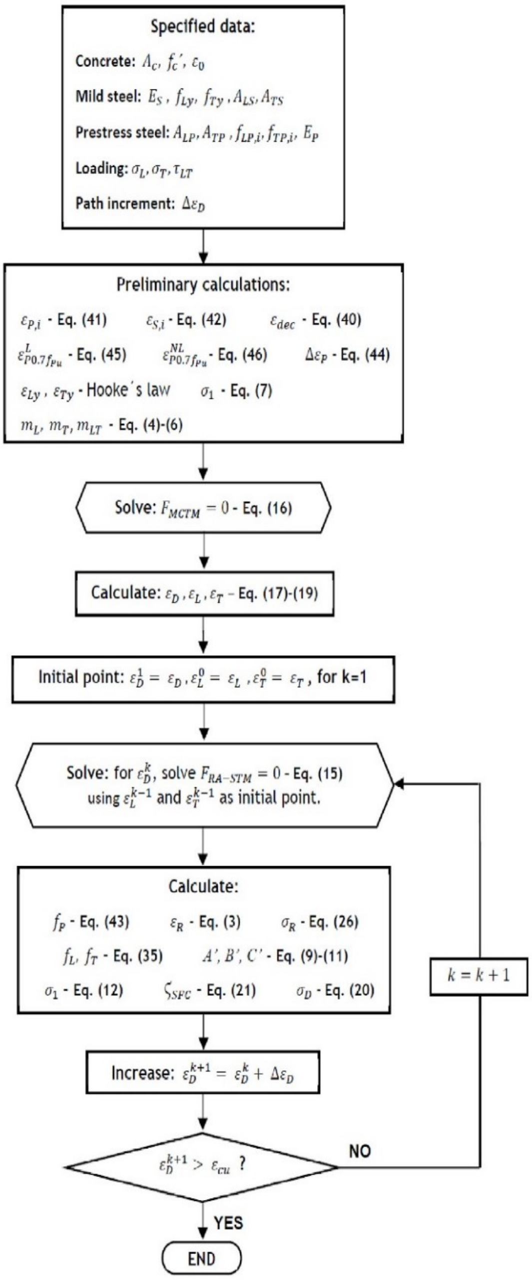

Fig. 4. Flowchart of the algorithm.

After the previous initial calculation, all the remaining solution points are computed from the efficient RA-STM PSFC procedure. In each step, the strainε_D is incremented by $\Delta\varepsilon_D$ ($\varepsilon_D^{k+1} = \varepsilon_D^k + \Delta\varepsilon_D$) and the new stress and deformation state of the membrane element is sequentially computed by solving Eq. (15) for ε_L and ε_T. For each step, the initial point is considered to be the solution point from the previous step. The calculation procedure holds until the conventional value specified by the user for SFC in compression (ε_{cu}) is reached ($\varepsilon_D^{k+1} \geq \varepsilon_{cu}$). It should be noted that the efficient RA-STM PSFC procedure is a smeared truss model. Therefore, only failure modes which can be inferred from the average response of the materials can be predicted. Specific local failure modes, such as the loss of bridging effect of the steel fibers across the tensile cracks, or even the tensile failure of the steel fibers, are not captured by the model.

The algorithm for the efficient RA-STM PSFC procedure was implemented with software MATLAB [57]. The function *lsqnonlin* was used to solve numerically both Eq. (15) and Eq. (16) with the least squares method.

3. Validation of the efficient RA-STM PSFC procedure

In this section, the predictions from the efficient RA-STM PSFC procedure are checked against some experimental results found in the literature. As referred in the introduction of Section 2.3, Hoffman in 2010 [55] was the only author found in the literature who reported experimental results related with PSFC panels under in-plane stresses, namely the ones tested with the Universal Panel Tester at the University of Houston. Two series of PSFC panels were tested according to the angle of tendons α_2 with respect to the applied principal stresses (see Fig. 2): series TEF and series TAF.

Series TEF consisted of five PSFC panels with $\alpha_2 = 90^\circ$ under sequential and biaxial compression-tension loading. These panels were specifically designed and tested to study the constitutive relationships of the materials. These experimental results were not used in this study to check the efficient RA-STM PSFC procedure because the model assumes proportional loading, which commonly constitutes the loading type in practice.

Series TAF consisted of five PSFC panels with $\alpha_2 = 45^\circ$ under proportional loading and symmetrical biaxial stresses in the 1–2 coordinate system ($\sigma_2 = -\sigma_1$), with tendons oriented at $\alpha_2 = 45^\circ$ (see Fig. 5). Hence, these panels were tested under pure shear in the L-T coordinate system ($\sigma_L = \sigma_T = 0$, see Fig. 1). All PSFC panels have 139.8 × 139.8 × 17.8 cm size and prestress was only applied in the longitudinal direction of the L-T coordinate system (with no longitudinal mild reinforcement). Two variables were studied: (1) the percentage of prestressing tendons in the longitudinal direction (ρ_{LP}), and (2) the steel fiber factor (*FF*). The experimental results from TAF panels were used to check the efficient RA-STM PSFC procedure.

Table 1 summarizes the properties of the five reference PSFC panels from series TAF. Except for $f_{cP,i}$, which represents the initial SFC compressive stress due to prestress in the longitudinal direction, all parameters were already defined in the previous sections. Panels TAF-1 to TAF-4 had two layers of tendons, while panel TAF-5 has only one layer of tendons located at the middle plane.

The efficient RA-STM PSFC procedure was used to compute the behavior of each of the five PSFC panels from series TAF. In Fig. 6 and for each panel, the theoretical shear stress (τ_{LT}) – shear strain (γ_{LT}) curves from the efficient RA-STM PSFC procedure ("eff. RA-STM") are compared with the experimental ones ("Exp.") reported by Hoffman in 2010 [55]. For comparison, the graphs in Fig. 6 also include the theoretical curves reported by Hoffman in 2010 [55] and computed from the softened membrane model extended for PSFC panels ("SMM-PSFC"). For this study, both "Exp." and "SMM-PSFC" $\tau_{LT} - \gamma_{LT}$ curves were carefully drawn from the graphs presented by Hoffman in 2010 [55].

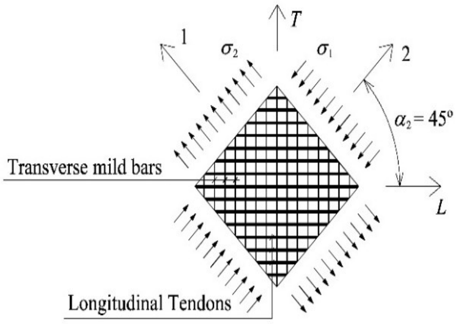

Fig. 5. TAF panels [55]: loading condition and reinforcement.

Fig. 6 shows that, in general, the full behavior of the tested panels is well captured by the efficient RA-STM PSFC procedure, including the transition between the different behavioral stages of the panels. Fig. 6 also shows that the theoretical curves from the efficient RA-STM PSFC procedure are generally in good agreement with the ones from the SMM-PSFC model, at least until the maximum shear stress is reached. As referred in the introduction section, the SMM incorporates the Poisson's effect after cracking. For this reason, and as explained by Zhu and Hsu in 2002 [43], for the SMM the descending branch after the peak load is less steep and longer than the one predicted by the RA-STM. However, Fig. 6 shows that for some of the Panels (TAF-1, TAF-3 and TAF-4) the descending branch after the peak load predicted by the efficient RA-STM PSFC procedure agrees better with the experimental curve. For Panel TAF-3, the experimental curve seems to show a premature loss of the maximum shear stress when compared with the theoretical ones. Hoffman in 2010 [55] reported that both panels TAF-1 and TAF-3 suffered a shear slide failure influenced by the local corner failure. Since such local effect was not considered by the theoretical smeared models, this could explain the observed deviation between the curves for panel TAF-3. In general, Fig. 6 shows that the efficient RA-STM PSFC procedure can be considered a reliable model, in spite to be a simpler model when compared with the SMM.

Table 2 presents, for each TAF panel, the experimental and theoretical values for some key values of the $\tau_{LT} - \gamma_{LT}$ curves, namely: the cracking shear stress ($\tau_{cr,exp}$, $\tau_{cr,th}^{\text{RA-STM}}$ and $\tau_{cr,th}^{\text{SMM}}$), the peak shear stress or ultimate value ($\tau_{u,exp}$, $\tau_{u,th}^{\text{RA-STM}}$ and $\tau_{u,th}^{\text{SMM}}$) and the corresponding shear strain ($\gamma_{u,exp}$, $\gamma_{u,th}^{\text{RA-STM}}$ and $\gamma_{u,th}^{\text{SMM}}$). The ratios of the experimental to the theoretical values are also presented ($\tau_{cr,exp}$, $\tau_{cr,th}^{\text{RA-STM}}$, $\tau_{cr,exp}/\tau_{cr,th}^{\text{SMM}}$, $\tau_{u,exp}/\tau_{u,th}^{\text{RA-STM}}$, $\tau_{u,exp}/\tau_{u,th}^{\text{SMM}}$, and $\gamma_{u,exp}/\gamma_{u,th}^{\text{SMM}}$). Although only five panels were studied, Table 2 also presents the values for the mean ($\overline{x}$), standard deviation (*s*) and coefficient of variation (*cv*) for the ratios. All the key values for both "Exp." and "SMM-PSFC" $\tau_{LT} - \gamma_{LT}$ curves were obtained approximatively from the graphs drawn in Fig. 6. Because of this, it was not possible to obtain accurate values for the shear strain corresponding to the cracking shear stress. In such part of the graphs the shear strains are still very small and very difficult to read.

Table 2 shows that the efficient RA-STM PSFC procedure was able to predict well, and generally on the safety side, the cracking shear stress τ_{cr} ($\overline{x} = 0.906$) and with a very low degree of dispersion ($cv = 2.93\%$), as for the SMM-PSFC with a somewhat higher degree of dispersion ($\overline{x} = 0.981$ and $cv = 11.28\%$). Both theoretical models also predicted well the ultimate shear stress τ_u, although the predictions from the efficient RA-STM PSFC procedure seemed to be slightly better ($\overline{x} = 0.973$ and $cv = 4.64\%$) than the ones from the SMM-PSFC ($\overline{x} = 0.927$ and $cv = 3.41\%$). For the ultimate shear strain γ_u, Table 2 shows that both theoretical models had difficulty to predict well this parameter, with a degree of dispersion very high. The results of the SMM-PSFC ($\overline{x} = 0.486$ and $cv = 79.11\%$) are a little worse that the ones from the efficient RA-STM PSFC procedure ($\overline{x} = 0.853$ and $cv = 62.91\%$) because for some panels the corresponding theoretical $\tau_{LT} - \gamma_{LT}$ curve is too much extended in the ultimate stage (see Fig. 6). As observed in previous studies with RC and PC membrane elements [43,47,53,54], smeared approaches show difficulties to predict well the deformation corresponding to the peak load. However, as also referred in such studies, this parameter is generally not an important key value for design.

Again, the results from Table 2 show that the efficient RA-STM PSFC procedure can be considered a reliable model. To help sustain this, Fig. 7 shows the same theoretical and experimental $\tau_{LT} - \gamma_{LT}$ curves from Fig. 6 for some of the panels from series TAF. In addition, each graph includes the theoretical and experimental $\tau_{LT} - \gamma_{LT}$ curves of similar PC panels from series TA tested at the same loading conditions by Laskar et al., in 2007 [47], also at the University of Houston. The main difference

Table 1
Properties of PSFC panels from series TAF [55].

Panel	f_c' MPa	ε_0 %	ρ_{LP}[a] %	ρ_T[a] %	f_{Pu} MPa	E_P GPa	E_S GPa	f_{Ty} MPa	$f_{cP,i}$ MPa	$f_{P,i}$ MPa	L_f/D_f	V_f %	FF
TAF-1	37.6	0.21	0.84	0.42	1862	200	197	414	8.3	986	55	0.5	0.28
TAF-2	44.0	0.17	0.84	0.77	1862	200	192	415	8.3	794	55	1.0	0.55
TAF-3	38.1	0.22	0.84	0.42	1862	200	197	414	8.3	794	55	1.5	0.83
TAF-4	56.4	0.19	0.59	0.42	1862	200	197	414	5.8	983	80	1.0	0.80
TAF-5	33.1	0.20	0.42	0.77	1862	200	192	415	4.1	986	80	1.5	1.20

[a] $\rho_{LP} = A_{LP}/A_c$; $\rho_T = A_{TS}/A_c$

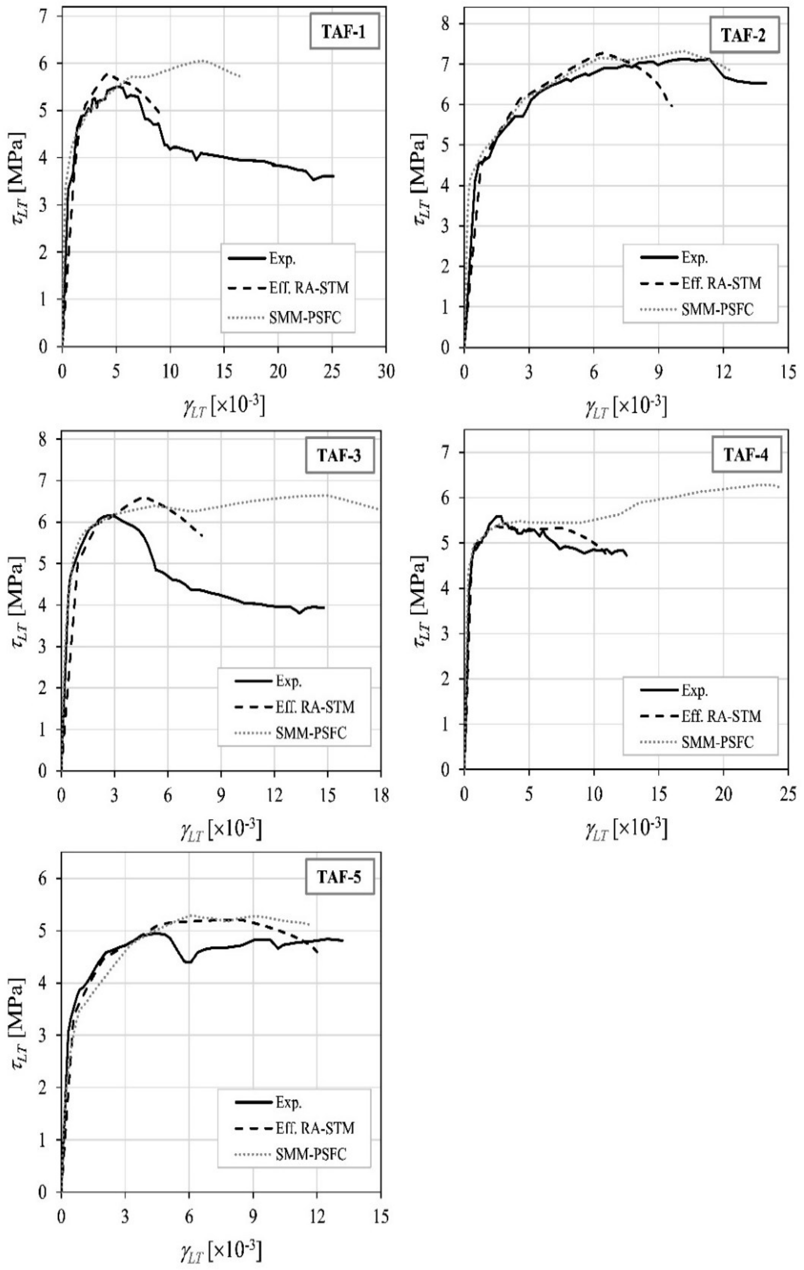

Fig. 6. $\tau_{LT} - \gamma_{LT}$ curves for panels from series TAF.

between TAF and TA panels in each graph is the inclusion of steel fiber reinforcement for the first ones. The theoretical curves presented for the TA panels were computed from a previous version of the efficient RA-STM procedure for PC membrane elements [53]. The aim is to check if, for each pair of TAF and TA panels, the efficient RA-STM PSFC procedure predicts well the effect of the steel fiber reinforcement when compared to similar PC panel without fiber reinforcement.

Fig. 7 shows that, except for Panels TA1 and TAF-1 for which no

Table 2
Comparative analysis of key values.

Panel	$\tau_{cr,exp}$ MPa	$\tau_{cr,th}^{RA-STM}$ MPa	$\frac{\tau_{cr,exp}}{\tau_{cr,th}^{RA-STM}}$	$\tau_{cr,th}^{SMM}$ MPa	$\frac{\tau_{cr,exp}}{\tau_{cr,th}^{SMM}}$	$\tau_{u,exp}$ MPa	$\tau_{u,th}^{RA-STM}$ MPa	$\frac{\tau_{u,exp}}{\tau_{u,th}^{RA-STM}}$	$\tau_{u,th}^{SMM}$ MPa	$\frac{\tau_{u,exp}}{\tau_{u,th}^{SMM}}$	$\gamma_{u,exp}$ $\times 10^{-3}$	$\gamma_{u,th}^{RA-STM}$ $\times 10^{-3}$	$\frac{\gamma_{u,exp}}{\gamma_{u,th}^{RA-STM}}$	$\gamma_{u,th}^{SMM}$ $\times 10^{-3}$	$\frac{\gamma_{u,exp}}{\gamma_{u,th}^{SMM}}$
TAF-1	3.33	3.62	0.92	3.39	0.98	5.51	5.77	0.95	6.05	0.91	5.10	4.23	1.21	13.01	0.39
TAF-2	4.10	4.41	0.93	4.21	0.97	7.13	7.27	0.98	7.33	0.97	10.33	6.41	1.61	10.13	1.02
TAF-3	4.41	4.94	0.89	3.79	1.16	6.16	6.60	0.93	6.65	0.93	2.70	4.69	0.58	14.96	0.18
TAF-4	3.96	4.58	0.87	4.38	0.90	5.58	5.33	1.05	6.29	0.89	2.48	7.46	0.33	23.29	0.11
TAF-5	3.06	3.31	0.93	3.47	0.88	4.94	5.21	0.95	5.29	0.94	4.42	8.24	0.54	6.05	0.73
		$x =$	0.906		0.981			0.973		0.927			0.853		0.486
		$s -$	0.027		0.111			0.045		0.032			0.536		0.384
		$cv =$	2.93%		11.28%			4.64%		3.41%			62.91%		79.11%

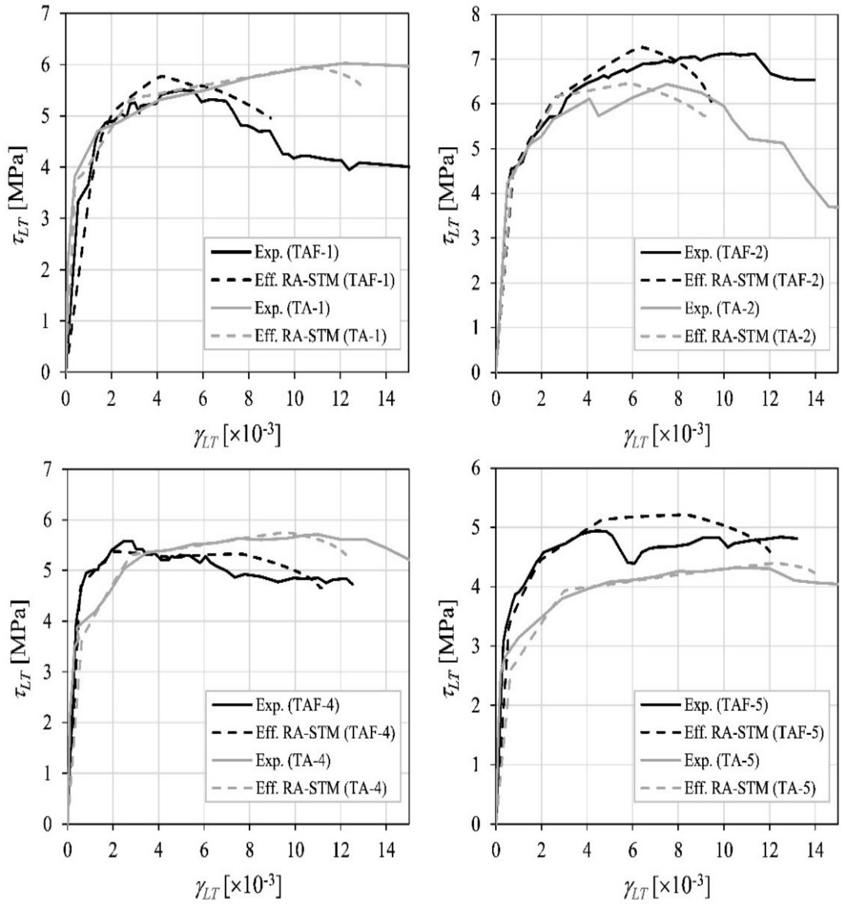

Fig. 7. Comparison between similar PC and PSFC panels.

noticeable effect is visualized due to the incorporation of the steel fiber reinforcement (probably because the fiber volume for panel TAF-1 is only 0.5%), for the remaining corresponding TA and TAF panels the efficient RA-STM PSFC procedure is able to predict the positive effects of the steel fiber reinforcement after cracking. Such effects are related with the tendency to increase the post-cracking tensile performance, namely the increase of the cracking shear stress, the peak shear stress, the stiffness and the toughness.

Finally, Fig. 8 presents some examples of additional behavioral curves for panel TAF-5 as example, namely the $\sigma_D - \varepsilon_D$, $\sigma_R - \varepsilon_R$, $f_T - \varepsilon_T$ and $f_{PL} - \varepsilon_{PL}$ curves. Only theoretical curves are presented since no experimental ones were reported by Hoffman in 2010 [55] for panels from series TAF. Fig. 8 shows that, in general, the theoretical curves show the expected shapes. The $f_{PL} - \varepsilon_{PL}$ curve do not starts from zero because the efficient RA-STM PSFC procedure only starts the calculations after concrete decompression, as referred before.

4. Conclusions

In this article, the efficient RA-STM procedure previously proposed and validated by the authors for RC and PC membrane elements was extended to PSFC membrane elements. The extended model was called efficient RA-STM PSFC procedure. For this, the smeared nonlinear $\sigma - \varepsilon$ relationships for the materials were modified to account for the influence of the steel fiber reinforcement. In addition, a new smeared nonlinear $\sigma - \varepsilon$ relationship for SFC in tension was incorporated. After being implemented in a computer with MATLAB software, the model was checked against some experimental results related with PSFC panels under shear and also with the predictions from another smeared model (SMM-PSFC). The following conclusions can be drawn:

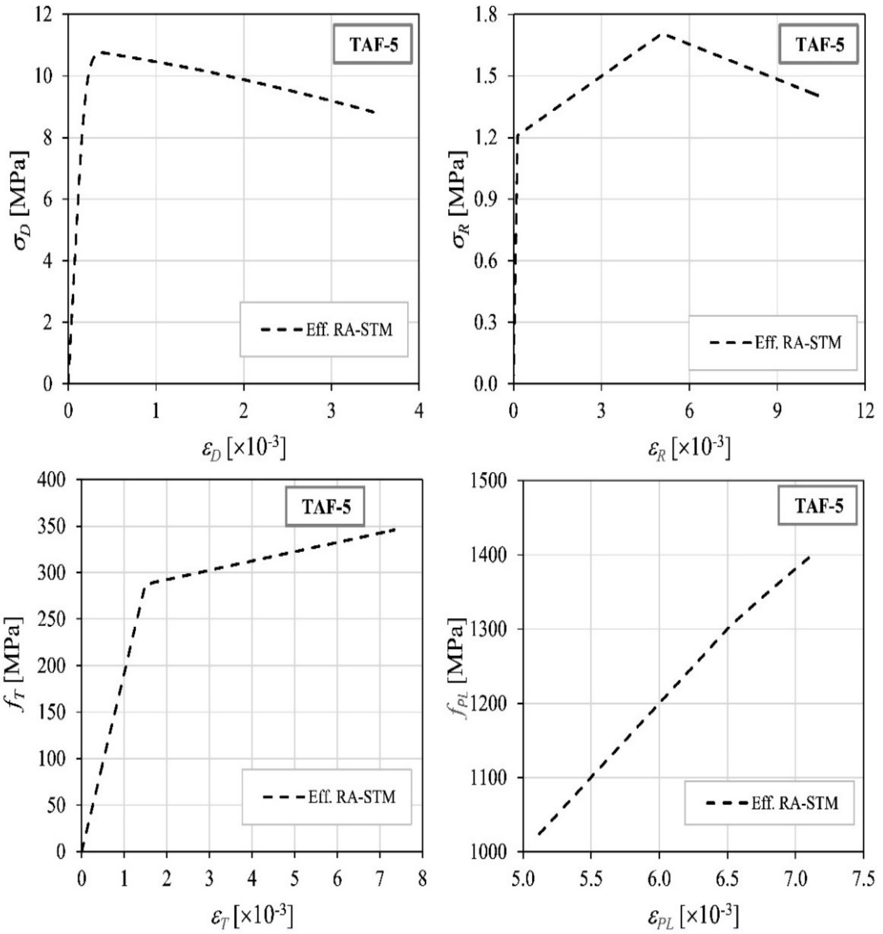

Fig. 8. Additional behavioral curves for Panel TAF-5.

- When compared with the experimental results from some PSFC panels tested under shear until failure, the efficient RA-STM PSFC procedure has proven to be a reliable model and to predict well the full response of the panels;
- In particular, the efficient RA-STM PSFC procedure provided good predictions for the cracking and peak shear stresses of the PSFC panels;
- When the predictions of the model were compared to the experimental results of similar PC and PSFC panels under shear, the efficient RA-STM PSFC procedure showed to be able to capture the positive influence of the steel fiber reinforcement, namely to increase the post-cracking tensile performance of the panels;
- The efficient RA-STM-PSFC procedure also showed to provide solutions with high numerical efficiency and stability. The numerical results were obtained in few seconds with a current computer.

In this study, the efficient RA-STM-PSFC procedure was checked against the experimental results of only five PSFC panels under in-plane stresses, whose results were found in the literature. Additional experimental results are of great need in order to better check and calibrate theoretical models, such as the one proposed in this study.

Finally, it should be referred that for engineering practice, the efficient RA-STM PSFC procedure, as presented in this article, is limited to the study of the local behavior of PSFC wall-type structures, such as parts of shear walls or webs of shear beam with uniform in-plane loading and reinforcement layout. In addition, in the present form, the efficient RA-STM PSFC procedure can only incorporates the effect of in-plane stress condition. For a wider application, the proposed model can be used to develop a RA-STM PSFC-based shell element to be implemented in a non-linear finite element analysis program. This development can be based on the degenerated shell theory with a layered approach and taking into account the RA-STM PSFC to define constitutive relation modules and the analysis procedure. With this approach, the effect of out-of-plane stress condition can be considered and the global behavior of PSFC wall-type or shell-type structures can be predicted. This approach was successively performed with the SMM [25] and also the CSMM (SMM extended for in-plane cyclic shear) for RC structures [58]. This further development constitutes one of the future goals of the authors.

Declaration of competing interest

The authors declare that they have no known competing financial interests or personal relationships that could have appeared to influence the work reported in this paper.

References

[1] Aci Committee 544, Design considerations for steel fiber reinforced concrete, ACI Struct. J. 85 (5) (1998) 563–580.
[2] fib Cep-Fip, Fibre-reinforced Concrete: from Design to Structural Applications - FRC 2014: ACI-Fib International Workshop, International Federation for Structural Concrete, Lausanne, Switzerland, 2016. FIB BULLETIN NO. 79.(fib).
[3] L.A. Traina, S.A. Mansour, Biaxial strength and deformational behavior of plain and steel fiber concrete, ACI Mater. J. 88 (4) (1991) 353–362.
[4] J. Thomas, A. Ramaswamy, Mechanical properties of steel fiber-reinforced concrete, J. Mater. Civ. Eng. ASCE 19 (5) (2007).

[5] S.-C. Lee, J.-Y. Cho, F.J. Vecchio, Diverse embedment model or steel fiber-reinforced concrete in tension: model development, ACI Mater. J. 108 (5) (2011) 516–525.

[6] S.-C. Lee, J.-Y. Cho, F.J. Vecchio, Diverse embedment model or steel fiber-reinforced concrete in tension: model verification, ACI Mater. J. 108 (5) (2011) 526–535.

[7] S.-C. Lee, J.-Y. Cho, F.J. Vecchio, Simplified diverse embedment model for steel fiber- reinforced concrete elements in tension, ACI Mater. J. 110 (4) (2013) 403–412.

[8] S.-C. Lee, J.-Y. Cho, F.J. Vecchio, Tension-stiffening model for steel fiber-reinforced concrete containing conventional reinforcement, ACI Struct. J. 110 (4) (2013) 639–648.

[9] X.D. Hu, R. Day, P. Dux, Biaxial failure model for fiber reinforced concrete, J. Mater. Civ. Eng. ASCE 15 (6) (2003).

[10] K.S. Kim, D.H. Lee, J. Hwang, D.A. Kuchma, Shear behavior model for steel fiber-reinforced concrete members without transverse reinforcements, Compos. B Eng. 43 (2012) 2324–2334.

[11] Y.K. Kwak, M.O. Eberhard, W.S. Kim, J. Kim, Shear strength of steel fiber reinforced concrete beams without stirrups, ACI Struct. J. 99 (2012) 530–538.

[12] F. Minelli, F.J. Vecchio, Compression field modeling of fiber- reinforced concrete members under shear loading, ACI Struct. J. 103 (2) (2006) 244–252.

[13] A.M. Bernat, N. Spinella, A. Recupero, A. Cladera, Mechanical model for the shear strength of steel fiber reinforced concrete (SFRC) beams without stirrups, Mater. Struct. 53 (28) (2020) 20.

[14] N. Spinella, P. Colajanni, A. Recupero, Simple plastic model for shear critical SFRC beams, J. Struct. Eng. 136 (2010) 390–400.

[15] Spinella N Shear strength of full-scale steel fibre reinforced concrete beams without stirrups, Comput. Concr. 11 (2013) 365–382.

[16] N. Spinella, P. Colajanni, L. La Mendola, Nonlinear analysis of beams reinforced in shear with stirrups and steel fibers, ACI Struct. J. 109 (2012) 53–64.

[17] P. Colajanni, A. Recupero, N. Spinella, Generalization of shear truss model to the case of SFRC beams with stirrups, Comput. Concr. 9 (2012) 227–244.

[18] J. Susetyo, P. Gauvreau, F.J. Vecchio, Effectiveness of steel fiber as minimum shear reinforcement, ACI Struct. J. 108 (4) (2011) 488–496.

[19] H.B. Dhonde, Y.L. Mo, T.C. Hsu, Fiber Reinforcement in Prestressed Concrete Beams, Texas Department of Transportation, 2006. Report 0-4819, March.

[20] T.P. Rao, N.S. Hoffman, T.C. Hsu, Y.L. Mo, J. Vogel, Steel Fiber Replacement of Mild Steel in Prestressed Concrete Beams, Texas Department of Transportation, 2010. Report FHWA/TX-09/0-5255-2, October.

[21] J.H. Hwang, D.H. Lee, H. Ju, K.S. Kim, S.Y. Seo, J.W. Kang, Shear behavior models of steel fiber reinforced concrete beams modifying softened truss model approaches, Materials 6 (2013) 4847–4867.

[22] H. Ju, D.H. Lee, J.H. Hwang, J.W. Kang, K.S. Kim, Y.H. Oh, Torsional behavior model of steel fiber-reinforced concrete members modifying fixed-angle softened-truss model, Compos. B Eng. 45 (2013) 215–231.

[23] D.H. Lee, J.H. Hwang, H. Ju, K.S. Kim, D.A. Kuchma, Nonlinear finite element analysis of steel fiber-reinforced concrete members using direct tension force transfer model, Finite Elem. Anal. Des. 50 (2012) 266–286.

[24] A.A. Pisano, P. Fuschi, D. De Domenico, Peak loads and failure modes of steel-reinforced concrete beams: predictions by limit analysis, Eng. Struct. 56 (2013) 477–488.

[25] T.T.C. Hsu, Y.L. Mo, Unified Theory of Concrete Structures, Wiley, 2010.

[26] J.R. Robinson, J.M. Demorieux, Essais de Traction-Compression sur Modèles d'Âme de Poutre en Béton Armé. IRABA Report, Part 1, June, Institut de Recherches Appliquées du Béton Armé, 1968, p. 44 (in French).

[27] F. Vecchio, M.P. Collins, Stress-strain Characteristic of Reinforced Concrete in Pure Shear. IABSE Colloquium, Advanced Mechanics of Reinforced Concrete, Delft, Final Report, International Association of Bridge and Structural Engineering, Zurich, Switzerland, 1981, pp. 221–225.

[28] F.J. Vecchio, M.P. Collins, Response of Reinforced Concrete to in Plane Shear and Normal Stresses, University of Toronto, Toronto, Canada, 1982. Report No.82-03.

[29] F.J. Vecchio, M.P. Collins, The modified compression-field theory for reinforced concrete elements subjected to shear, ACI J. 83 (2) (1986) 219–231.

[30] S. Balakrishnan, D.W. Murray, Prediction of R/C panels and deep beam behavior by NLFEA, J. Struct. Eng. ASCE 114 (10) (1988) 2323–2342.

[31] M.A. Crisfield, J. Wills, Analysis of R/C panels using different concrete models, J. Eng. Mech. ASCE 115 (3) (1989) 578–597.

[32] W. Kaufmann, P. Marti, Structural concrete: cracked membrane model, J. Struct. Eng. ASCE 124 (12) (1998) 1467–1475.

[33] F.J. Vecchio, Disturbed stress field model for reinforced concrete: formulation, J. Struct. Eng. ASCE 126 (9) (2000) 1070–1077.

[34] F.J. Vecchio, Disturbed stress field model for reinforced concrete: implementation, J. Struct. Eng. ASCE 127 (1) (2001) 12–20.

[35] T.T.C. Hsu, Stresses and crack angles in concrete membrane elements, J. Struct. Eng. ASCE 124 (12) (1998) 1476–1484.

[36] A. Belarbi, T.T.C. Hsu, Constitutive laws of concrete in tension and reinforcing bars stiffened by concrete, Struct. J. Am. Concr. Inst. 91 (4) (1994) 465–474.

[37] A. Belarbi, T.T.C. Hsu, Constitutive laws of softened concrete in biaxial tension-compression, Struct. J. Am. Concr. Inst. 92 (5) (1995) 562–573.

[38] X.B. Pang, T.T.C. Hsu, Behavior of reinforced concrete membrane elements in shear, Struct. J. Am. Concr. Inst. 92 (6) (1995) 665–679.

[39] X.B. Pang, T.T.C. Hsu, Fixed-Angle softened truss model for reinforced concrete, Struct. J. Am. Concr. Inst. 93 (2) (1996) 197–207.

[40] T.T.C. Hsu, L.X. Zhang, Nonlinear analysis of membrane elements by fixed-angle softened-truss model, Struct. J. Am. Concr. Inst. 94 (5) (1997) 483–492.

[41] L.X. Zhang, T.T.C. Hsu, Behavior and analysis of 100 MPa concrete membrane elements, J. Struct. Eng. ASCE 124 (1) (1998) 24–34.

[42] B. Belletti, R. Cerioni, I. Iori, Physical approach for reinforced-concrete (PARC) membrane elements, J. Struct. Eng. ASCE 127 (12) (2001) 1412–1426.

[43] T.T.C. Hsu, R.R.H. Zhu, Softened membrane model for reinforced concrete elements in shear, Struct. J. Am. Concr. Inst. 99 (4) (2002) 460–469.

[44] R.H. Zhu, T.T.C. Hsu, Poisson effect of reinforced concrete membrane elements, Struct. J. Am. Concr. Inst. 99 (5) (2002) 631–640.

[45] R.H. Zhu, T.T.C. Hsu, J.Y. Lee, Rational shear modulus for smeared crack analysis of reinforced concrete, Struct. J. Am. Concr. Inst. 98 (4) (2001) 443–450.

[46] P. Marti, J. Meyboom, Response of prestressed concrete elements to in-plane shear forces, ACI Struct. J. 89 (5) (1992) 503–514.

[47] A. Laskar, J. Wang, T.T.C. Hsu, Y.L. Mo, Rational Shear Provisions for AASHTO LRFD Specifications, University of Houston, 2007, p. 192. Technical Report.

[48] G.G. Greene, A. Belarbi, Model for reinforced concrete members under torsion, bending, and shear. I: theory, J. Eng. Mech. 135 (9) (2009) 961–969.

[49] J. Silva, B. Horowitz, L. Bernardo, Efficient analysis of beam sections using softened truss model, ACI Struct. J. 114 (3) (2017) 765–774.

[50] H.F. Wong, J.S. Kuang, Predicting shear strength of RC interior beam-column joints by modified rotating-angle softened-truss model, Comput. Struct. 133 (2014) 12–17.

[51] L.F.A. Bernardo, J.M.A. Andrade, N.C.G. Nunes, Generalized softened variable angle truss-model for reinforcement concrete beams under torsion, Mater. Struct. 48 (7) (2015) 2169–2193.

[52] T. Ji, A new algorithm for the rotating-angle, softened-truss model of reinforced concrete elements, Mag. Concr. Res. 57 (6) (2005) 353–360.

[53] L.F.A. Bernardo, B.M.V.C. Filho, B. Horowitz, Predicting the behavior of prestressed concrete membrane elements by refined rotating-angle softened-truss model with efficient solution procedure, Struct. Concr. 21 (2020) 934–948.

[54] L.F.A. Bernardo, B.M.V.C. Filho, B. Horowitz, Refinement of the rotating-angle softened truss model with efficient solution for RC membranes, Eng. Struct. 213 (2020) 110552, https://doi.org/10.1016/j.engstruct.2020.110552.

[55] N.S. Hoffman, Constitutive Relationships of Prestressed Steel Fiber Concrete Membrane Elements, Department of Civil and Environmental Engineering, University of Houston, 2010. Ph.D. Thesis.

[56] T.T.C. Hsu, Nonlinear analysis of membrane elements, Struct. J. Am. Concr. Inst. 88 (5) (1991) 552–561.

[57] MathWorks (2018) MATLAB_R2018a.

[58] C.H. Luu, Y.L. Mo, T.T.C. Hsu, Development of CSMM-based shell element for reinforced concrete structures, Eng. Struct. 132 (2017) 778–790.

Notation

A_c: Area of SF concrete cross section
A_{LP}: Area of longitudinal prestress steel reinforcement
A_P: Area of prestress steel reinforcement
A_S: Area of mild steel reinforcement
A_{TS}: Area of transverse mils steel reinforcement
CF: Correction factor to account for the confinement effect due to prestress tendons
D_f: Diameter of steel fiber
E_c: Young's modulus for SF concrete
E_{c1}: Young's modulus for SFC before cracking
E_{c2}: Modulus for SFC just after cracking
E_{c3}: Extended modulus for SFC
E_P: Young's modulus for prestress steel
E_P': Young's modulus of Ramberg-Osgood
E_S: Young's modulus for mild steel
FF: Fiber factor
F_{MCTM}: Residual function for the MCTM
$F_{RA-STM}^{(i)}$: Residual function i for the RA-STM
f: Normal stress in the steel reinforcement
f_c': Uniaxial compressive strength of SF concrete
$f_{cP,i}$: Initial compressive stress in SF concrete due to prestress
f_{cpk}: Peak stress of SF concrete
f_{cr}: Tensile strength of plain concrete
f_{cy}: Effective "yield" stress of SFC for proportional loading
f_L: Tensile stress in the longitudinal mild steel reinforcement
f_{LP}: Tensile stress in the longitudinal prestress steel reinforcement
$f_{LP,i}$: Initial tensile stress in the longitudinal prestress reinforcement due to prestress
$f_{LP0.1\%}$: Proportional conventional limit stress to 0.1% for the longitudinal prestress steel
f_{Ly}: Yielding stress of the longitudinal mild steel reinforcement
f_P: Tensile stress in the prestress steel reinforcement
$f_{P,i}$: Initial tensile stress in the prestress reinforcement due to prestress
f_{Pu}: Tensile strength of the prestress steel
f_S: Average tensile stress in the mild steel bars
f_{Sy}: Uniaxial yielding stress of the mild steel bars
f_T: Tensile stress in the transverse mild reinforcement
f_{TP}: Tensile stress in the transverse prestress steel reinforcement
$f_{TP,i}$: Initial tensile stress in the transverse prestress reinforcement due to prestress
$f_{TP0.1\%}$: Proportional conventional limit stress to 0.1% for the transverse prestress steel
f_{Ty}: Yielding stress of the transverse mild steel reinforcement
f_y': Yielding stress of the embedded mild steel bars
L_f: Length of steel fiber

m_L: Longitudinal proportionality coefficient
m_{LT}: Shear proportionality coefficient
m_T: Transverse proportionality coefficient
V_f: Percentual volume of steel fiber
W_f: Correction factor to account for the steel fiber reinforcement
α_2: Angle of the principal compressive stresses in the PSFC membrane element
α_D: Angle of the principal compressive stresses in the SFC membrane element
ε_0: Strain corresponding to the SF concrete compressive peak stress
ε_{cpk}: Strain corresponding to f_{cpk}
ε_{cu}: Ultimate strain for SF concrete in compression
ε_{cy}: Yield strain corresponding to f_{cy}
ε_D: Principal average compressive strain
ε_{dec}: Decompression strain
$\varepsilon_{\max}$: Maximum strain of SF concrete
ε_P: Strain in the prestress steel bars
$\varepsilon_{P0.7f_{Pu}}$: strain in the prestress steel corresponding to $0.7f_{Pu}$
$\varepsilon^{L}_{P0.7f_{Pu}}$: Strain corresponding to $0.7f_{Pu}$ in the linear (L) part of the $\sigma-\varepsilon$ curve
$\varepsilon^{NL}_{P0.7f_{Pu}}$: Strain corresponding to $0.7f_{Pu}$ in the nonlinear (NL) part of the $\sigma-\varepsilon$ curve
$\varepsilon_{P,i}$: Initial tensile strain in the prestress steel bars due to prestress
ε_L: Longitudinal average strain
ε_R: Principal average tensile strain
ε_S: Average strain in the mild steel bars
$\varepsilon_{S,i}$: Initial compressive strain in the mild steel bars due to prestress
ε_T: Transverse average strain
ε_{Ty}: Yielding strain of the transverse mild steel bars
γ_{LT}: Average shear strain
η: Ratio of the transverse to the longitudinal tensile strength of reinforcements
ζ: Softening coefficient
ζ_{SFC}: Softening coefficient for SF concrete
ρ: Reinforcement ratio
ρ_L: Longitudinal mild steel reinforcement ratio
ρ_{LP}: Longitudinal prestress steel reinforcement ratio
ρ_T: Transverse mils steel reinforcement ratio
ρ_{TP}: Transverse prestress steel reinforcement ratio
σ_1: Principal tensile stress d in the PSFC membrane element
σ_2: Principal compressive stress applied in the PSFC membrane element
σ_D: Principal compressive stress in the SFC membrane element
σ_L: Longitudinal normal stress applied in the PSFC membrane element
σ^c_L: Longitudinal normal stress in the SFC membrane element
σ_R: Principal tensile strain in the SFC membrane element
σ_T: Transverse normal stress applied in the PSFC membrane element
σ^c_T: Transverse normal stress in the SFC membrane element
τ_{LT}: Shear stress applied in the PSFC membrane element
τ^c_{LT}: Shear stress in the SFC membrane element

Capítulo 8

Conclusões e recomendações para trabalhos futuros.

1.Introdução

Este capítulo decreve as principais conclusões resultantes da investigacão apresentada nesta tese. Adicionalmente, apresenta alguns tópicos de pesquisa relacionados aos trabalhos desenvolvidos neste programa de doutoramento que podem ser abordados no futuro.

Conforme apresentado ao longo deste trabalho, pode-se concluir que os objetivos propostos para esta investigação foram plenamente alcançados e que estudos porvindouros são desejáveis e necessários para o contínuo avanço dos modelos de treliça plana com ângulo variável aplicados à análise estrutural.

2. Conclusões

O desenvolvimento do modelo refinado de campo de tensões proposto neste trabalho foi guiado pelo cumprimento dos objetivos aqui alviltrados. A nomenclatura do modelo foi adaptada às especificidades requeridas de cada aplicação contemplada, de modo a favorecer a identificação do procedimento de cálculo e sua respectiva utilização.

Relativamente a implementação de forma numericamente eficiente do modelo RA-STM modificados por Silva [1], Cerquido [2] e Lyrio [3] no MATLAB e a incorporação da influência do concreto submetido a tração, conforme aqui apresentadas nos Capítulo 4 e Capítulo 5 , e complementadas no Anexo I, Anexo II, Anexo III e Anexo IV, verificou-se que o Modelo de Treliça com Amolecimento e Ângulo Variável Eficiente (Eff. RA-STM) proposto neste trabalho, foi capaz de evidenciar o comportamento dos elementos estruturais analisados para estágios de baixo carregamento e a transição entre os estágios não fissurado e fissurado.

Adicionalmente, demonstrou a sua fiabilidade ao prever com aproximação satisfatória a tensão tangencial de fissuração, a rigidez ao cisalhamento no estado fissurado, a tensão de resistência ao cisalhamento e a deformação de cisalhamento correspondente. Para lograr esses objetivos, as equações do modelo RA-STM provenientes de estudos prévios [1-3] foram reformuladas de maneira a incorporar esta contribuição adicional e leis constitutivas apropriadas para concreto submetido a tração foram introduzidas [4], conforme apresentado no Capítulo 4 na subsecção 2.3 e no Capítulo 5 na subsecção 2.2.

As previsões oriundas do modelo proposto foram comparadas com sucesso a resultados experimentais relevantes encontrados na literatura [5-10]. Adicionalmente os novos procedimentos de cálculo foram apresentados, conforme consta no Capítulo 4 na secção 3 e no Capítulo 5 na subsecção 3.4. Constatou-se a facilidade de implementação computacional e o baixo esforço de cálculo, a resposta completa dos diferentes elementos estruturais estudados foi rapidamente calculada (tempo médio de processamento aproximadamente igual a 8-12 segundos).

Com relação a extensão da aplicabilidade do Eff. RA-STM de forma a incorporar previsões comportamentais de placas de concreto estrutural reforçadas com lâminas de FRP (*Fiber Reinforced Polymer*) aderidas externamente e submetidas a um estado plano de tensões, doravante denominado Eff. RA-STM FRP, conforme aqui arrazoada no Capítulo 6 e complementada no Anexo V e Anexo VI, certificou-se que o procedimento de cálculo proposto captura bem as características mais importantes da resposta das placas analisadas submetidas ao cisalhamento para todos os estágios de carregamento, ou seja, o cisalhamento máximo e a transição entre o estágio não fissurado e o estágio fissurado.

Para alcançar esse objetivo as equações de equilíbrio e as relações constitutivas dos materiais proveniente de estudos precedentes [7,11], foram modificadas de forma a incorporar a contribuição do reforço FRP, de acordo com as aclarações inclusas no Capítulo 6, nas subsecções 2.1 e 2.2. Cabe ainda referir que o novo procedimento de cálculo foi apresentado, de acordo com o Capítulo 6 na subsecção 2.4.4. Evidenciou-se a simplicidade analítica, facilidade de implementação computacional e celeridade na disponibilização dos resultados em oposição a modelos teóricos anteriores, como o SMM-FRP, que utiliza uma técnica de tentativa e erro e necessita de um grande número de estimativas iniciais.

A validação do Eff. RA-STM FRP ocorreu por análise comparativa com alguns resultados experimentais [12,13] e foi complementada com as previsões de outro modelo teórico, SMM-FRP [14], devido ao número limitado de resultados experimentais, desse modo o espectro comparativo foi ampliado.

Quanto a mais uma extensão da aplicabilidade do Eff. RA-STM, dessa vez para incorporar previsões comportamentais de placas de concreto estrutural que contenham fibras de aço em sua matriz de concreto (SFC - *Steel Fiber Concrete*), e que possam ser dotadas adicionalmente de armaduras protendidas submetidas ao estado plano de tensões, doravante denominado Eff. RA-STM SFC, em conformidade com as explanações contidas no Capítulo 7 e complementadas no Anexo VII e Anexo VII, constatou-se que o modelo teórico proposto foi capaz de evidenciar a resposta comportamental completa dos elementos estruturais estudados.

Adicionalmente, o Eff. RA-STM SFC mostrou ser capaz de capturar a influência positiva da utilização do SFC no aumento do desempenho de tração pós-fissuração das placas de concreto estrutural, como também forneceu boas previsões para as tensões de fissuração e cisalhamento máximo dos elementos estruturais analisados. Esse objetivo foi alcançado à partir da modificação das relações constitutivas dos materiais originárias de estudos anteriores [7,11] e dos Capítulos 4 e Capítulo 5 deste trabalho, e da inclusão de uma relação constitutiva para o SFC [15], conforme apresentado no Capítulo 7 na subsecção 2.3.

Os resultados numéricos fornecidos pelo referido modelo analítico foram confrontados a alguns resultados experimentais relacionados com placas PSFC submetidas ao cisalhamento [15], e também com as previsões de outro modelo teórico (SMM-PSFC) [15]. Adicionalmente o procedimento de cálculo proposto, apresentado no Capítulo 7 na subsecção 2.4, demonstrou sua capacidade ao fornecer os resultados numéricos em poucos segundos com um computador corrente.

Dessa maneira, pode-se concluir que o Eff. RA-STM mostrou-se um modelo teórico confiável, pois atestou a sua capacidade de previsão do comportamento global de elementos do tipo placa submetidos ao estado plano de tensões, que considera a influência do concreto a tração, outra tipologia de composição do concreto e a técnica de utilização de reforço estrutural abordada neste trabalho. Em adição, pode-se considerar bem sucedida a reformulação do procedimento de solução que atua com alta eficiência numérica e estabilidade computacional.

3. Recomendações para trabalhos futuros

Com fundamentos nas exposições discorridas ao longo deste trabalho e em direção ao sequente progresso dos métodos analíticos baseado nas treliças planas com ângulo variável, nomeadamente nas etapas de validação dos modelos teóricos e calibração das leis constitutivas dos materiais, considera-se de especial importância a abordagem e desenvolvimentos futuros dos seguintes tópicos:

- Executar uma vasta gama de ensaios, em condições controladas, de placas de concreto protendido submetidas a diferentes combinações de solicitações no seu plano;

- Realizar uma campanha de ensaios, em condições controladas, de placas de concreto estrutural reforçados com FRP sujeitas a diversas combinações de solicitações no seu plano;

- Efetuar de uma ampla gama de ensaios, em condições controladas, de placas de concreto com adição de PSFC, para melhor verificar e calibrar modelos teóricos, como o proposto neste estudo;

- Extender o campo de aplicação do Eff. RA-STM a placas sujeitas ao corte cíclico;

- Reformular o procedimento de cálculo do Eff. RA-STM tendo por base critérios energéticos com vista a aumentar ainda mais a eficiência computacional.

Referências Bibliográficas

[1] Silva, J. R. B. e Horowitz, B. (2015), “Procedimento Eficiente Para Estimar o Comportamento Carga-Deformação de Painéis de Concreto Armado Submetidos a Esforços de Membrana Usando o Modelo de Treliça com Amolecimento e Ângulo Variável”, CILAMCE 2015 – XXXVI Iberian Latin American Congresso on Computacional Methods in Engineering, Rio de Janeiro-RJ, Brasil.

[2] Bernardo, L. F .A, Cerquido, B. M. D, Silva, J. R .B and Horowitz, B. (2018), “Efficient refined rotating-angle softened truss model procedure to analyze reinforced concrete membrane elements”, Structural Concrete, 2018, pp. 1971-1982, Wiley Online Library.

[3] Bernardo, L. F. A, Lyrio, A. R. B, Silva, J. R. B and Horowitz, B. (2018), “Refined softened truss model with efficient solution procedure for prestressed concrete membranes”, Journal of Structural, 2018, ascelibrary.org.

[4] Belarbi, A. and Hsu, T. T. C. (1994), “Constitutive Laws of Concrete in Tension and Reinforcing Bars Stiffened by Concrete”, Structural Journal of the American Concrete Institute, Vol. 91, No. 4, pp. 465-474.

[5] Zhang, L. X. and Hsu, T. T. C. (1998), “Behavior and Analysis of 100Mpa Concrete Membrane Elements”, Journal of Structural Engineering, ASCE, Vol. 124, No. 1, Jan. 1998, pp. 24-34.

[6] Hsu T. T. C. and Zhu R. R. H. (2002), “Softened membrane model for reinforced concrete elements in shear”, Structural Journal of American Concrete Institute, Vol 99, No. 4, pp. 460–469.

[7] Pang, X. B. and Hsu, T. T. C. (1995), “Behavior of Reinforced Concrete Membrane Elements in Shear”, Structural Journal of the American Concrete Institute, Vol. 92, No. 6, pp. 665-679.

[8] Hsu T. T. C. and Zhang L. X. (1996), “Tension stiffening in reinforced concrete membrane elements”, Structural Journal of American Concrete Institute, Vol. 93, No.1, pp. 108–115.

[9] Laskar A, Wang J, Hsu T. T. C and Mo Y.L (2007), “Rational shear provisions for AASHTO LRFD specifications”, Technical Report, University of Houston, 192.

[10] Marti, P. and Meyboom, J. (1992), “ Response of Prestressed Concrete Elements to In-Plane Shear Forces”, J.Am. Concr.Inst., Vol. 89, No. 5, 1992, pp. 503-514.

[11] Hsu, T. T. C, MO, Y. L. (2010), “Unified Theory of Concrete Structures”, Wiley.

[12]. Zomorodian M., Yang G., Belarbi A., Ayoub A. (2018), “Behavior of FRP-strengthened RC elements subjected to pure shear”, Construction and Building Materials, Vol. 170, pp. 378-391.

[13]. Zomorodian M. (2015), “Behavior of FRP strengthened concrete panel elements subjected to pure shear”, Ph.D. Thesis, Faculty of the Department of Civil and Environmental Engineering, University of Houston.

[14]. Zomorodian M, Belarbi A, Ayoub A. (2017), “Finite element model for predicting the shear behavior of FRP-strengthened RC members”, Engineering Structures. Vol. 153, pp. 239-253.

[15]. Hoffman N. S. (2010), “Constitutive Relationships of Prestressed Steel Fiber Concrete Membrane Elements”, Ph.D. Thesis, Department of Civil and Environmental Engineering, University of Houston.

Anexos

Anexo I. Código em MATLAB do RA-STM RC v2

Script para iniciar o RA-STM RC v2

```
%//////////////////////////////////////////////////////////////////////////////
% RA-STM RC v2 - ROTATING ANGLE SOFTENED TRUSS MODEL - REINFORCED CONCRETE v2 /
%//////////////////////////////////////////////////////////////////////////////

% INICIO //////////////////////////////////////////////////////////////////
clear all; clc;

% PAINEIL / DADOS DE ENTRADA //////////////////////////////////////////////
DADOS_INICIAIS; tic;

% CÁLCULO DAS ESTIMATIVAS INICIAIS (MCTM) /////////////////////////////////
alfaD1 = (lsqnonlin(@(alfaD) MCTM_PLACA(alfaD),0.01,[],0))*180/pi;

% SOLUÇÃO /////////////////////////////////////////////////////////////////
COMP_PLACA;

% CURVAS DE COMPORTAMENTO /////////////////////////////////////////////////
toc; PLOT_PLACA;
```

Função para a escolha das placas / Introdução dos dados iniciais

```
function DADOS_INICIAIS

%//////////////////////////////////////////////////////////////////////////
% SELEÇÃO DA PLACA / INTRODUÇÃO DOS DADOS INICIAIS                       /
%//////////////////////////////////////////////////////////////////////////

disp('Selecione os dados iniciais');
disp(' ');
disp('Placas de Betão Armado solicitadas com ALFA2=45°');
disp('1  - VA0 [fcm = 98,8 MPa  | roL = 0,0060  | roT = 0,0060]  - ZHANG e HSU
(1998)');
disp('2  - VA1 [fcm = 95,1 MPa  | roL = 0,0120  | roT = 0,0120]  - ZHANG e HSU
(1998)');
disp('3  - VA2 [fcm = 98,2 MPa  | roL = 0,0239  | roT = 0,0239]  - ZHANG e HSU
(1998)');
disp('4  - VA3 [fcm = 94,6 MPa  | roL = 0,0359  | roT = 0,0359]  - ZHANG e HSU
(1998)');
disp('5  - VA4 [fcm = 103,1 MPa | roL = 0,0524  | roT = 0,0524]  - ZHANG e HSU
(1998)');
disp('6  - VB1 [fcm = 98,2 MPa  | roL = 0,0239  | roT = 0,0120]  - ZHANG e HSU
(1998)');
disp('7  - VB2 [fcm = 97,6 MPa  | roL = 0,0359  | roT = 0,0120]  - ZHANG e HSU
(1998)');
disp('8  - VB3 [fcm = 102,3 MPa | roL = 0,0598  | roT = 0,0120]  - ZHANG e HSU
(1998)');
disp('9  - VB4 [fcm = 96,9 MPa  | roL = 0,0180  | roT = 0,0060]  - ZHANG e HSU
(1998)');
disp('10 - A1R [fcm = 42,2 MPa  | roL = 0,0077  | roT = 0,0077]  - (1997)');
disp('11 - A2  [fcm = 41,2 MPa  | roL = 0,0119  | roT = 0,0119]  - PANG e HSU
(1995)');
disp('12 - A3  [fcm = 41,6 MPa  | roL = 0,0179  | roT = 0,0179]  - PANG e HSU
(1995)');
disp('13 - A4  [fcm = 42,5 MPa  | roL = 0,0298  | roT = 0,0298]  - PANG e HSU
(1995)');
disp('14 - B1  [fcm = 45,2 MPa  | roL = 0,0119  | roT = 0,0060]  - PANG e HSU
(1995)');
disp('15 - B2  [fcm = 44,1 MPa  | roL = 0,0179  | roT = 0,0119]  - PANG e HSU
(1995)');
disp('16 - B3  [fcm = 44,9 MPa  | roL = 0,0179  | roT = 0,0060]  - PANG e HSU
(1995)');
disp('17 - B4  [fcm = 44,8 MPa  | roL = 0,0298  | roT = 0,0060]  - PANG e HSU
(1995)');
disp('18 - B5  [fcm = 42,8 MPa  | roL = 0,0298  | roT = 0,0119]  - PANG e HSU
(1995)');
disp('19 - B6  [fcm = 43,0 MPa  | roL = 0,0298  | roT = 0,0179]  - PANG e HSU
(1995)');
disp(' ');
disp('Placas de Betão Armado solicitadas com ALFA2=90°');
disp('20 - F2  [fcm = --,- MPa  | roL = 0,----  | roT = 0,----]  - BELARBI e
HSU (19--)');
disp('21 - F3  [fcm = --,- MPa  | roL = 0,----  | roT = 0,----]  - BELARBI e
HSU (19--)');
disp('22 - F4  [fcm = --,- MPa  | roL = 0,----  | roT = 0,----]  - BELARBI e
HSU (19--)');
disp(' ');
disp('23 - Introduzir manualmente os dados iniciais');
disp(' ');
disp('0 - Sair');
disp(' ');
IND = input('Escolha uma opção: ');

if IND >= 0 & IND <= 24
    switch IND
        case 1
            VA0_ZHANG_e_HSU;
        case 2
```

```
            VA1_ZHANG_e_HSU;
        case 3
            VA2_ZHANG_e_HSU;
        case 4
            VA3_ZHANG_e_HSU;
        case 5
            VA4_ZHANG_e_HSU;
        case 6
            VB1_ZHANG_e_HSU;
        case 7
            VB2_ZHANG_e_HSU;
        case 8
            VB3_ZHANG_e_HSU;
        case 9
            VB4_ZHANG_e_HSU;
        case 10
            A1R_1997;
        case 11
            A2_PANG_e_HSU;
        case 12
            A3_PANG_e_HSU;
        case 13
            A4_PANG_e_HSU;
        case 14
            B1_PANG_e_HSU;
        case 15
            B2_PANG_e_HSU;
        case 16
            B3_PANG_e_HSU;
        case 17
            B4_PANG_e_HSU;
        case 18
            B5_PANG_e_HSU;
        case 19
            B6_PANG_e_HSU;
        case 20
            F2_BELARBI_e_HSU;
        case 21
            F3_BELARBI_e_HSU;
        case 22
            F4_BELARBI_e_HSU;
        case 23
            INTRODUZIR_DADOS;
        case 0
            error('SCRIPT INTERROMPIDO!')
            clc
    end
else
    disp(' ');
    disp('O VALOR INTRODUZIDO NÃO É VÁLIDO!');
    disp(' ');
    DADOS_INICIAIS
end
end
```

Exemplo de dados experimentais: Placa A2

```
function A2_PANG_e_HSU

%//////////////////////////////////////////////////////////////////////////
% DADOS EXPERIMENTAIS DA PLACA A2 - PANG E HSU (1995)                    /
%//////////////////////////////////////////////////////////////////////////

global roL roT Es fLy fTy Ec fcm e0 tal sigL sigT eLy eTy
global sig1 mLT mL mT
global e_plot sigmaD_plot eR_plot aco_plot eL_plot eT_plot fL_plot fT_plot
global alfa_plot tal_plot gama_plot tal_Teo gama_Teo sigmaR_plot eRaux_plot a b c

%//////////////////////////////////////////////////////////////////////////
% DADOS INICIAIS                                                          /
%//////////////////////////////////////////////////////////////////////////

% Taxas de armadura
roL = 0.01193;
roT = 0.01193;

% Propriedades mecânicas dos aços
Es   = 200000;           %Módulo de elasticidade do aço (MPa)
fLy = 462.64;            %Tensão de cedência da armadura longitudinal (MPa)
fTy = 462.64;            %Tensão de cedência da armadura transversal (MPa)

% Propriedades mecânicas do betão
fcm = 41.2;                   %Resistência média do betão (MPa)
Ec = 3875*sqrt(fcm); %Módulo de elast. do betão (MPa) - Belarbi e Hsu (1994)
e0  = -2.1;                   %Extensão última do betão (1/1000)

% Solicitações no elemento de betão armado (L-T):
tal  = 2;                     %Tensão tangencial (MPa)
sigL = 0;                     %Tensão de tração longitudinal (MPa)
sigT = 0;                     %Tensão de compressão transversal (Mpa)

%//////////////////////////////////////////////////////////////////////////
% CÁLCULOS PRELIMINARES                                                   /
%//////////////////////////////////////////////////////////////////////////

eLy  = fLy/Es*1000;
eTy  = fTy/Es*1000;
sig1 = (sigL + sigT)/2 + sqrt(((sigL - sigT)/2)^2 + tal^2);
mLT  = tal/sig1;
mL   = sigL/sig1;
mT   = sigT/sig1;

%//////////////////////////////////////////////////////////////////////////
% DADOS CURVAS EXPERIMENTAIS E TEÓRICAS                                   /
%//////////////////////////////////////////////////////////////////////////

e_plot      = 0;
sigmaD_plot = 0;
sigmaR_plot = 0;
eR_plot     = 0;
eRaux_plot  = 0;
aco_plot    = 0;
eL_plot     = [0; 1.600; 1.900; 2.886; 4.730; 13.190; 15.864; 19.000];
eT_plot     = 0;
fL_plot     = [0; 342.035; 375.764; 379.212; 410.445; 428.785; 389.554;
    317.159];
fT_plot     = 0;
alfa_plot   = 0;
tal_plot    = [0; 0.317; 0.724; 0.979; 1.338; 1.655; 1.862; 2.034; 2.620;
    3.482; 3.896; 4.344; 4.947; 4.895; 5.206; 5.283; 5.266; 5.309; 5.394];
gama_plot   = [0; 0; 0; 0; 0.150; 0.800; 1.100; 1.250; 1.900; 3.000; 3.350;
    3.660; 4.700; 6.143; 10.600; 14.720; 18.220; 23.140; 28.000];
tal_Teo     = [0; 1.565; 1.606; 2.758; 4.743; 4.935; 4.992; 5.394];
gama_Teo    = [0;0; 0.800; 2.100; 4.000; 6.000; 11.000; 28.000];
```

```
%Legenda
a = 'A2 Exp.';
b = 'eff. RA-STM';
c = ' RA-STM [Pang&Hsu-1995]';
end
```

Função para a introdução manual dos dados iniciais

```
function INTRODUZIR_DADOS

%/////////////////////////////////////////////////////////////////////
% DADOS INTRODUZIDOS MANUALMENTE                                     /
%/////////////////////////////////////////////////////////////////////

global roL roT Es fLy fTy Ec fcm e0 tal sigL sigT eLy eTy
global sig1 mLT mL mT
global e_plot sigmaD_plot sigmaR_plot eR_plot aco_plot eL_plot eT_plot fL_plot
fT_plot
global alfa_plot tal_plot gama_plot tal_Teo gama_Teo eRaux_plot a b c

%/////////////////////////////////////////////////////////////////////
% DADOS INICIAIS                                                     /
%/////////////////////////////////////////////////////////////////////

% Dados inicias a introduzir pelo utilizador através de uma caixa de diálogo
prompt={'Taxa de armadura longitudinal:','Taxa de armadura transversal:',...
    'Módulo de elasticidade do aço (MPa):','Tensão de cedência da armadura
longitudinal (MPa):',...
    'Tensão de cedência da armadura transversal (MPa):','Resistência do betão
à compressão (MPa):',...
    'Módulo de elasticidade do betão (MPa):','Extensão de compressão do betão
correspondente ao pico de tensão (‰):',...
    'Tensão tangencial no referencial L-T (MPa):','Tensão normal na direção L
(MPa):','Tensão normal na direção T (MPa):'};
title='Dados iniciais';
dims=[1 70];
definput={'0.01193','0.01193','200000','462.6','462.6','41.2','24872.6','-
2.1','2','0','0'}; % Valores por defeito
dados=inputdlg(prompt,title,dims,definput);
dados1=str2double(dados);

% Taxas de armadura:
roL = dados1(1);
roT = dados1(2);

% Propriedades mecânicas dos aços:
Es  = dados1(3); %Módulo de elasticidade do aço (MPa)
fLy = dados1(4); %Tensão de cedência da armadura longitudinal (MPa)
fTy = dados1(5); %Tensão de cedência da armadura transversal (MPa)

% Propriedades mecânicas do betão:
fcm = dados1(6); %Resistência média do betão(MPa)
Ec  = dados1(7); %Módulo de elasticidade do betão (MPa)
e0  = dados1(8); %Extensão última do betão (1/1000)

% Solicitações no elemento de betão armado (L-T):
tal  = dados1(9);

%Tensão tangencial (MPa)
sigL = dados1(10); %Tensão de tração longitudinal (MPa)
sigT = dados1(11); %Tensão de compressão transversal (Mpa)

%/////////////////////////////////////////////////////////////////////
% CÁLCULOS PRELIMINARES                                              /
%/////////////////////////////////////////////////////////////////////
eLy  = fLy/Es*1000;
eTy  = fTy/Es*1000;
sig1 = (sigL + sigT)/2 + sqrt(((sigL - sigT)/2)^2 + tal^2);
mLT  = tal/sig1;
mL   = sigL/sig1;
mT   = sigT/sig1;

%/////////////////////////////////////////////////////////////////////
% DADOS CURVAS EXPERIMENTAIS E TEÓRICAS  (não existem)               /
%/////////////////////////////////////////////////////////////////////
```

```
e_plot       = 0;
sigmaD_plot = 0;
sigmaR_plot = 0;
eR_plot      = 0;
eRaux_plot  = 0;
aco_plot     = 0;
eL_plot      = 0;
eT_plot      = 0;
fL_plot      = 0;
fT_plot      = 0;
alfa_plot    = 0;
tal_plot     = 0;
gama_plot    = 0;
tal_Teo      = 0;
gama_Teo     = 0;

%Legenda
a = 'Exp.';
b = 'RA-STM';
c = 'RA-STM [49]';

end
```

Função para o cálculo das estimativas iniciais (MCTM)

```
function F = MCTM_PLACA(alfaD)

%//////////////////////////////////////////////////////////////////////////
% COMPORTAMENTO LINEAR DA PLACA (MCTM) - ESTIMATIVAS INICIAIS PARA O RA-STM /
%//////////////////////////////////////////////////////////////////////////

global roL roT Es Ec eL eT eD sig1 mLT mL mT

% Equações de equilíbrio
eL=(mL+mLT*cot(alfaD))/(Es*roL)*0.001*sig1 ;
eT=(mT+mLT*tan(alfaD))/(Es*roT)*0.001*sig1;
eD=-mLT/(Ec*sin(alfaD)*cos(alfaD))*0.001*sig1;

% Equação não linear
F = (eL-eD)/(eT-eD)-(tan(alfaD))^2;

end
```

Função do RA-STM

```
function COMP_PLACA
%//////////////////////////////////////////////////////////////////////////
% COMPORTAMENTO CARGA-DEFORMÇÃO DA PLACA (RASTM_PAINEL)                  /
%//////////////////////////////////////////////////////////////////////////
global eL eT eD sigmaD eR fL fT fcm roL roT sigmaR
global ED SIGMAD TAL GAMA EL ET FL FT ALFAD ER ROLFL_ROTFT tal_plot gama_plot
SIGMAR

% Estimativa inicial com base no MCTM:
x(1) = eL*1000;
x(2) = eT*1000;
ed1  = eD*1000;

% Número máximo de pontos e tamanho do passo:
pontos = 1000;
passo  = 4/pontos;

% Cálculo comportamento tensão-deformação:
for i = 1:pontos

    options = optimset('TolX',10^-10,'TolFun',10^-10);
    x = lsqnonlin(@(x) RASTM_PLACA(x,ed1-passo*i),x,[0,0],[],options);

    % Criar vetores de comportamento:
    %%%% ED(i)    = eD - passo*i;    % Original do Cerquido...
    ED(i)    = ed1 - passo*i;   % Corrigido (mas não altera...)
    SIGMAD(i)= sigmaD;
    SIGMAR(i)= sigmaR;
    COS      = (x(2)-ED(i))/(eR-ED(i));
    SIN      = (x(1)-ED(i))/(eR-ED(i));
    TAL(i)   = (-SIGMAD(i)+SIGMAR(i))*sqrt(COS*SIN);
    GAMA(i)  = 2*(eR-ED(i))*sqrt(COS*SIN);
    EL(i)    = x(1);
    ET(i)    = x(2);
    FL(i)    = fL;
    FT(i)    = fT;
    ALFAD(i) = -atan(sqrt(SIN/COS))*180/pi;
    ER(i) = EL(i) + ET(i) - ED(i);
    ROLFL_ROTFT (i) =  FL(i)*roL + FT(i)*roT;

    % Critérios de paragem (betão normal e de alta resistência)
    % (Eqs. 2.19 e 2.20..):
    if fcm <= 58
        if - ED(i) >= 3.5;
            break
        end
    else
        if - ED(i) >= 2.8 + 27 * ((98-fcm)/100)^4;
            break
        end
    end

end
MAXTAL = max(TAL);
MAXGAMAj = GAMA(find(TAL==max(TAL)));
MAXTAL_PLOT = max(tal_plot);
MAXGAMA_PLOT = gama_plot(find(tal_plot==max(tal_plot)));
disp('Valores últimos (máximos) são:');
fprintf('Tau_u,th: %f kN.m\n',MAXTAL);
fprintf('Gama_u,th: %f rad/m\n',MAXGAMAj);
fprintf('Tau_u,exp: %f kN.m\n',MAXTAL_PLOT);
fprintf('Gama_u,exp: %f rad/m\n',MAXGAMA_PLOT);
fprintf('\n')


end
```

```
function F = RASTM_PLACA(x,ed1)

%///////////////////////////////////////////////////////////////////////////
% COMPORTAMENTO NÃO-LINEAR DA PLACA (RA-STM)                              /
%///////////////////////////////////////////////////////////////////////////

global roL roT Es fcm fLy fTy e0 mLT mL mT sigmaD csi eR fL fT eLy eTy sigmaR
global Ec sigL sigT

% CÁLCULOS INICIAIS /////////////////////////////////////////////////////

% Princípio da Invariância
eR = x(1) + x(2) - ed1;

% Coeficiente de Amolecimento
R = 5.8/(sqrt(fcm));
if   R <= 0.9
    R_linha = R;
else
    R_linha = 0.9;
end

n = (roT*fTy-sigT)/(roL*fLy-sigL);
if   n <= 1
    n_linha = n;
else
    n_linha = 1/n;
end

csi = R_linha/(sqrt(1+((0.4*eR)/n_linha)));

% Relação constitutiva do betão à compressão
if ed1 > csi*e0
    sigmaD = -csi*fcm*(2*(ed1/(csi*e0))-(ed1/(csi*e0))^2);
else
    sigmaD = -csi*fcm*(1-((ed1/(csi*e0)-1)/((4/csi)-1))^2);
end

% Relação constitutiva do aço
fcr = 0.311 * sqrt(fcm);

% Armadura Longitudinal
BL   = (1/roL)*(fcr/fLy)^1.5;
enL = eLy*10^-3*(0.93-2*BL);

if x(1)*10^-3 <= enL
    fL = x(1)*10^-3*Es;
else
    fL = fLy*((0.91-2*BL)+(0.02+0.25*BL)*(x(1)/eLy));
end

% Armadura Transversal
BT   = (1/roT)*(fcr/fTy)^1.5;
enT = eTy*10^-3*(0.93-2*BT);

if x(2)*10^-3 <= enT
    fT   = x(2)*10^-3*Es;
else
    fT = fTy*((0.91-2*BT)+(0.02+0.25*BT)*(x(2)/eTy));
end


% Relação constitutiva do betão à tração
ecr = 0.08;
sigmaR = fcr*(ecr/(eR+ecr))^0.4;

% Tensão principal de tração
A = mL*mT - mLT^2;
```

```
B = mL*(sigmaR + roT*fT) + mT*(sigmaR + roL*fL);
C = (sigmaR + roT*fT)*(sigmaR + roL*fL);
sigma1 = (1/(2*A))*(B-sqrt(B^2-4*A*C));


% COMPORTAMENTO NÃO LINEAR RA-STM ///////////////////////////////////////////

% Sistema de equações não-linear
F(1) = sigmaD*(x(1)-ed1)/(eR-ed1)-mT*sigma1+roT*fT + sigmaR*(x(2)-ed1)/(eR-
ed1);
F(2) = sigmaD*(x(2)-ed1)/(eR-ed1)-mL*sigma1+roL*fL + sigmaR*(x(1)-ed1)/(eR-
ed1);
end
```

Função para impressão das curvas de comportamento da placa

```
function PLOT_PLACA

%///////////////////////////////////////////////////////////////////////////
% IMPRESSÃO DAS CURVAS DE COMPORTAMENTO TENSÃO-DEFORMAÇÃO DA PLACA         /
%///////////////////////////////////////////////////////////////////////////

global ED SIGMAD TAL GAMA EL ET FL FT ER ROLFL_ROTFT SIGMAR
global e_plot sigmaD_plot eR_plot aco_plot eL_plot eT_plot fL_plot fT_plot
global tal_plot gama_plot tal_Teo gama_Teo sigmaR_plot eRaux_plot a b c

% DADOS INICIAIS ////////////////////////////////////////////////////////////

% Opção:
disp('1 - Curva tensão-deformação de compressão do betão');
disp('2 - Curva tensão-deformação de tração do betão');
disp('3 - Curva tensão-deformação da armadura longitudinal');
disp('4 - Curva tensão-deformação da armadura transversal');
disp('5 - Curva tensão-deformação da armadura longitudinal e transversal');
disp('6 - Curva tensão-deformação de corte da placa');
disp(' ');
disp('7 - Voltar ao inicio');
disp('0 - Sair');
disp(' ');
IND = input('Escolha uma opção: ');

% IMPRESSÃO DAS CURVAS //////////////////////////////////////////////////////

while IND > 0
    switch IND

        case 1
            % 1 - Curva tensão-deformação de compressão do betão
            hold on
            plot(-e_plot,-sigmaD_plot,'-rs','LineWidth',2,'MarkerSize',7)
            plot(-[0 ED],-[0 SIGMAD],'--b','LineWidth',2)%1.5)

            % Títulos
            xlabel('\epsilon_D (1/1000)');
            ylabel('\sigma_D (MPa)');
            legend(a,...
                b,'Location','southeast');
            grid on
            hold off

        case 2
            % 2 - Curva tensão-deformação de tração do betão
            hold on
            plot(eRaux_plot,sigmaR_plot,'-rs','LineWidth',2,'MarkerSize',7)
            plot([0 ER],[0 SIGMAR],'--b','LineWidth',2)%1.5)

            % Títulos
            xlabel('\epsilon_R (1/1000)');
            ylabel('\sigma_R (MPa)');
            legend(a,...
                b,'Location','southeast');
            grid on
            hold off

        case 3
            % 3 - Curva tensão-deformação da armadura longitudinal
            hold on
            plot(eL_plot,fL_plot,'--rs','LineWidth',2,'MarkerSize',7)
            plot([0 EL],[0 FL],'-g','LineWidth',2)
```

```
            % Títulos
            xlabel('\epsilon_L(1/1000)');
            ylabel('f_L (MPa)');
            legend(a,...
                b,'Location','southeast');
            grid on
            hold off

        case 4
            % 4 - Curva tensão-deformação da armadura transversal
            hold on
            plot(eT_plot,fT_plot,'--rs','LineWidth',2,'MarkerSize',7)
            plot([0 ET],[0 FT],'-g','LineWidth',2)

            % Títulos
            xlabel('\epsilon_T (1/1000)');
            ylabel('f_T (MPa)');
            legend(a,...
                b,'Location','southeast');
            grid on
            hold off

        case 5
            % 5 - Curva tensão-deformação da armadura long. e transv.
            hold on
            plot(eR_plot,aco_plot,'--rs','LineWidth',2,'MarkerSize',7)
            plot([0 ER],[0 ROLFL_ROTFT],'-g','LineWidth',2)

            % Títulos
            xlabel('\epsilon_R (1/1000)');
            ylabel('\rho_Lf_L+\rho_Tf_T (MPa)');
            legend(a,...
                b,'Location','southeast');
            grid on
            hold off

        case 6
            % 6 - Curva tensão-deformação de corte da placa
            hold on
            plot(gama_plot,tal_plot,'-rs','LineWidth',2,'MarkerSize',7)
            plot([0 GAMA],[0 TAL],'--b','LineWidth',2)
            plot (gama_Teo, tal_Teo,'-k','LineWidth',1)

            % Títulos
            xlabel('\gamma_L_T (1/1000)');
            ylabel('\tau_L_T (MPa)');
            legend(a,...
                b,...
                c,'Location','southeast');
            grid on
            hold off


        case 7
            if IND == 7
                inicio;
                break
            end
end
    disp(' ');
    IND = input('Escolha uma opção: ');

end
end
```

Anexo II. Previsões teóricas do RA-STM RC v2

Placa VA0 (Zhang e Hsu, 1998)

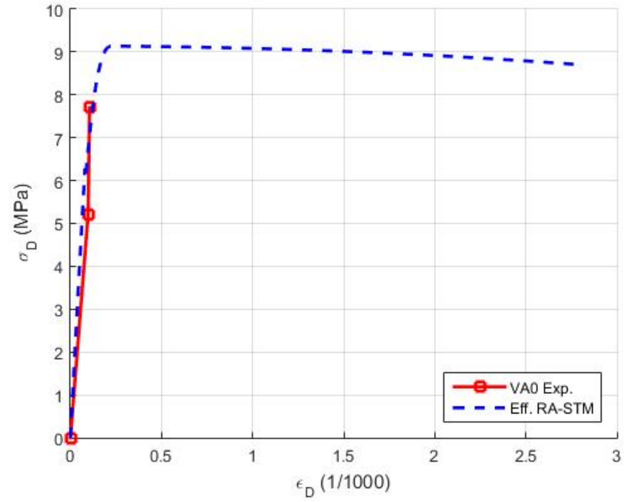

Curva $\sigma_D - \varepsilon_D$

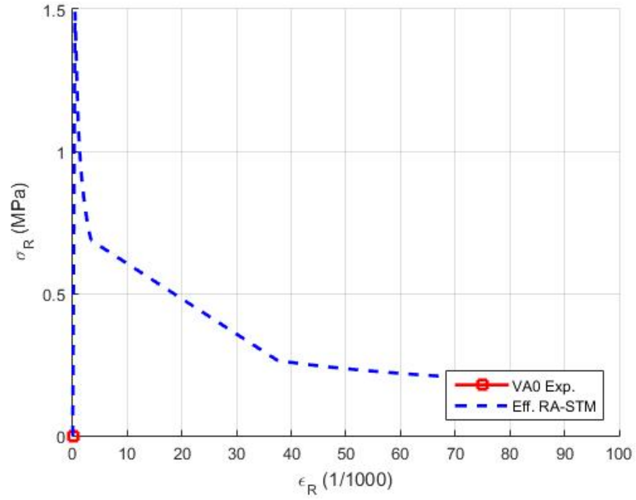

Curva $\sigma_R - \varepsilon_R$

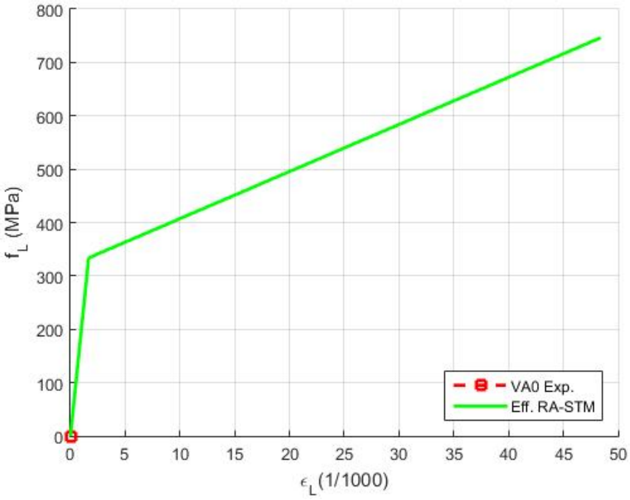

Curva $f_L - \varepsilon_L$

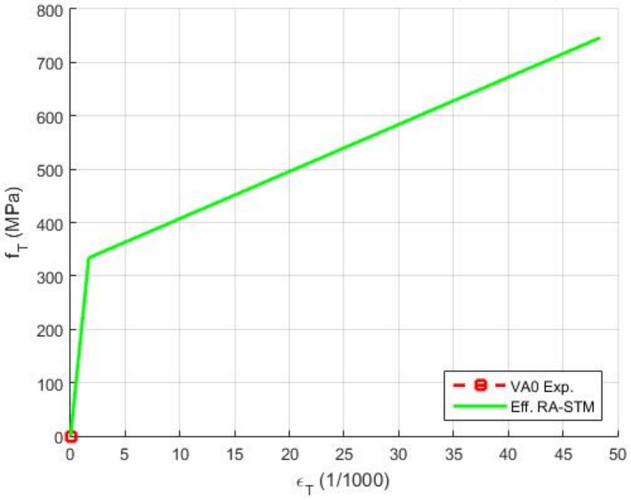

Curva $f_T - \varepsilon_T$

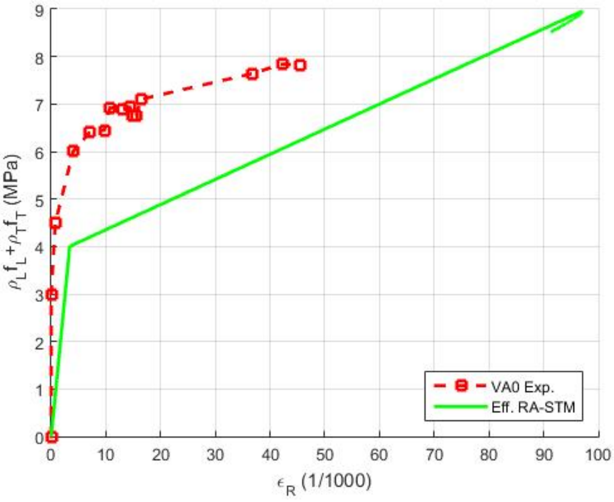

Curva $\rho_L f + \rho_T f_T - \varepsilon_R$

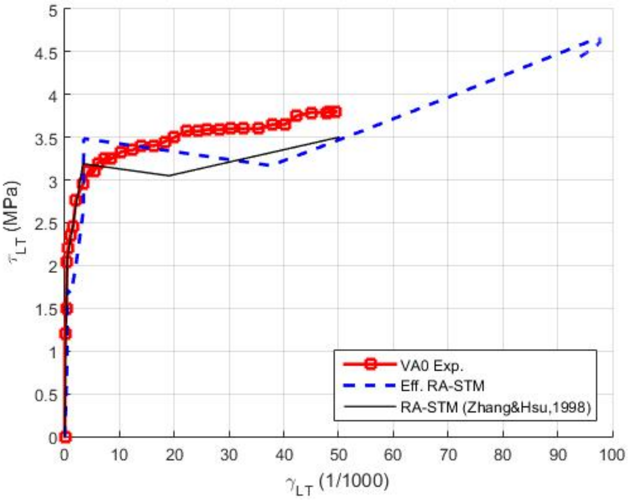

Curva $\tau_{LT} - \gamma_{LT}$

Placa VA1 (Zhang e Hsu, 1998)

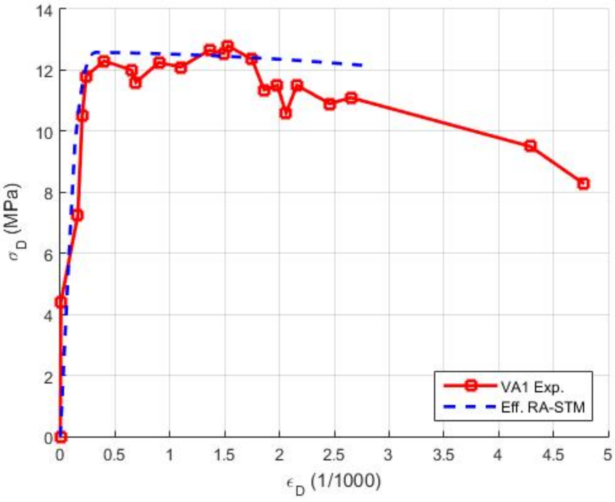

Curva $\sigma_D - \varepsilon_D$

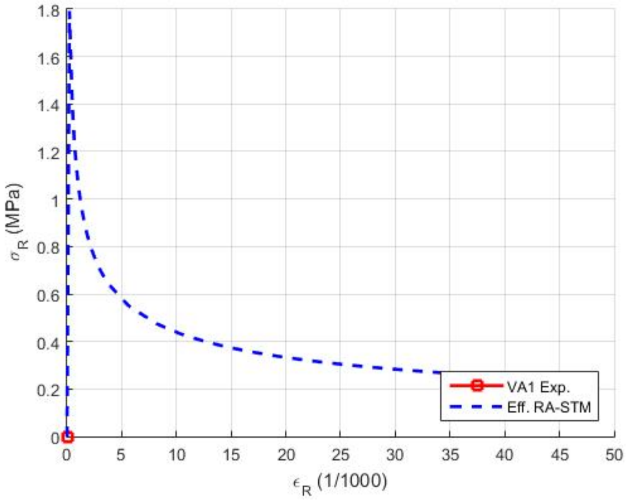

Curva $\sigma_R - \varepsilon_R$

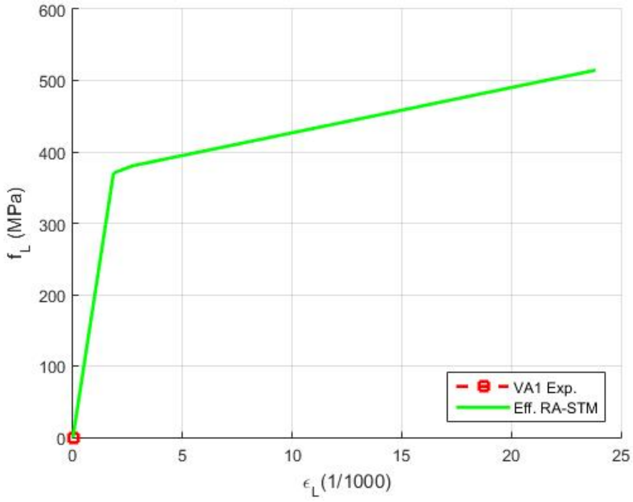

Curva $f_L - \varepsilon_L$

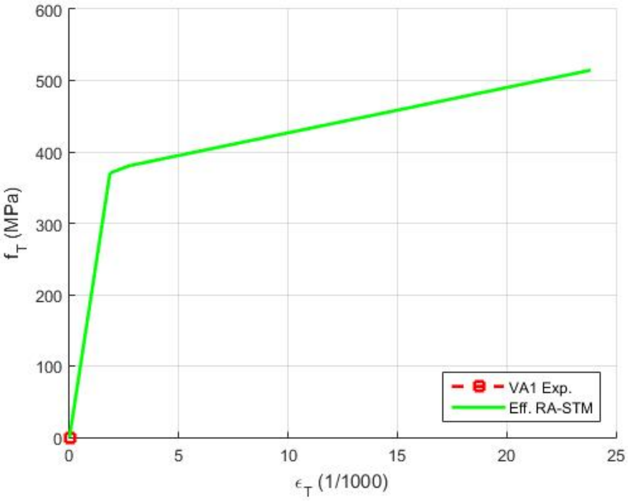

Curva $f_T - \varepsilon_T$

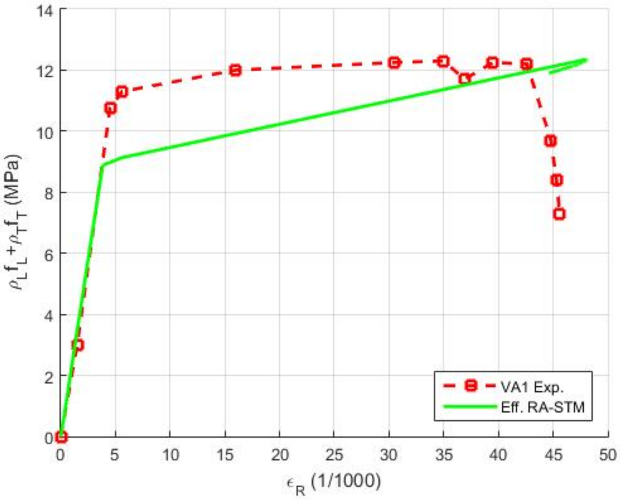

Curva $\rho_L f + \rho_T f_T - \varepsilon_R$

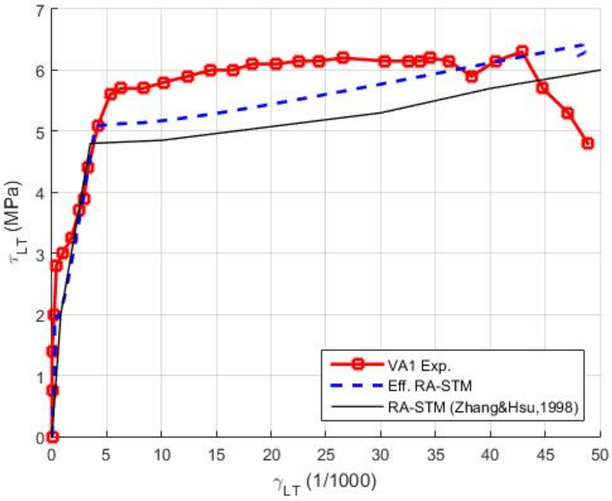

Curva $\tau_{LT} - \gamma_{LT}$

Placa VA2 (Zhang e Hsu, 1998)

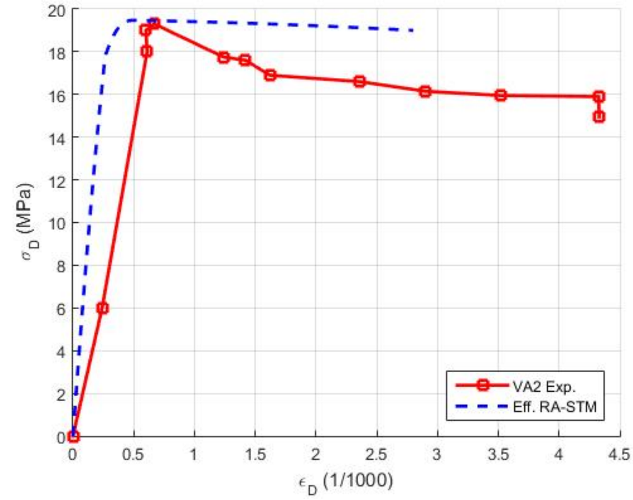

Curva $\sigma_D - \varepsilon_D$

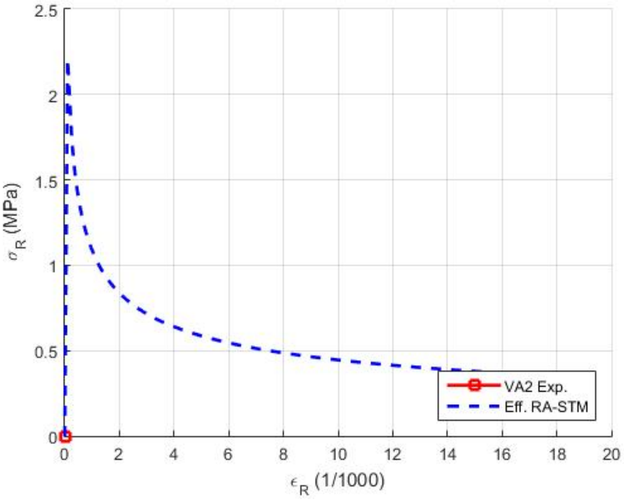

Curva $\sigma_R - \varepsilon_R$

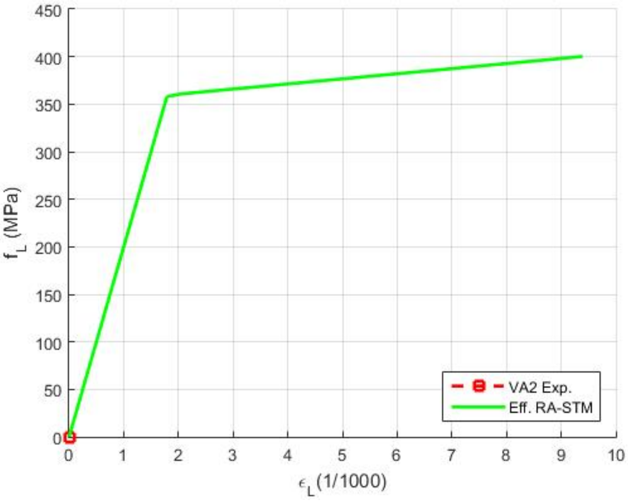

Curva $f_L - \varepsilon_L$

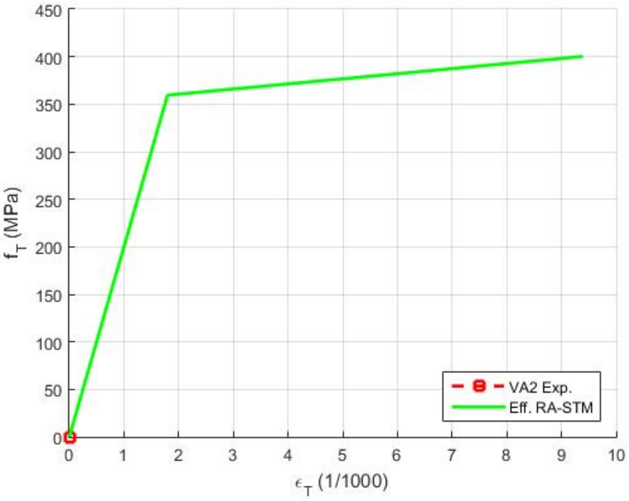

Curva $f_T - \varepsilon_T$

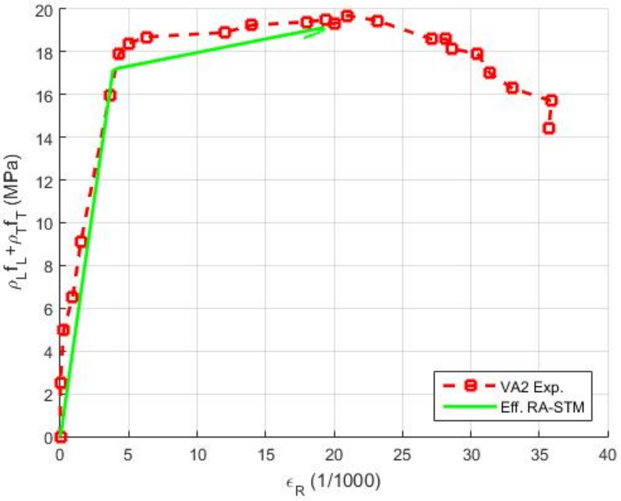

Curva $\rho_L f + \rho_T f_T - \varepsilon_R$

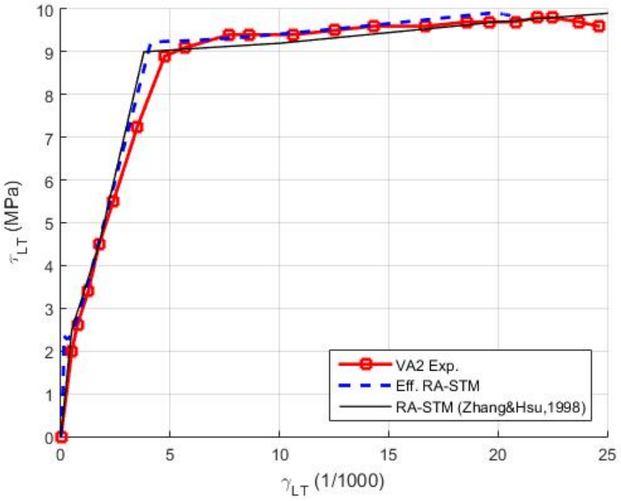

Curva $\tau_{LT} - \gamma_{LT}$

Placa VA3 (Zhang e Hsu, 1998)

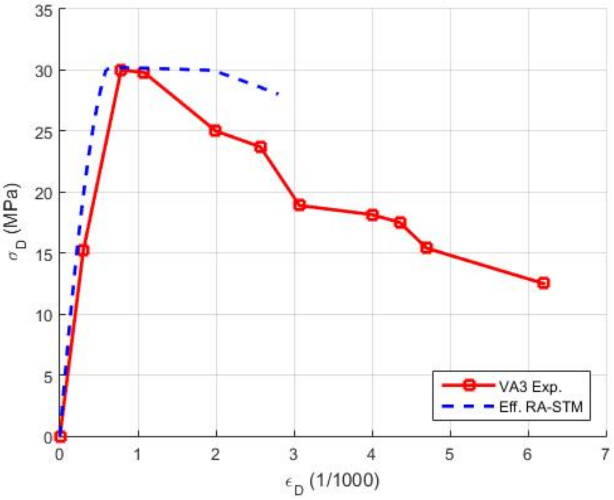

Curva $\sigma_D - \varepsilon_D$

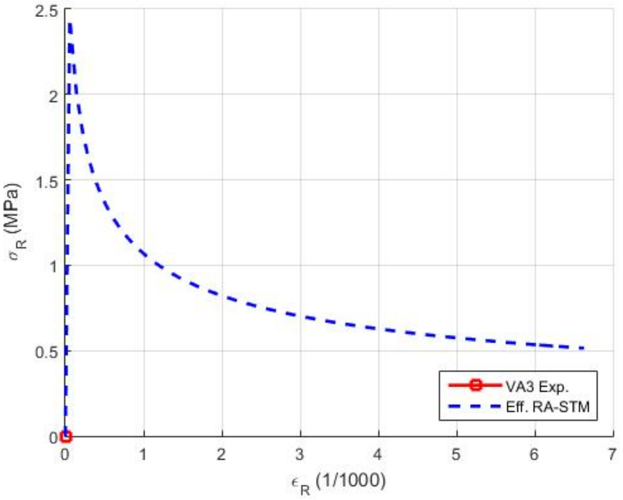

Curva $\sigma_R - \varepsilon_R$

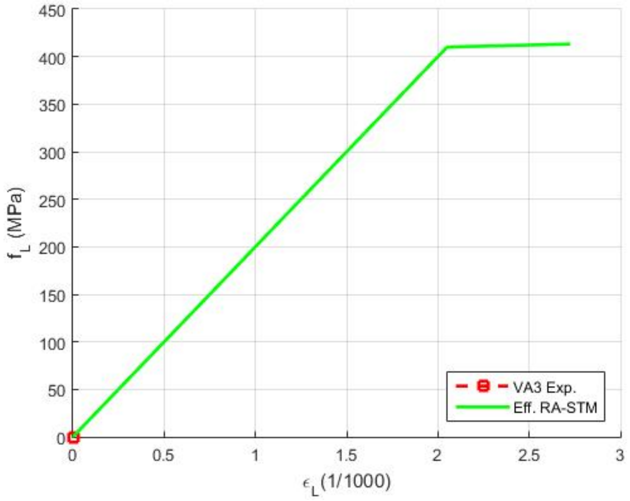

Curva $f_L - \varepsilon_L$

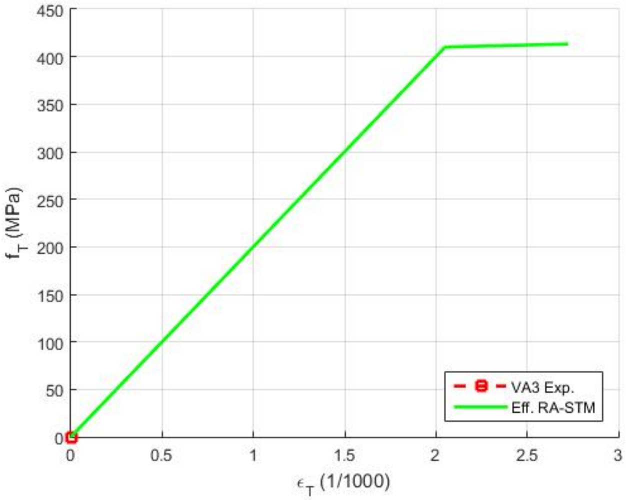

Curva $f_T - \varepsilon_T$

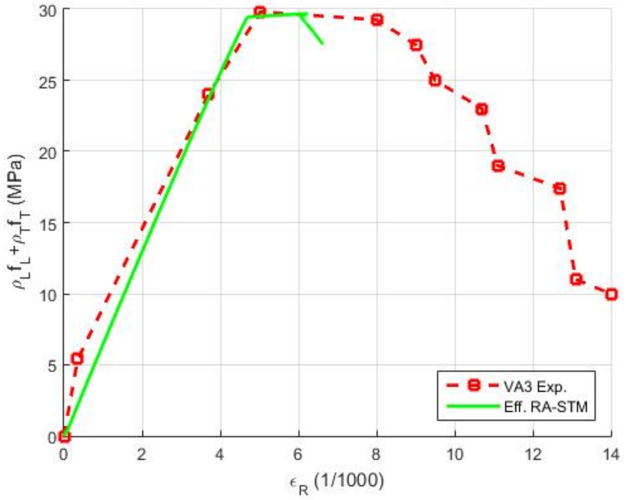

Curva $\rho_L f + \rho_T f_T - \varepsilon_R$

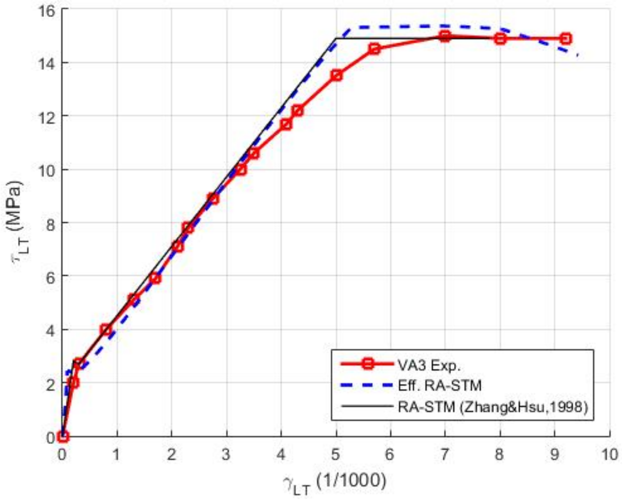

Curva $\tau_{LT} - \gamma_{LT}$

Placa VA4 (Zhang e Hsu, 1998)

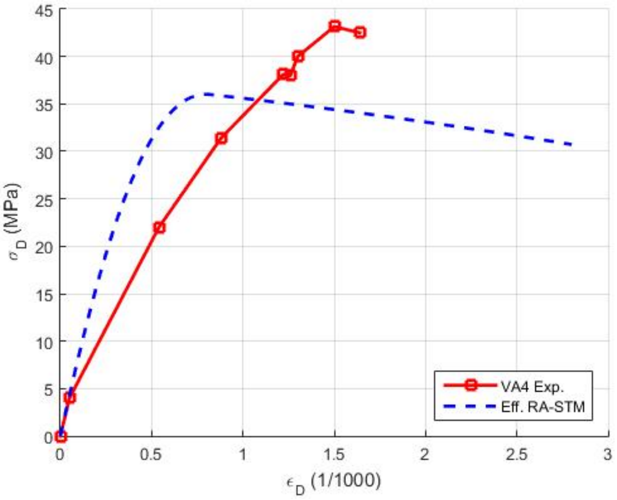

Curva $\sigma_D - \varepsilon_D$

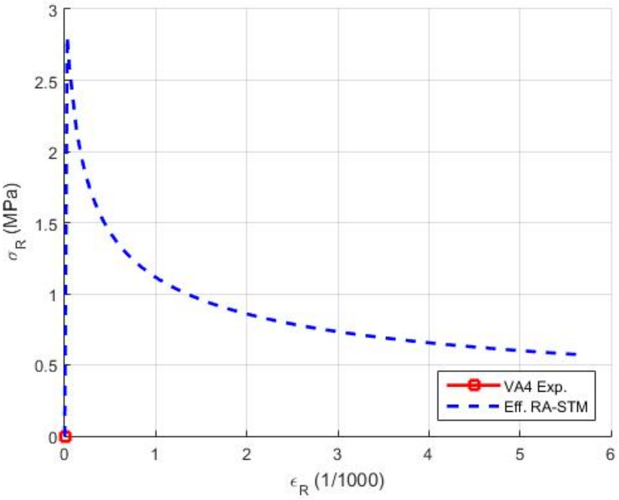

Curva $\sigma_R - \varepsilon_R$

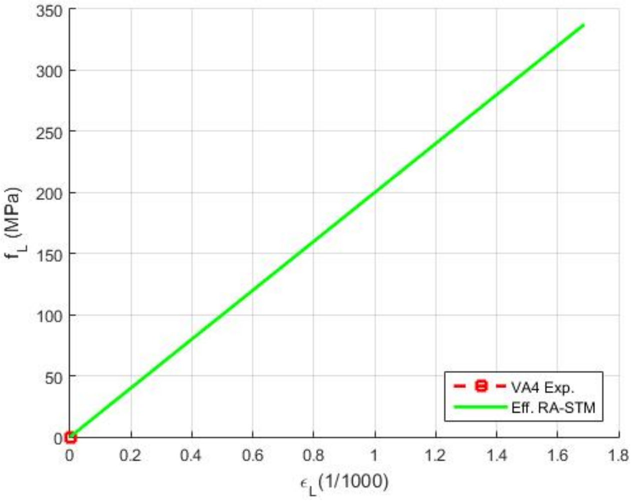

Curva $f_L - \varepsilon_L$

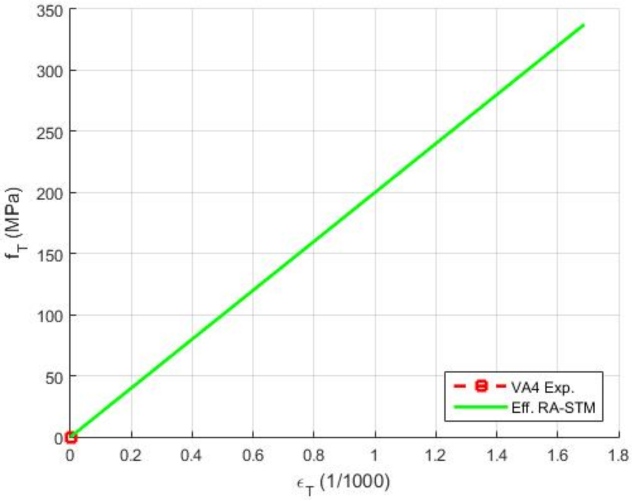

Curva $f_T - \varepsilon_T$

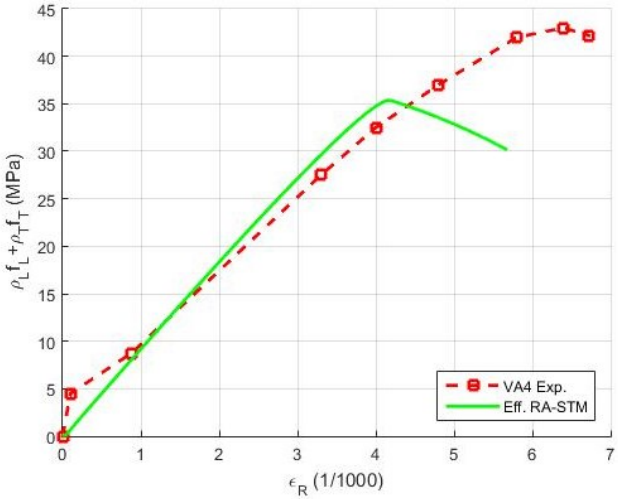

Curva $\rho_L f + \rho_T f_T - \varepsilon_R$

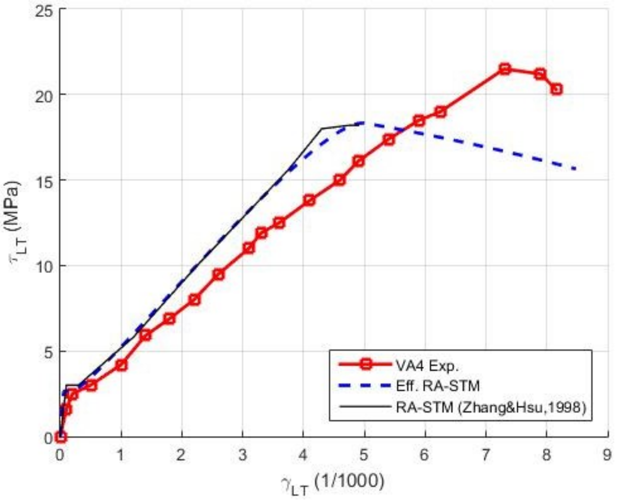

Curva $\tau_{LT} - \gamma_{LT}$

Placa VB1 (Zhang e Hsu, 1998)

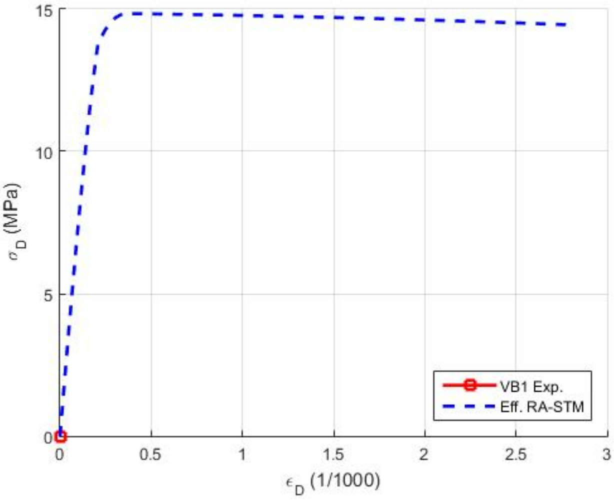

Curva $\sigma_D - \varepsilon_D$

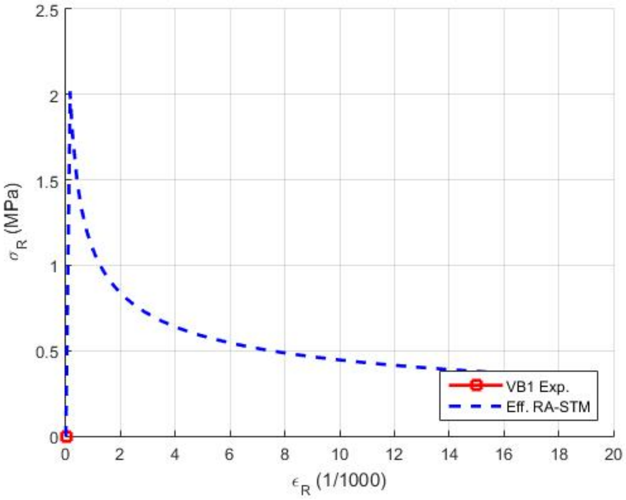

Curva $\sigma_R - \varepsilon_R$

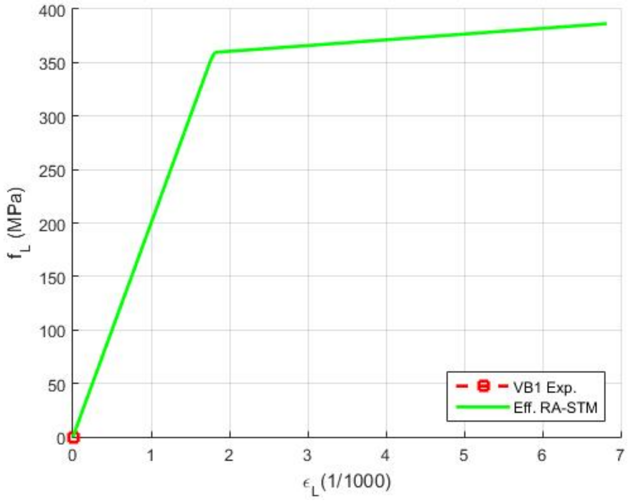

Curva $f_L - \varepsilon_L$

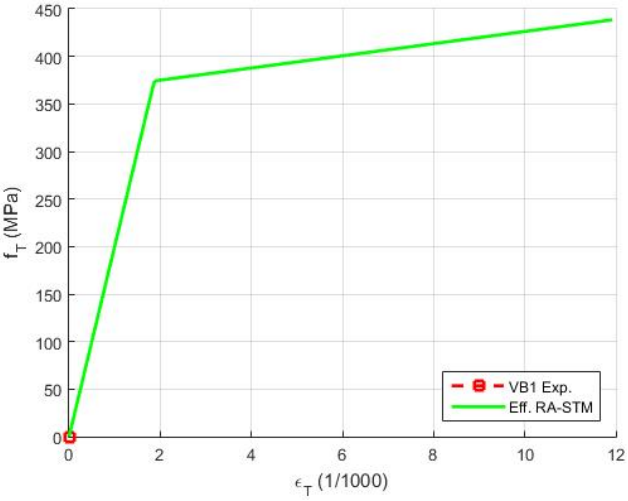

Curva $f_T - \varepsilon_T$

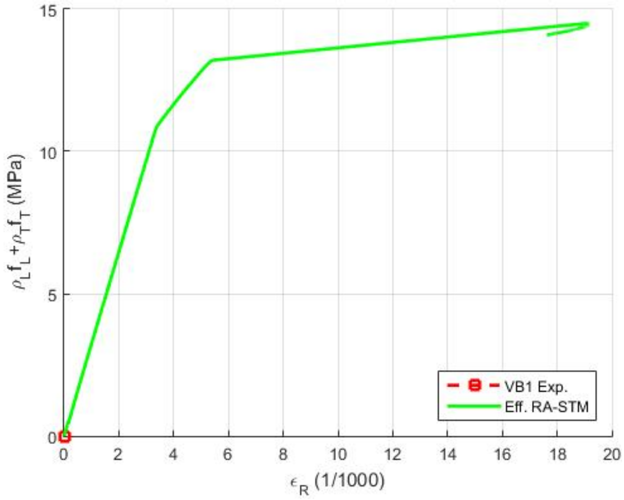

Curva $\rho_L f + \rho_T f_T - \varepsilon_R$

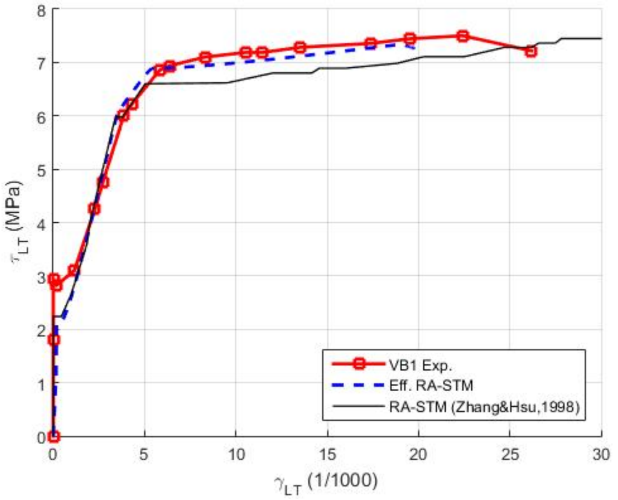

Curva $\tau_{LT} - \gamma_{LT}$

Placa VB2 (Zhang e Hsu, 1998)

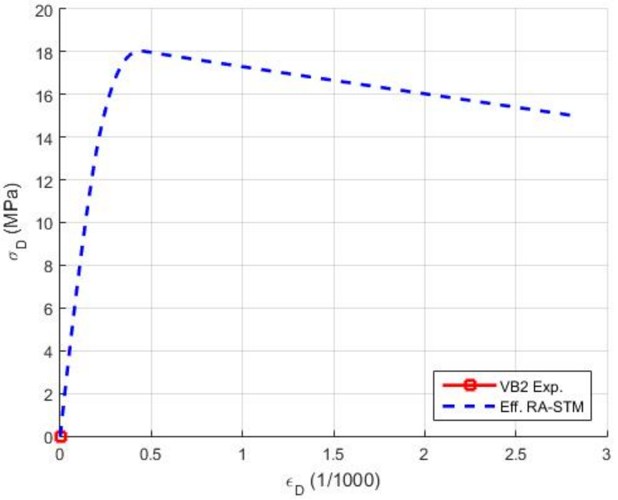

Curva $\sigma_D - \varepsilon_D$

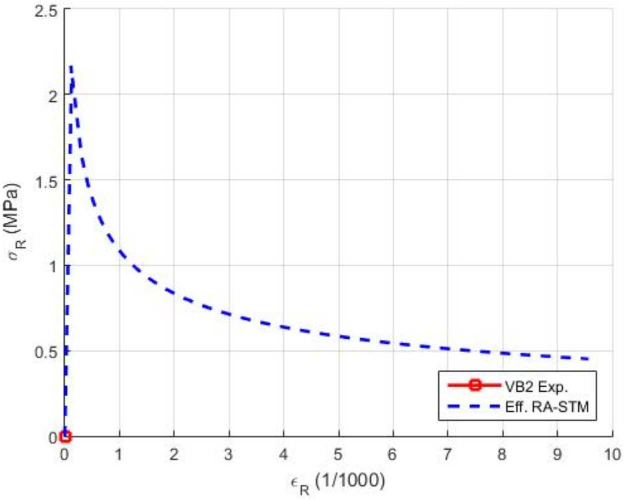

Curva $\sigma_R - \varepsilon_R$

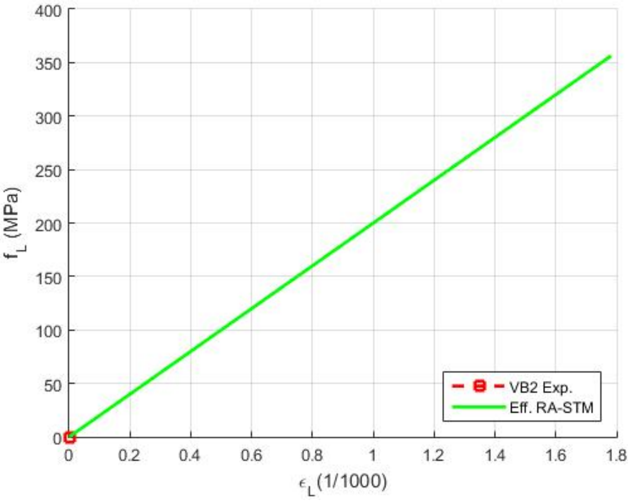

Curva $f_L - \varepsilon_L$

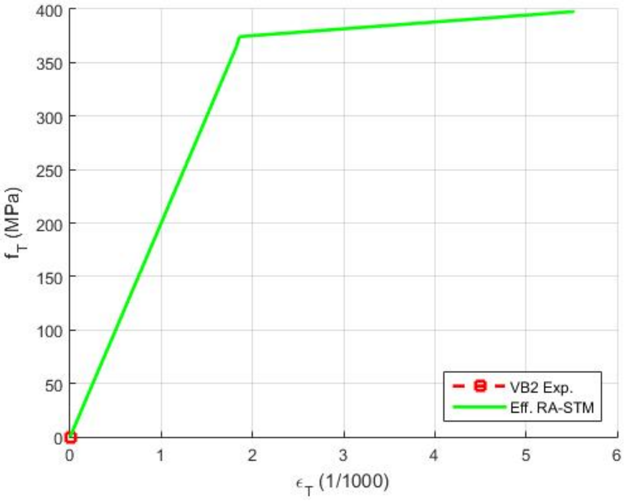

Curva $f_T - \varepsilon_T$

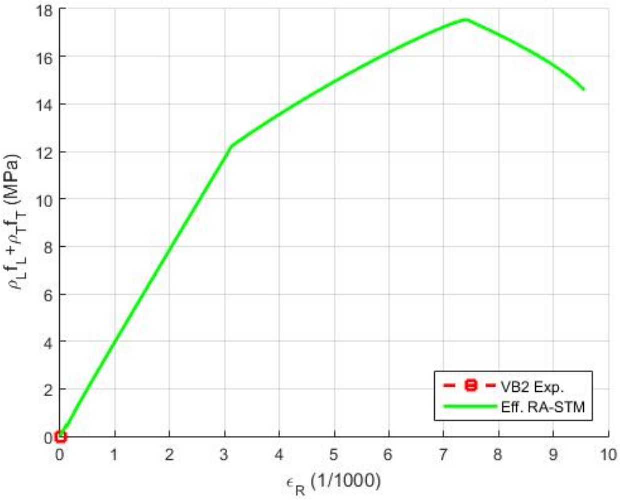

Curva $\rho_L f + \rho_T f_T - \varepsilon_R$

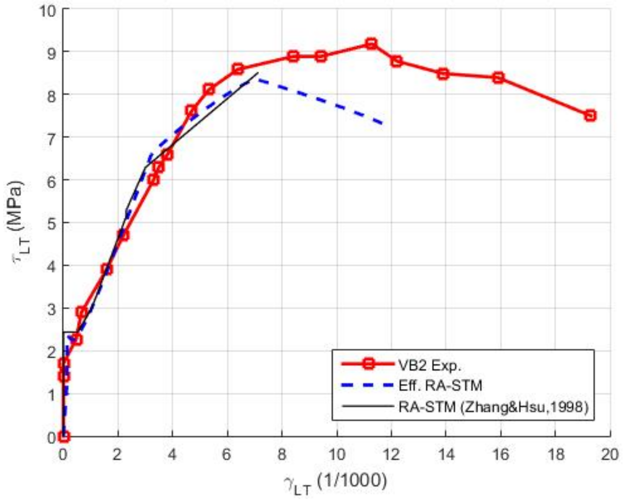

Curva $\tau_{LT} - \gamma_{LT}$

Placa VB3 (Zhang e Hsu, 1998)

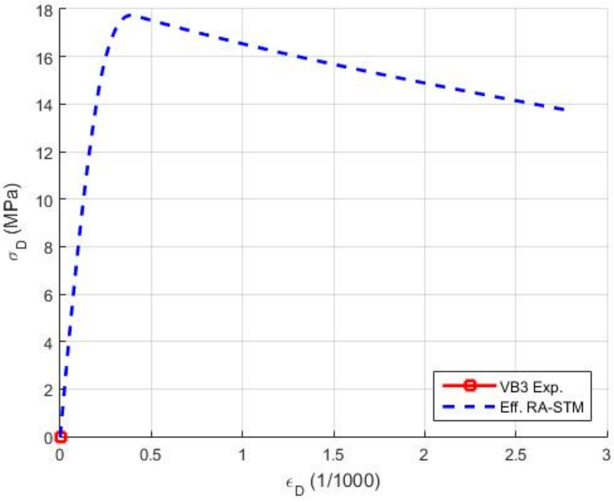

Curva $\sigma_D - \varepsilon_D$

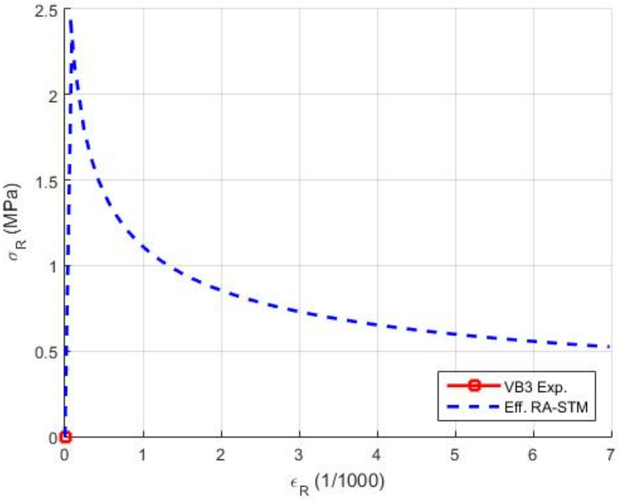

Curva $\sigma_R - \varepsilon_R$

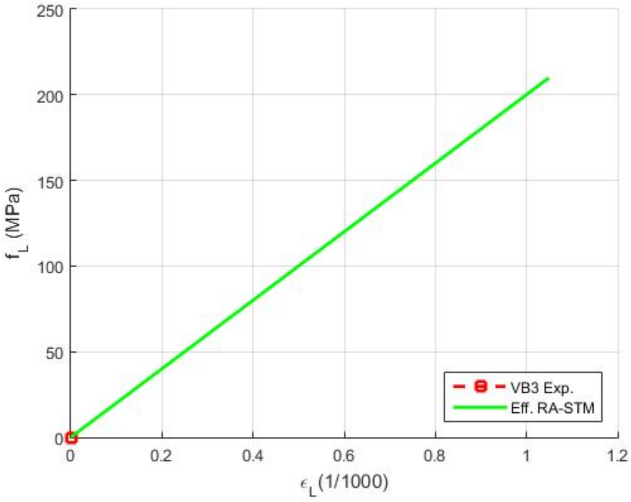

Curva $f_L - \varepsilon_L$

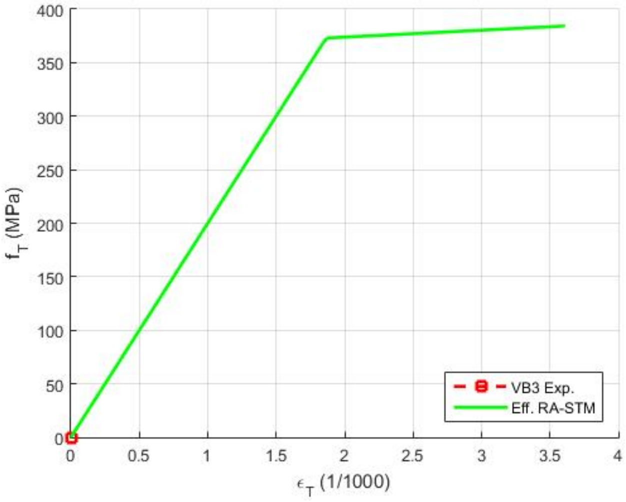

Curva $f_T - \varepsilon_T$

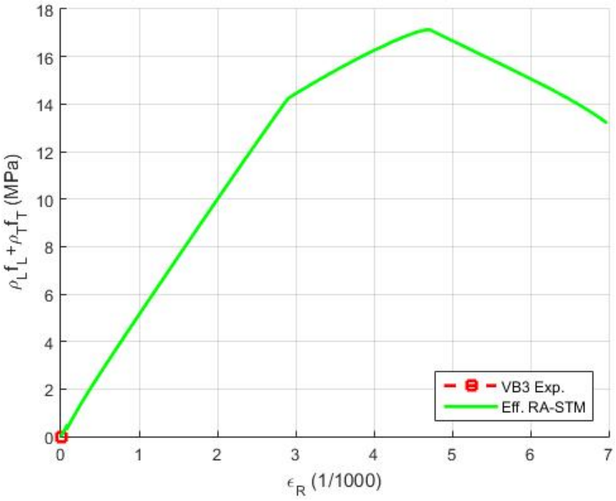

Curva $\rho_L f + \rho_T f_T - \varepsilon_R$

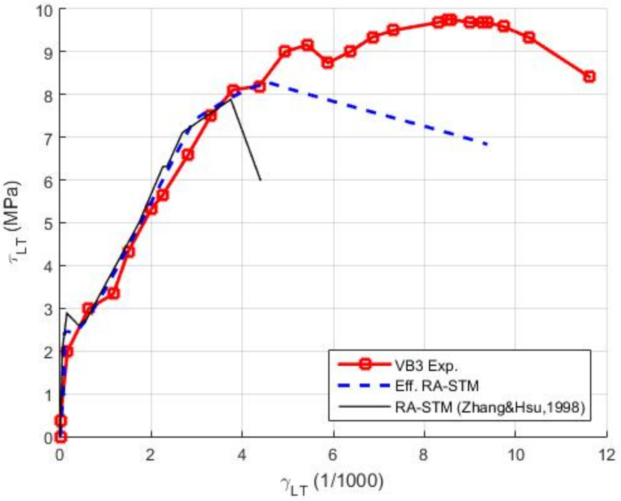

Curva $\tau_{LT} - \gamma_{LT}$

Placa VB4 (Zhang e Hsu, 1998)

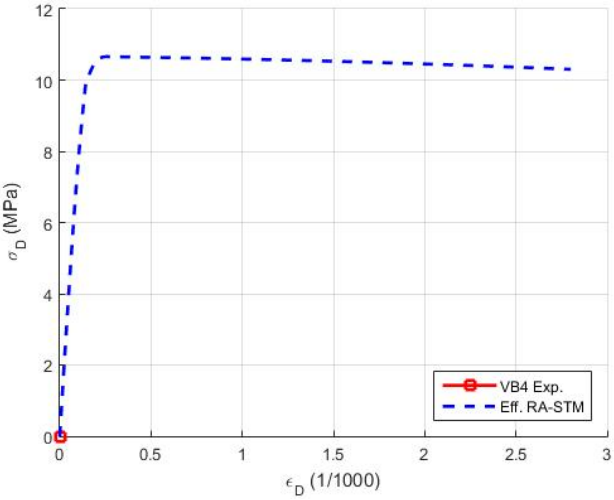

Curva $\sigma_D - \varepsilon_D$

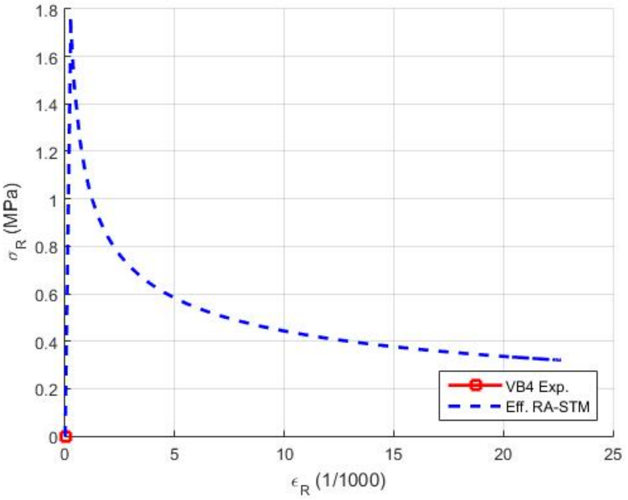

Curva $\sigma_R - \varepsilon_R$

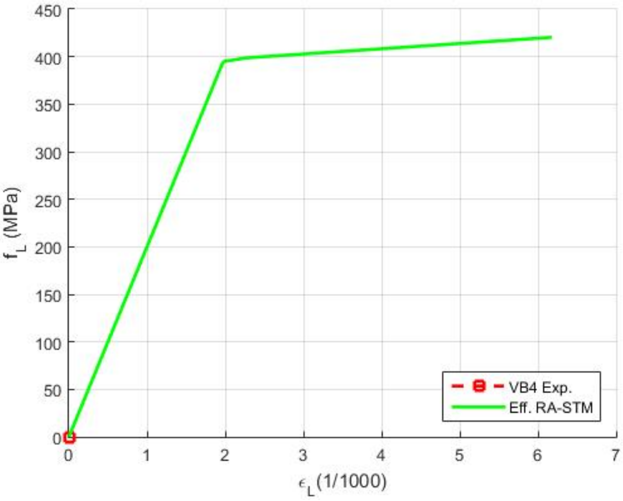

Curva $f_L - \varepsilon_L$

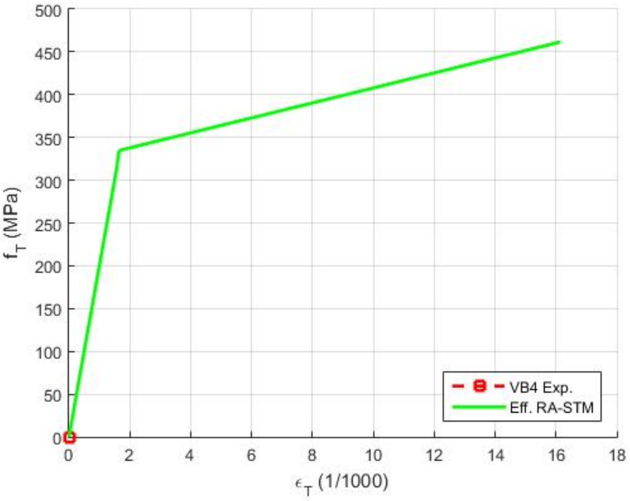

Curva $f_T - \varepsilon_T$

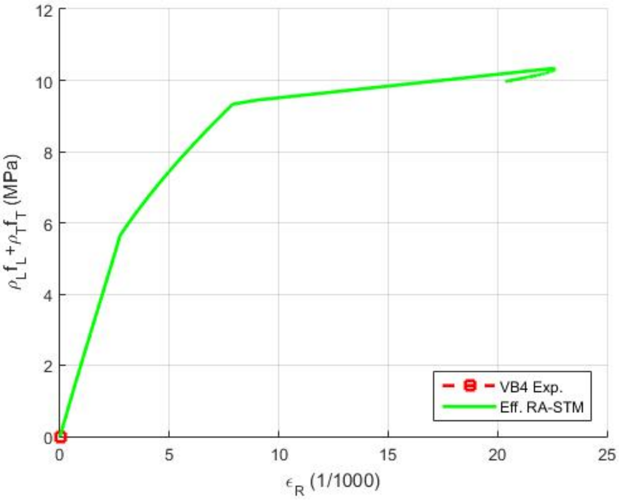

Curva $\rho_L f + \rho_T f_T - \varepsilon_R$

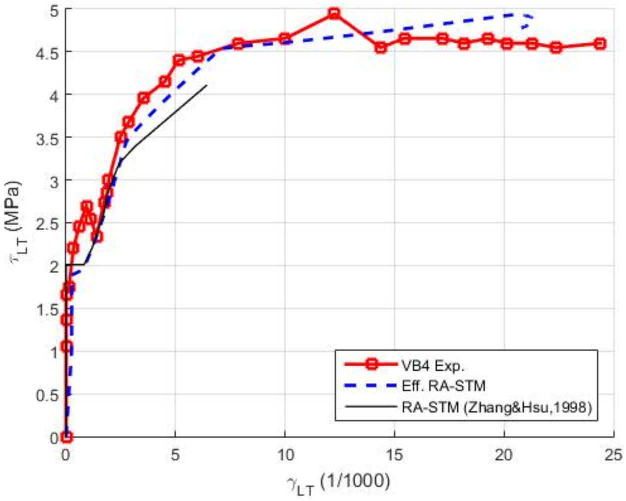

Curva $\tau_{LT} - \gamma_{LT}$

Placa A1R (Hsu e Zhu, 2002)

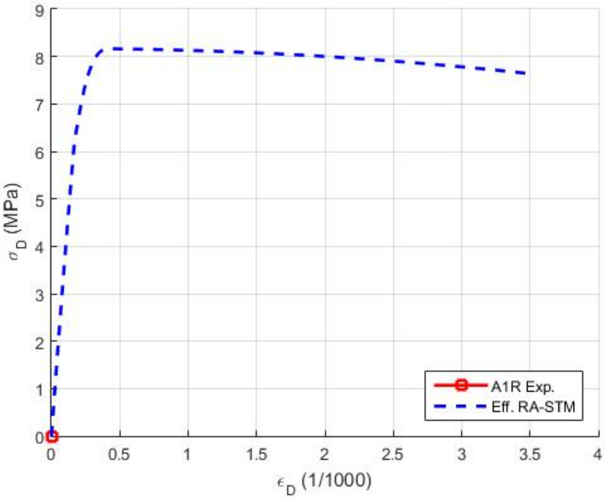

Curva $\sigma_D - \varepsilon_D$

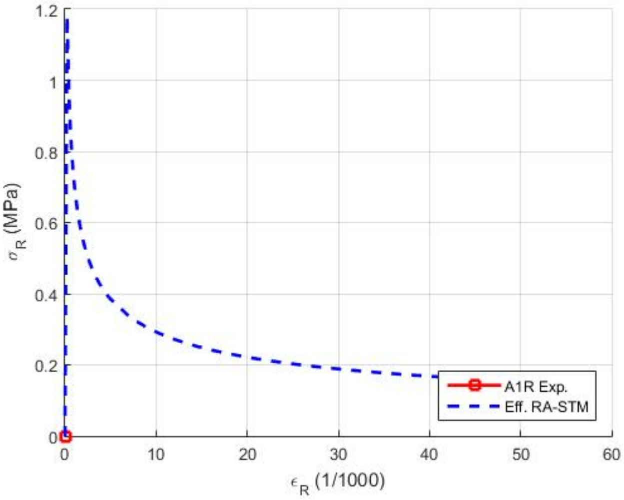

Curva $\sigma_R - \varepsilon_R$

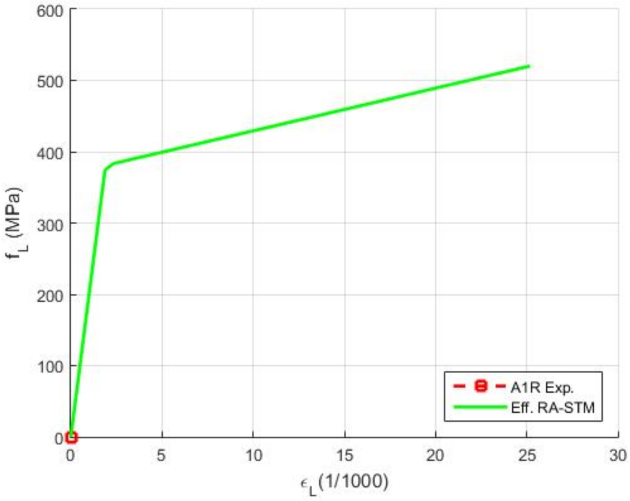

Curva $f_L - \varepsilon_L$

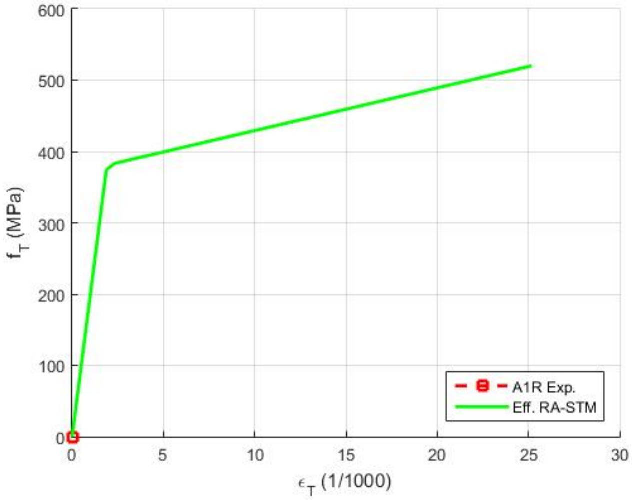

Curva $f_T - \varepsilon_T$

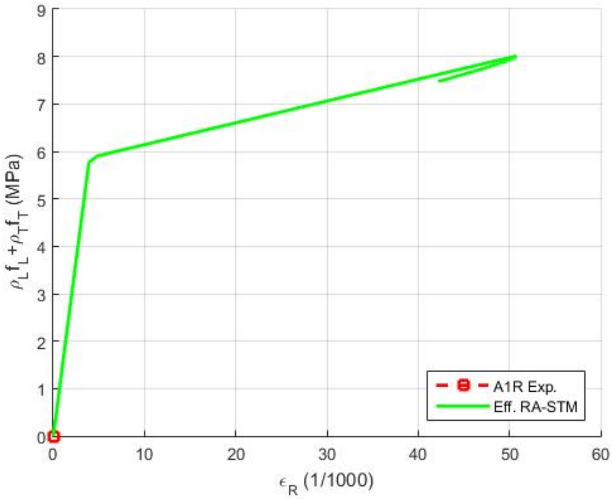

Curva $\rho_L f + \rho_T f_T - \varepsilon_R$

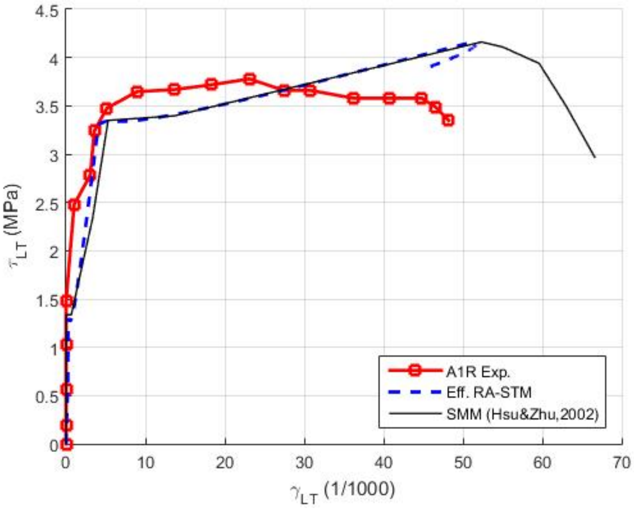

Curva $\tau_{LT} - \gamma_{LT}$

Placa A2 (Pang e Hsu, 1995)

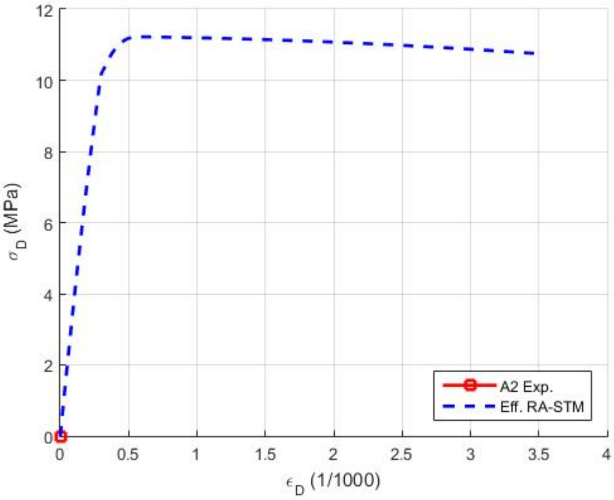

Curva $\sigma_D - \varepsilon_D$

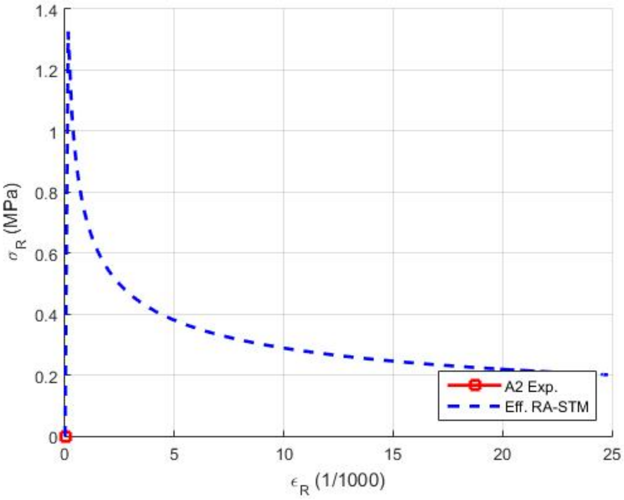

Curva $\sigma_R - \varepsilon_R$

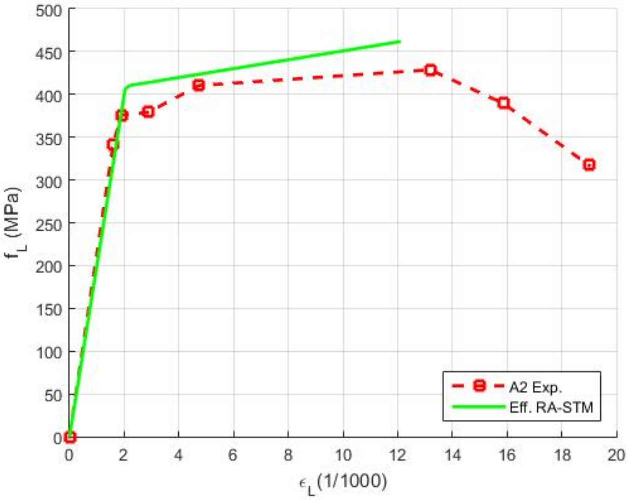

Curva $f_L - \varepsilon_L$

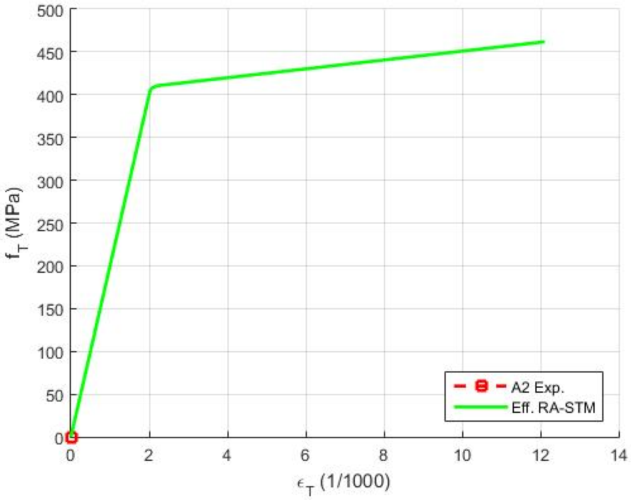

Curva $f_T - \varepsilon_T$

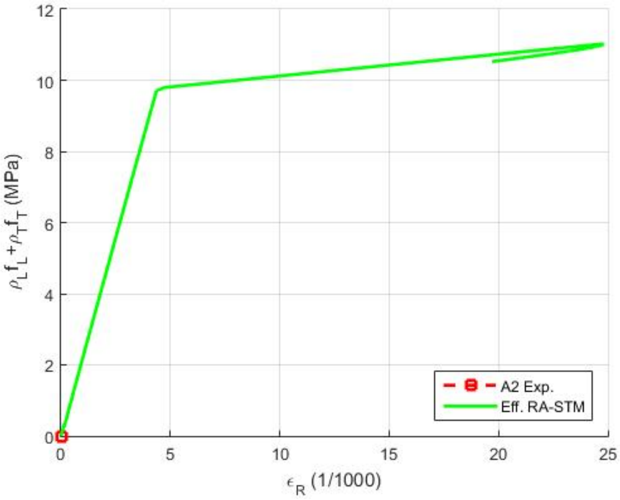

Curva $\rho_L f + \rho_T f_T - \varepsilon_R$

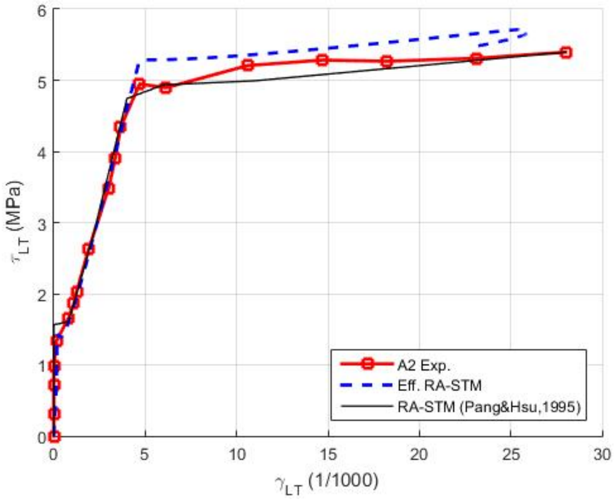

Curva $\tau_{LT} - \gamma_{LT}$

Placa A3 (Pang e Hsu, 1995)

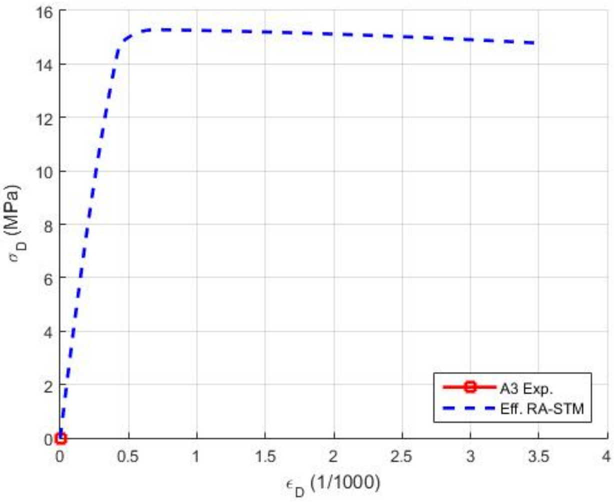

Curva $\sigma_D - \varepsilon_D$

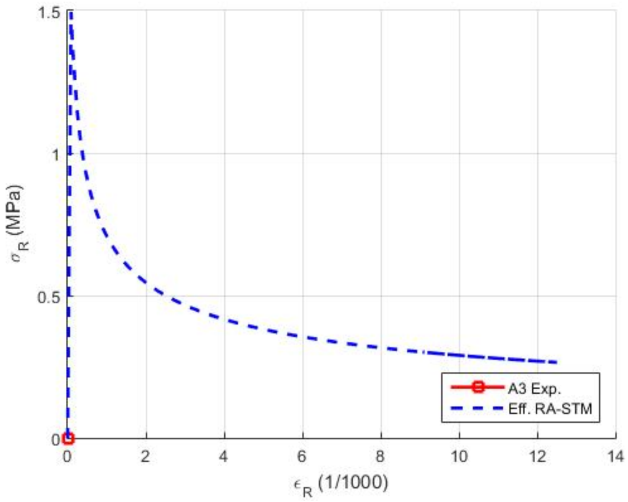

Curva $\sigma_R - \varepsilon_R$

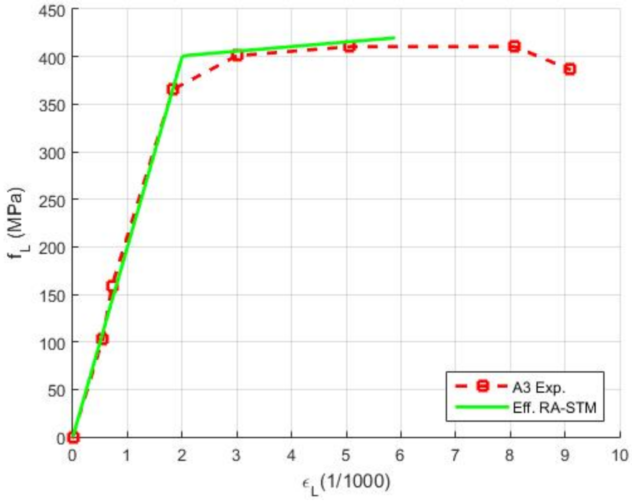

Curva $f_L - \varepsilon_L$

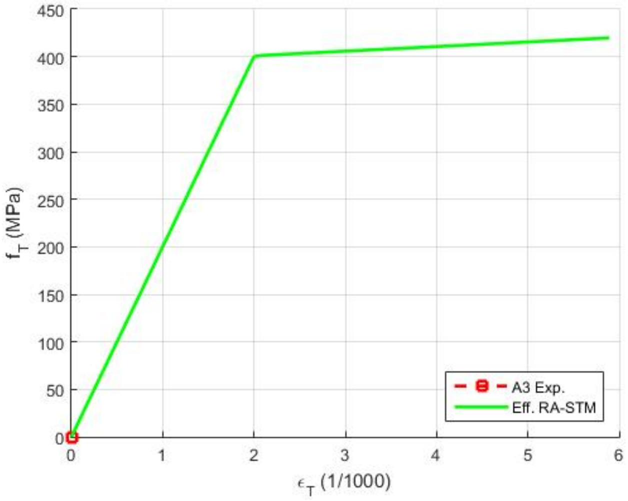

Curva $f_T - \varepsilon_T$

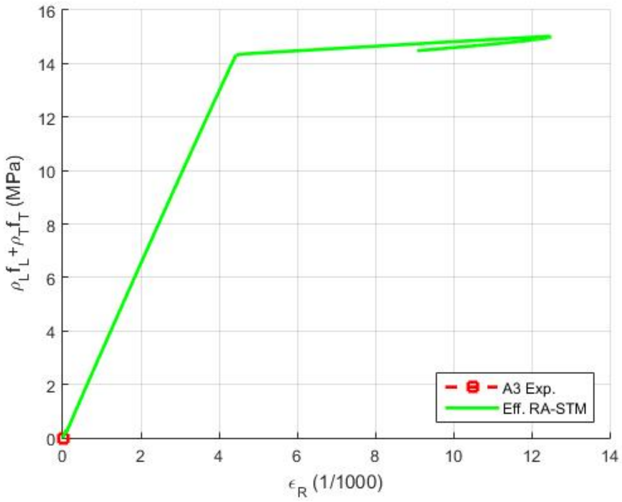

Curva $\rho_L f + \rho_T f_T - \varepsilon_R$

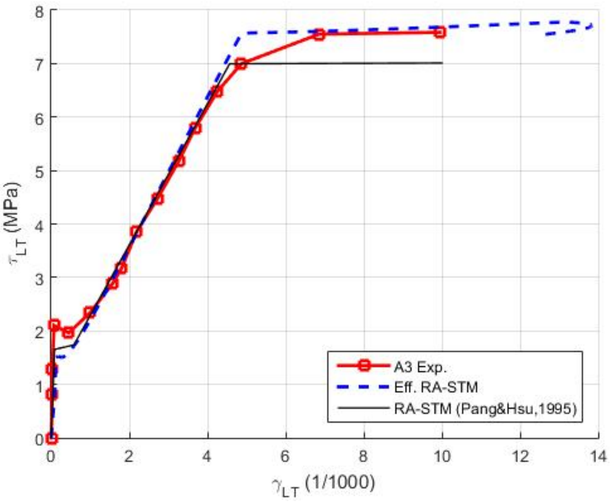

Curva $\tau_{LT} - \gamma_{LT}$

Placa A4 (Pang e Hsu, 1995)

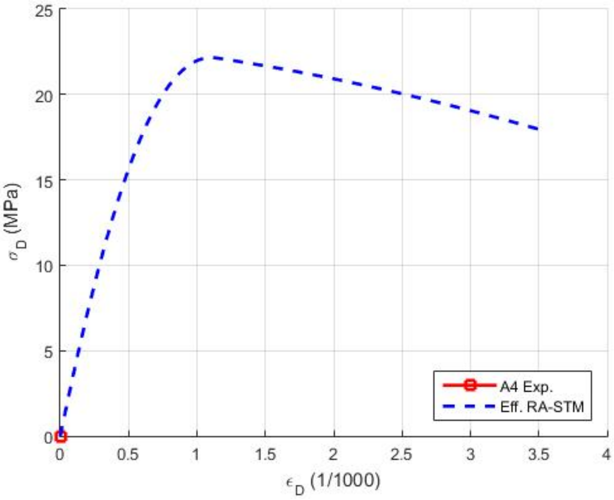

Curva $\sigma_D - \varepsilon_D$

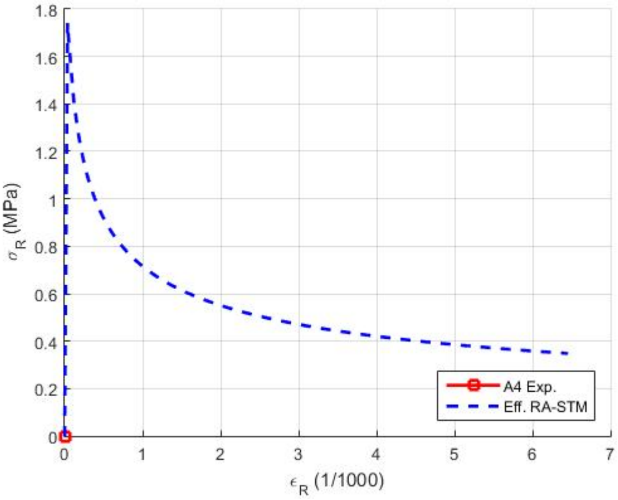

Curva $\sigma_R - \varepsilon_R$

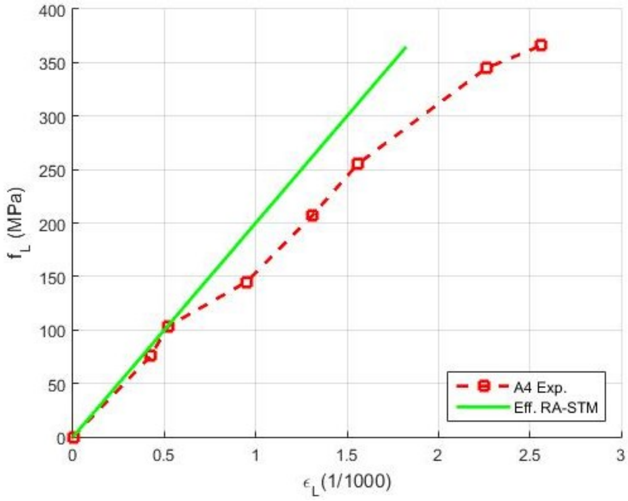

Curva $f_L - \varepsilon_L$

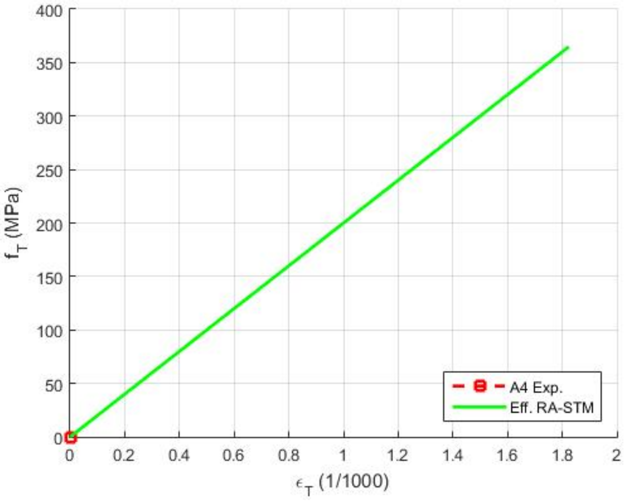

Curva $f_T - \varepsilon_T$

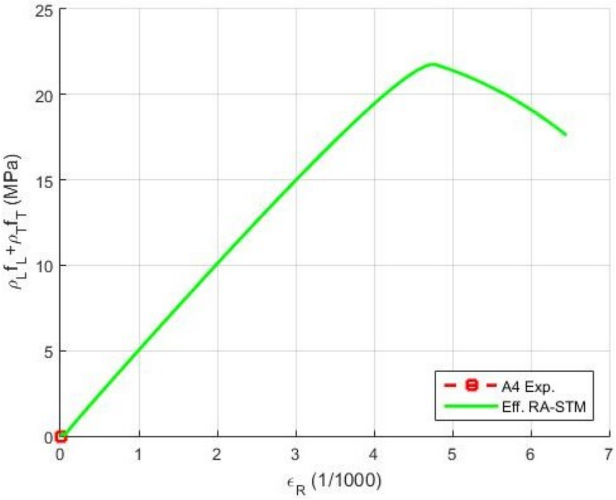

Curva $\rho_L f + \rho_T f_T - \varepsilon_R$

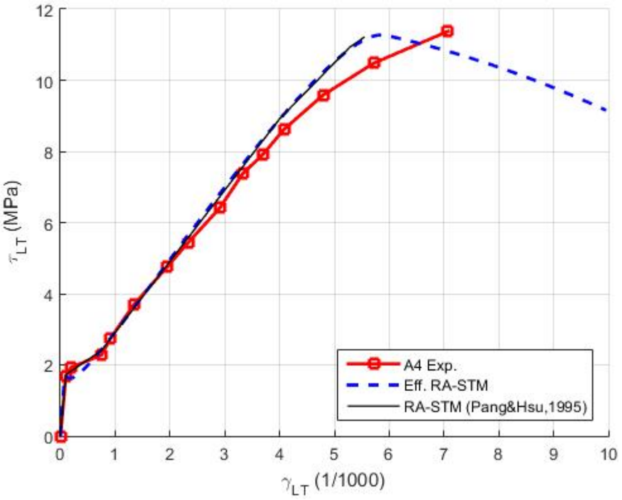

Curva $\tau_{LT} - \gamma_{LT}$

Placa B1 (Pang e Hsu, 1995)

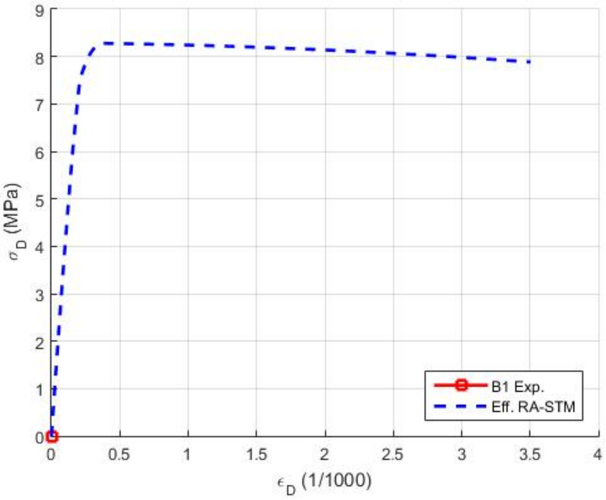

Curva $\sigma_D - \varepsilon_D$

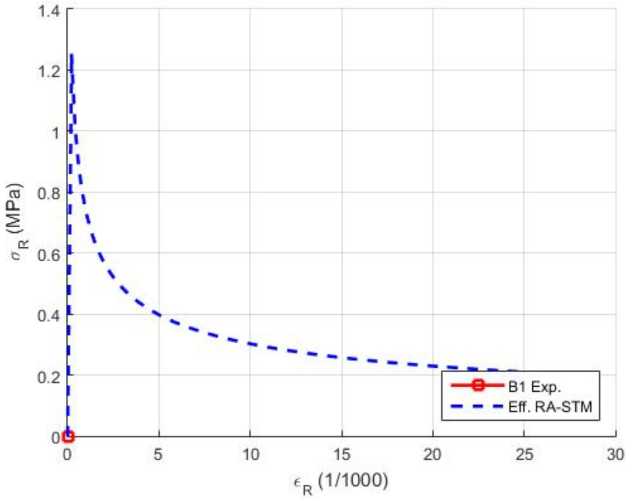

Curva $\sigma_R - \varepsilon_R$

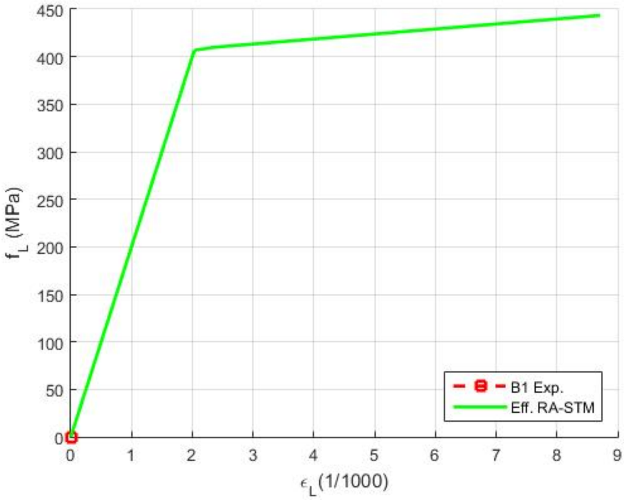

Curva $f_L - \varepsilon_L$

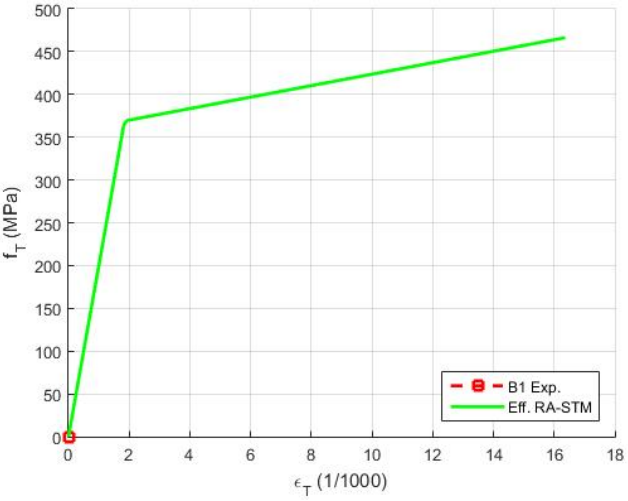

Curva $f_T - \varepsilon_T$

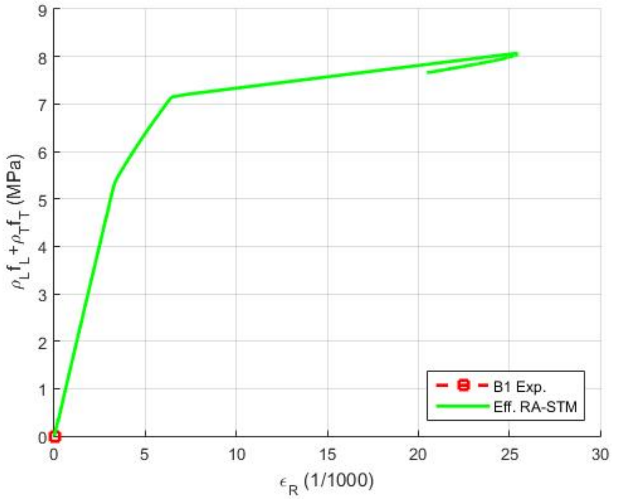

Curva $\rho_L f + \rho_T f_T - \varepsilon_R$

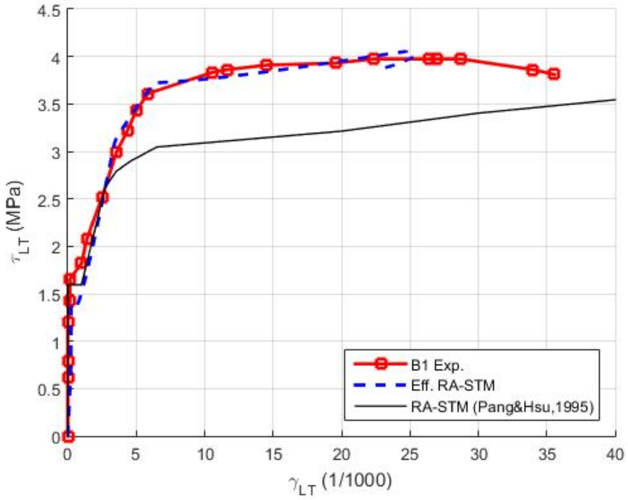

Curva $\tau_{LT} - \gamma_{LT}$

Placa B2 (Pang e Hsu, 1995)

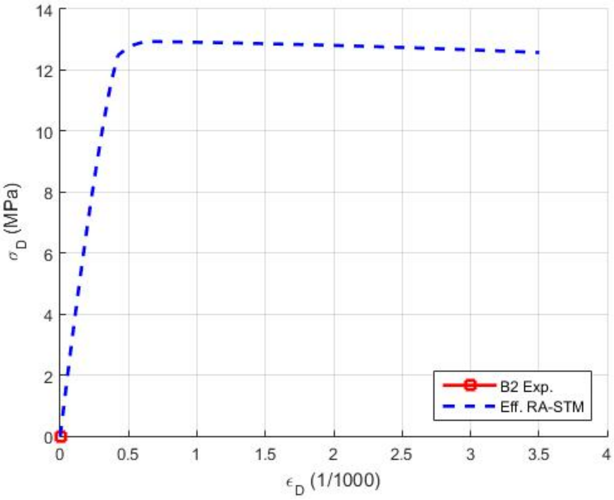

Curva $\sigma_D - \varepsilon_D$

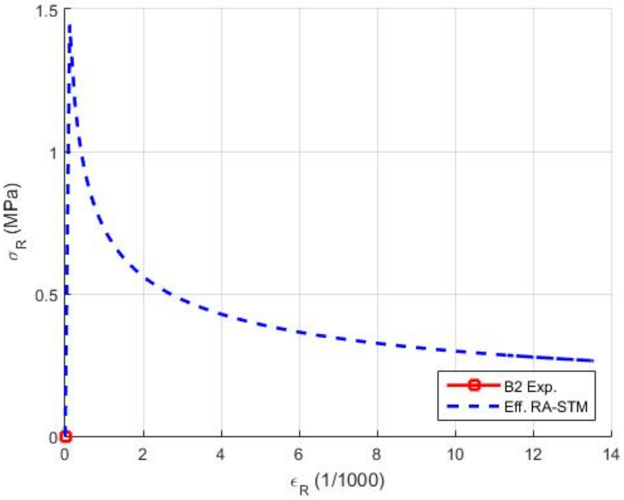

Curva $\sigma_R - \varepsilon_R$

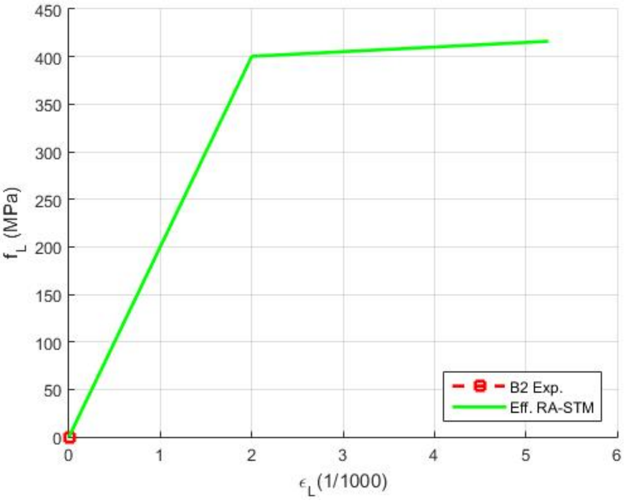

Curva $f_L - \varepsilon_L$

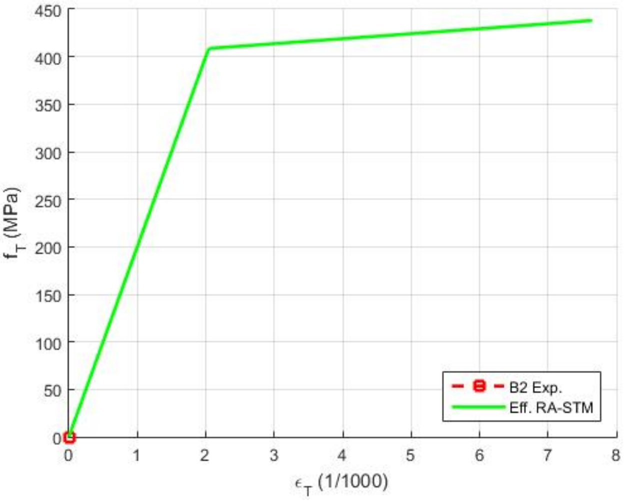

Curva $f_T - \varepsilon_T$

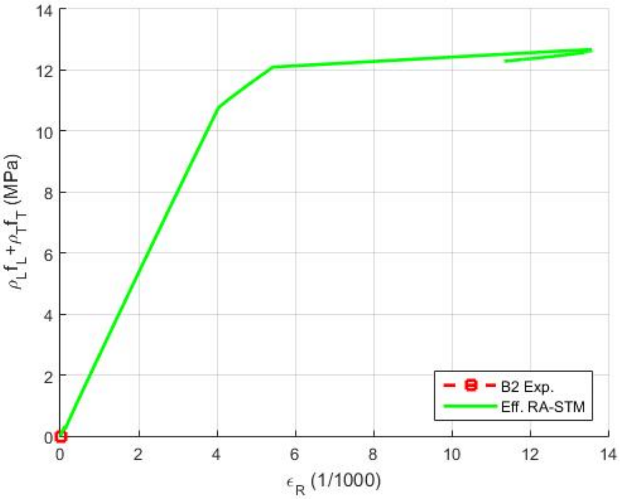

Curva $\rho_L f + \rho_T f_T - \varepsilon_R$

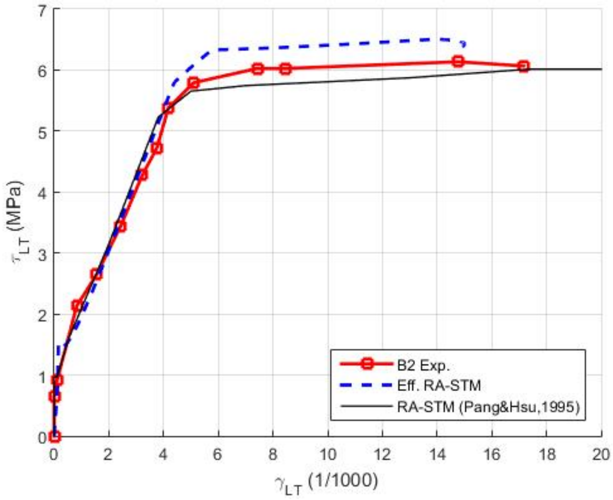

Curva $\tau_{LT} - \gamma_{LT}$

Placa B3 (Pang e Hsu, 1995)

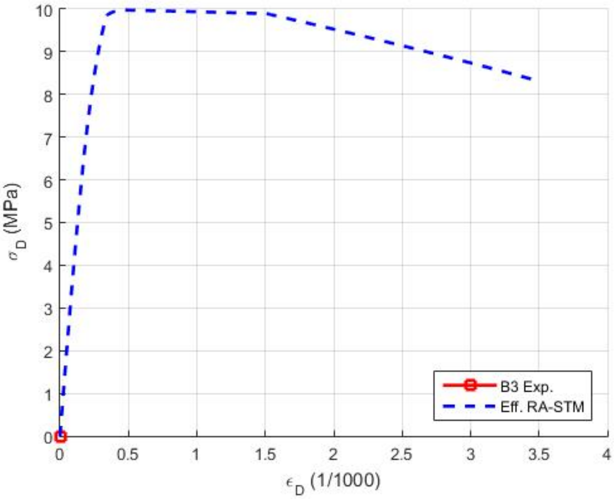

Curva $\sigma_D - \varepsilon_D$

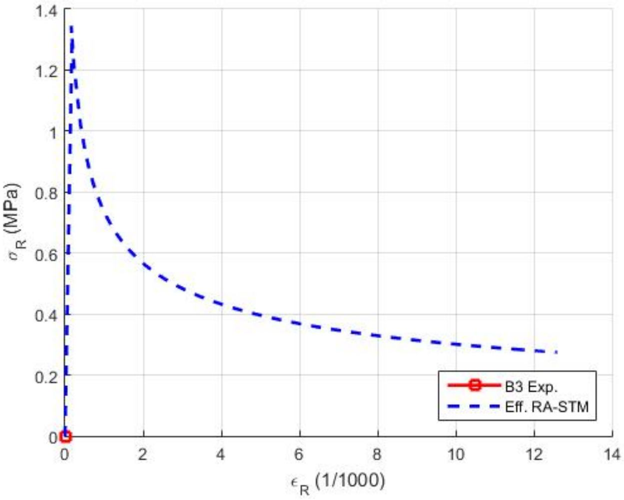

Curva $\sigma_R - \varepsilon_R$

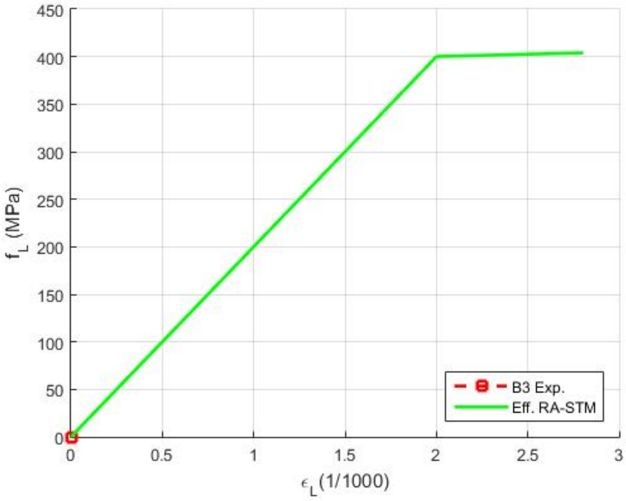

Curva $f_L - \varepsilon_L$

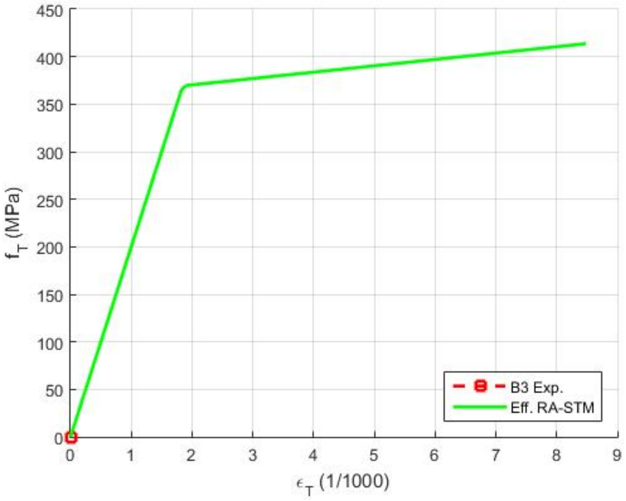

Curva $f_T - \varepsilon_T$

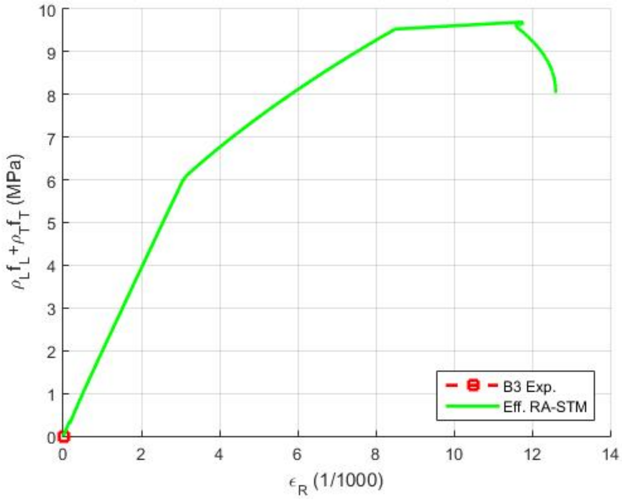

Curva $\rho_L f + \rho_T f_T - \varepsilon_R$

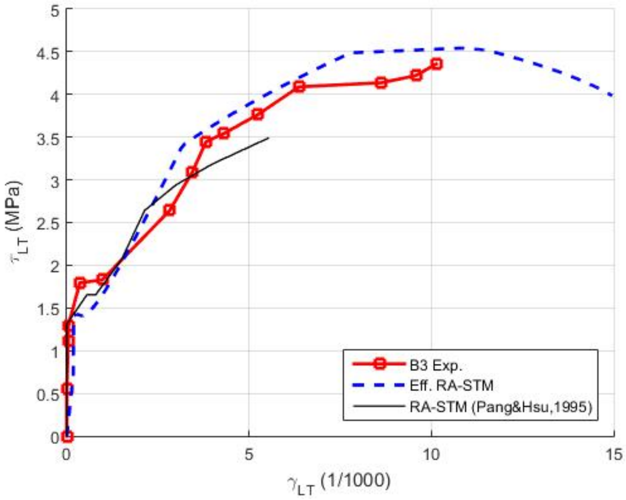

Curva $\tau_{LT} - \gamma_{LT}$

Placa B4 (Pang e Hsu, 1995)

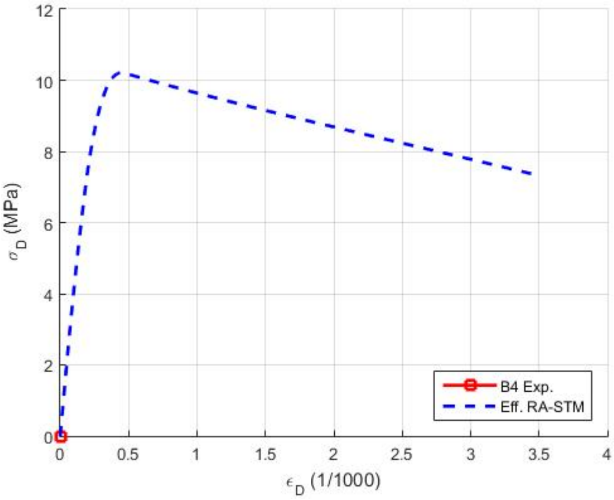

Curva $\sigma_D - \varepsilon_D$

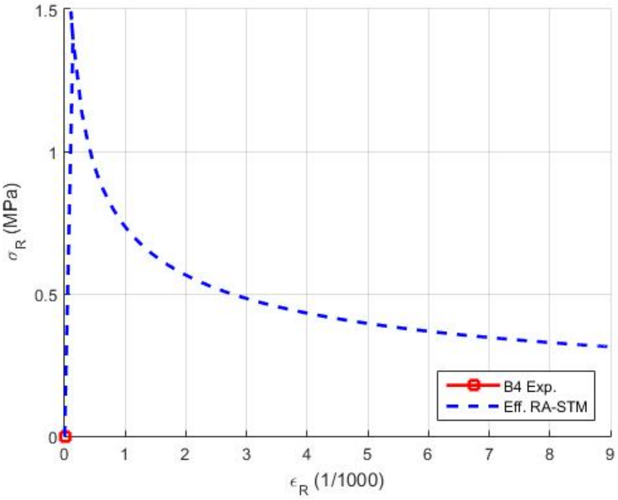

Curva $\sigma_R - \varepsilon_R$

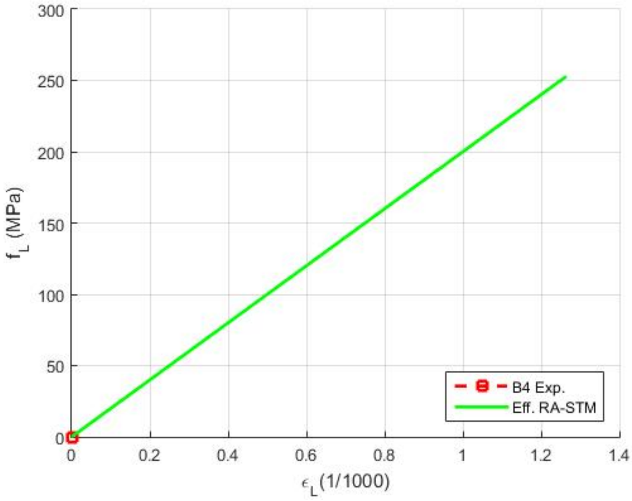

Curva $f_L - \varepsilon_L$

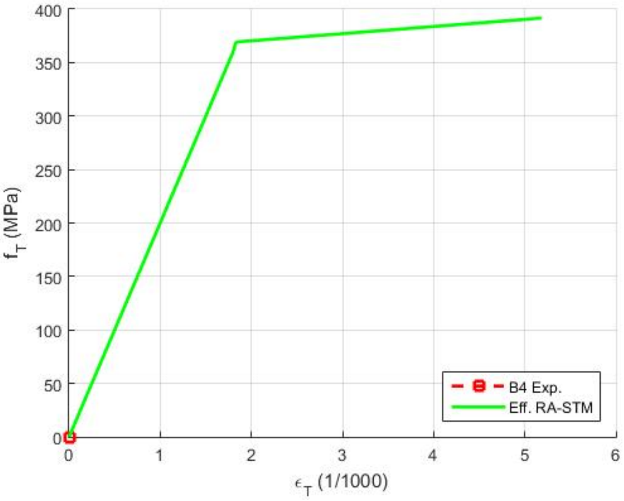

Curva $f_T - \varepsilon_T$

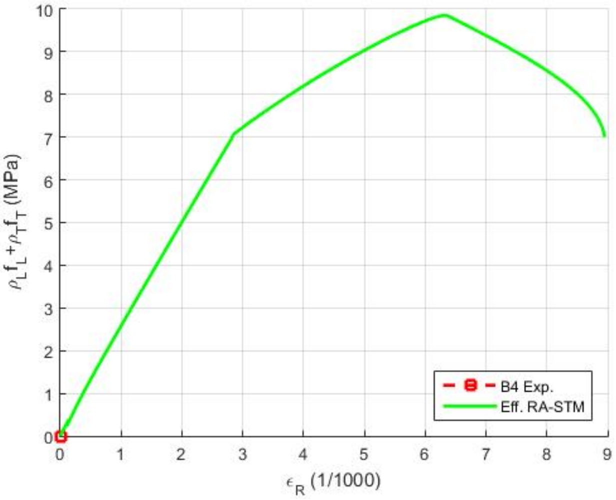

Curva $\rho_L f + \rho_T f_T - \varepsilon_R$

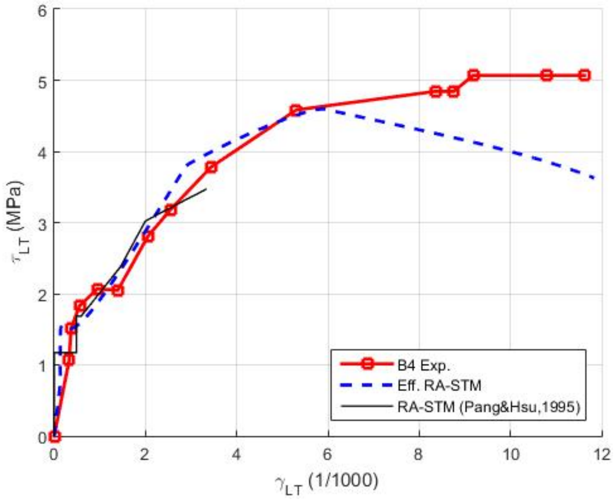

Curva $\tau_{LT} - \gamma_{LT}$

Placa B5 (Pang e Hsu, 1995)

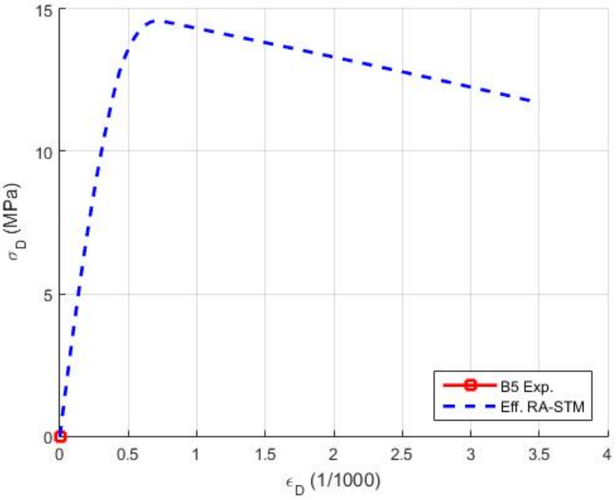

Curva $\sigma_D - \varepsilon_D$

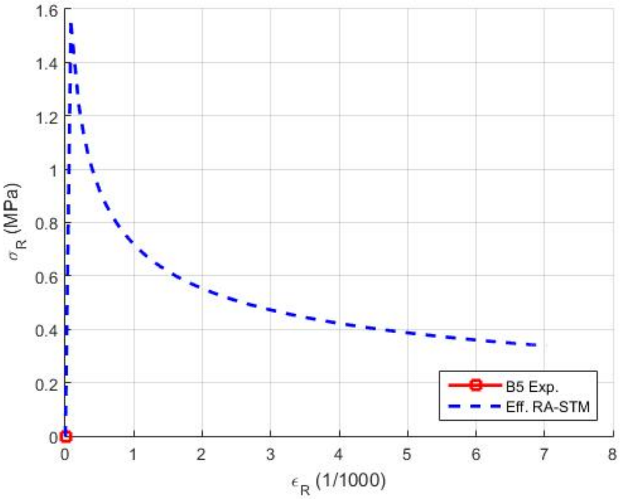

Curva $\sigma_R - \varepsilon_R$

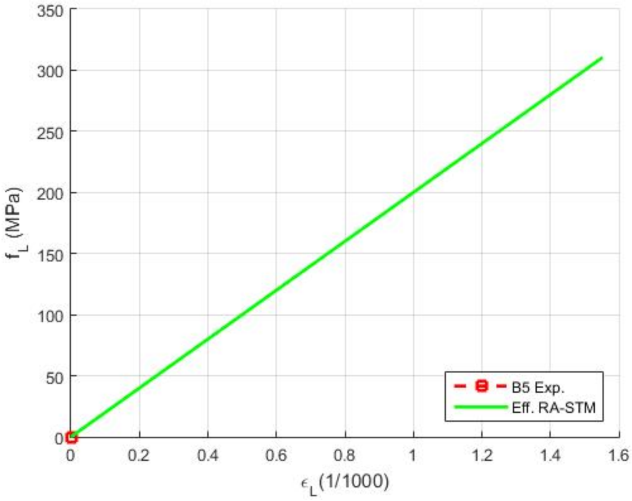

Curva $f_L - \varepsilon_L$

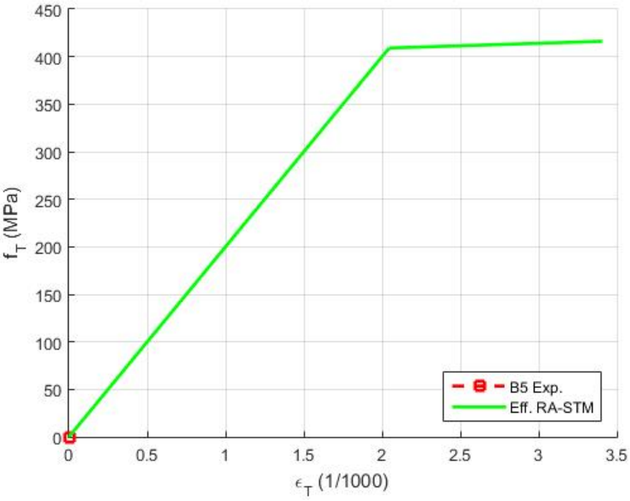

Curva $f_T - \varepsilon_T$

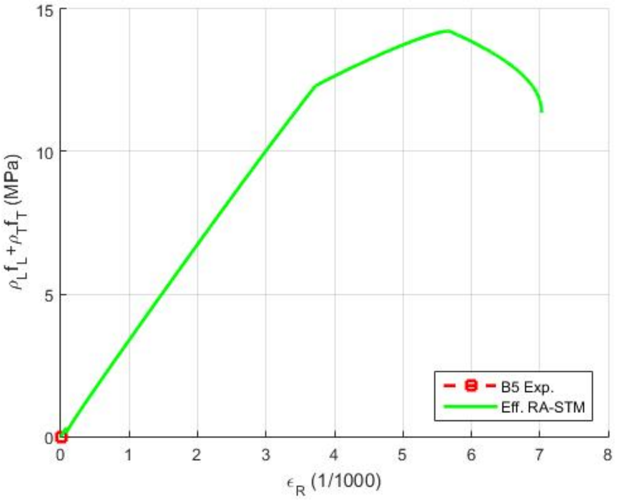

Curva $\rho_L f + \rho_T f_T - \varepsilon_R$

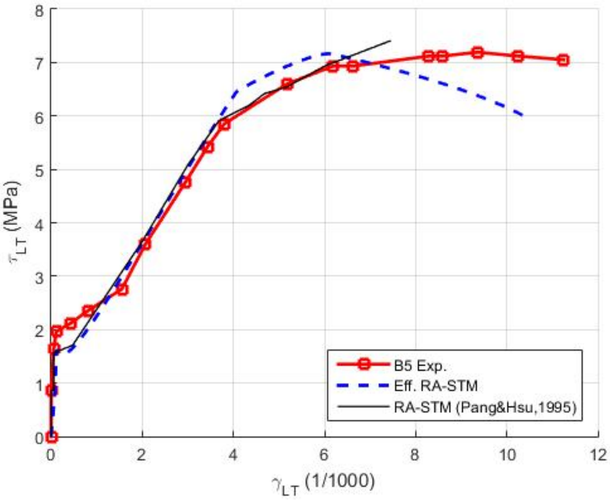

Curva $\tau_{LT} - \gamma_{LT}$

Placa B6 (Pang e Hsu, 1995)

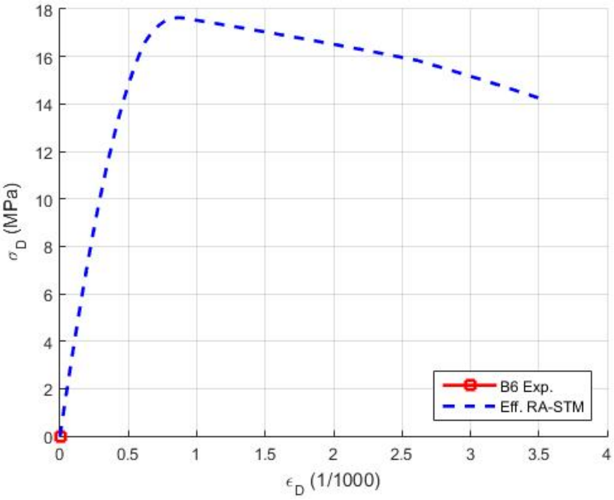

Curva $\sigma_D - \varepsilon_D$

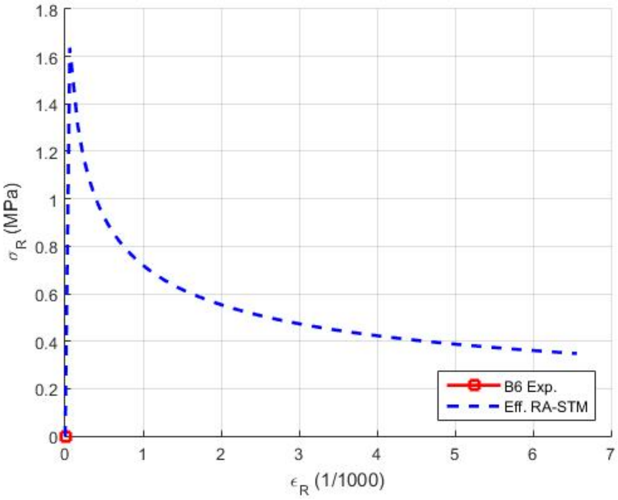

Curva $\sigma_R - \varepsilon_R$

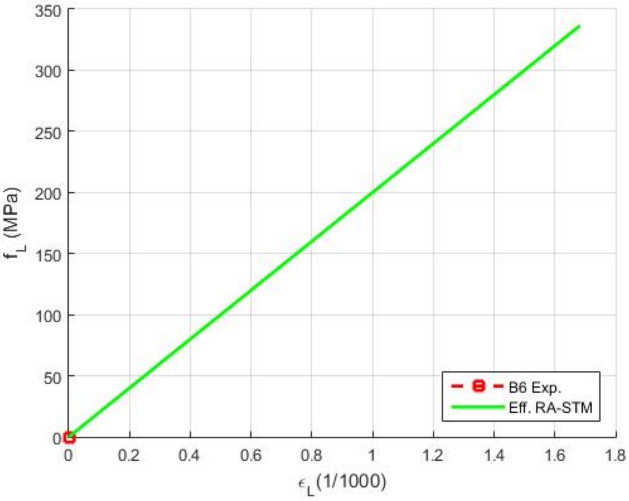

Curva $f_L - \varepsilon_L$

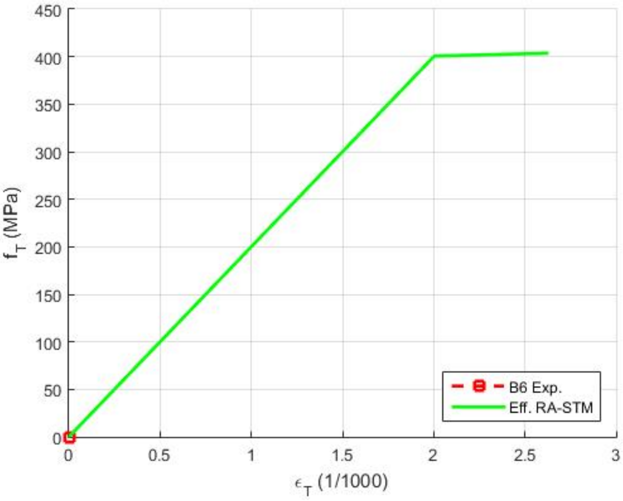

Curva $f_T - \varepsilon_T$

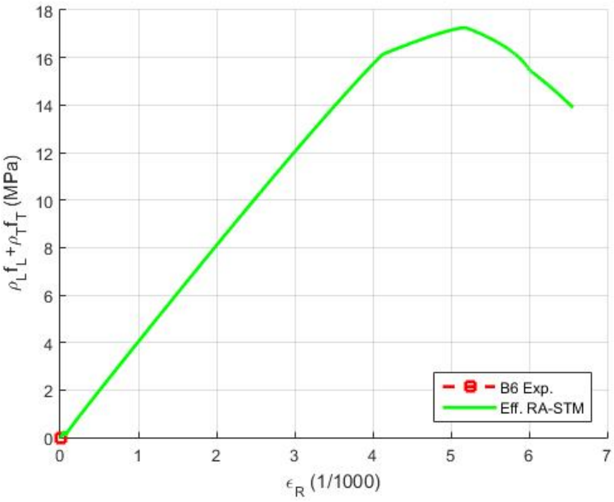

Curva $\rho_L f + \rho_T f_T - \varepsilon_R$

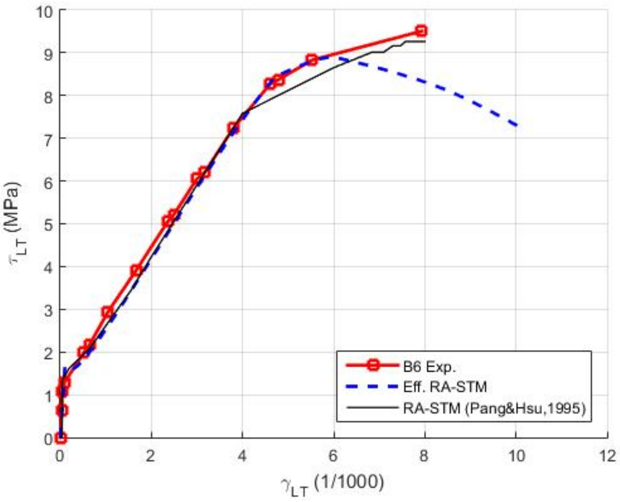

Curva $\tau_{LT} - \gamma_{LT}$

Placa F2 (Hsu e Zhang, 1996)

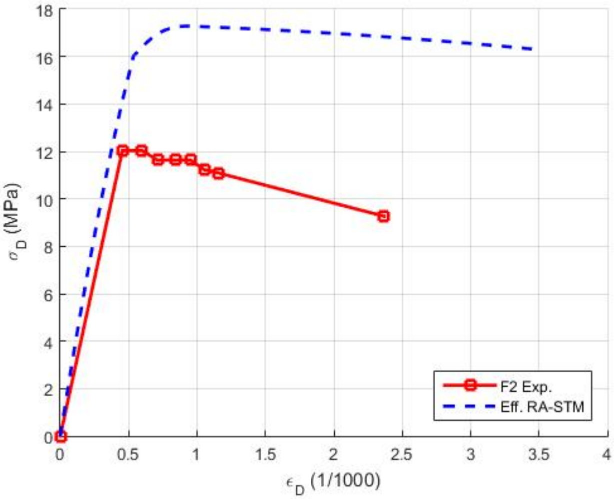

Curva $\sigma_D - \varepsilon_D$

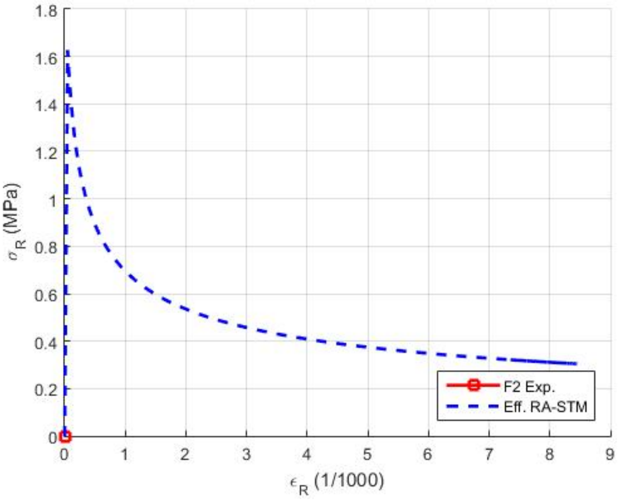

Curva $\sigma_R - \varepsilon_R$

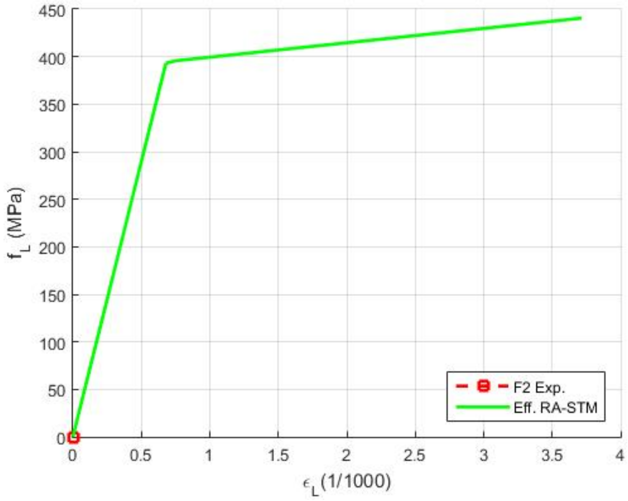

Curva $f_L - \varepsilon_L$

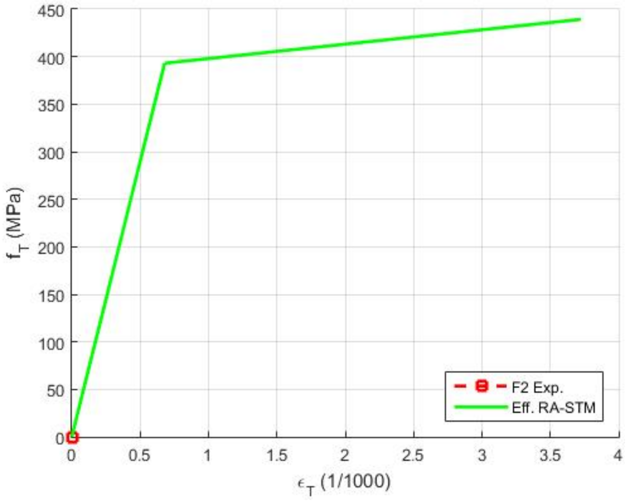

Curva $f_T - \varepsilon_T$

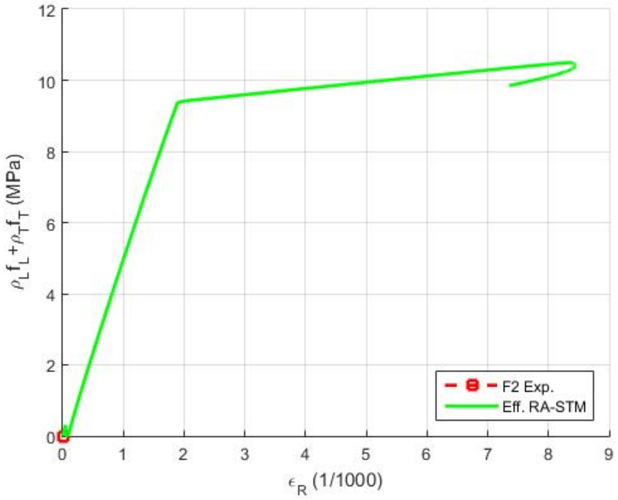

Curva $\rho_L f + \rho_T f_T - \varepsilon_R$

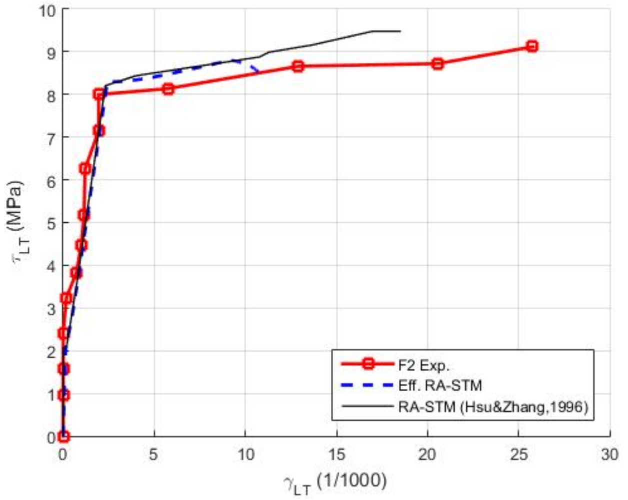

Curva $\tau_{LT} - \gamma_{LT}$

Placa F3 (Hsu e Zhang, 1996)

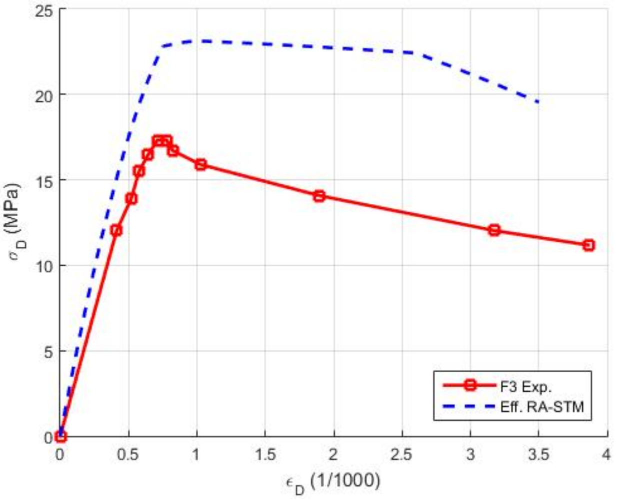

Curva $\sigma_D - \varepsilon_D$

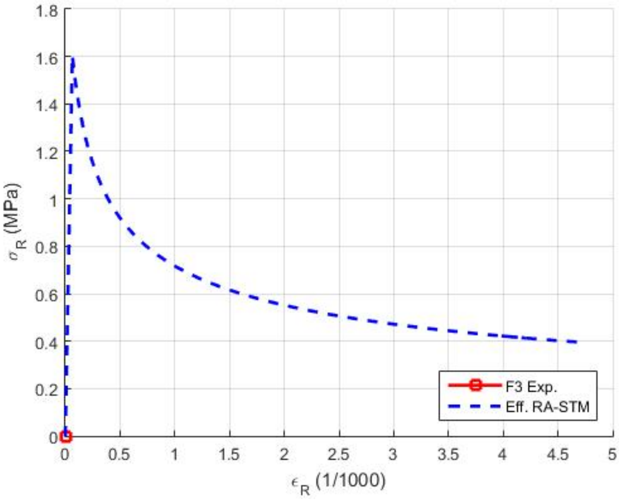

Curva $\sigma_R - \varepsilon_R$

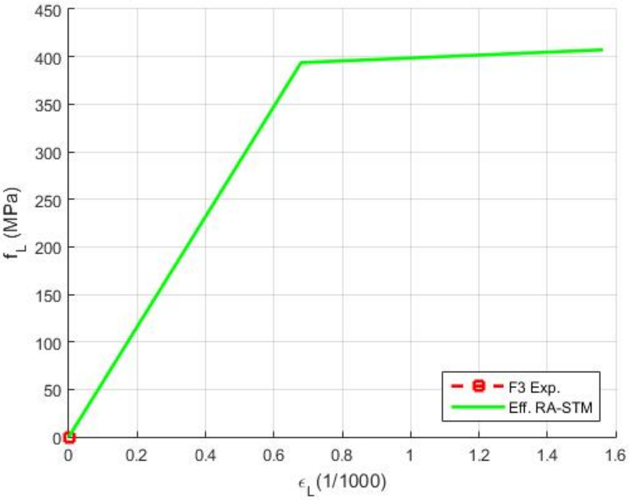

Curva $f_L - \varepsilon_L$

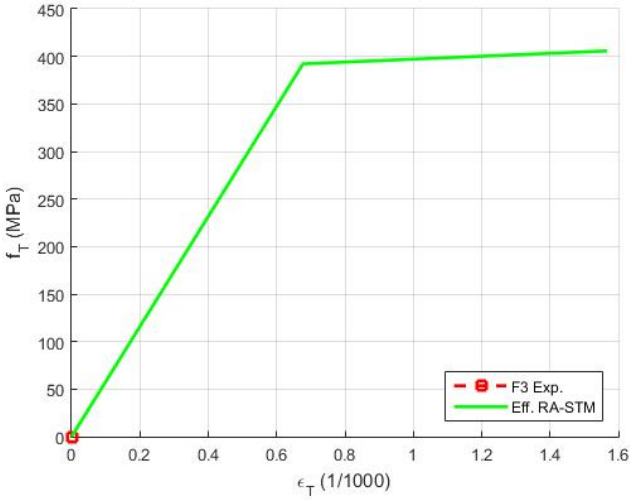

Curva $f_T - \varepsilon_T$

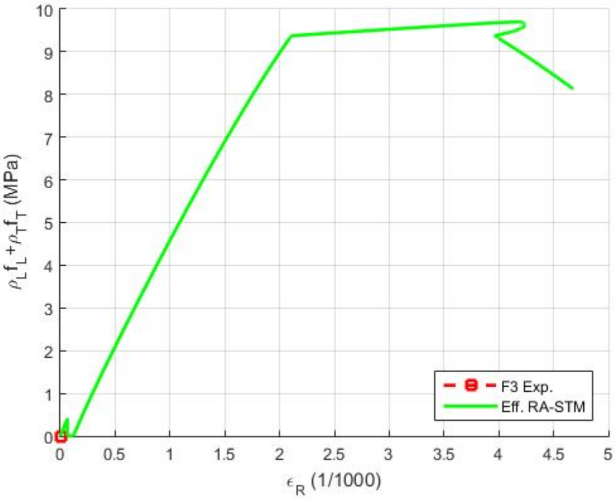

Curva $\rho_L f + \rho_T f_T - \varepsilon_R$

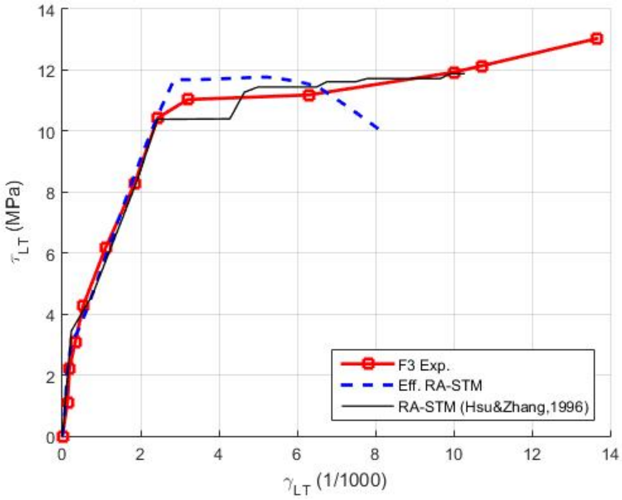

Curva $\tau_{LT} - \gamma_{LT}$

Placa F4 (Hsu e Zhang, 1996)

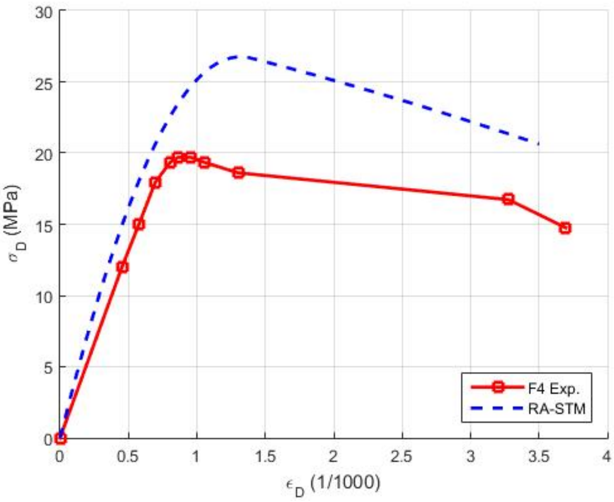

Curva $\sigma_D - \varepsilon_D$

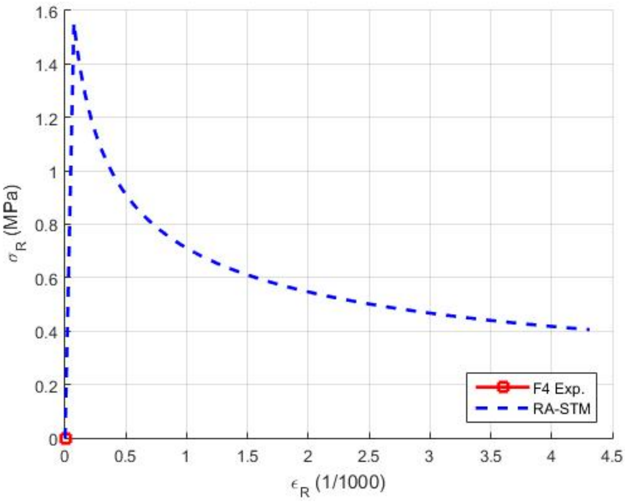

Curva $\sigma_R - \varepsilon_R$

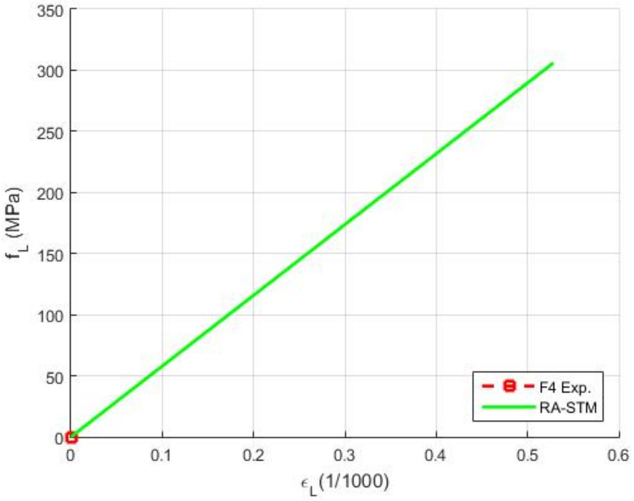

Curva $f_L - \varepsilon_L$

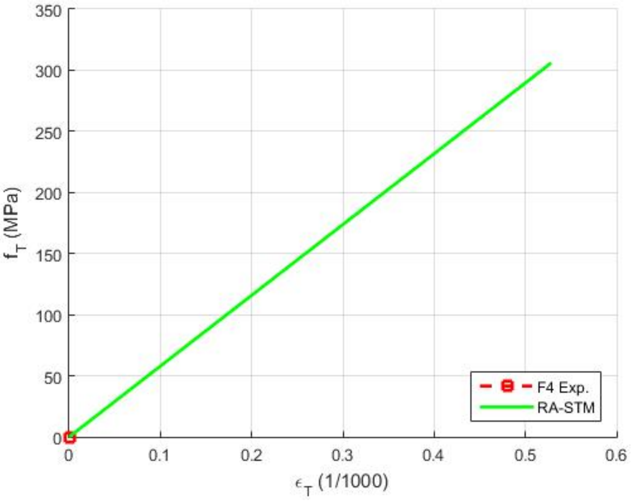

Curva $f_T - \varepsilon_T$

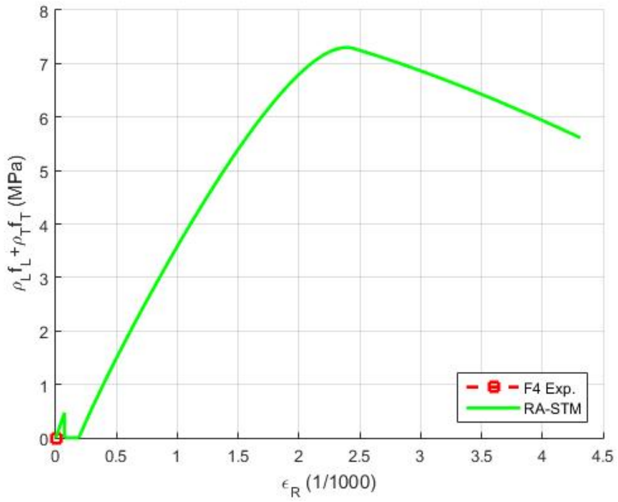

Curva $\rho_L f + \rho_T f_T - \varepsilon_R$

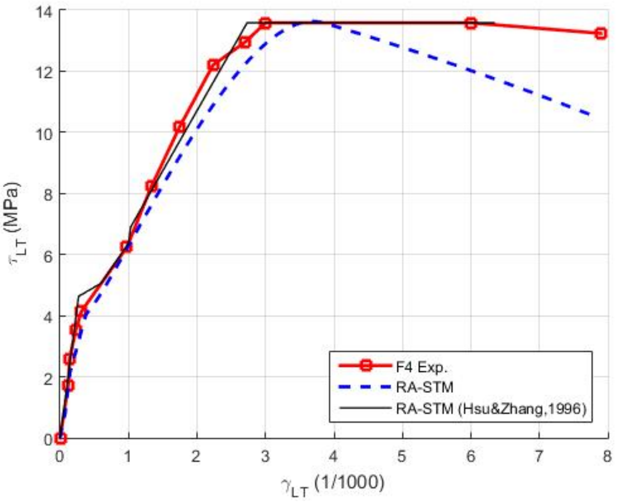

Curva $\tau_{LT} - \gamma_{LT}$

Anexo III. Código em MATLAB do RA-STM PC v2

Script para iniciar o RA-STM PC v2

```
%/////////////////////////////////////////////////////////////////////////////
///
% RA-STM PC v2 - ROTATING ANGLE SOFTENED TRUSS MODEL - PRESSTRESSED CONCRETE
v2 /
%/////////////////////////////////////////////////////////////////////////////
///

% Início
clear all; clc;

% Dados de entrada e escolha da placa
DADOS_INICIAIS; tic;

% Cálculo das estimativas iniciais (MCTM)
alfaD1 = (lsqnonlin(@(alfaD) MCTM_PLACA(alfaD),0.01,[],0))*180/pi;

% Vetores finais e solução
COMP_PLACA;

% Plotagem
toc; PLOT_PLACA;
```

Função para a escolha das placas / Introdução dos dados iniciais

```
function DADOS_INICIAIS

%//////////////////////////////////////////////////////////////////////////
% SELEÇÃO DA PLACA                                                        /
%//////////////////////////////////////////////////////////////////////////

disp('Selecione os dados iniciais');
disp(' ');
disp('1 - TA-1 - NSC: fcm=41.47 MPa - Laskar, A. et al. (2007)');
disp('2 - TA-2 - NSC: fcm=41.33 MPa - Laskar, A. et al. (2007)');
disp('3 - TA-3 - NSC: fcm=42.21 MPa - Laskar, A. et al. (2007)');
disp('4 - TA-4 - NSC: fcm=42.54 MPa - Laskar, A. et al. (2007)');
disp('5 - TA-5 - NSC: fcm=41.08 MPa - Laskar, A. et al. (2007)');
disp('6 - PP2 - NSC: fcm=28.10 MPa - Marti e Meyboom (1992)');
disp('7 - PP3 - NSC: fcm=27.70 MPa - Marti e Meyboom (1992)');
disp(' ');
disp('8 - Introduzir manualmente os dados iniciais');
disp(' ');
disp('0 - Sair');
disp(' ');

INDD = input('Escolha uma opção: ');

if INDD >= 0 & INDD <= 8
    switch INDD

        case 1
            TA_1_LASKAR_e_al;
        case 2
            TA_2_LASKAR_e_al;
        case 3
            TA_3_LASKAR_e_al;
        case 4
            TA_4_LASKAR_e_al;
        case 5
            TA_5_LASKAR_e_al;
        case 6
            PP2_MARTI_e_MEYBOOM;
        case 7
            PP3_MARTI_e_MEYBOOM;
        case 8
            INTRODUZIR_DADOS;
        case 0
            error('SCRIPT INTERROMPIDO')
            clc
    end
else
    disp(' ');
    disp('O VALOR INTRODUZIDO NÃO É VÁLIDO!');
    disp(' ');
    DADOS_INICIAIS
end
end
```

Exemplo de dados experimentais: Placa TA-5

```
function TA_5_LASKAR_e_al

%//////////////////////////////////////////////////////////////////////////
% DADOS EXPERIMENTAIS DA PLACA TA-5 - Laskar et al (2007)                /
%//////////////////////////////////////////////////////////////////////////

global roL roT Es fLy fTy Ec fcm e0 tal sigL sigT eLy eTy fp01
global sig1 mLT mL mT
global e_plot sigmaD_plot tal_smm_plot gama_smm_plot fpulinha
global tal_plot gama_plot a b Ac m ed_plot tal_ed_plot
global roLP roTP ElpsL ElpsT EpsL EpsT edecL edecT fpu fpiL fpiT zL zT ApsT
ApsL  dET dEL yL yT
global AsL AsT Aps ePiL ePiT eLiL eLiT er_plot tal_er_plot e_smm_plot
sigmaD_smm_plot d

%Propriedades da secção de betão
Ac= 17.8*139.8; %Área bruta da secção de betão (cm^2)

%Propriedades mecânicas dos aços ordinários:
Es  = 192200; %Módulo de elasticidade do aço (MPa)
fLy = 415.1; %Tensão de cedência do aço longitudinal (MPa)
fTy = 415.1; %Tensão de cedência do aço transversal (MPa)
AsL= 2.76;  %Área mínima de aço ordinário Longitudinal (cm^2)
AsT= 19.16; %Área de aço ordinário Transversal (cm^2)

%Criar vetores:
roL = AsL/Ac; %Taxa Mec. de armadura ordinária Longitudinal.
roT = AsT/Ac; %Taxa Mec. de armadura ordinária Transversal.

%Propriedades mecânicas dos aços de pré-esforço:
ElpsL = 209000; %Módulo de elasticidade de Ramberg-Osgood P.E-Longitudinal
(MPa)
ElpsT = 209000; %Módulo de elasticidade de Ramberg-Osgood P.E-Transversal
(MPa)
EpsL = 200000; %Módulo de elasticidade da armadura de P.E-Longitudinal (MPa)
EpsT = 200000; %Módulo de elasticidade da armadura de P.E-Transversal (MPa)
fpu = 1793;
fpulinha= 1862; %Tensão última da armadura de P.E. (MPa)
fp01 = 1670;  %Tensão de propocionalidade (MPa)
m =5;
ApsL= 10.45;
ApsT= 0;
fpiL=986;
fpiT=0;


% Propriedades mecânicas do betão:
fcm = 41.08;         %Resistência média do betão(MPa)
Ec = 3875*sqrt(fcm); %Módulo de elasticidade do betão (MPa)(Belarbi e Hsu
(1994))
e0  = -2.1;          %Deformação última do betão (1/1000)

%CÁLCULOS PRELIMINARES RELATIVOS AO PRÉ-ESFORÇO
Aps=ApsT+ApsL;  %Área total de armadura de P.E.
roLP = ApsL/Ac;  %Taxa Mec. de armadura de P.E-longitudinal
roTP = ApsT/Ac; %Taxa Mec. de armadura de P.E-transversal.
ePiL= fpiL/EpsL; %Extensão inicial no aço de P.E-longitudinal
ePiT= fpiT/EpsT; %Extensão inicial no aço de P.E-transversal.
eLiL= ApsL*fpiL/(AsL*(Es-Ec)+Ec*(Ac-ApsL)); %Extensão no aço ordinário
longitudinal
eLiT= ApsT*fpiT/(AsT*(Es-Ec)+Ec*(Ac-ApsT)); %Extensão no aço ordinário
transversal
edecT = ePiT+eLiT;  %Extensão de descompressão transversal
edecL = ePiL+eLiL;   %Extensão de descompressão longitudinal

%Solicitações no elemento de betão armado (L-T):
tal  = -3.69;  %Tensão de corte (MPa)
```

```
sigL =  0;     %Tensão de tração longitudinal (MPa)
sigT =  0;     %Tensão de compressão transversal (MPa)

%CÁLCULOS PRELIMINARES
eLy  = fLy/Es*1000;
eTy  = fTy/Es*1000;
sig1 = (sigL + sigT)/2 + sqrt(((sigL - sigT)/2)^2 + tal^2);
mL   = sigL/sig1;
mT   = sigT/sig1;
mLT  = tal/sig1;

%CORREÇÃO DA CURVA
%Resolução do valor de extensão (Y) para a equação não-linear:
%Análise Longitudinal
%Definir yL como variável simbólica
syms yL
%Equação a resolver
y=-0.7*fpulinha+ElpsL*(yL)/(1+(ElpsL*(yL)/fpu)^m)^(1/m);
yL=solve(y,yL);
%Retornar o valor em número:
yL=double(yL);
%Análise Transversal;
%Definir yT como variável simbólica
syms yT
%Equação a resolver
y=-0.7*fpulinha+ElpsT*(yT)/(1+(ElpsT*(yT)/fpu)^m)^(1/m);
yT=solve(y,yT);
%Retornar o valor em número:
yT=double(yT);
%Resolução do valor de extensão (Z) para a equação linear:
%Análise Longitudinal
zL=0.7*fpulinha/EpsL;
%Análise Transversal
zT=0.7*fpulinha/EpsT;
%Calculo do delta E
%Análise longitudinal
dEL= zL-yL;
%Análise transversal
dET= zT-yT;

%DADOS PLOTAGEM DA PLACA TA-5
e_plot      = [0;-0.0005*10^2;-0.0007*10^2;-0.0013*10^2;-0.0007*10^2;-
0.0014*10^2;-0.0017*10^2;-0.0018*10^2;-0.0021*10^2;-0.0025*10^2;-0.0023*10^2;-
0.0020*10^2;-0.0019*10^2;-0.0031*10^2;-0.0053*10^2;-0.0117*10^2;-0.0138*10^2;-
0.0164*10^2;-0.0248*10^2;-0.0333*10^2];
sigmaD_plot = [0;-2.0743;-2.4236;-3.4245;-3.5880;-4.3917;-5.1051;-6.3701;-
7.2823;-8.0491;-8.4663;-8.8341;-9.0645;-9.3766;-9.3134;-8.9090;-8.7938;-
8.7715;-8.4009;-8.1730];
e_smm_plot  =
[0;0.0010*10^2;0.0015*10^2;0.0021*10^2;0.0026*10^2;0.0030*10^2;0.0032*10^2;0.0
036*10^2;0.0041*10^2;0.0045*10^2;0.0056*10^2;0.0090*10^2;0.0143*10^2;0.0185*10
^2;0.0196*10^2;0.0266*10^2;0.0355*10^2];
sigmaD_smm_plot =
[0;3.8163;5.6827;7.2782;8.0703;8.6450;9.0112;9.3144;9.6175;9.7311;9.7122;9.453
3;9.0933;8.7585;8.5432;7.9269;7.1273];

tal_plot    =
[0;1.7113;2.8281;3.1311;3.4866;3.8684;4.2211;4.3975;4.5343;4.5702;4.6321;4.736
2;4.7264;4.7948;4.7851;4.5603;4.5179;4.4919;4.3187;4.2079;4.0112;3.9233;3.7930
;3.5291;3.2131];
gama_plot   =
[0;0.0001*10^3;0.0002*10^3;0.0004*10^3;0.0010*10^3;0.0020*10^3;0.0029*10^3;0.0
040*10^3;0.0050*10^3;0.0060*10^3;0.0070*10^3;0.0080*10^3;0.0090*10^3;0.0105*10
^3;0.0120*10^3;0.0131*10^3;0.0140*10^3;0.0151*10^3;0.0176*10^3;0.0195*10^3;0.0
215*10^3;0.0235*10^3;0.0276*10^3;0.0296*10^3;0.0306*10^3];
tal_smm_plot =
[0;1.988305;2.748599;3.509252;3.435904;3.373009;3.743467;4.156094;4.296016;4.4
```

```
40923;4.584589;4.750968;4.950161;4.948201;4.645234;4.454937;4.291455;4.093453;
3.767343;3.401383;2.862037];
gama_smm_plot =
[0;0.000072*10^3;0.000136*10^3;0.000227*10^3;0.000674*10^3;0.001227*10^3;0.002
110*10^3;0.003161*10^3;0.004413*10^3;0.005310*10^3;0.006098*10^3;0.007382*10^3
;0.009312*10^3;0.009749*10^3;0.011971*10^3;0.013344*10^3;0.013989*10^3;0.01540
5*10^3;0.017388*10^3;0.019351*10^3;0.021708*10^3];

er_plot     =
[0;0.0001*10^2;0.0003*10^2;0.0009*10^2;0.0018*10^2;0.0028*10^2;0.0038*10^2;0.0
049*10^2;0.0058*10^2;0.0069*10^2;0.0079*10^2;0.0089*10^2;0.0103*10^2;0.0116*10
^2;0.0119*10^2;0.0127*10^2;0.0135*10^2;0.0151*10^2;0.0162*10^2;0.0174*10^2;0.0
186*10^2;0.0197*10^2;0.0208*10^2;0.0218*10^2;0.0222*10^2];
tal_er_plot =
[0;2.7819;3.0835;3.4723;3.8085;4.1552;4.3233;4.4490;4.4910;4.5751;4.6696;4.698
4;4.7327;4.7117;4.5330;4.4805;4.4280;4.2599;4.1821;3.9552;3.8606;3.8017;3.7451
;3.4509;3.1672];
ed_plot     =
[0;0.000012*10^3;0.000030*10^3;0.000065*10^3;0.000089*10^3;0.000099*10^3;0.000
116*10^3;0.000135*10^3;0.000165*10^3;0.000199*10^3;0.000181*10^3;0.000163*10^3
;0.000147*10^3;0.000141*10^3;0.000098*10^3;0.000260*10^3;0.000476*10^3;0.00111
5*10^3;0.001327*10^3;0.001581*10^3;0.002414*10^3];
tal_ed_plot =
[0;0.365346;1.010266;1.703109;2.429199;2.796658;3.115346;3.474420;3.815117;4.1
94067;4.369897;4.498361;4.578853;4.678480;4.671198;4.788921;4.753095;4.550107;
4.483645;4.465054;4.306580];

a = 'TA-5 Exp.';
b = 'Eff. RA-STM';
d = 'SMM-PC (Laskar et al.,2007)';

end
```

Função para a introdução manual dos dados iniciais

```
function INTRODUZIR_DADOS

%//////////////////////////////////////////////////////////////////////////
% DADOS INTRODUZIDOS MANUALMENTE                                          /
%//////////////////////////////////////////////////////////////////////////

global roL roT Es fLy fTy Ec fcm e0 tal sigL sigT eLy eTy fp01
global sig1 mLT mL mT
global e_plot sigmaD_plot tal_smm_plot gama_smm_plot fpulinha
global tal_plot gama_plot a b Ac m ed_plot tal_ed_plot
global roLP roTP  ElpsL ElpsT EpsL EpsT edecL edecT fpu fpiL fpiT zL zT ApsT
ApsL  dET dEL yL yT
global AsL AsT Aps ePiL ePiT eLiL eLiT er_plot tal_er_plot e_smm_plot
sigmaD_smm_plot d

%//////////////////////////////////////////////////////////////////////////
% DADOS INICIAIS                                                          /
%//////////////////////////////////////////////////////////////////////////

% Dados inicias a introduzir pelo utilizador através de uma caixa de
% diálogo
prompt={'Área bruta da secção de betão (cm^2):','Área de armadura longitudinal
ordinária (cm^2):',...
    'Área de armadura transversal ordinária (cm^2):','Tensão de cedência da
armadura longitudinal ordinária (MPa):',...
    'Tensão de cedência da armadura transversal ordinária (MPa):','Módulo de
Elasticidade da armadura ordinária (MPa)',...
    'Área de armadura de pré-esforço longitudinal (cm^2):','Área de armadura
de pré-esforço longitudinal (cm^2):',...
    'Tensão limite de propocionalidade a 0.1% da armadura de pré-esforço
(MPa):',...
    'Tensão última da armadura de pré-esforço (MPa):','Módulo de Elasticidade
da armadura de pré-esforço (MPa):',...
    'Tensão de pré-esforço inicial na armadura de pré-esforço longitudinal
(MPa):',...
    'Tensão de pré-esforço inicial na armadura de pré-esforço transversal
(MPa):',...
    'Resistência do betão à compressão(MPa):','Módulo de elasticidade do betão
(MPa):',...
    'Extensão de compressão do betão correspondente ao pico de tensão
(‰):',...
    'Tensão tangencial no referencial L-T (MPa):','Tensão normal na direção L
(MPa):','Tensão normal na direção T (MPa):'};
title='Dados iniciais';
dims=[0.8 80];
definput={'2488.44','1','19.6','415.1','415.1','192200','10.45','0','1670','17
93','200000','1084.6','0',...
          '41.08','24836','-2.1','-3.69','0','0'}; % Valores por defeito

dados=inputdlg(prompt,title,dims,definput);
dados1=str2double(dados);

% Propriedades da secção de betão:
Ac = dados1(1); %Área bruta da secção de betão (cm^2)

%Propriedades mecânicas das armaduras ordinárias:
AsL = dados1(2); %Área de aço ordinário Longitudinal (cm^2)
AsT = dados1(3); %Área de aço ordinário Transversal (cm^2)
fLy = dados1(4); %Tensão de cedência do aço longitudinal (MPa)
fTy = dados1(5); %Tensão de cedência do aço transversal (MPa)
Es  = dados1(6); %Módulo de elasticidade do aço (MPa)

%Criar vetores:
roL = AsL/Ac; %Taxa Mec. de armadura ordinária Longitudinal.
roT = AsT/Ac; %Taxa Mec. de armadura ordinária Transversal.

%Propriedades mecânicas dos aços de pré-esforço:
```

```
ElpsL = 209000; %Módulo de elasticidade de Ramberg-Osgood P.E-Longitudinal
(MPa)
ElpsT = 209000; %Módulo de elasticidade de Ramberg-Osgood P.E-Transversal
(MPa)
ApsL= dados1(7); %Área de aço de pré-esforço longitudinal (cm^2)
ApsT= dados1(8); %Área de aço de pré-esforço transversal (cm^2)
fp01 = dados1(9);  %Tensão limite de propocionalidade a 0.1% da armadura de
pré-esforço (MPa)
fpu = dados1(10); %Tensão última da armadura de pré-esforço (MPa)
fpulinha= 1862; %Tensão última da armadura de P.E. (MPa)
m =5;
EpsL = dados1(11); %Módulo de elasticidade da armadura de P.E-Longitudinal
(MPa)
EpsT = dados1(11); %Módulo de elasticidade da armadura de P.E-Transversal
(MPa)
fpiL = dados1(12); %Tensão de pré-esforço inicial na armadura de P.E.
longitudinal (MPa)
fpiT = dados1(13); %Tensão de pré-esforço inicial na armadura de P.E.
transversal (MPa)

% Propriedades mecâncias do betão:
fcm = dados1(14); %Resitência do betão à compressão(MPa)
Ec = dados1(15); %Módulo de elasticidade do betão
e0  = dados1(16); % Extensão correspondente ao pico de tensão (1/1000)

%CÁLCULOS PRELIMINARES RELATIVOS AO PRÉ-ESFORÇO
Aps=ApsT+ApsL;  %Área total de armadura de P.E.
roLP = ApsL/Ac;  %Taxa Mec. de armadura de P.E-longitudinal
roTP = ApsT/Ac; %Taxa Mec. de armadura de P.E-transversal.
ePiL= fpiL/EpsL; %Extensão inicial no aço de P.E-longitudinal
ePiT= fpiT/EpsT; %Extensão inicial no aço de P.E-transversal.
eLiL= ApsL*fpiL/(AsL*(Es-Ec)+Ec*(Ac-ApsL)); %Extensão no aço ordinário
longitudinal
eLiT= ApsT*fpiT/(AsT*(Es-Ec)+Ec*(Ac-ApsT)); %Extensão no aço ordinário
transversal
edecT = ePiT+eLiT;  %Extensão de descompressão transversal
edecL = ePiL+eLiL;  %Extensão de descompressão longitudinal

%Solicitações no elemento de betão armado (L-T):
tal  = dados1(17);  %Tensão de corte (MPa)
sigL =  dados1(18); %Tensão de tração longitudinal (MPa)
sigT =  dados1(19); %Tensão de compressão transversal (MPa)

%CÁLCULOS PRELIMINARES
eLy  = fLy/Es*1000;
eTy  = fTy/Es*1000;
sig1 = (sigL + sigT)/2 + sqrt(((sigL - sigT)/2)^2 + tal^2);
mL   = sigL/sig1;
mT   = sigT/sig1;
mLT  = tal/sig1;

%CORREÇÃO DA CURVA PARA ESTA PLACA
%Resolução do valor de extensão (Y) para a equação não-linear:
%Análise Longitudinal
%Definir yL como variável simbólica
syms yL
%Equação a resolver
y=-0.7*fpulinha+ElpsL*(yL)/(1+(ElpsL*(yL)/fpu)^m)^(1/m);
yL=solve(y,yL);
%Retornar o valor em número:
yL=double(yL);
%Análise Transversal;
%Definir yT como variável simbólica
syms yT
%Equação a resolver
y=-0.7*fpulinha+ElpsT*(yT)/(1+(ElpsT*(yT)/fpu)^m)^(1/m);
yT=solve(y,yT);
%Retornar o valor em número:
```

```
yT=double(yT);
%Resolução do valor de extensão (Z) para a equação linear:
%Análise Longitudinal
zL=0.7*fpulinha/EpsL;
%Análise Transversal
zT=0.7*fpulinha/EpsT;
%Calculo do delta E
%Análise longitudinal
dEL= zL-yL;
%Análise transversal
dET= zT-yT;

%DADOS PLOTAGEM
e_plot       = 0;
sigmaD_plot = 0;
e_smm_plot   = 0;
sigmaD_smm_plot = 0;
tal_plot     = 0;
gama_plot    = 0;
tal_smm_plot = 0;
gama_smm_plot = 0;

er_plot      = 0;
tal_er_plot = 0;
ed_plot      = 0;
tal_ed_plot = 0;

a = ' ';
b = 'Eff. RA-STM';
d = ' ';

end
```

Função para o cálculo das estimativas iniciais (MCTM)

```
function F=MCTM_PLACA (alfaD)

%/////////////////////////////////////////////////////////////////////////
% COMPORTAMENTO LINEAR DA PLACA (MTCM) - ESTIMATIVAS INICIAIS PARA O RA-STM/
%/////////////////////////////////////////////////////////////////////////

global roL roT Es Ec eL eT eD sig1 mLT mL mT roLP roTP fpiL fpiT

eL = (mL+mLT*cot(alfaD))/(Es*roL)*0.001*sig1-((roLP*fpiL/(Es*roL))*0.001);
eT = (mT+mLT*tan(alfaD))/(Es*roT)*0.001*sig1-((roTP*fpiT/(Es*roT))*0.001);
eD = -mLT/(Ec*sin(alfaD)*cos(alfaD))*0.001*sig1;

%Equação não-linear de estimativa inicial MCTM
F = (eL-eD)/(eT-eD)-(tan(alfaD))^2;

end
```

Função do RA-STM

```
function COMP_PLACA

%//////////////////////////////////////////////////////////////////////////
% COMPORTAMENTO CARGA-DEFORMÇÃO DA PLACA (RASTM_PLACA)                   /
%//////////////////////////////////////////////////////////////////////////

global roL roT eR eL eT EL ET fL fT FL FT fcm fpT fpL FPT FPL
global ED SIGMAD TAL GAMA ALFAD ER ROLFL_ROTFT ETOTALL ETOTALT EDECL EDECT
SIGMAR
global eD sigmaD edecL edecT etotalL etotalT tal_plot gama_plot sigmaR

%Estimativa inicial com base no MCTM

x(1) = eL*1000;
x(2) = eT*1000;
ed1  = eD*1000;
etotalL = edecL+x(1);
etotalT = edecT+x(2);

%Número máximo de pontos e tamanho do passo
pontos = 1000;
passo  = 4/pontos;

%Cálculo comportamento carga-deformação
for i = 1:pontos

options = optimset('TolX',10^-10,'TolFun',10^-10);
x = lsqnonlin(@(x) RASTM_PLACA (x,ed1-passo*i),x,[0,0],[],options);

%Criar vetores de comportamento:
    ED(i)     = ed1 - passo*i;
    SIGMAD(i)= sigmaD;
    SIGMAR(i)= sigmaR;
    COS       = (x(2)-ED(i))/(eR-ED(i));
    SIN       = (x(1)-ED(i))/(eR-ED(i));
    TAL(i)    = (-SIGMAD(i)+SIGMAR(i))*sqrt(COS*SIN);
    GAMA(i)   = 2*(eR-ED(i))*sqrt(COS*SIN);
    EL(i)     = x(1);%*10^-3;
    ET(i)     = x(2);%*10^-3;
    FL(i)     = fL;
    FT(i)     = fT;
    ALFAD(i) = -atan(sqrt(SIN/COS))*180/pi;
    ER(i)        = EL(i)+ET(i)-ED(i);
    ROLFL_ROTFT (i) = FL(i)*roL+FT(i)*roT;

    %Relativamente ao pré-esforço
    FPT(i)      = fpT;
    FPL(i)      = fpL;
    ETOTALL(i) = etotalL;
    ETOTALT(i) = etotalT;
    EDECL (i)   = edecL;
    EDECT (i)   = edecT;

    %Critérios de paragem (betão de resistência normal ou betão de alta
 % resistência)
    if fcm <= 58
        if - ED(i) >= 3.5;
            break
        end

    else
        if - ED(i) >= 2.8 + 27 * ((98-fcm)/100)^4;
            break
        end
    end
end
```

```
MAXTAL = max(TAL);
MAXGAMAj = GAMA(find(TAL==max(TAL)));
MAXTAL_PLOT = max(tal_plot);
MAXGAMA_PLOT = gama_plot(find(tal_plot==max(tal_plot)));
disp('Valores últimos (máximos) são:');
fprintf('Tau_u,th: %f kN.m\n',MAXTAL);
fprintf('Gama_u,th: %f rad/m\n',MAXGAMAj);
fprintf('Tau_u,exp: %f kN.m\n',MAXTAL_PLOT);
fprintf('Gama_u,exp: %f rad/m\n',MAXGAMA_PLOT);
fprintf('\n')

end
```

```
function F = RASTM_PLACA(x,ed1)

%///////////////////////////////////////////////////////////////////////////
% COMPORTAMENTO NÃO-LINEAR DA PLACA (RA-STM)                              /
%///////////////////////////////////////////////////////////////////////////

global m roL roLP roTP roT eR Es EpsL EpsT ElpsT ElpsL zL zT dEL dET
global e0 eLy eTy edecL edecT etotalL etotalT
global fL fT fTy fpT fpL fpu fcm fp01 fLy mLT mL mT sigmaD csi Ec sigL sigT
sigmaR

%Cálculos iniciais

%Princípio da Invariância
eR = x(1)+x(2)-ed1;

%Coeficiente de Amolecimento
R = 5.8/(sqrt(fcm));

if   R<= 0.9
    R_linha = R;
else
    R_linha = 0.9;
end

n = ((roL*fLy)+(roLP*fp01)-sigL)/((roT*fTy)+(roTP*fp01)-sigT);

if  n <= 1
    n_linha = n;
else
    n_linha = 1/n;
end

csi = R_linha/(sqrt(1+((0.4*eR)/n_linha)));

%Lei constitutiva do betão à compressão

if abs(ed1)<csi*abs(e0)
    sigmaD = -csi*fcm*(2*(ed1/(csi*e0))-(ed1/(csi*e0))^2);
else
    sigmaD = -csi*fcm*(1-((ed1/(csi*e0)-1)/((4/csi)-1))^2);
end

%Lei constitutiva do betão à tração

fcr = 0.311*sqrt(fcm);
ecr = 0.08;
sigmaR = fcr*(ecr/(eR+ecr))^0.4;


%Relação constitutiva do aço ordinário e de pré-esforço

%Armadura ordinária longitudinal
BNL  = (1/roL)*(fcr/fLy)^1.5;
enL = eLy*10^-3*(0.93-2*BNL);

if x(1)*10^-3 <= enL
    fL = x(1)*10^-3*Es;
else
    fL = fLy*((0.91-2*BNL)+((0.02+0.25*BNL)*(x(1)/eLy)));
end

%Armadura ordinária transversal
BNT  = (1/roT)*(fcr/fTy)^1.5;
enT = eTy*10^-3*(0.93-2*BNT);

if x(2)*10^-3 <= enT
    fT = x(2)*10^-3*Es;
```

```
else
    fT = fTy*((0.91-2*BNT)+((0.02+0.25*BNT)*(x(2)/eTy)));
end


%Armadura de pré-esforço
etotalL = edecL+x(1)*10^-3;
etotalT = edecT+x(2)*10^-3;

%Armadura de pré-esforço longitudinal
if  edecL ~= 0
        if etotalL > zL
            fpL = ElpsL*(etotalL-dEL)/(1+(ElpsL*(etotalL-dEL)/fpu)^m)^(1/m);
        else
            fpL = EpsL*(etotalL);
        end
    else
        fpL=0;
    end


%Armadura de pré-esforço transversal
if  edecT ~= 0
        if etotalT > zT
            fpT = ElpsT*(etotalT-dET)/(1+(ElpsT*(etotalT-dET)/fpu)^m)^(1/m);
        else
            fpT = EpsT*(etotalT);
        end
    else
        fpT=0;
    end

%Tensão principal de tração
S = mL*mT-mLT^2;
B = mL*(sigmaR+roT*fT+roTP*fpT)+mT*(sigmaR+roL*fL+roLP*fpL);
C = (sigmaR+roT*fT+roTP*fpT)*(sigmaR+roL*fL+roLP*fpL);
sigma1 = (1/(2*S))*(B-sqrt(B^2-4*S*C));


%Comportamento não linear RA-STM
% Sistema de equações não-linear
F(1) = sigmaD*(x(1)-ed1)/(eR-ed1)-mT*sigma1+roT*fT+roTP*fpT+sigmaR*(x(2)-
ed1)/(eR-ed1);
F(2) = sigmaD*(x(2)-ed1)/(eR-ed1)-mL*sigma1+roL*fL+roLP*fpL+sigmaR*(x(1)-
ed1)/(eR-ed1);

end
```

Função para impressão das curvas de comportamento da placa

```
function PLOT_PLACA

%//////////////////////////////////////////////////////////////////////////
% IMPRESSÃO DAS CURVAS DE COMPORTAMENTO DA PLACA                          /
%//////////////////////////////////////////////////////////////////////////

global a b d
global gama1 tal1 gama2 tal2 gama3 tal3 gama4 tal4 gama5 tal5 gama6 tal6 gama7
global tal7 gama8 tal8 gama9
global e_plot sigmaD_plot er_plot tal_er_plot
global tal_plot gama_plot tal_ed_plot tal_smm_plot
global gama_smm_plot ed_plot e_smm_plot sigmaD_smm_plot
global FPL FPT ETOTALL ETOTALT ED SIGMAD TAL GAMA EL ET FL FT ER ALFAD SIGMAR

% Opção:
disp(' ');
disp('PLACAS SÉRIE "TA" ou PLACA COM DADOS INTRODUZIDOS');
disp(' ');
disp('1 - Curva Tensão de corte x Deformação de tração');
disp('2 - Curva Tensão de corte x Deformação de compressão');
disp('3 - Curva Tensão de compressão x Deformação de compressão do betão');
disp('4 - Curva Tensão de tração x Deformação de tração do betão');
disp('5 - Curva Tensão de tração x Deformação de tração da armadura
longitudinal ordinária');
disp('6 - Curva Tensão de tração x Deformação de tração da armadura
transversal ordinária');
disp('7 - Curva Tensão de tração x Deformação de tração da armadura
longitudinal de pré-esforço');
disp('8 - Curva Tensão de tração x Deformação de tração da armadura
transversal de pré-esforço');
disp('9 - Curva Tensão de corte x Deformação de corte');
disp('10 - Ângulo (alfaD) x Deformação de compressão do betão');
disp(' ');
disp('PLACAS SÉRIE "PP"');
disp(' ');
disp('11 - Curva Tensão de compressão x Deformação de compressão do betão');
disp('12 - Curva Tensão de tração x Deformação de tração do betão');
disp('13 - Curva Tensão de tração x Deformação de tração da armadura
longitudinal ordinária');
disp('14 - Curva Tensão de tração x Deformação de tração da armadura
transversal ordinária');
disp('15 - Curva Tensão de tração x Deformação de tração da armadura
longitudinal de pré-esforço');
disp('16 - Curva Tensão de corte x Deformação de corte');
disp(' ');
disp('17 - Voltar ao início');
disp(' ');
disp('0 - Sair');
disp(' ');
IND = input('Escolha uma opção: ');

%Casos de plotagem e impressão das curvas

while IND > 0
    switch IND

% PLACAS SÉRIE "TA" ou PLACA COM DADOS INTRODUZIDOS

        case 1
            % 1 - Curva Tensão de corte x Deformação de tração
            hold on
            plot(er_plot, tal_er_plot,'-rs','LineWidth',2,'MarkerSize',7)
            plot([0 ER*0.1],[0 TAL],'--b','LineWidth',2)


            % Títulos
```

```
            xlabel('\epsilon_R (1/1000)');
            ylabel('\tau_L_T (MPa)');
            legend(a,...
                b,'Location','southeast');
            grid on
            hold off


        case 2
            % 2 - Curva Tensão de corte x Deformação de compressão
            hold on
            plot(ed_plot, tal_ed_plot,'-rs','LineWidth',2,'MarkerSize',7)
            plot(-[0 ED],[0 TAL],'--b','LineWidth',2)

            % Títulos
            xlabel('\epsilon_D (1/1000)');
            ylabel('\tau_L_T (MPa)');
            legend(a,...
                b,'Location','southeast');
            grid on
            hold off


        case 3
            % 3 - Curva Tensão de compressão x Deformação de compressão do
betão
            hold on
            plot(-e_plot,-sigmaD_plot,'-rs','LineWidth',2,'MarkerSize',7)
            plot(e_smm_plot,sigmaD_smm_plot,'-g','LineWidth',2)
            plot(-[0 ED],-[0 SIGMAD],'--b','LineWidth',2)

            % Títulos
            xlabel('\epsilon_D (1/1000)');
            ylabel('\sigma_D (MPa)');
            legend(a,...
                d,...
                b,'Location','southeast');
            grid on
            hold off


        case 4
            % 4 - Curva Tensão de tração x Deformação de tração do betão
            hold on
            plot([0 ER],[0 SIGMAR],'--b','LineWidth',2)

            % Títulos
            xlabel('\epsilon_R (1/1000)');
            ylabel('\sigma_R (MPa)');
            legend(b,'Location','southeast');
            grid on
            hold off


         case 5
            % 5 - Curva Tensão de tração x Deformação de tração da armadura
                % longidudinal ordinária
            hold on
            plot([0 EL],[0 FL],'--b','LineWidth',2)

            % Títulos
            xlabel('\epsilon_L (1/1000)');
            ylabel('f_L (MPa)');
            legend(b,'Location','southeast');
            grid on
            hold off
```

```
 case 6
    % 6 - Curva Tensão de tração x Deformação de tração da armadura
        % transversal ordinária
    hold on
    plot([0 ET],[0 FT],'--b','LineWidth',2)

    % Títulos
    xlabel('\epsilon_T (1/1000)');
    ylabel('f_T (MPa)');
    legend(b,'Location','southeast');
    grid on
    hold off


 case 7
    % 7 - Curva Tensão de tração x Deformação de tração da armadura
        % longidudinal de pré-esforço
    hold on
    plot([ETOTALL*1000],[FPL],'--b','LineWidth',2)

    % Títulos
    xlabel('\epsilon_p_L (1/1000)');
    ylabel('f_p_L (MPa)');
    legend(b,'Location','southeast');
    grid on
    hold off


 case 8
    % 8 - Curva Tensão de tração x Deformação de traçã da armadura
        % transversal de pré-esforço
    hold on
    plot([ETOTALT*1000],[FPT],'--b','LineWidth',2)

    % Títulos
    xlabel('\epsilon_p_T (1/1000)');
    ylabel('f_p_T (MPa)');
    legend(b,'Location','southeast');
    grid on
    hold off


case 9
    % 9 - Curva Tensão de corte x Deformação de corte
    hold on
    plot(gama_plot,tal_plot,'-rs','LineWidth',2)
    plot(gama_smm_plot,tal_smm_plot,'-g','LineWidth',2,'MarkerSize',7)
    plot([0 GAMA],[0 TAL],'--b','LineWidth',2)

    % Títulos
    xlabel('\gamma_L_T (1/1000)');
    ylabel('\tau_L_T (MPa)');
    legend(a,...
        d,...
        b,'Location','southeast');
    grid on
    hold off


case 10
    % 10 - Ângulo (alfaD) x Deformação de compressão do betão
    hold on
    plot(-ED,-ALFAD,'--b','LineWidth',2,'MarkerSize',7)

    % Títulos
    xlabel('\epsilon_D (1/1000)');
    ylabel('\alpha_D (°)');
    legend(b,'Location','southeast');
```

```
            grid on
            hold off


% PLACAS SÉRIE "PP"

        case 11
            % 11 - Curva Tensão de compressão x Deformação de compressão do
betão
            hold on
            plot(-e_plot,-sigmaD_plot,'-rs','LineWidth',2,'MarkerSize',7)
            plot(e_smm_plot,sigmaD_smm_plot,'-g','LineWidth',2)
            plot(-[0 ED],-[0 SIGMAD],'--b','LineWidth',2)

            % Títulos
            xlabel('\epsilon_D (1/1000)');
            ylabel('\sigma_D (MPa)');
            legend(b,'Location','southeast');
            grid on
            hold off


        case 12
            % 12 - Curva Tensão de tração x Deformação de tração do betão
            hold on
            plot([0 ER],[0 SIGMAR],'--b','LineWidth',2)

            % Títulos
            xlabel('\epsilon_R (1/1000)');
            ylabel('\sigma_R (MPa)');
            legend(b,'Location','southeast');
            grid on
            hold off


         case 13
            % 13 - Curva Tensão de tração x Deformação de tração da armadura
                % longidudinal ordinária
            hold on
            plot([0 EL],[0 FL],'--b','LineWidth',2)

            % Títulos
            xlabel('\epsilon_L (1/1000)');
            ylabel('f_L (MPa)');
            legend(b,'Location','southeast');
            grid on
            hold off


         case 14
            % 14 - Curva Tensão de tração x Deformação de tração da armadura
                % transversal ordinária
            hold on
            plot([0 ET],[0 FT],'--b','LineWidth',2)

            % Títulos
            xlabel('\epsilon_T (1/1000)');
            ylabel('f_T (MPa)');
            legend(b,'Location','southeast');
            grid on
            hold off


         case 15
            % 15 - Curva Tensão de tração x Deformação de tração da armadura
                % longidudinal de pré-esforço
            hold on
            plot([ETOTALL*1000],[FPL],'--b','LineWidth',2)
```

```
            % Títulos
            xlabel('\epsilon_p_L (1/1000)');
            ylabel('f_p_L (MPa)');
            legend(b,'Location','southeast');
            grid on
            hold off


         case 16
            % 16 - Curva Tensão de corte x Deformação de corte
            hold on

            plot(gama1,tal1,'-rs','LineWidth',2)
            plot([0 GAMA],[0 TAL],'--b','LineWidth',2)
            plot(gama2,tal2,'-rs','LineWidth',2)
            plot(gama3,tal3,'-rs','LineWidth',2)
            plot(gama4,tal4,'-rs','LineWidth',2)
            plot(gama5,tal5,'-rs','LineWidth',2)
            plot(gama6,tal6,'-rs','LineWidth',2)
            plot(gama7,tal7,'-rs','LineWidth',2)
            plot(gama8,tal8,'-rs','LineWidth',2)
            plot(gama9,tal9,'-rs','LineWidth',2)

            % Títulos
            xlabel('\gamma_L_T (1/1000)');
            ylabel('\tau_L_T (MPa)');
            legend(a,b,'Location','southeast');
            grid on
            hold off


         case 17
             inicio;
    end

    disp(' ');
    IND = input('Escolha uma opção:');

end
end
```

Anexo IV. Previsões teóricas do RA-STM PC v2

Placa TA-1 (Laskar et al., 2007)

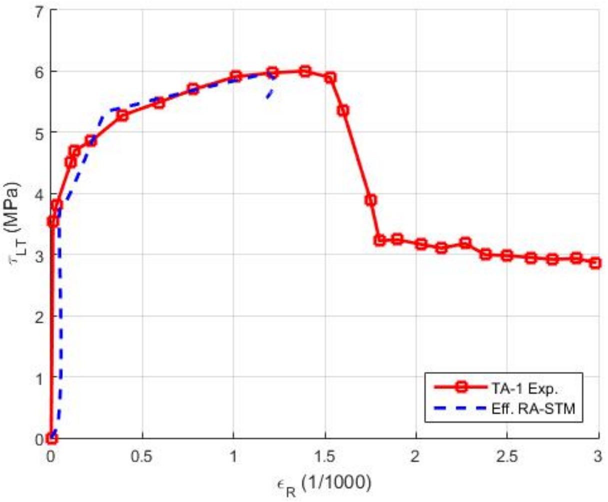

Curva $\tau_{LT} - \varepsilon_R$

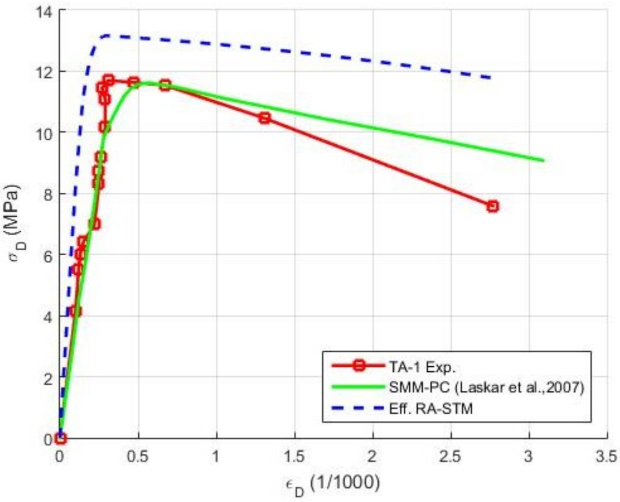

Curva $\sigma_D - \varepsilon_D$

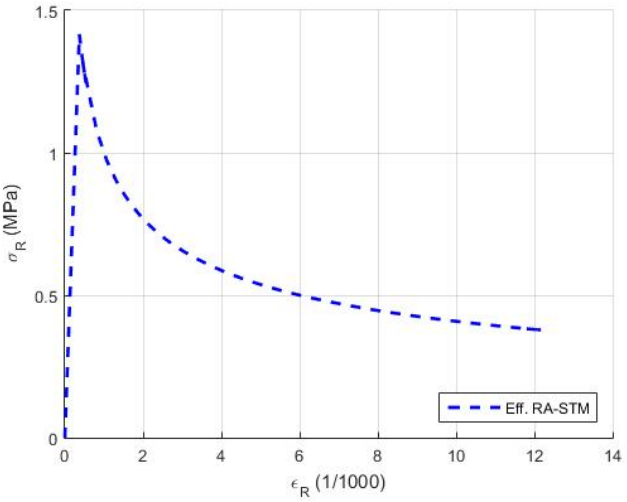

Curva $\sigma_R - \varepsilon_R$

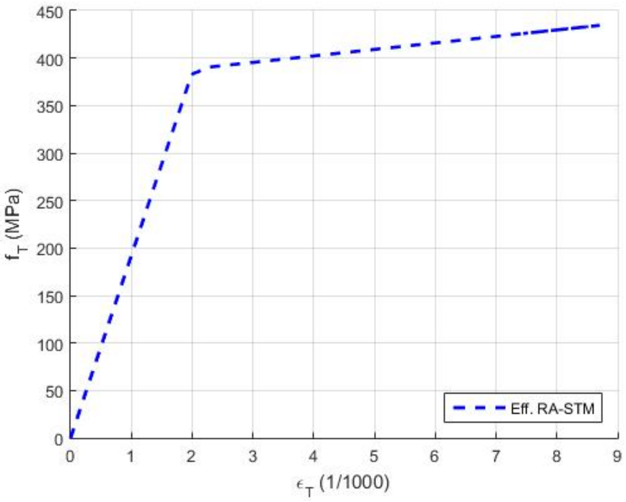

Curva $f_T - \varepsilon_T$

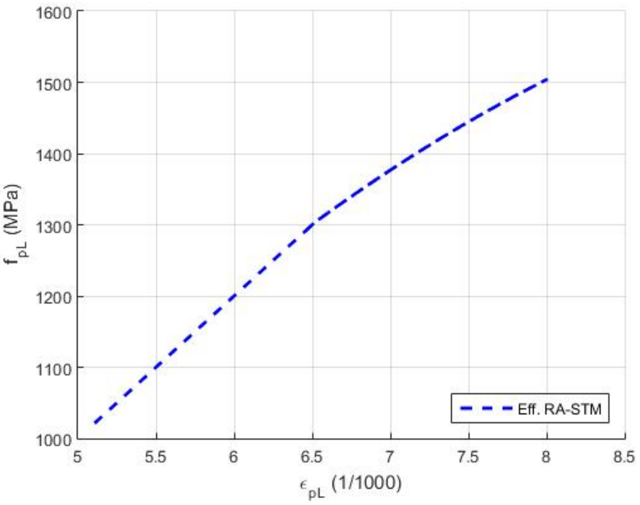

Curva $f_{pL} - \varepsilon_{pL}$

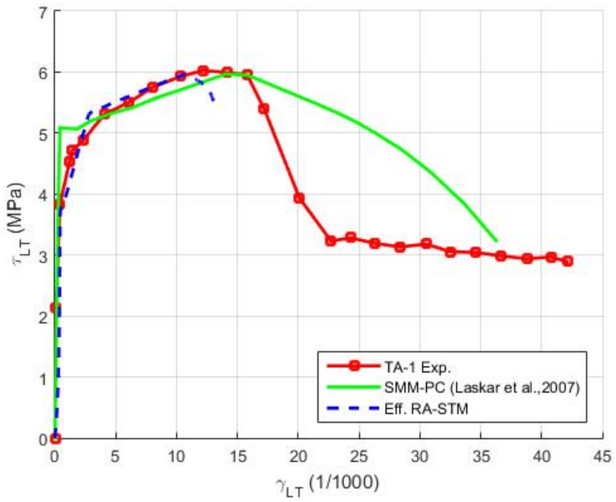

Curva $\tau_{LT} - \gamma_{LT}$

Placa TA-2 (Laskar et al., 2007)

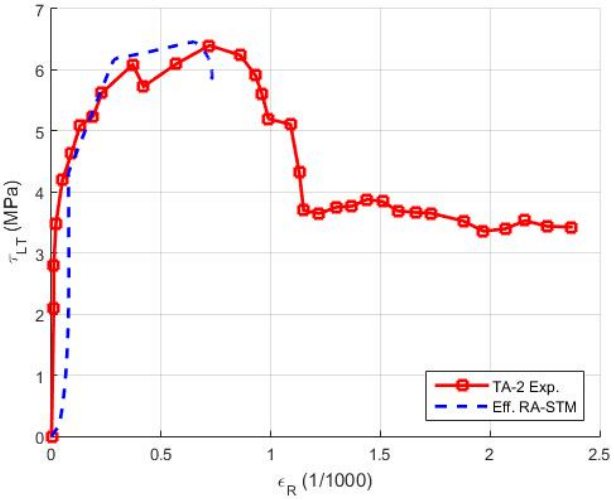

Curva $\tau_{LT} - \varepsilon_R$

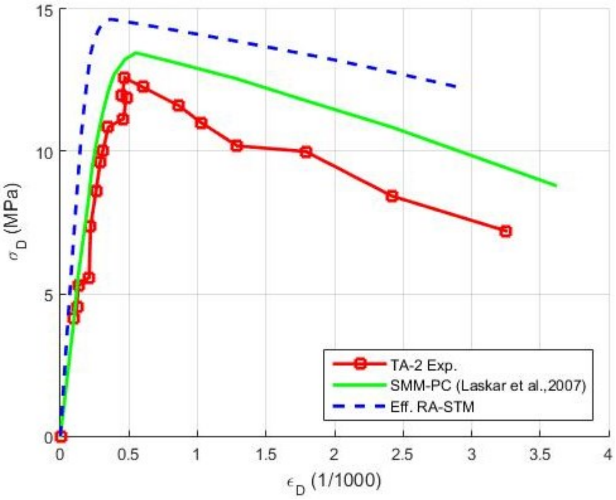

Curva $\sigma_D - \varepsilon_D$

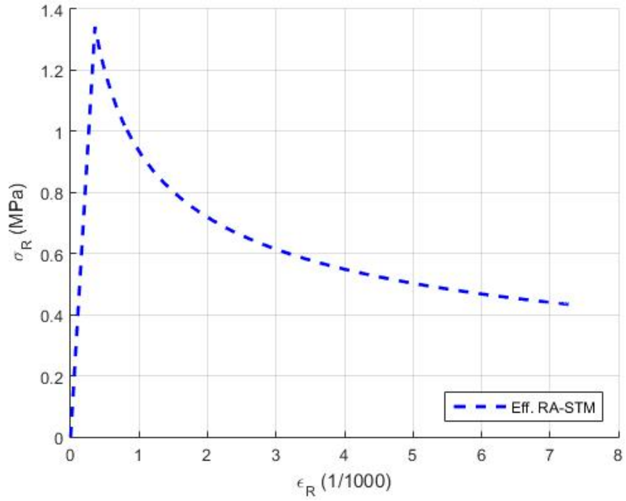

Curva $\sigma_R - \varepsilon_R$

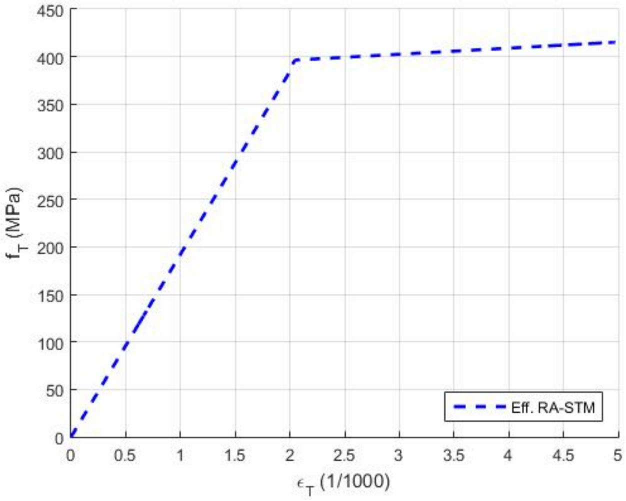

Curva $f_T - \varepsilon_T$

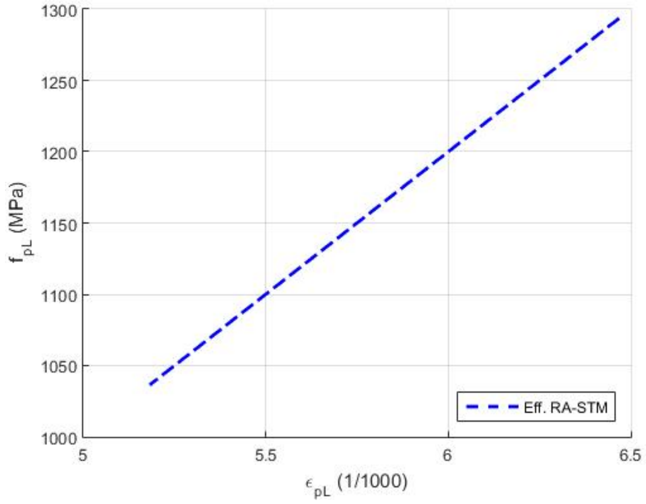

Curva $f_{pL} - \varepsilon_{pL}$

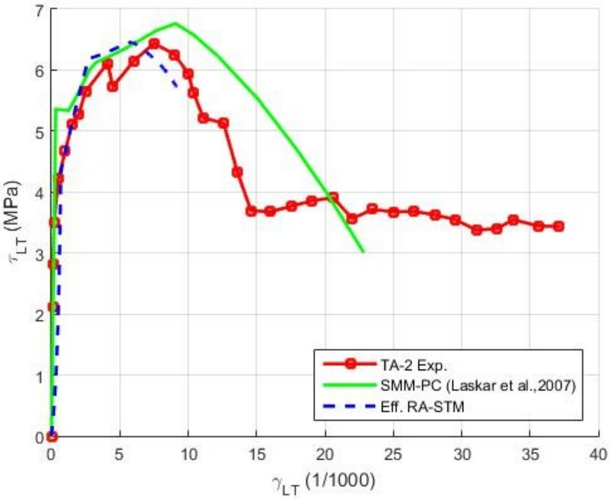

Curva $\tau_{LT} - \gamma_{LT}$

Placa TA-3 (Laskar et al., 2007)

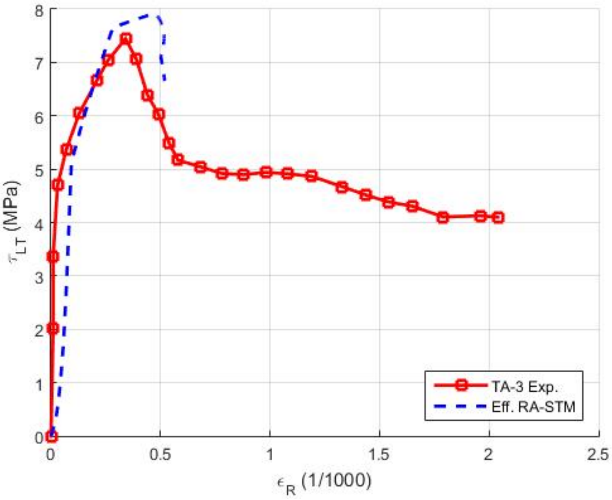

Curva $\tau_{LT}-\varepsilon_R$

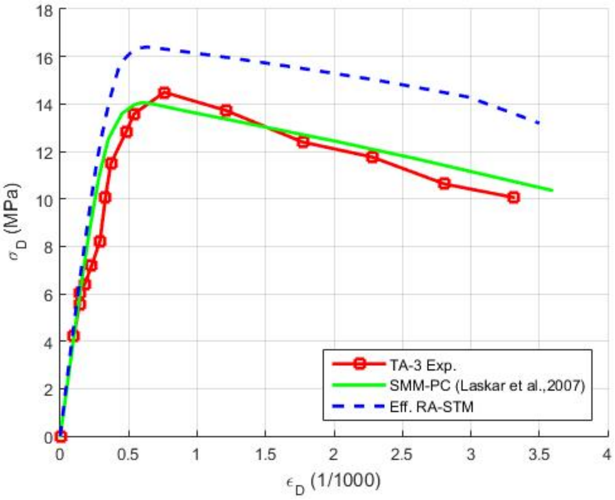

Curva $\sigma_D-\varepsilon_D$

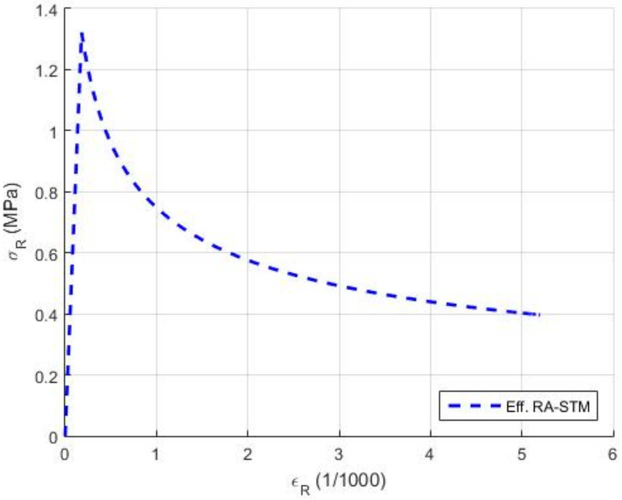

Curva $\sigma_R-\varepsilon_R$

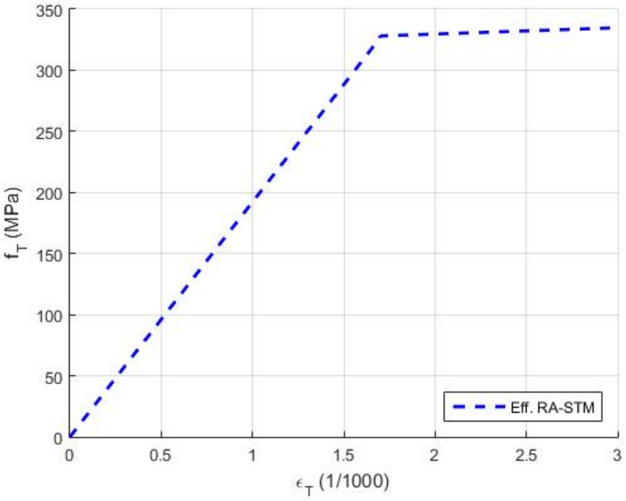

Curva $f_T-\varepsilon_T$

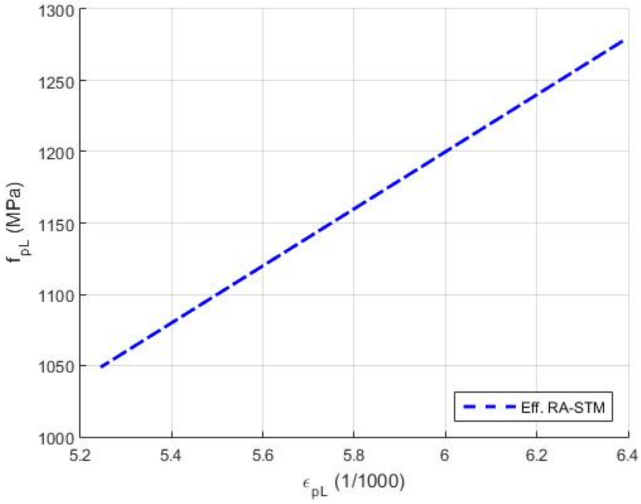

Curva $f_{pL}-\varepsilon_{pL}$

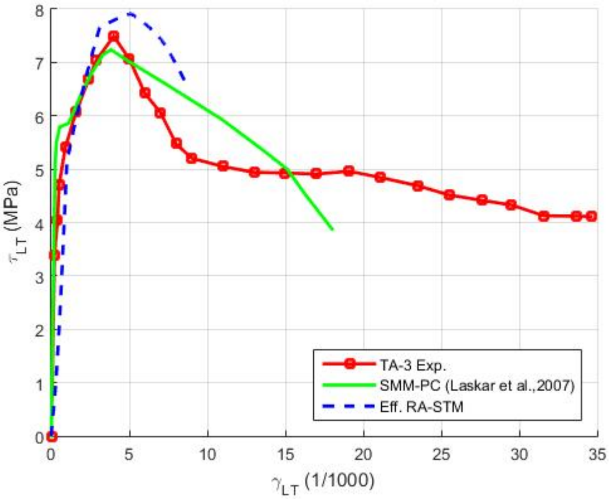

Curva $\tau_{LT}-\gamma_{LT}$

Placa TA-4 (Laskar et al., 2007)

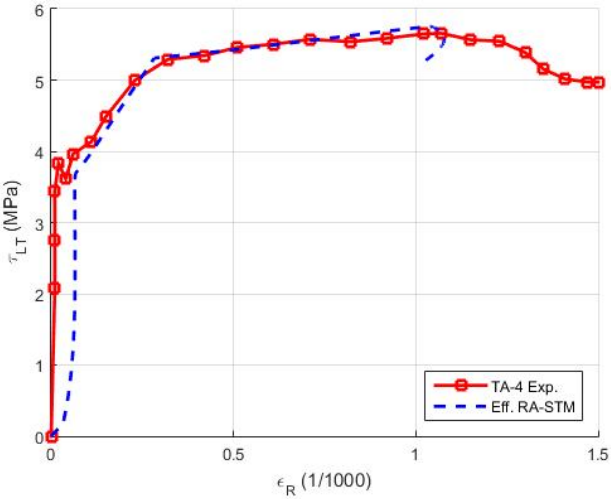

Curva $\tau_{LT} - \varepsilon_R$

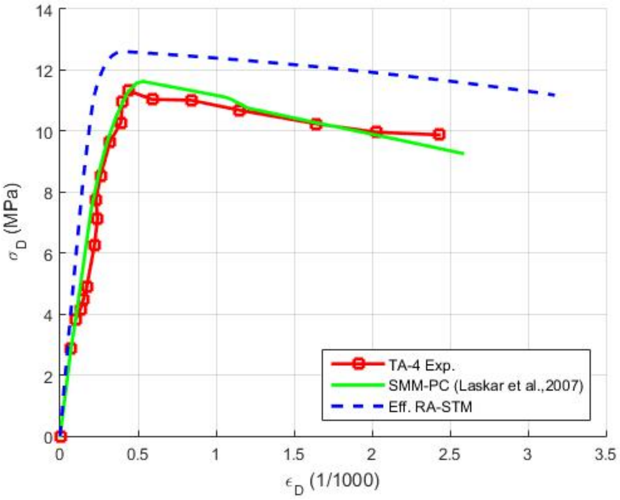

Curva $\sigma_D - \varepsilon_D$

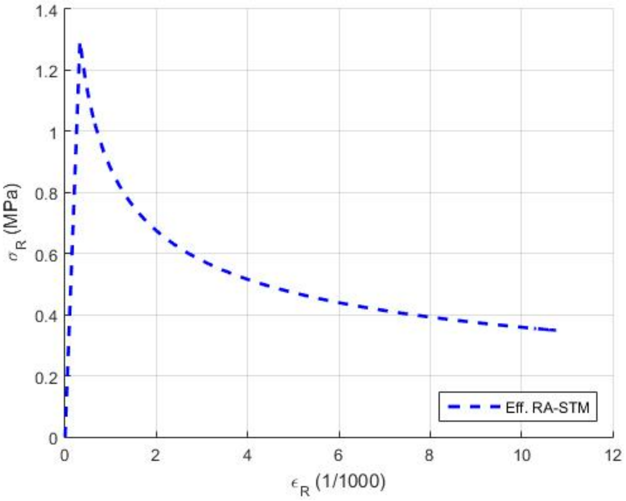

Curva $\sigma_R - \varepsilon_R$

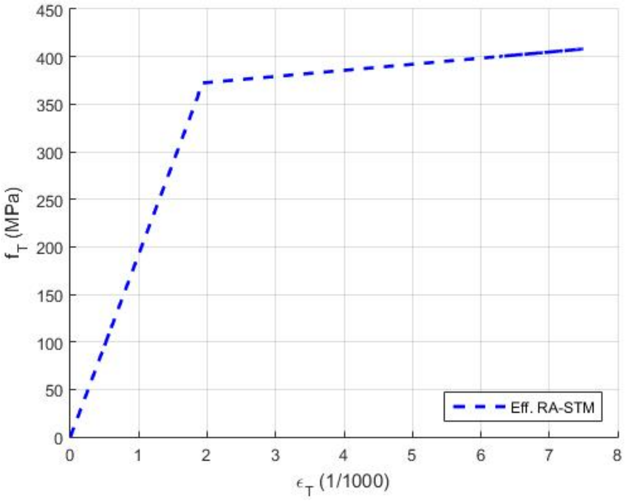

Curva $f_T - \varepsilon_T$

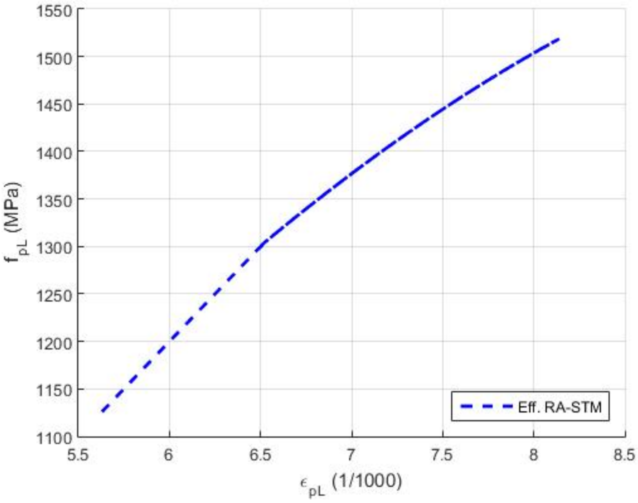

Curva $f_{pL} - \varepsilon_{pL}$

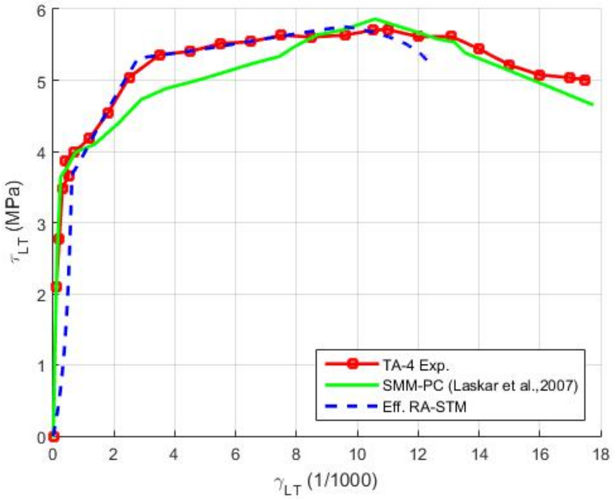

Curva $\tau_{LT} - \gamma_{LT}$

Placa TA-5 (Laskar et al., 2007)

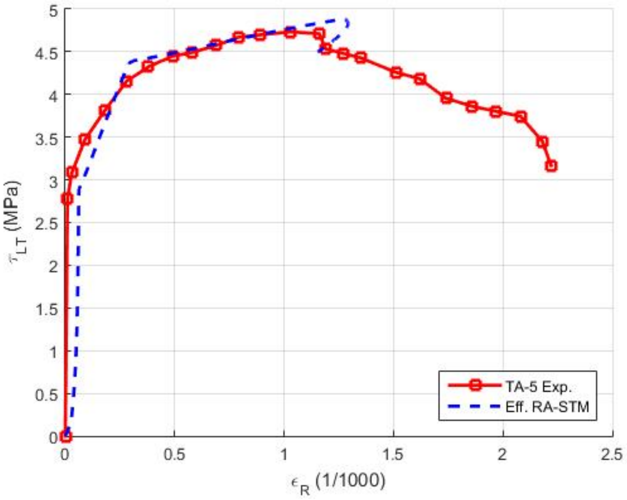

Curva $\tau_{LT}-\varepsilon_R$

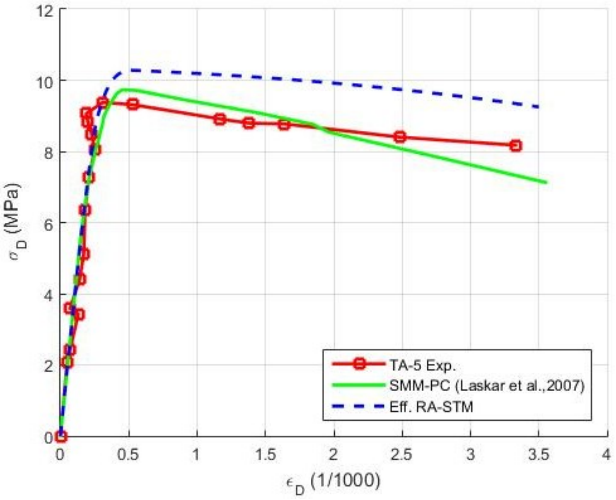

Curva $\sigma_D-\varepsilon_D$

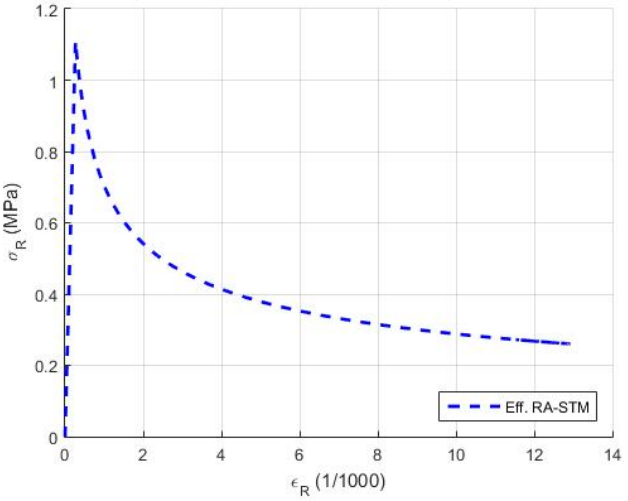

Curva $\sigma_R-\varepsilon_R$

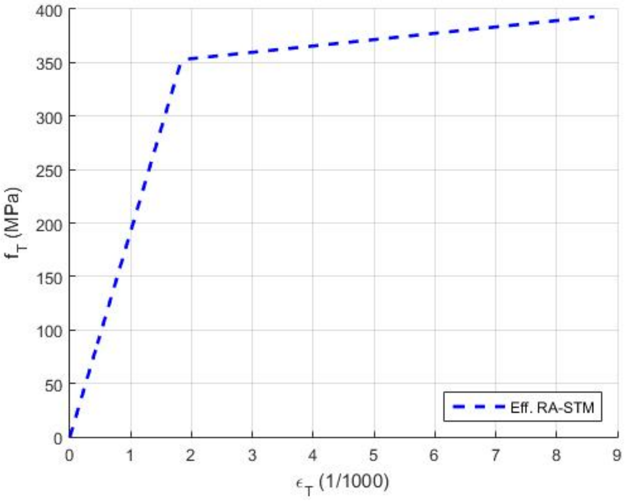

Curva $f_T-\varepsilon_T$

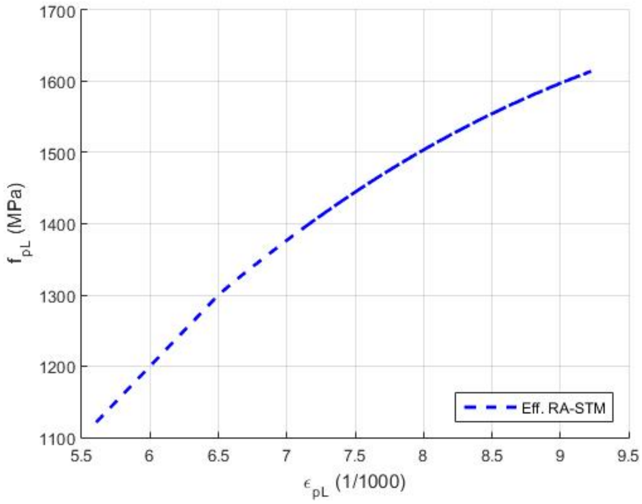

Curva $f_{pL}-\varepsilon_{pL}$

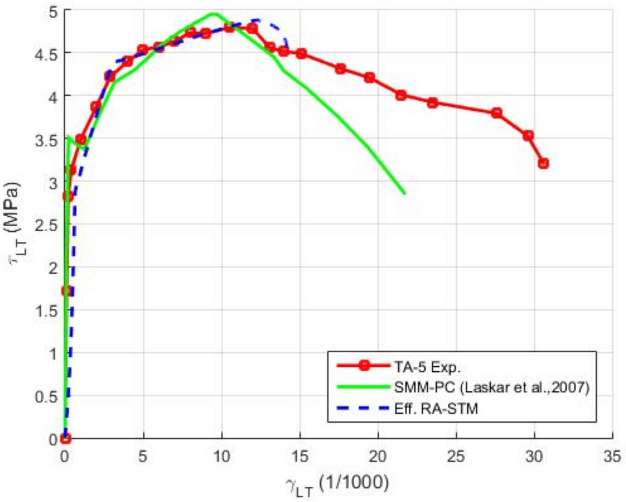

Curva $\tau_{LT}-\gamma_{LT}$

Placa PP2 (Marti e Meyboom, 1992)

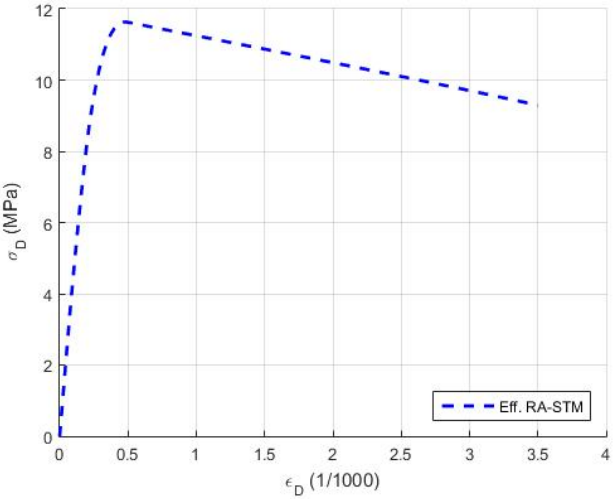

Curva $\sigma_D - \varepsilon_D$

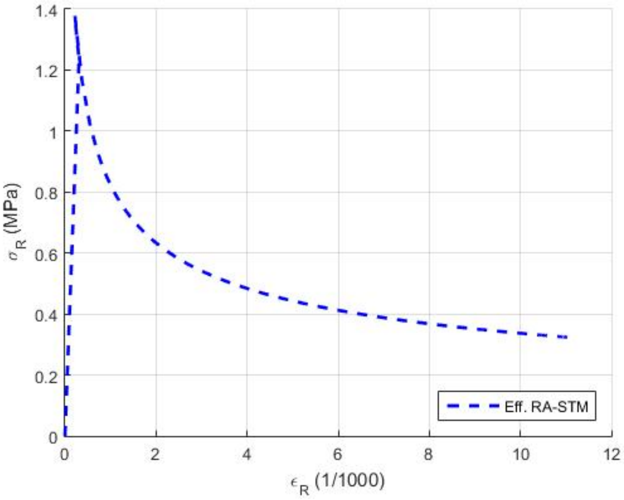

Curva $\sigma_R - \varepsilon_R$

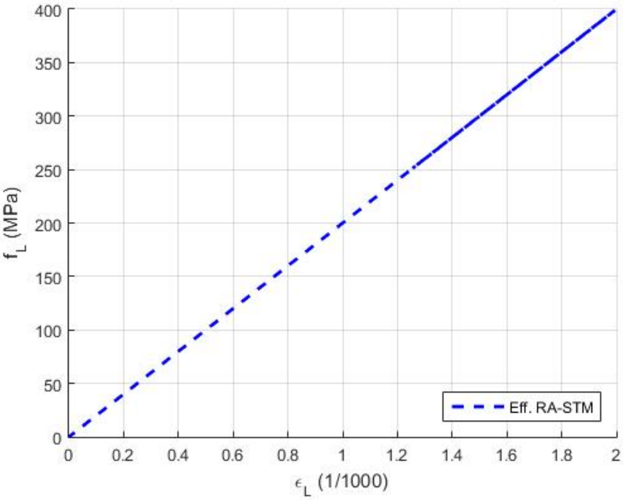

Curva $f_L - \varepsilon_L$

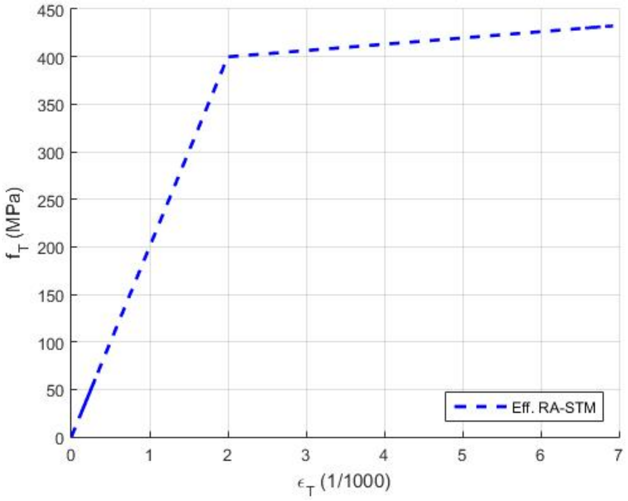

Curva $f_T - \varepsilon_T$

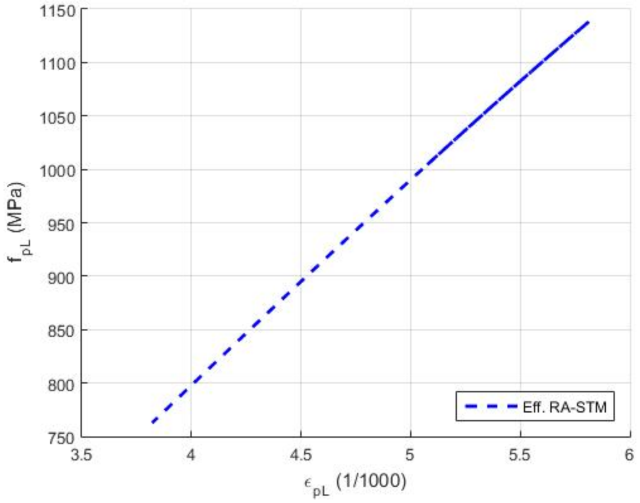

Curva $f_{pL} - \varepsilon_{pL}$

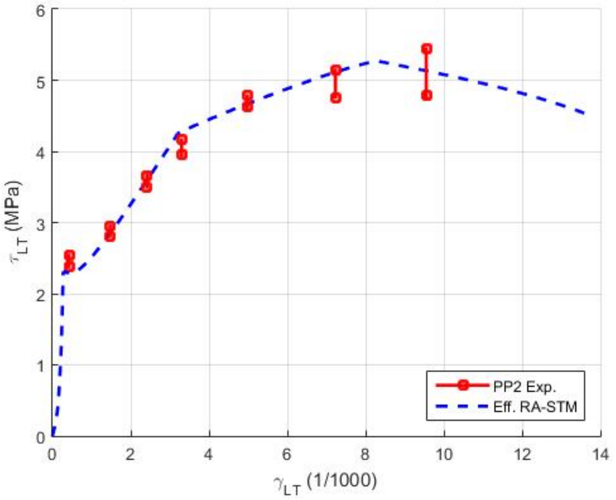

Curva $\tau_{LT} - \gamma_{LT}$

Placa PP3 (Marti e Meyboom, 1992)

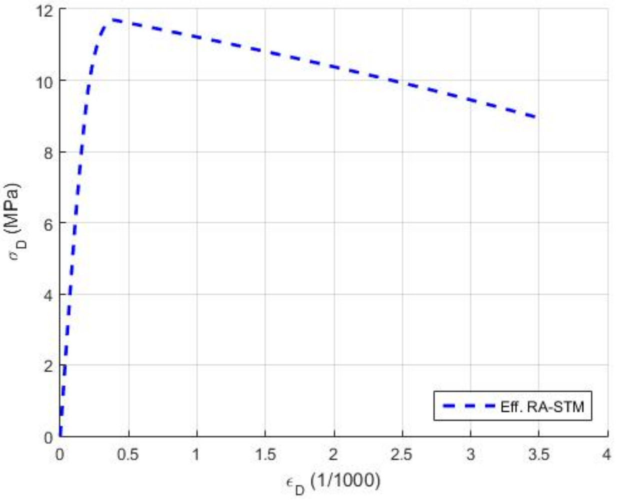

Curva $\sigma_D - \varepsilon_D$

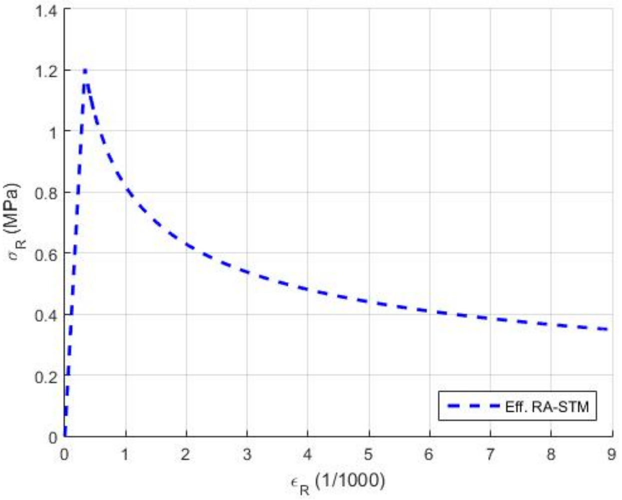

Curva $\sigma_R - \varepsilon_R$

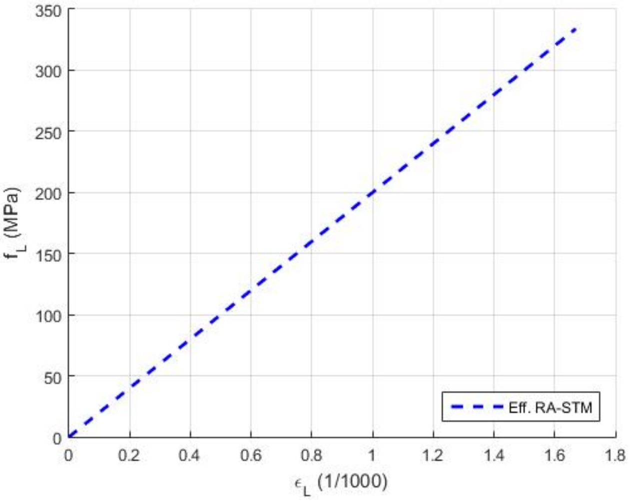

Curva $f_L - \varepsilon_L$

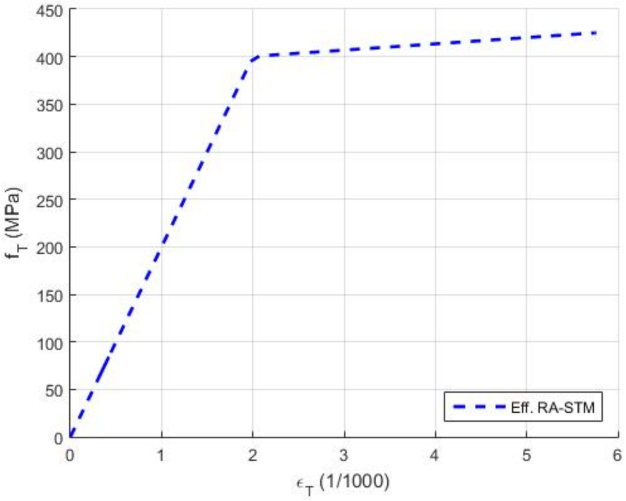

Curva $f_T - \varepsilon_T$

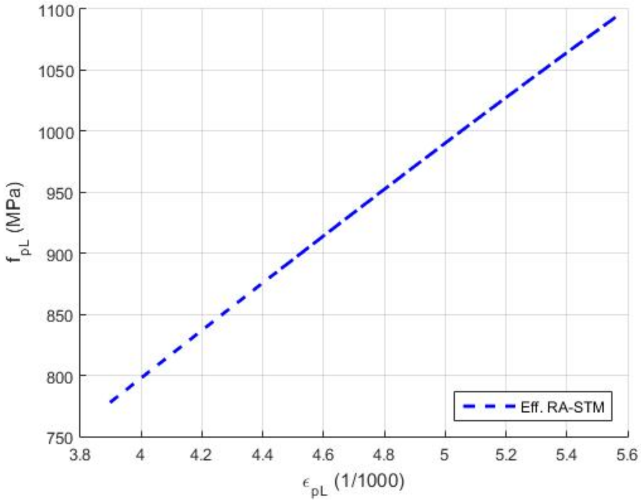

Curva $f_{pL} - \varepsilon_{pL}$

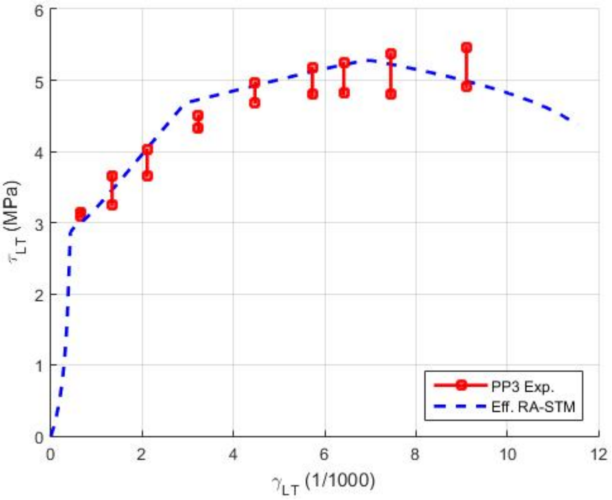

Curva $\tau_{LT} - \gamma_{LT}$

Anexo V. Código em MATLAB do RA-STM FRP

Script para iniciar o RA-STM FRP

```
%///////////////////////////////////////////////////////////////////////////
% RA-STM FRP - ROTATING ANGLE SOFTENED TRUSS MODEL - REINFORCED CONCRETE    /
%              STRENGTHENED WITH FRP                                        /
%///////////////////////////////////////////////////////////////////////////

% INICIO /////////////////////////////////////////////////////////////////
clear all; clc;

% DADOS DE ENTRADA ///////////////////////////////////////////////////////
DADOS_INICIAIS; tic;

% CÁLCULO DA ESTIMATIVA INICIAL (MCTM) ///////////////////////////////////
alfaD1 = (lsqnonlin(@(alfaD) MCTM_PLACA(alfaD),0.01,[],0))*180/pi;

% SOLUÇÃO ////////////////////////////////////////////////////////////////
COMP_PLACA;

% CURVAS TENSÃO-DEFORMAÇÃO ///////////////////////////////////////////////
toc; PLOT_PLACA;
```

Função para a escolha das placas / Introdução dos dados iniciais

```
function DADOS_INICIAIS
%//////////////////////////////////////////////////////////////////////////
% SELEÇÃO DA PLACA / INTRODUÇÃO DOS DADOS INICIAIS                       /
%//////////////////////////////////////////////////////////////////////////
disp('Selecione os dados iniciais');
disp(' ');
disp('Placas de Betão Armado de referência solicitadas com ALFA2=45°');
disp('1  - REF-P3 [fcm = 53 MPa  | roL = 0,0076  | roT = 0,0043  | roTf = 0]
- ZOMORODIAN et al. (2018)');
disp('2  - REF-P4 [fcm = 53 MPa  | roL = 0,0076  | roT = 0,0076  | roTf = 0]
- ZOMORODIAN et al. (2018)');
disp(' ');
disp('Placas de Betão Armado reforçadas com FRP e solicitadas com ALFA2=45°');
disp('3  - P3-025-FW [fcm = 51 MPa  | roL = 0,0076  | roT = 0,0043  | roTf =
0,0054]  - ZOMORODIAN et al. (2018)');
disp('4  - P3-040-FW [fcm = 50 MPa  | roL = 0,0076  | roT = 0,0043  | roTf =
0,0087]  - ZOMORODIAN et al. (2018)');
disp('5  - P4-025-FW [fcm = 45 MPa  | roL = 0,0076  | roT = 0,0076  | roTf =
0,0054]  - ZOMORODIAN et al. (2018)');
disp('6  - P4-040-FW [fcm = 52 MPa  | roL = 0,0076  | roT = 0,0076  | roTf =
0,0087]  - ZOMORODIAN et al. (2018)');
disp('7  - P4-080-FW [fcm = 54 MPa  | roL = 0,0076  | roT = 0,0076  | roTf =
0,0174]  - ZOMORODIAN et al. (2018)');
disp('8  - P4-040-SB [fcm = 44 MPa  | roL = 0,0076  | roT = 0,0076  | roTf =
0,0087]  - ZOMORODIAN et al. (2018)');
disp('9  - P4-025-FA [fcm = 52 MPa  | roL = 0,0076  | roT = 0,0076  | roTf =
0,0054]  - ZOMORODIAN et al. (2018)');
disp('10 - P4-040-FA [fcm = 52 MPa  | roL = 0,0076  | roT = 0,0076  | roTf =
0,0087]  - ZOMORODIAN et al. (2018)');
disp('0 - Sair');
disp(' ');
IND = input('Escolha uma opção: ');

if IND >= 0 & IND <= 11
    switch IND
        case 1
            REF_P3_ZOMORODIAN_et_al;
        case 2
            REF_P4_ZOMORODIAN_et_al;
        case 3
            P3_025_FW_ZOMORODIAN_et_al;
        case 4
            P3_040_FW_ZOMORODIAN_et_al;
        case 5
            P4_025_FW_ZOMORODIAN_et_al;
        case 6
            P4_040_FW_ZOMORODIAN_et_al;
        case 7
            P4_080_FW_ZOMORODIAN_et_al;
        case 8
            P4_040_SB_ZOMORODIAN_et_al;
        case 9
            P4_025_FA_ZOMORODIAN_et_al;
        case 10
            P4_040_FA_ZOMORODIAN_et_al;
        case 0
            error('SCRIPT INTERROMPIDO!')
            clc
    end
else
    disp(' ');
    disp('O VALOR INTRODUZIDO NÃO É VÁLIDO!');
    disp(' ');
    DADOS_INICIAIS
end
end
```

Exemplo de dados experimentais: Placa P4-040-SB

```
function P4_040_SB_ZOMORODIAN_et_al

%//////////////////////////////////////////////////////////////////////////
% DADOS EXPERIMENTAIS DA PLACA P4-040-SB - ZOMORODIAN et al. (2018)       /
%//////////////////////////////////////////////////////////////////////////

global roL roT Es fLy fTy Ec fcm e0 tal sigL sigT eLy eTy fcr
global sig1 mLT mL mT
global e_plot sigmaD_plot eR_plot eL_plot eT_plot fL_plot fT_plot
global alfa_plot tal_plot gama_plot tal_Teo gama_Teo sigmaR_plot a b c
eRaux_plot
global roLf roTf Ef fu rof ros Kw eLf_plot eTf_plot fLf_plot fTf_plot % FRP

%//////////////////////////////////////////////////////////////////////////
% DADOS INICIAIS                                                          /
%//////////////////////////////////////////////////////////////////////////

% Taxas de armadura
roL = 0.0076;
roT = 0.0076;
ros = 0.0076; % = roT

% Taxas de FRP
roLf = 0;
roTf = 0.0087;
rof = 0.0087; % = roTf

% Propriedades mecânicas dos aços
Es   = 190000;        %Módulo de elasticidade do aço (MPa)
fLy = 462;            %Tensão de cedência da armadura longitudinal (MPa)
fTy = 462;            %Tensão de cedência da armadura transversal (MPa)

% Propriedades mecânicas do FRP
Ef = 72400;         %Módulo de elasticidade na direção das fibras (MPa)
fu = 876;            %Tensão de rotura na direção das fibras (MPa)
Kw = 1.6;             %Influência do tipo de amarração (SB - Side Bond)

% Propriedades mecânicas do betão:
fcm = 44;                   %Resistência média do betão(MPa)
fcr = 0.311 * sqrt(fcm);    %Resistência média à tração do betão(MPa)
Ec = 3875*sqrt(fcm); %Módulo de elast. do betão - Belarbi e Hsu (1994)
e0   = -2.0;                  %Extensão última do betão (1/1000)

% Solicitações no elemento de betão armado (L-T):
tal   = 2;                    %Tensão tangencial (MPa)
sigL = 0;                     %Tensão de tração longitudinal (MPa)
sigT = 0;                     %Tensão de compressão transversal (Mpa)

%//////////////////////////////////////////////////////////////////////////
% CÁLCULOS PRELIMINARES                                                   /
%//////////////////////////////////////////////////////////////////////////

eLy  = fLy/Es*1000;
eTy  = fTy/Es*1000;
sig1 = (sigL + sigT)/2 + sqrt(((sigL - sigT)/2)^2 + tal^2);
mLT  = tal/sig1;
mL   = sigL/sig1;
mT   = sigT/sig1;

%//////////////////////////////////////////////////////////////////////////
% DADOS CURVAS EXPERIMENTAIS E TEÓRICAS                                   /
%//////////////////////////////////////////////////////////////////////////

e_plot      = 0;
sigmaD_plot = 0;
sigmaR_plot = 0;
eR_plot     = 0;
```

```
eRaux_plot  = 0;
eL_plot     = 0;
eT_plot     = 0;
fL_plot     = 0;
fT_plot     = 0;
alfa_plot   = 0;
tal_plot    = [0; 0.398; 0.867; 1.343; 1.693; 1.76; 2.043; 2.203; 2.482;
2.722; 3.068;
    3.094; 3.323; 3.385; 3.64; 3.618; 3.737; 3.949; 4.098; 4.168; 4.23; 4.347;
4.327;
    4.381; 4.228; 3.912; 3.615];  % Exp
gama_plot   = [0; 0; 0.041; 0.074; 0.095; 0.699; 1.084; 1.2; 1.429; 2.33;
3.291;
    3.567; 4.205; 4.448; 5.261; 5.596; 6.277; 6.799; 7.281; 7.867; 8.178;
8.753; 9.468;
    10.005; 10.419; 10.692; 11.012]; % Exp
tal_Teo     = [0; 2.117; 1.799; 2.339; 2.865; 3.548; 3.866; 4.164; 4.349;
4.498; 4.653;
              4.805; 4.883; 4.932; 4.971; 5.003; 5.003; 5; 4.975; 4.951;
4.92]; % SMM-FRP
gama_Teo    = [0; 0.152; 1.378; 2.233; 2.999; 4.002; 4.5; 5.644; 7.42; 8.902;
10.46;
              11.978; 12.876; 13.436; 13.963; 14.294; 14.732; 15.832; 17.162;
18.546; 20]; % SMM-FRP
eLf_plot     = 0;
eTf_plot     = 0;
fLf_plot     = 0;
fTf_plot     = 0;

%Legenda
a = 'P4-040-SB Exp.';
b = 'Eff. RA-STM FRP';
c = 'SMM-FRP (Zomoradian et al.,2018)';
end
```

Função para o cálculo das estimativas iniciais (MCTM)

```
function F = MCTM_PLACA(alfaD)

%/////////////////////////////////////////////////////////////////////////
% COMPORTAMENTO LINEAR DDA PLACA (MCTM) - ESTIMATIVAS INICIAIS PARA O RA-STM /
%/////////////////////////////////////////////////////////////////////////
global roL roT Es Ec eL eT eD sig1 mLT mL mT

% Equações de equilíbrio (Eqs. 2.53-2.55):
eL=(mL+mLT*cot(alfaD))/(Es*roL)*0.001*sig1 ;
eT=(mT+mLT*tan(alfaD))/(Es*roT)*0.001*sig1;
eD=-mLT/(Ec*sin(alfaD)*cos(alfaD))*0.001*sig1;

% Eq. não linear (Eq. 2.5):
F = (eL-eD)/(eT-eD)-(tan(alfaD))^2;

end
```

Função do RA-STM

```
function COMP_PLACA

%//////////////////////////////////////////////////////////////////////////
% COMPORTAMENTO CARGA-DEFORMÇÃO DA PLACA (RASTM_PAINEL)                  /
%//////////////////////////////////////////////////////////////////////////

global eL eT eD sigmaD eR fL fT fcm sigmaR
global ED SIGMAD TAL GAMA EL ET FL FT ALFAD ER tal_plot gama_plot SIGMAR
global FTF FLF ETF ELF eTf eLf fTf fLf Ef fu %  FRP

% Estimativa inicial com base no MCTM:
x(1) = eL*1000;
x(2) = eT*1000;
ed1  = eD*1000;
eLf = x(1);
eTf = x(2);

% Número máximo de pontos e tamanho do passo:
pontos = 1000;
passo  = 4/pontos;

% Cálculo comportamento tensão-deformção:
for i = 1:pontos

    options = optimset('TolX',10^-10,'TolFun',10^-10);
    x = lsqnonlin(@(x) RASTM_PLACA(x,ed1-passo*i),x,[0,0],[],options);

    % Criar vetores de comportamento:
    ED(i)     = ed1 - passo*i;
    SIGMAD(i)= sigmaD;
    SIGMAR(i)= sigmaR;
    COS       = (x(2)-ED(i))/(eR-ED(i));
    SIN       = (x(1)-ED(i))/(eR-ED(i));
    TAL(i)    = (-SIGMAD(i)+SIGMAR(i))*sqrt(COS*SIN);
    GAMA(i)   = 2*(eR-ED(i))*sqrt(COS*SIN);
    EL(i)     = x(1);
    ET(i)     = x(2);
    FL(i)     = fL;
    FT(i)     = fT;
    ALFAD(i) = -atan(sqrt(SIN/COS))*180/pi;
    ER(i) = EL(i) + ET(i) - ED(i);
    % Relativo ao FRP
    FTF(i)    = fTf;
    FLF(i)    = fLf;
    ETF(i)    = eTf;
    ELF(i)    = eLf;


    % Critérios de paragem (betão normal e de alta resistência)
    % (Eqs. 2.19 e 2.20..):

    if fcm <= 58
        if - ED(i) >= 3.5;
            break
        end
    else
        if - ED(i) >= 2.8 + 27 * ((98-fcm)/100)^4;
            break
        end
    end

end

MAXTAL = max(TAL);
MAXGAMAj = GAMA(find(TAL==max(TAL)));
MAXTAL_PLOT = max(tal_plot);
MAXGAMA_PLOT = gama_plot(find(tal_plot==max(tal_plot)));
```

```
disp('Valores últimos (máximos) são:');
fprintf('Tau_u,th: %f kN.m\n',MAXTAL);
fprintf('Gama_u,th: %f rad/m\n',MAXGAMAj);
fprintf('Tau_u,exp: %f kN.m\n',MAXTAL_PLOT);
fprintf('Gama_u,exp: %f rad/m\n',MAXGAMA_PLOT);
fprintf('\n')


end
```

```
function F = RASTM_PLACA(x,ed1)

%//////////////////////////////////////////////////////////////////////////
% COMPORTAMENTO NÃO-LINEAR DA PLACA (RA-STM)                             /
%//////////////////////////////////////////////////////////////////////////

global roL roT Es fcm fLy fTy e0 mLT mL mT sigmaD csi eR fL fT eLy eTy sigmaR
global Ec sigL sigT fcr
global roLe roTe rof ros fu roLf roTf csi_FRP f_FRP Ef eTf fTf eLf fLf Kw %
FRP

% CÁLCULOS INICIAIS ///////////////////////////////////////////////////////

% Princípio da Invariância (Eq. 2.8):
eR = x(1) + x(2) - ed1;

% Coeficiente de Amolecimento (Eqs. 2.15-2.18):
R = 5.8/(sqrt(fcm));
if   R <= 0.9
    R_linha = R;
else
    R_linha = 0.9;
end

n = (roT*fTy+roTf*fu-sigT)/(roL*fLy+roLf*fu-sigL);
if   n <= 1
    n_linha = n;
else
    n_linha = 1/n;
end

csi = R_linha/(sqrt(1+((0.4*eR)/n_linha)));
f_FRP = 1+0.0076*sqrt(rof*Ef);
csi_FRP = csi*f_FRP;

% Relação constitutiva do betão à compressão (Eq. 2.12):
if ed1 > csi_FRP*e0
    sigmaD = -csi_FRP*fcm*(2*(ed1/(csi_FRP*e0))-(ed1/(csi_FRP*e0))^2);
else
    sigmaD = -csi_FRP*fcm*(1-((ed1/(csi_FRP*e0)-1)/((4/csi_FRP)-1))^2);
end

% Relação constitutiva do aço (Eqs. 2.23-2.26):

% Armadura Longitudinal
roLe = roL + (Ef/Es)*rof;
BL   = (1/roLe)*(fcr/fLy)^1.5;
enL = eLy*10^-3*(0.93-2*BL);

if x(1)*10^-3 <= enL
    fL = x(1)*10^-3*Es;
else
    fL = fLy*((0.91-2*BL)+(0.02+0.25*BL)*(x(1)/eLy));
end

% Armadura Transversal
roTe = roT + (Ef/Es)*rof;
BT   = (1/roTe)*(fcr/fTy)^1.5;
enT = eTy*10^-3*(0.93-2*BT);

if x(2)*10^-3 <= enT
    fT   = x(2)*10^-3*Es;
else
    fT = fTy*((0.91-2*BT)+(0.02+0.25*BT)*(x(2)/eTy));
end

% Relação constitutiva do betão à tração
```

```
ecr = 0.08;
if rof ~= 0
    Kfs = 0.25*((rof*Ef)/(ros*Es))+0.15;
    c_FRP = Kw*Kfs;
else
    c_FRP = 0.4;
end
sigmaR = fcr*(ecr/(eR+ecr))^c_FRP; % Correção alternativa para atenuar os
problemas de convergência iniciais

% Relação constitutiva do FRP
eLf = x(1);
eTf = x(2);
% FRP longitudinal
if roLf ~= 0
    if eLf < 1000*fu/Ef
       fLf = eLf*10^-3*Ef;
    else
        fLf = 0;
    end
else
    fLf = 0;
end
% FRP transversal
if roTf ~= 0
    if eTf < 1000*fu/Ef
       fTf = eTf*10^-3*Ef;
    else
        fTf = 0;
    end
else
    fTf = 0;
end


% Tensão principal de tracção (Eqs. 2.40-2.43):
A = mL*mT - mLT^2;
B = mL*(sigmaR + roT*fT + roTf*fTf) + mT*(sigmaR + roL*fL + roLf*fLf);
C = (sigmaR + roT*fT + roTf*fTf)*(sigmaR + roL*fL + roLf*fLf);
sigma1 = (1/(2*A))*(B-sqrt(B^2-4*A*C));


%COMPORTAMENTO NÃO LINEAR RA-STM //////////////////////////////////////////

% Sistema de equações não-linear (Eq. 2.57):
F(1) = sigmaD*(x(1)-ed1)/(eR-ed1)-mT*sigma1+roT*fT + roTf*fTf + sigmaR*(x(2)-
ed1)/(eR-ed1);
F(2) = sigmaD*(x(2)-ed1)/(eR-ed1)-mL*sigma1+roL*fL + roLf*fLf + sigmaR*(x(1)-
ed1)/(eR-ed1);

end
```

Função para impressão das curvas de comportamento da placa

```
function PLOT_PLACA

%//////////////////////////////////////////////////////////////////////////
% IMPRESSÃO DAS CURVAS DE COMPORTAMENTO TENSÃO-DEFORMAÇÃO DA PLACA       /
%//////////////////////////////////////////////////////////////////////////

global ED SIGMAD TAL GAMA EL ET FL FT ER SIGMAR
global e_plot sigmaD_plot eR_plot eL_plot eT_plot fL_plot fT_plot
global tal_plot gama_plot tal_Teo gama_Teo sigmaR_plot a b c eRaux_plot
global ELF ETF FLF FTF eLf_plot eTf_plot fLf_plot fTf_plot

% DADOS INICIAIS //////////////////////////////////////////////////////////

% Opção:
disp('1 - Curva tensão-deformação de compressão do betão');
disp('2 - Curva tensão-deformação de tração do betão');
disp('3 - Curva tensão-deformação da armadura longitudinal');
disp('4 - Curva tensão-deformação da armadura transversal');
disp('5 - Curva tensão-deformação do FRP longitudinal');
disp('6 - Curva tensão-deformação do FRP transversal');
disp('7 - Curva tensão-deformação de corte da placa');
disp(' ');
disp('8 - Voltar ao inicio');
disp('0 - Sair');
disp(' ');
IND = input('Escolha uma opção: ');

% IMPRESSÃO DAS CURVAS ////////////////////////////////////////////////////

while IND > 0
    switch IND

        case 1
            % 1 - Curva tensão-deformação de compressão do betão
            hold on
            plot(e_plot,sigmaD_plot,'-rs','LineWidth',2,'MarkerSize',7)
            plot(-[0 ED],-[0 SIGMAD],'--b','LineWidth',2)%1.5)

            % Títulos
            xlabel('\epsilon_D (1/1000)');
            ylabel('\sigma_D (MPa)');
            legend(a,...
                b,'Location','southeast');
            grid on
            hold off

        case 2
            % 2 - Curva tensão-deformação de tração do betão
            hold on
            plot(eRaux_plot,sigmaR_plot,'-rs','LineWidth',2,'MarkerSize',7)
            plot([0 ER],[0 SIGMAR],'--b','LineWidth',2)%1.5)

            % Títulos
            xlabel('\epsilon_R (1/1000)');
            ylabel('\sigma_R (MPa)');
            legend(a,...
                b,'Location','southeast');
            grid on
            hold off

        case 3
            % 3 - Curva tensão-deformação da armadura longitudinal
            hold on
            plot(eL_plot,fL_plot,'--rs','LineWidth',2,'MarkerSize',7)
            plot([0 EL],[0 FL],'-g','LineWidth',2)

            % Títulos
```

```
    xlabel('\epsilon_L(1/1000)');
    ylabel('f_L (MPa)');
    legend(a,...
        b,'Location','southeast');
    grid on
    hold off

case 4
    % 4 - Curva tensão-deformação da armadura transversal
    hold on
    plot(eT_plot,fT_plot,'--rs','LineWidth',2,'MarkerSize',7)
    plot([0 ET],[0 FT],'-g','LineWidth',2)

    % Títulos
    xlabel('\epsilon_T (1/1000)');
    ylabel('f_T (MPa)');
    legend(a,...
        b,'Location','southeast');
    grid on
    hold off


case 5
    % 5 - Curva tensão-deformação do FRP longitudinal
    hold on
    plot(eLf_plot,fLf_plot,'--rs','LineWidth',2,'MarkerSize',7)
    plot([0 ELF],[0 FLF],'-g','LineWidth',2)

    % Títulos
    xlabel('\epsilon_L_f (1/1000)');
    ylabel('f_L_f (MPa)');
    legend(a,...
        b,'Location','southeast');
    grid on
    hold off


case 6
    % 6 - Curva tensão-deformação do FRP transversal
    hold on
    plot(eTf_plot,fTf_plot,'--rs','LineWidth',2,'MarkerSize',7)
    plot([0 ETF],[0 FTF],'-g','LineWidth',2)

    % Títulos
    xlabel('\epsilon_T_f (1/1000)');
    ylabel('f_T_f (MPa)');
    legend(a,...
        b,'Location','southeast');
    grid on
    hold off

case 7
    % 7 - Curva tensão-deformação de corte da placa
    hold on
    plot(gama_plot,tal_plot,'-rs','LineWidth',2,'MarkerSize',7)
    plot([0 GAMA],[0 TAL],'--b','LineWidth',2)
    plot (gama_Teo, tal_Teo,'-k','LineWidth',1)

    % Títulos
    xlabel('\gamma_L_T (1/1000)');
    ylabel('\tau_L_T (MPa)');
    legend(a,...
        b,...
        c,'Location','southeast');
    grid on
    hold off
```

```
        case 8
            if IND == 8
                inicio;
                break
            end
end
    disp(' ');
    IND = input('Escolha uma opção: ');

end
end
```

Anexo VI. Previsões teóricas do RA-STM FRP

Placa REF-P3 (Zomorodian et al., 2018)

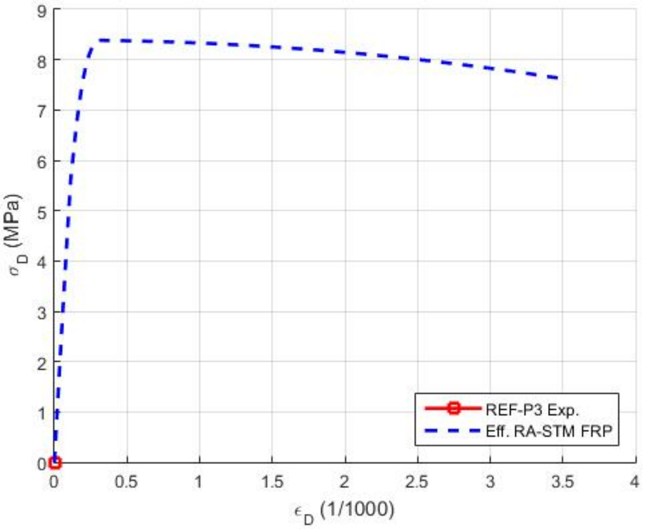

Curva $\sigma_D - \varepsilon_D$

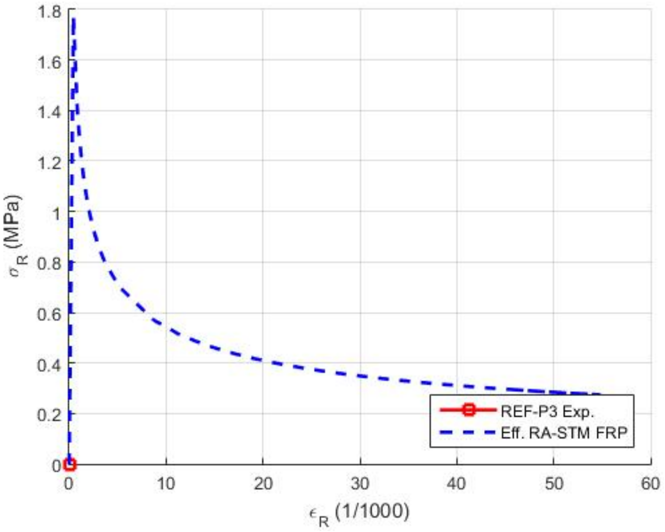

Curva $\sigma_R - \varepsilon_R$

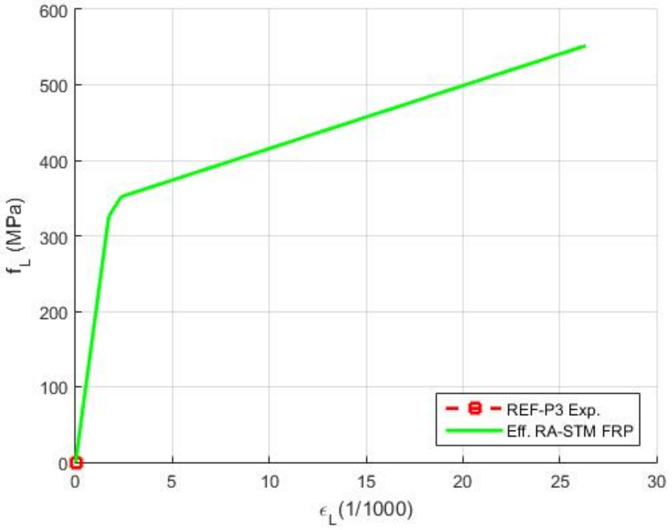

Curva $f_L - \varepsilon_L$

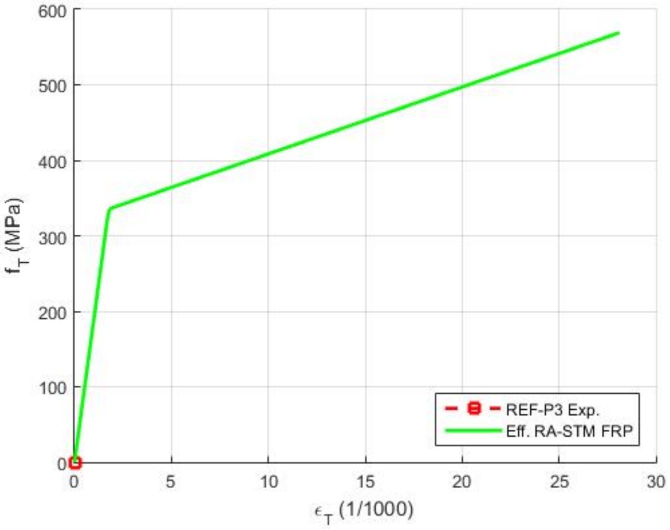

Curva $f_T - \varepsilon_T$

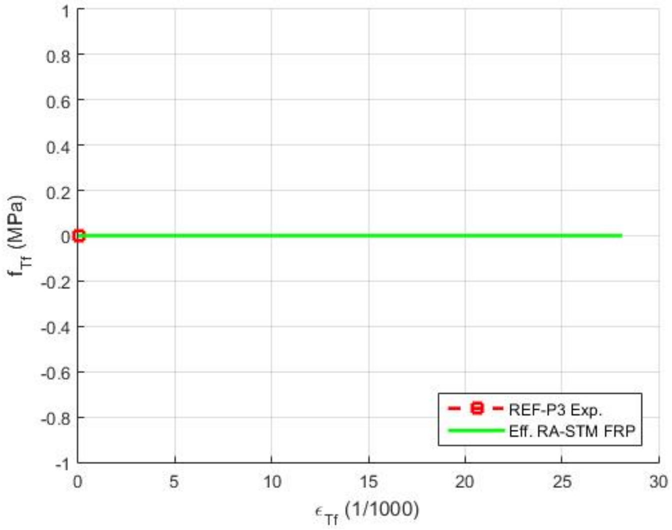

Curva $f_{Tf} - \varepsilon_{Tf}$

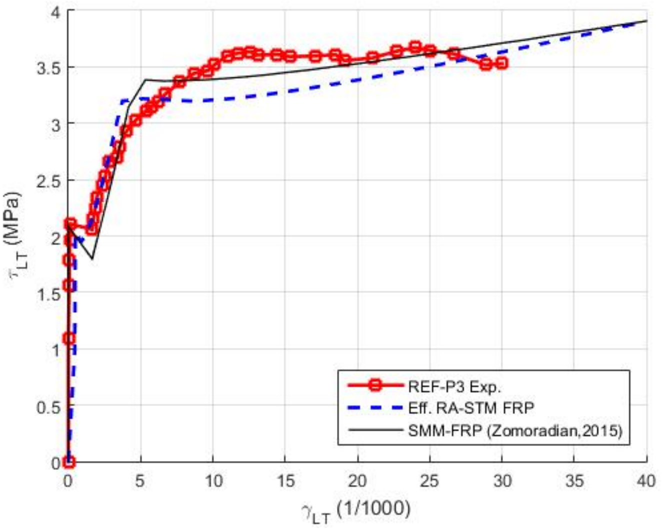

Curva $\tau_{LT} - \gamma_{LT}$

Placa REF-P4 (Zomorodian et al., 2018)

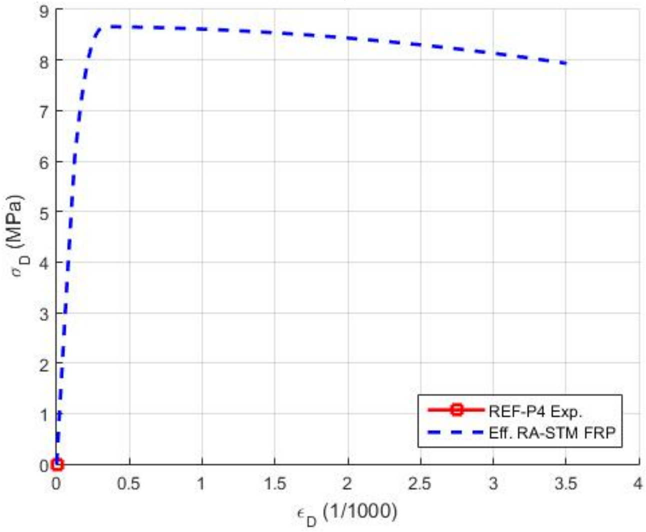

Curva $\sigma_D - \varepsilon_D$

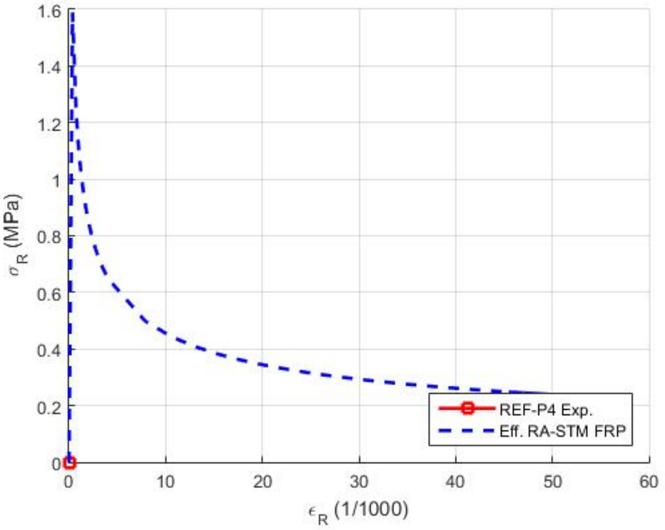

Curva $\sigma_R - \varepsilon_R$

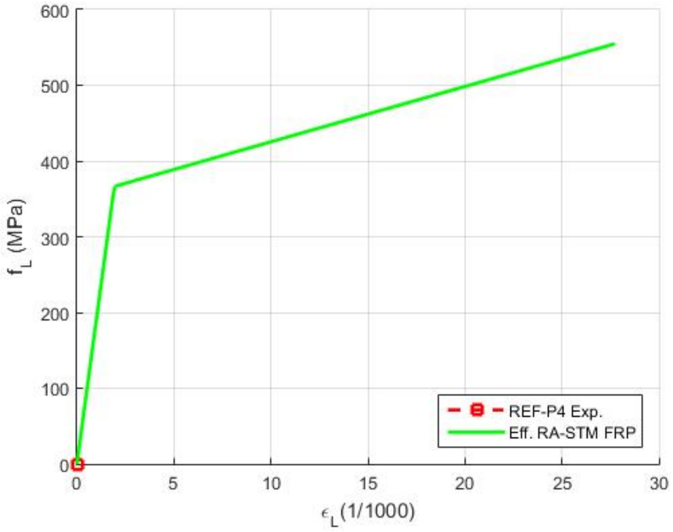

Curva $f_L - \varepsilon_L$

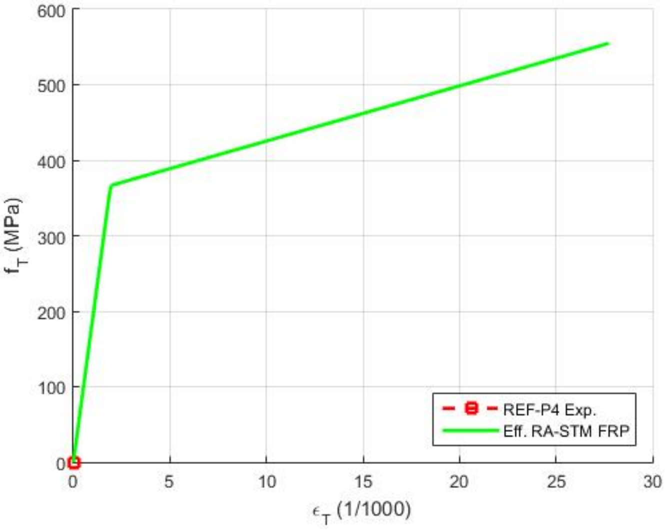

Curva $f_T - \varepsilon_T$

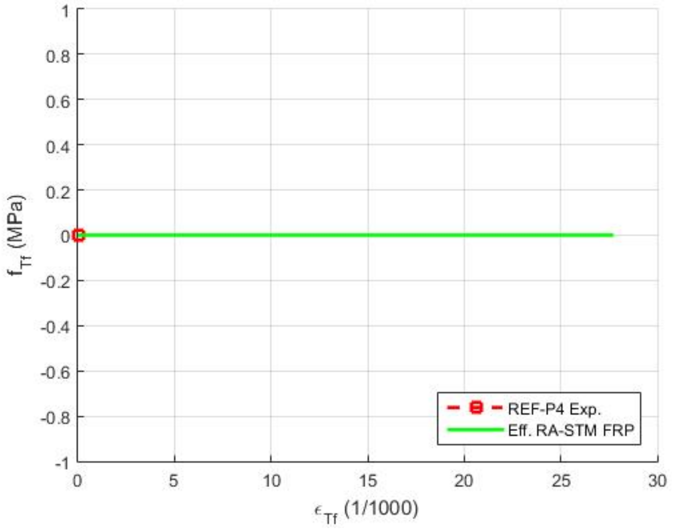

Curva $f_{Tf} - \varepsilon_{Tf}$

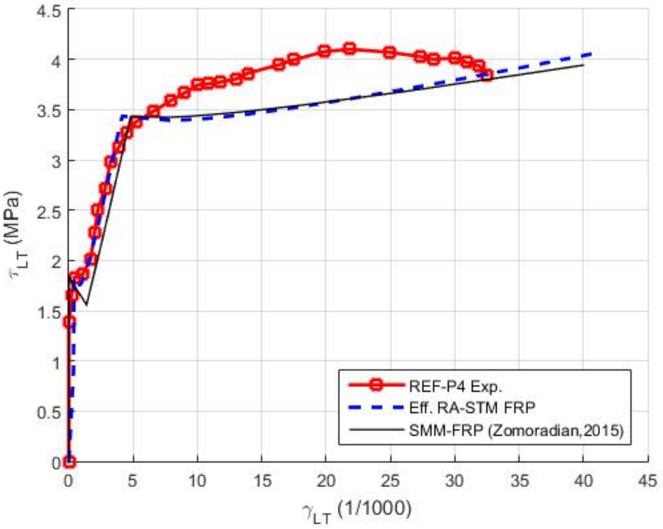

Curva $\tau_{LT} - \gamma_{LT}$

Placa P3-025-FW (Zomorodian et al., 2018)

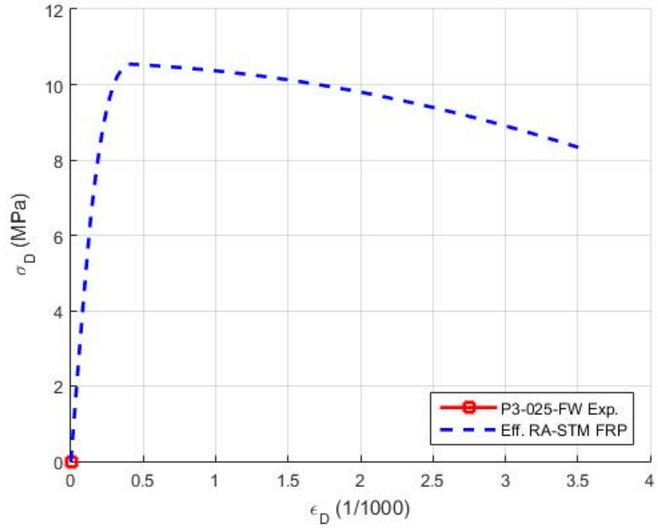

Curva $\sigma_D - \varepsilon_D$

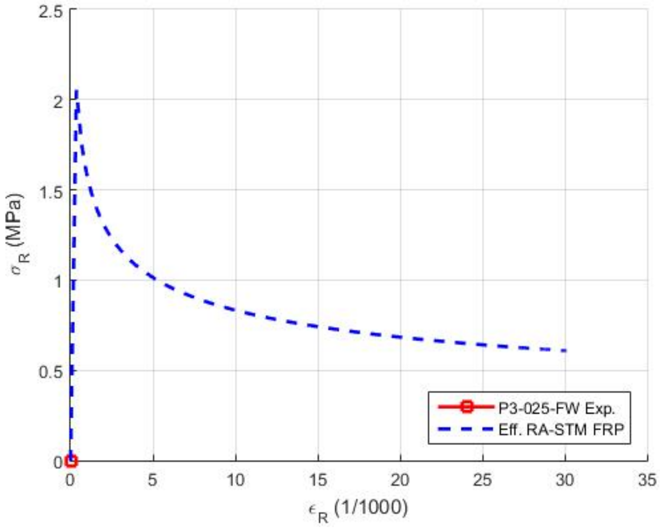

Curva $\sigma_R - \varepsilon_R$

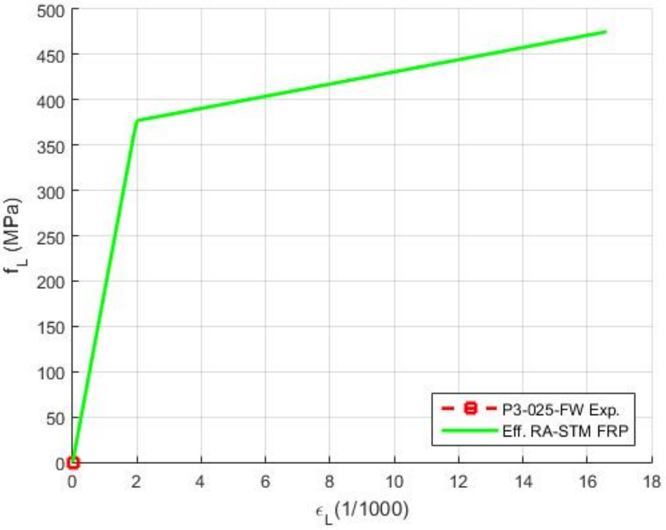

Curva $f_L - \varepsilon_L$

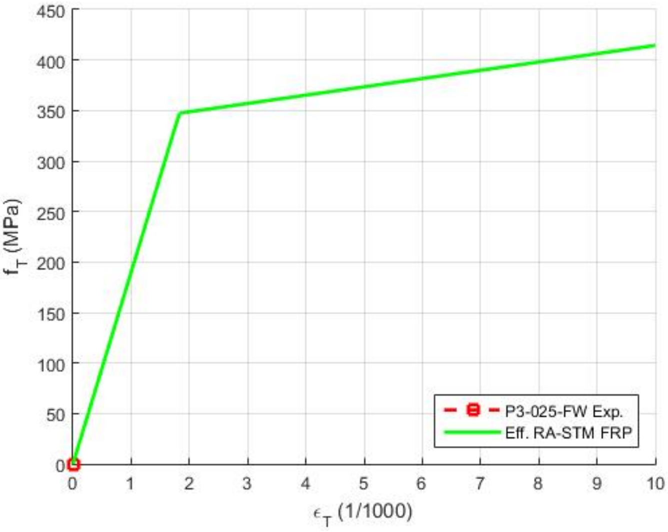

Curva $f_T - \varepsilon_T$

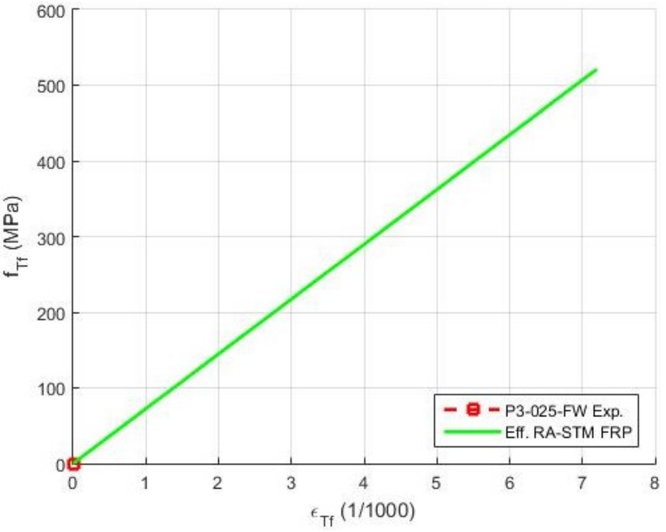

Curva $f_{Tf} - \varepsilon_{Tf}$

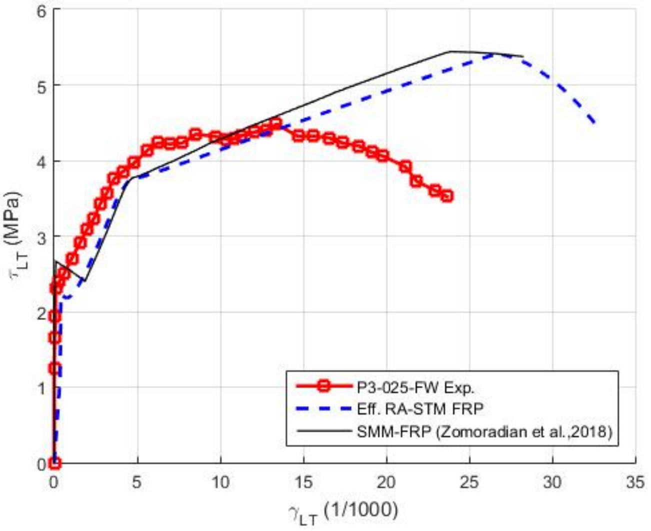

Curva $\tau_{LT} - \gamma_{LT}$

Placa P3-040-FW (Zomorodian et al., 2018)

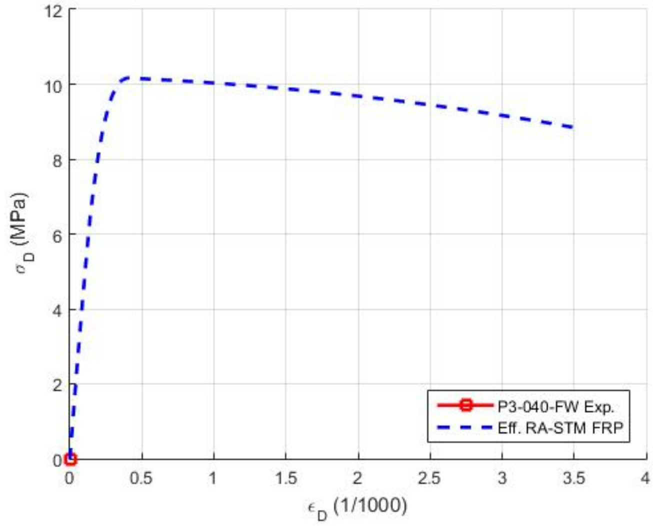

Curva $\sigma_D - \varepsilon_D$

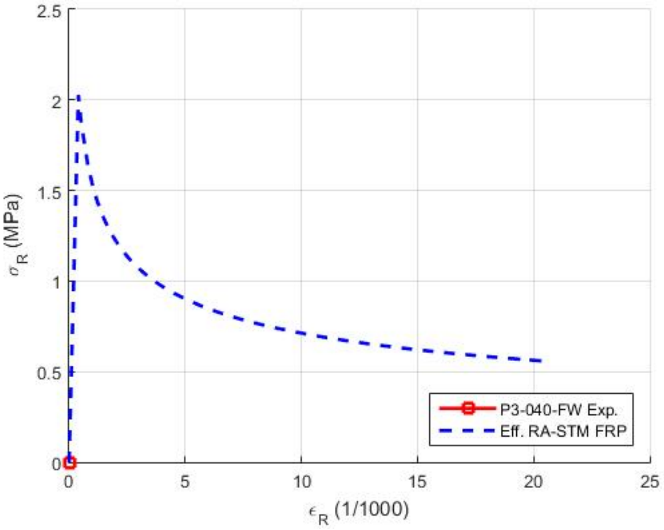

Curva $\sigma_R - \varepsilon_R$

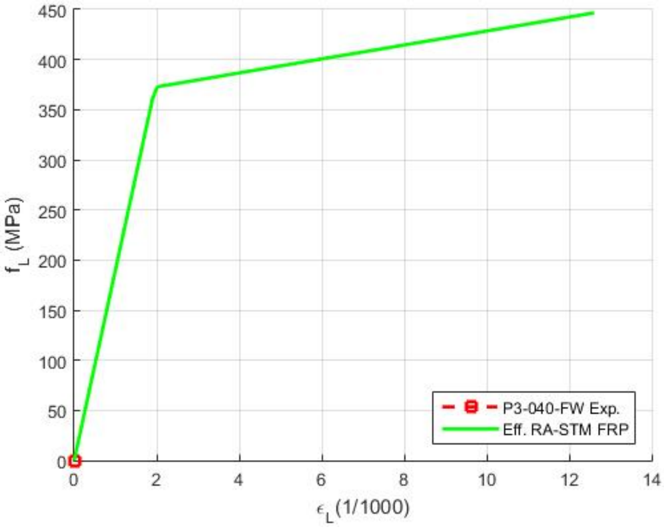

Curva $f_L - \varepsilon_L$

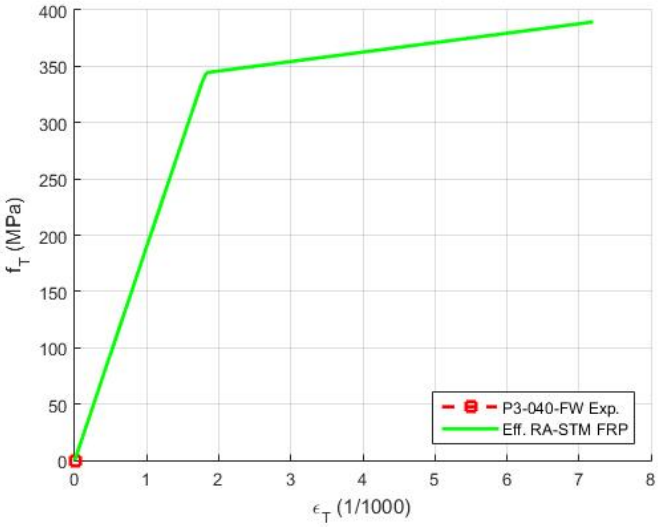

Curva $f_T - \varepsilon_T$

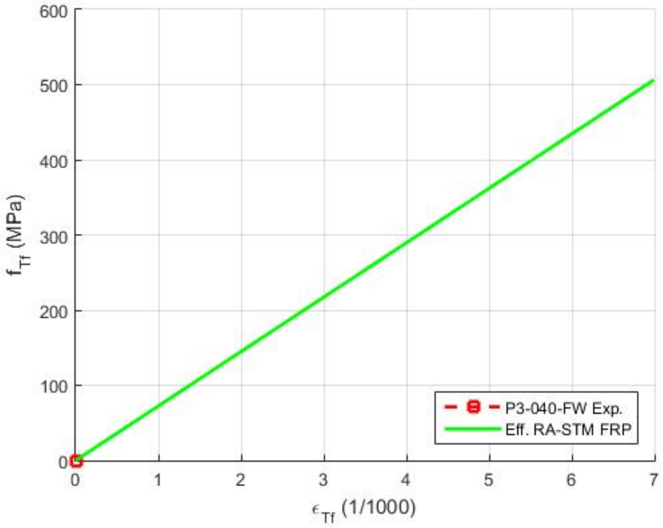

Curva $f_{Tf} - \varepsilon_{Tf}$

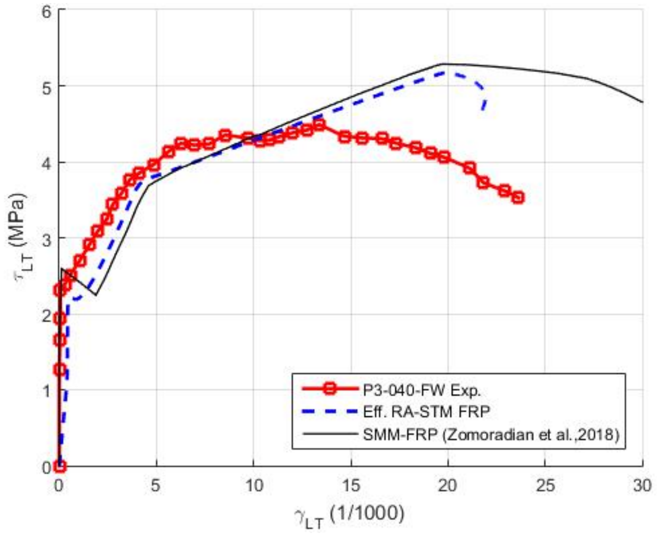

Curva $\tau_{LT} - \gamma_{LT}$

Placa P4-025-FW (Zomorodian et al., 2018)

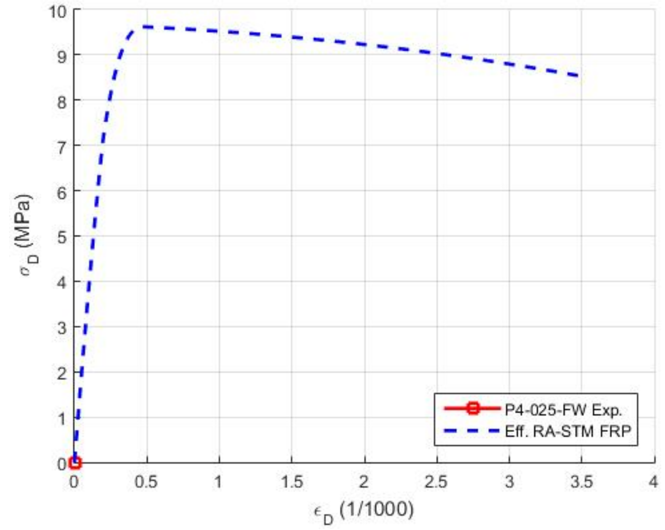

Curva $\sigma_D - \varepsilon_D$

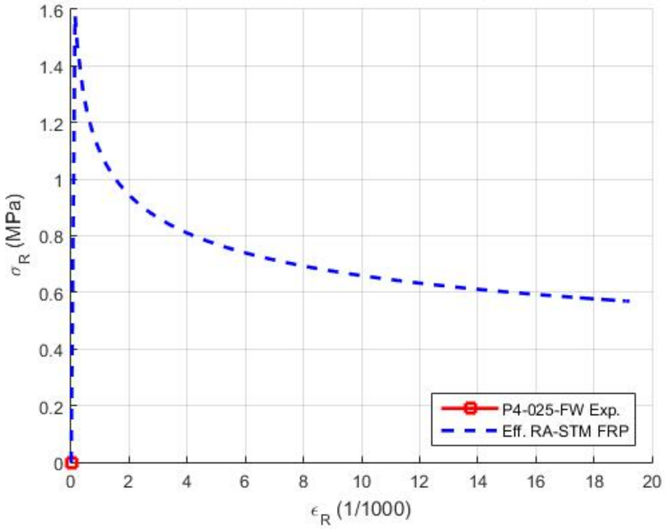

Curva $\sigma_R - \varepsilon_R$

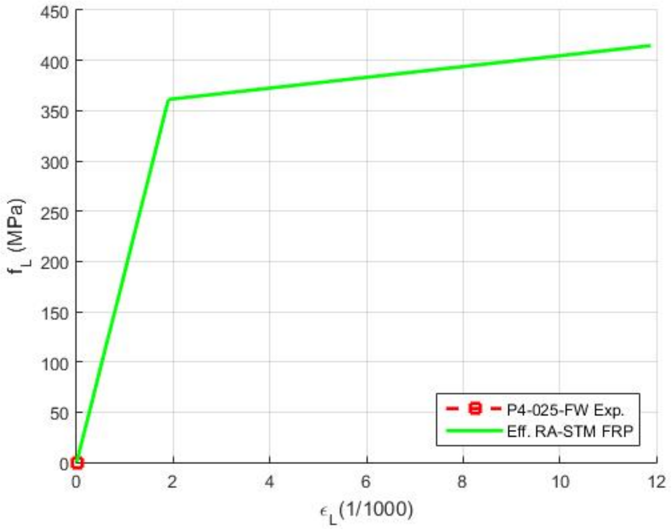

Curva $f_L - \varepsilon_L$

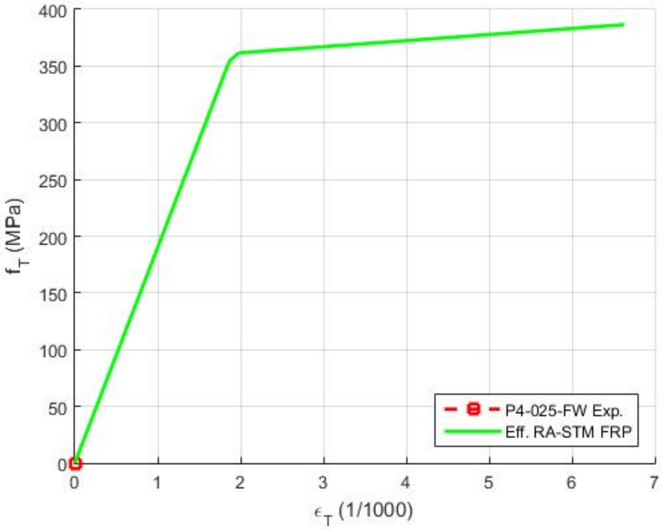

Curva $f_T - \varepsilon_T$

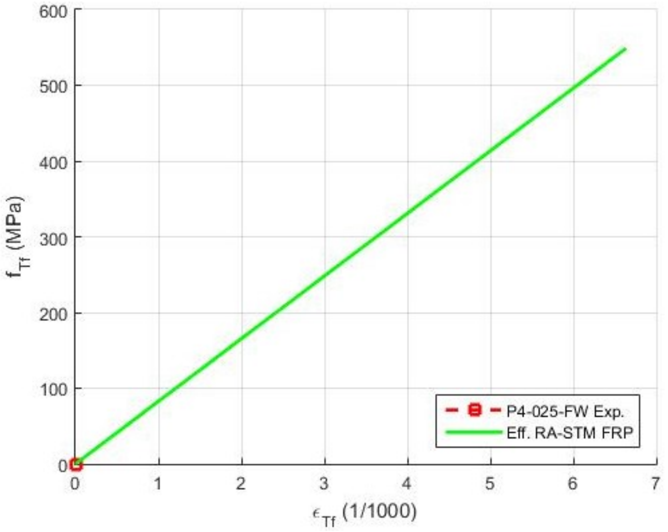

Curva $f_{Tf} - \varepsilon_{Tf}$

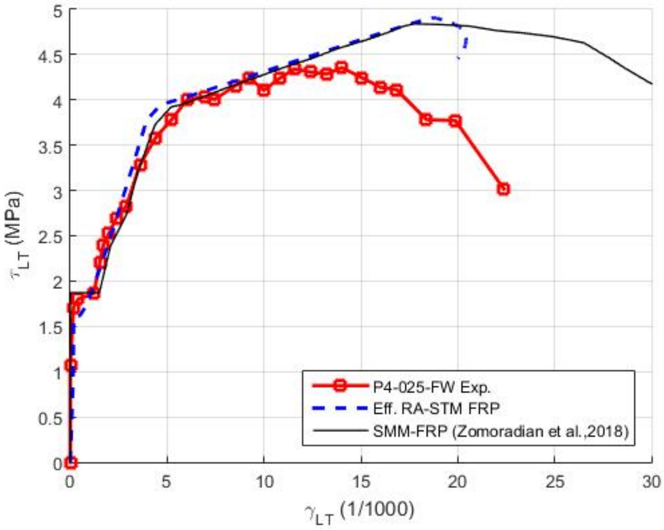

Curva $\tau_{LT} - \gamma_{LT}$

Placa P4-040-FW (Zomorodian et al., 2018)

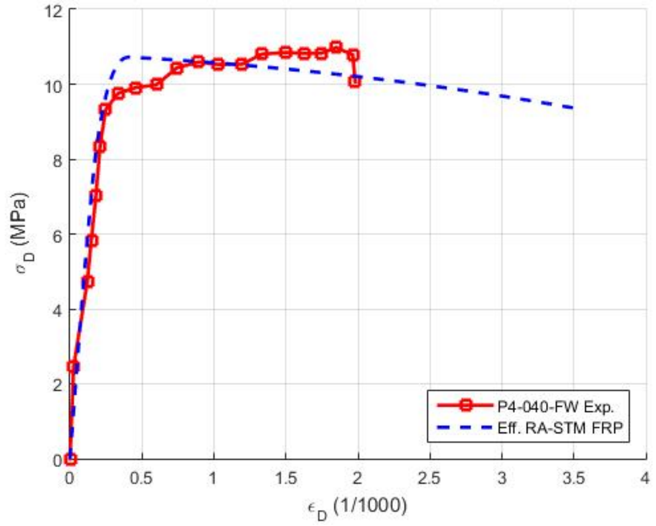

Curva $\sigma_D - \varepsilon_D$

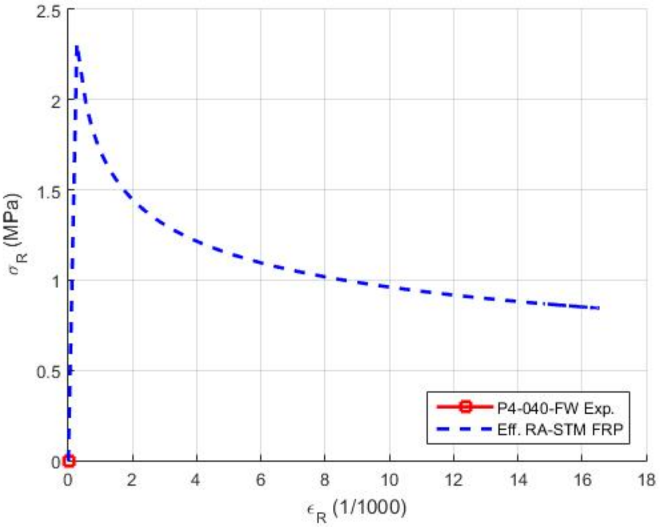

Curva $\sigma_R - \varepsilon_R$

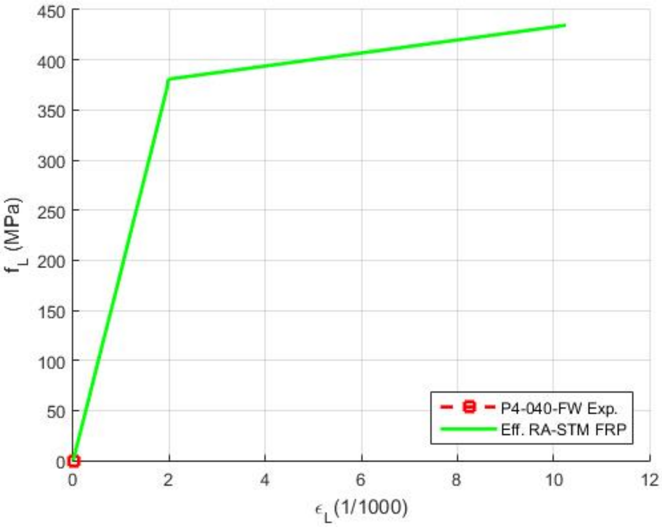

Curva $f_L - \varepsilon_L$

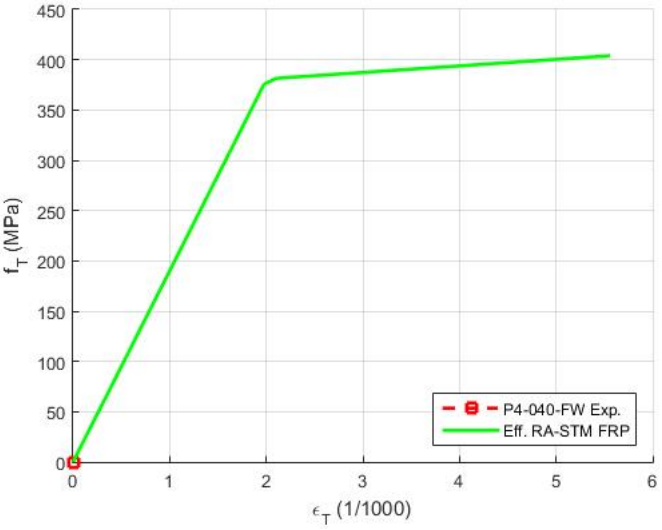

Curva $f_T - \varepsilon_T$

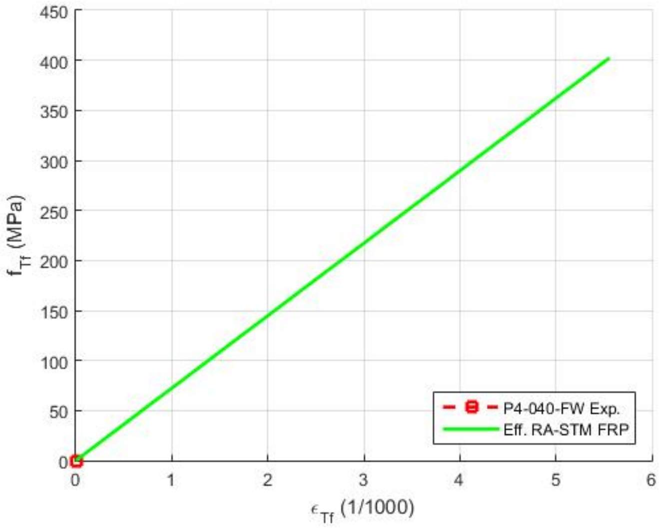

Curva $f_{Tf} - \varepsilon_{Tf}$

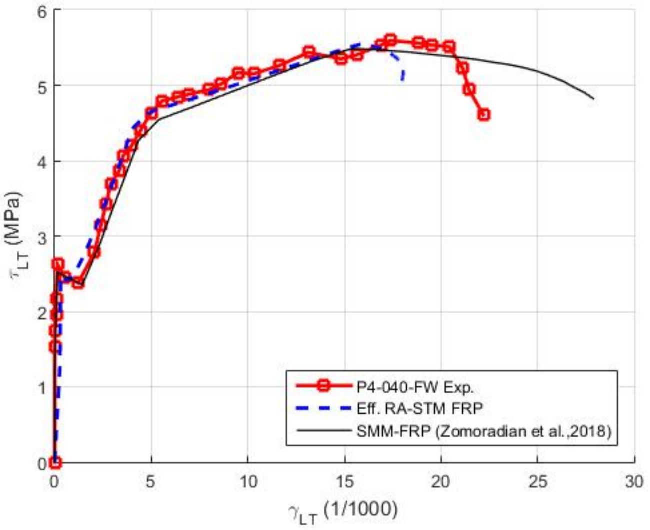

Curva $\tau_{LT} - \gamma_{LT}$

Placa P4-080-FW (Zomorodian et al., 2018)

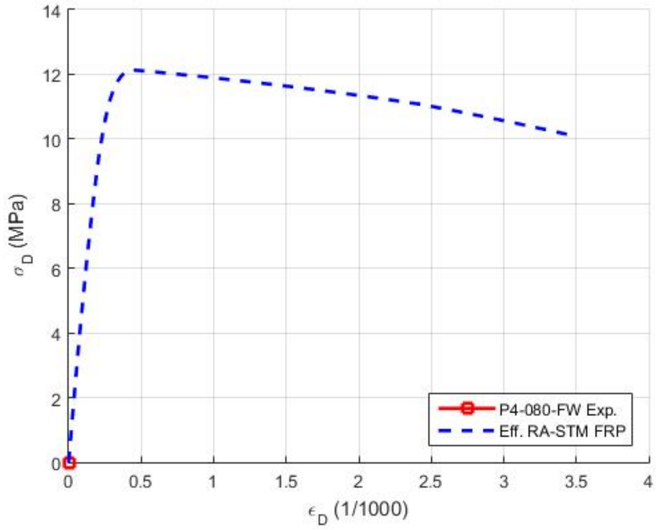

Curva $\sigma_D - \varepsilon_D$

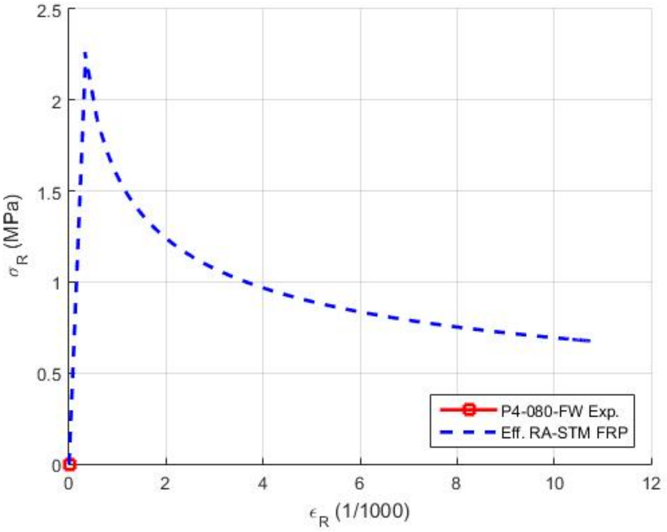

Curva $\sigma_R - \varepsilon_R$

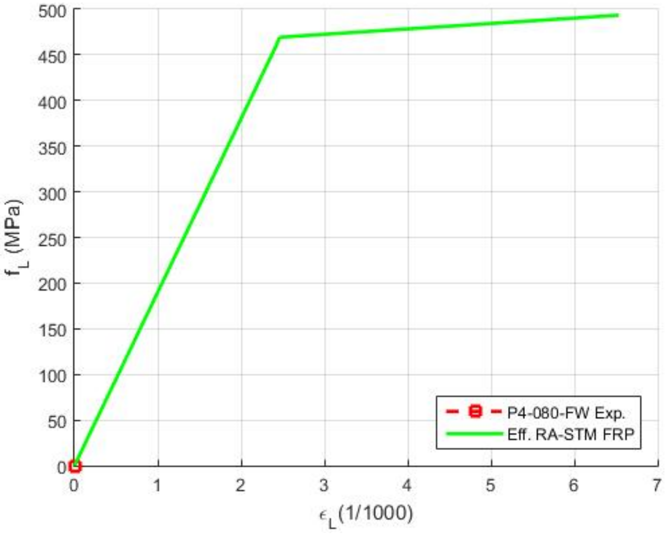

Curva $f_L - \varepsilon_L$

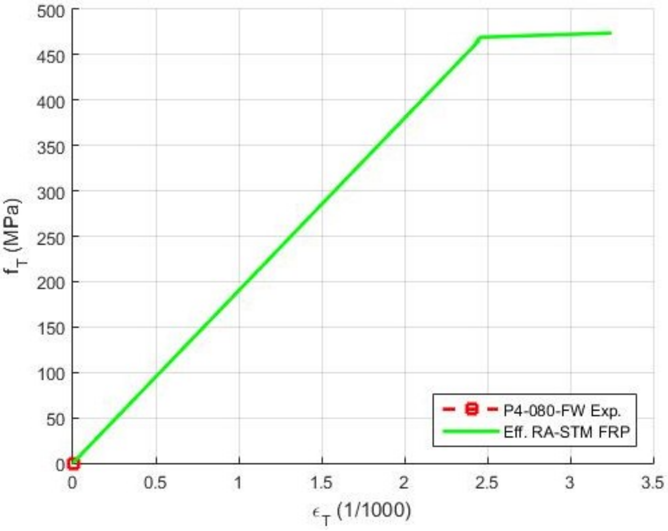

Curva $f_T - \varepsilon_T$

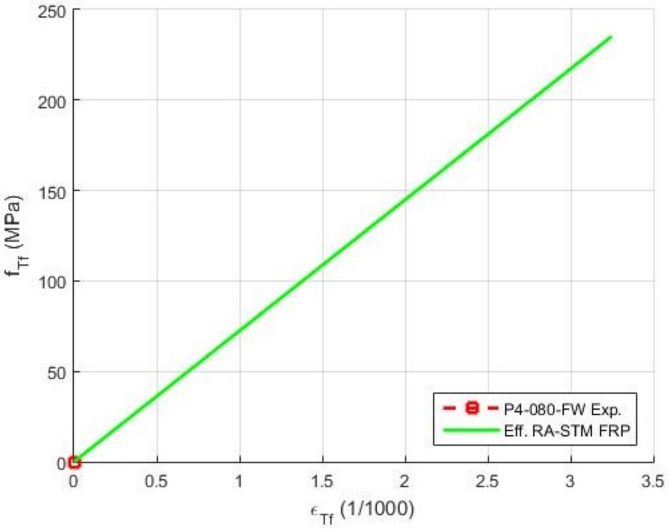

Curva $f_{Tf} - \varepsilon_{Tf}$

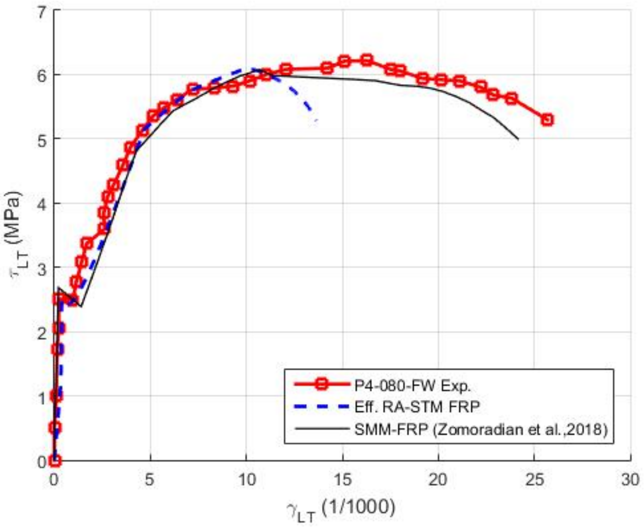

Curva $\tau_{LT} - \gamma_{LT}$

Placa P4-040-SB (Zomorodian et al., 2018)

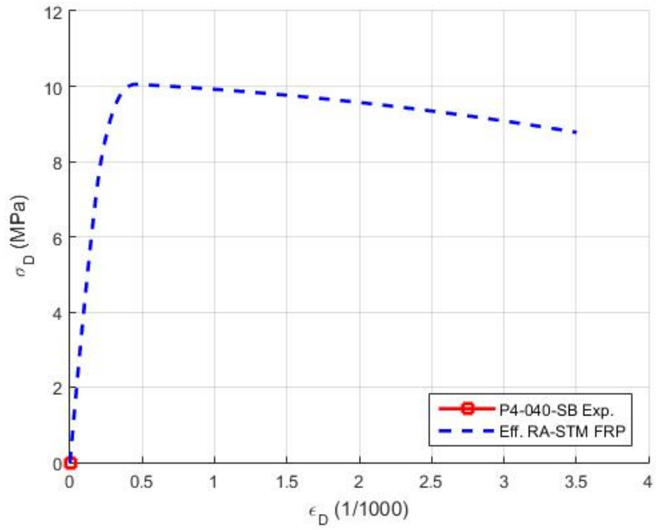

Curva $\sigma_D - \varepsilon_D$

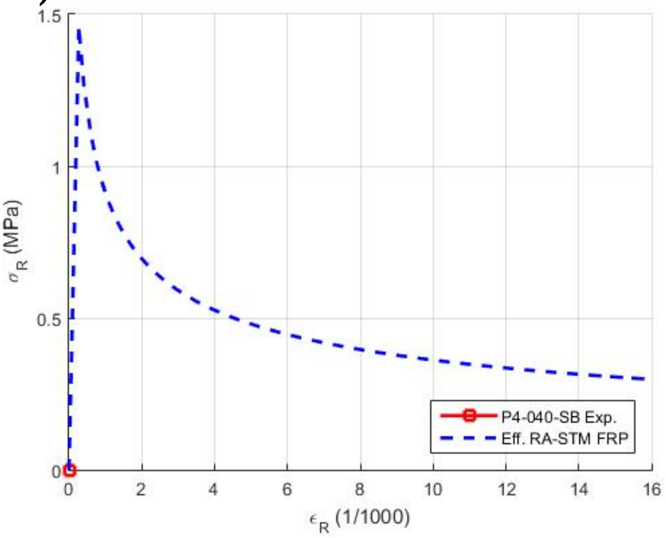

Curva $\sigma_R - \varepsilon_R$

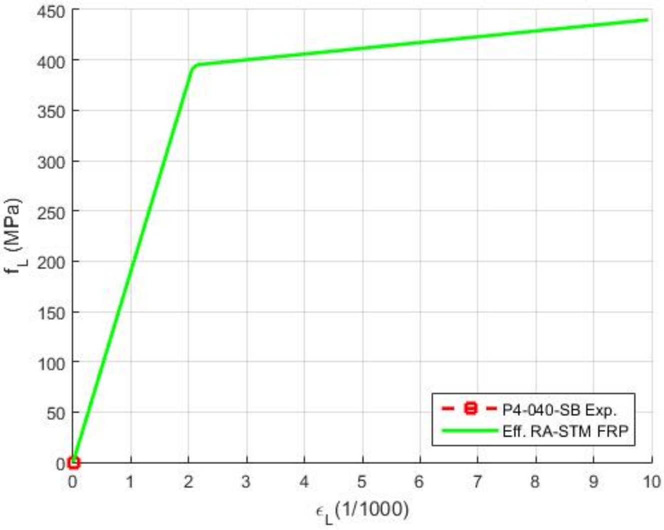

Curva $f_L - \varepsilon_L$

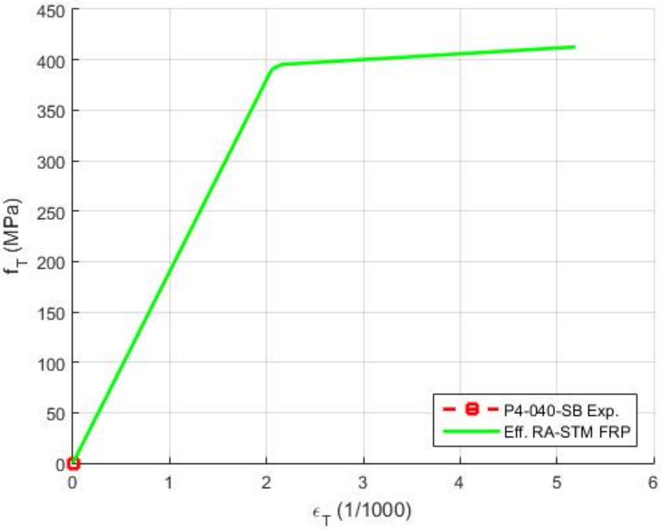

Curva $f_T - \varepsilon_T$

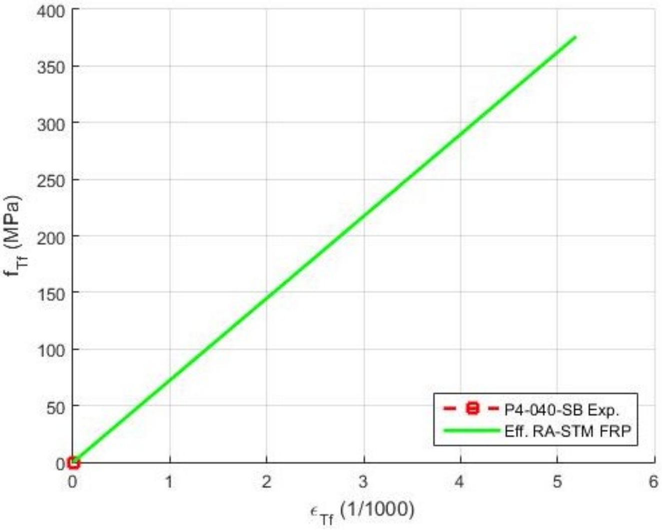

Curva $f_{Tf} - \varepsilon_{Tf}$

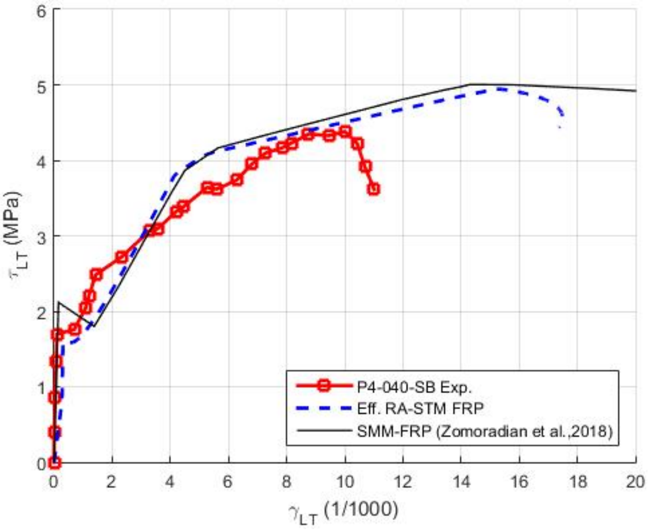

Curva $\tau_{LT} - \gamma_{LT}$

Placa P4-025-FA (Zomorodian et al., 2018)

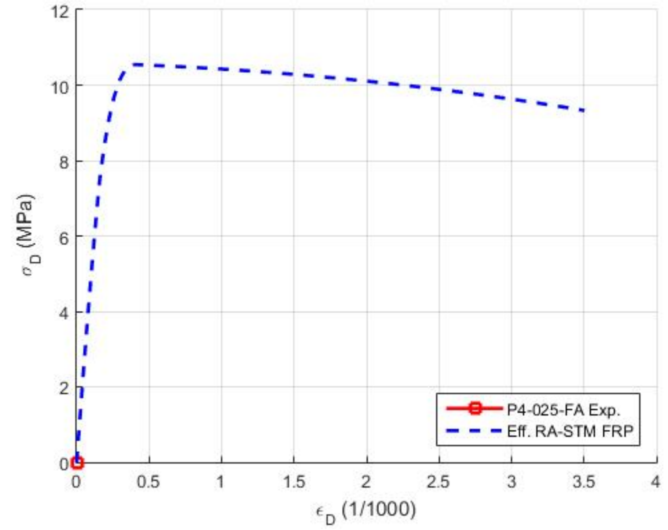

Curva $\sigma_D - \varepsilon_D$

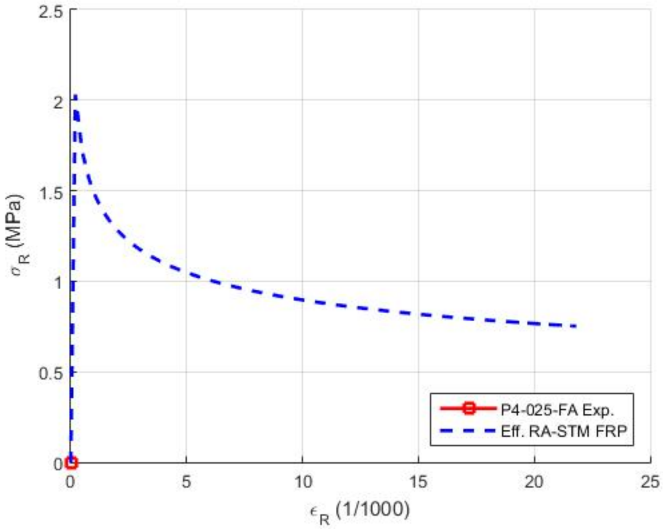

Curva $\sigma_R - \varepsilon_R$

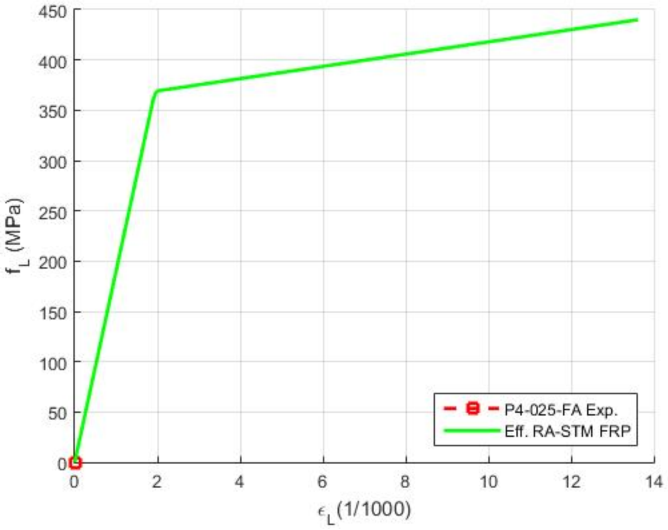

Curva $f_L - \varepsilon_L$

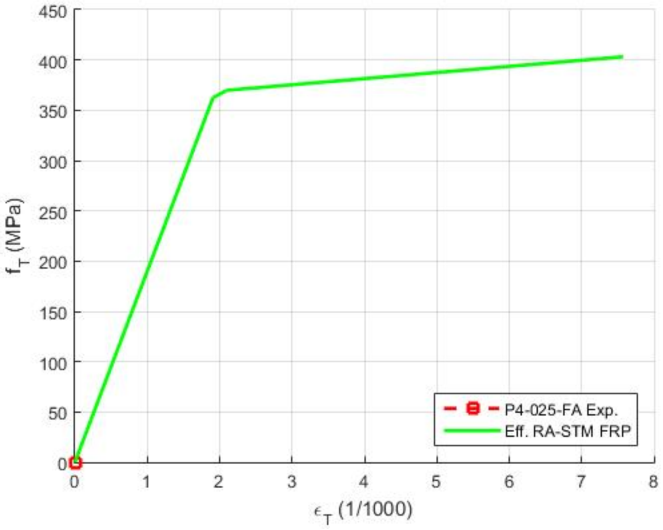

Curva $f_T - \varepsilon_T$

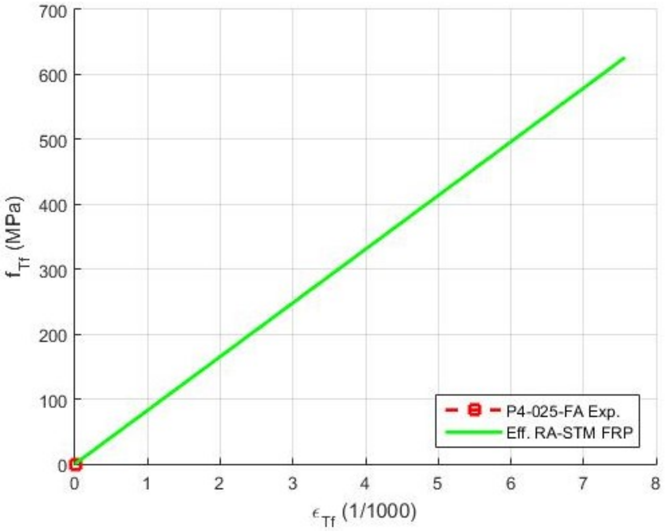

Curva $f_{Tf} - \varepsilon_{Tf}$

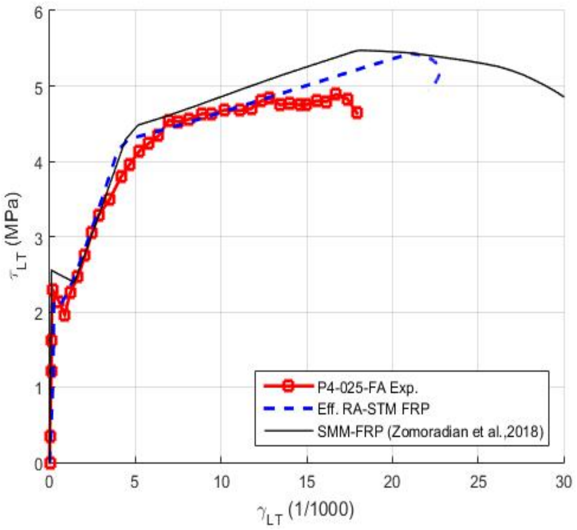

Curva $\tau_{LT} - \gamma_{LT}$

Placa P4-040-FA (Zomorodian et al., 2018)

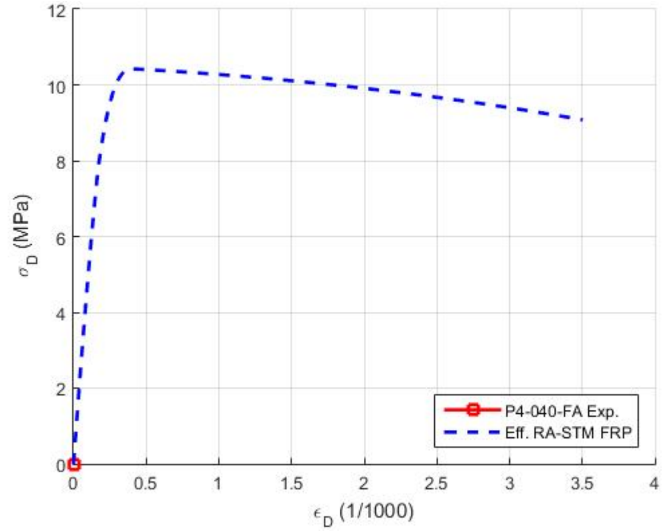

Curva $\sigma_D - \varepsilon_D$

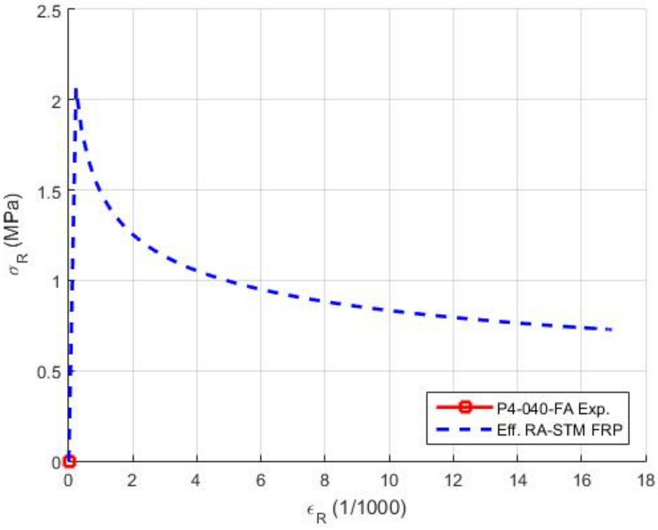

Curva $\sigma_R - \varepsilon_R$

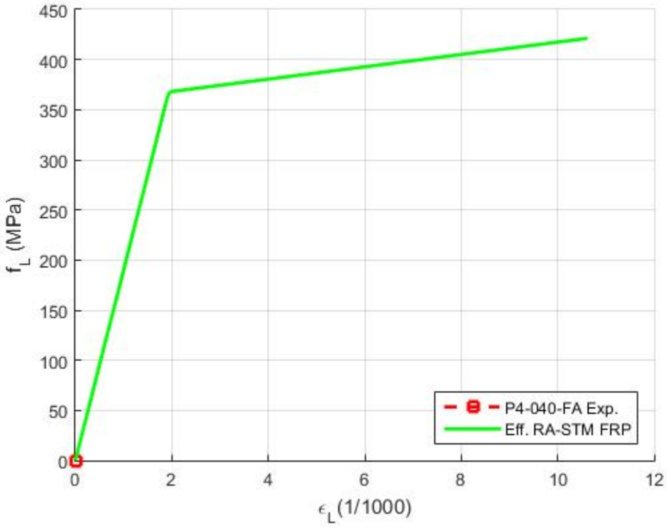

Curva $f_L - \varepsilon_L$

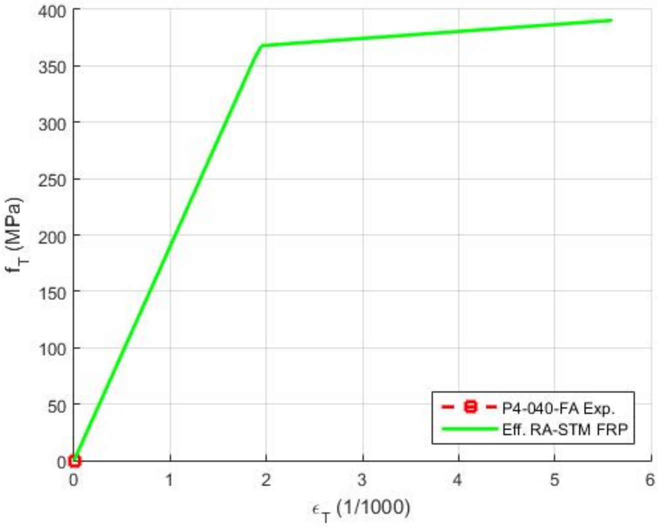

Curva $f_T - \varepsilon_T$

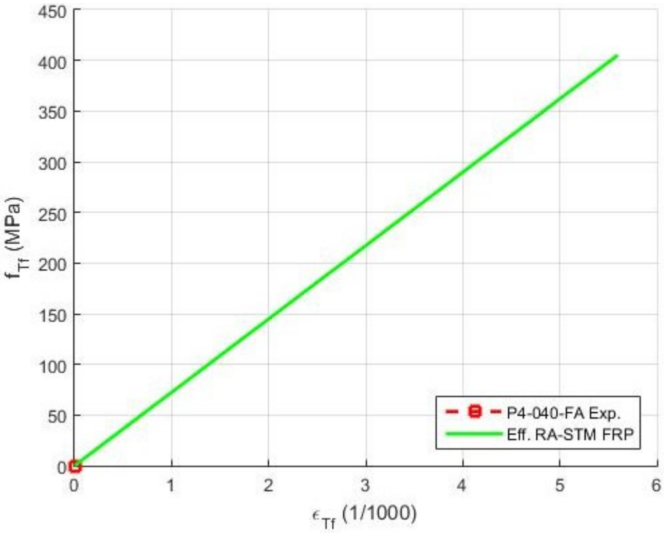

Curva $f_{Tf} - \varepsilon_{Tf}$

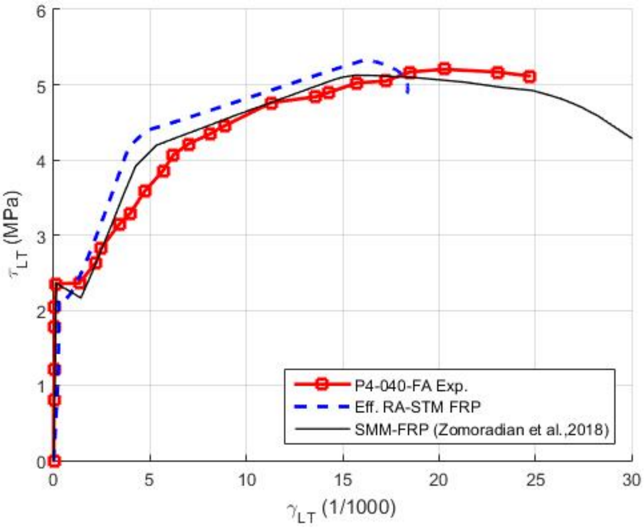

Curva $\tau_{LT} - \gamma_{LT}$

Anexo VII. Código em MATLAB do RA-STM PSFC

Script para iniciar o RA-STM PSFC

```
%////////////////////////////////////////////////////////////////////////////
//////////
% RA-STM PFSC - ROTATING ANGLE SOFTENED TRUSS MODEL - PRESTRESSED STEEL FIBER
CONCRETE /
%////////////////////////////////////////////////////////////////////////////
//////////

% Início
clear all; clc;

% Dados de entrada e escolha da placa
DADOS_INICIAIS; tic;

% Cálculo das estimativas iniciais (MCTM)
alfaD1 = (lsqnonlin(@(alfaD) MCTM_PLACA(alfaD),0.01,[],0))*180/pi;

% Vetores finais e solução
COMP_PLACA;

% Plotagem
toc; PLOT_PLACA;
```

Função para a escolha das placas

```
function DADOS_INICIAIS

%//////////////////////////////////////////////////////////////////////////
% SELEÇÃO DA PLACA                                                        /
%//////////////////////////////////////////////////////////////////////////

disp('Selecione os dados iniciais');
disp(' ');
disp('1 - TAF-1 - Hoffman N.S. (2010)');
disp('2 - TAF-2 - Hoffman N.S. (2010)');
disp('3 - TAF-3 - Hoffman N.S. (2010)');
disp('4 - TAF-4 - Hoffman N.S. (2010)');
disp('5 - TAF-5 - Hoffman N.S. (2010)');
disp(' ');
disp('0 - Sair');
disp(' ');
INDD = input('Escolha uma opção: ');

if INDD >= 0 & INDD <= 5
    switch INDD

        case 1
            TAF_1_HOFFMAN;
        case 2
            TAF_2_HOFFMAN;
        case 3
            TAF_3_HOFFMAN;
        case 4
            TAF_4_HOFFMAN;
        case 5
            TAF_5_HOFFMAN;
        case 0
            error('SCRIPT INTERROMPIDO')
            clc
    end
else
    disp(' ');
    disp('O VALOR INTRODUZIDO NÃO É VÁLIDO!');
    disp(' ');
    DADOS_INICIAIS
end
end
```

Exemplo de dados experimentais: Placa TAF-4

```
function TAF_4_HOFFMAN
%//////////////////////////////////////////////////////////////////////////
% DADOS EXPERIMENTAIS DA PLACA TAF-4 - Hoffman (2010)                     /
%//////////////////////////////////////////////////////////////////////////

global roL roT Es fLy fTy Ec fcm e0 tal sigL sigT eLy eTy fp01
global sig1 mLT mL mT
global eD_plot sigmaD_plot gama_smm_plot tal_smm_plot fpulinha
global  a b Ac m d tal_plot gama_plot
global roLP roTP  ElpsL ElpsT EpsL EpsT edecL edecT fpu fpiL fpiT  zL zT ApsT
ApsL  dET dEL yL yT
global AsL AsT Aps ePiL ePiT eLiL eLiT e_smm_plot sigmaD_smm_plot
global aspect_ratio_f v_f FF CF

%Propriedades da secção de betão
Ac = 17.8*197.71; %Área bruta da secção de betão (cm^2)

%Propriedades mecânicas dos aços ordinários:
Es  = 197000; %Módulo de elasticidade do aço (MPa)
fLy = 413.8; %Tensão de cedência corrigida do aço longitudinal (MPa)
fTy = 413.8; %Tensão de cedência corrigida do aço transversal (MPa)
AsL= 2.79; %Área mínima de aço ordinário longitudinal (cm^2) (não pode ser
zero!)
AsT= 14.93; %Área de aço ordinário transversal (cm^2)

roL = AsL/Ac; %Taxa Mec. de armadura ordinária Longitudinal.
roT = AsT/Ac; %Taxa Mec. de armadura ordinária Transversal.

%Propiedades mecânicas dos aços de pré-esforço:
ElpsL = 209000; %Módulo de elasticidade de Ramberg-Osgood P.E-Longitudinal
(MPa)
ElpsT = 209000; %Módulo de elasticidade de Ramberg-Osgood P.E-Transversal
(MPa)
EpsL = 200000; %Módulo de elasticidade da armadura de P.E-Longitudinal (MPa)
EpsT = 200000; %Módulo de elasticidade da armadura de P.E-Transversal (MPa)
fpu= 1862; %Tensão última da armadura de P.E. (MPa)
fpulinha = 1862;
fp01 = 1670;  %Tensão de propocionalidade (MPa)
m =5;
ApsL=20.76; %Área de aço de pré-esforço longitudinal (cm^2)
ApsT=0; %Área de aço de pré-esforço transversal (cm^2)
fpiL=983; %Tensão inicial de pré-eforço nos cordões longitudinais de pré-
esforço(MPa)
fpiT=0; %Tensão inicial de pré-eforço nos cordões longitudinais de pré-
esforço(MPa)

% Propriedades mecânicas do betão:
fcm = 56.4; %Resitência média à compressão do betão(MPa)
Ec = 3875*sqrt(fcm); %Módulo de Elasticidade - Belarbi e Hsu (1994)(MPa)
e0  = -1.9; %Extensão do betão para o pico de tensão (1/1000)

% Propriedades das fibras de aço:
aspect_ratio_f = 80; % Esbelteza da fibra
v_f = 1.0; %Volume de fibras (em %)

FF = aspect_ratio_f*v_f/100; %Fator de fibra

CF = 1; % betão confinado por dois planos de armaduras de pré-esforço
% CF = 0.5; % betão não confinado (um só plano de armaduras de pré-esforço)

%CÁLCULOS PRELIMINARES RELATIVOS AO PRÉ-ESFORÇO
Aps=ApsT+ApsL;  %Área total de armadura de P.E.
roLP = ApsL/Ac;  %Taxa Mec. de armadura de P.E-longitudinal
roTP = ApsT/Ac; %Taxa Mec. de armadura de P.E-transversal.
ePiL= fpiL/EpsL; %Extensão inicial no aço de P.E-longitudinal
ePiT= fpiT/EpsT; %Extensão inicial no aço de P.E-transversal.
```

```
eLiL= ApsL*fpiL/(AsL*(Es-Ec)+Ec*(Ac-ApsL)); %Extensão no aço ordinário
longitudinal
eLiT= ApsT*fpiT/(AsT*(Es-Ec)+Ec*(Ac-ApsT)); %Extensão no aço ordinário
transversal
edecT = ePiT+eLiT;  %Extensão de descompressão transversal
edecL = ePiL+eLiL;   %Extensão de descompressão longitudinal

%Solicitações no elemento de betão armado (L-T):
tal  = 1;%-3.69;  %Tensão de corte (MPa)
sigL =  0;     %Tensão de tração longitudinal (MPa)
sigT =  0;     %Tensão de compressão transversal (MPa)

%CÁLCULOS PRELIMINARES
eLy  = fLy/Es*1000;
eTy  = fTy/Es*1000;
sig1 = (sigL + sigT)/2 + sqrt(((sigL - sigT)/2)^2 + tal^2);
mL   = sigL/sig1;
mT   = sigT/sig1;
mLT  = tal/sig1;

%CORREÇÃO DA CURVA PARA ESTA PLACA

%Resolução do valor de extensão (Y) para a equação não-linear:
%Análise Longitudinal
%Definir yL como variável simbólica
syms yL
%Equação a resolver
y=-0.7*fpulinha+ElpsL*(yL)/(1+(ElpsL*(yL)/fpu)^m)^(1/m);
yL=solve(y,yL);
%Retornar o valor em número:
yL=double(yL);
%Análise Transversal;
%Definir yT como variável simbólica
syms yT
%Equação a resolver
y=-0.7*fpulinha+ElpsT*(yT)/(1+(ElpsT*(yT)/fpu)^m)^(1/m);
yT=solve(y,yT);
%Retornar o valor em número:
yT=double(yT);
%Resolução do valor de extensão (Z) para a equação linear:
%Análise Longitudinal
zL=0.7*fpulinha/EpsL;
%Análise Transversal
zT=0.7*fpulinha/EpsT;
%Calculo do delta E
%Análise longitudinal
dEL= zL-yL;
%Análise transversal
dET= zT-yT;


%DADOS PLOTAGEM DO TAF-4
% Curvas médias tensão tensão normal (MPa) - extensão do betão à compressão
% (1/1000)
% Experimental
eD_plot      = 0;
sigmaD_plot = 0;
% Teórico SMM-PSFC
e_smm_plot  = 0;
sigmaD_smm_plot = 0;

% Curvas médias tensão de corte (MPa) - distorção (1/1000)
% Experimental
tal_plot = [0.000;3.964;4.344;4.685;4.947;4.999;5.011;5.099;5.166;5.400;5.581;
            5.581;5.426;5.414;5.327;5.345;5.330;5.216;5.207;5.281;5.255;5.303;
            5.292;5.150;5.277;5.163;5.090;4.996;4.863;4.923;4.876;4.771;4.849;
            4.832;4.849;4.754;4.814;4.841;4.724];
```

```
gama_plot =
[0;0.368;0.502;0.618;0.81;1.033;1.333;1.391;1.646;1.928;2.479;2.849;

3.007;3.295;3.454;3.688;3.864;4.097;4.438;4.576;4.752;4.927;5.363;

5.815;6.059;6.262;6.526;6.98;7.349;7.772;8.509;9.246;9.929;10.493;
             11.025;11.361;11.654;12.239;12.521];


% Teórico SMM-PSFC
tal_smm_plot = [0.000;3.084;3.811;4.381;4.607;4.936;5.002;5.092;5.099;5.236;
                5.332;5.424;5.442;5.481;5.455;5.443;5.499;5.557;5.632;5.859;
                5.889;5.962;6.021;6.126;6.158;6.193;6.223;6.243;6.279;6.285;
                6.265;6.217];

gama_smm_plot = [0;0.187;0.25;0.311;0.498;0.693;0.834;1.172;1.348;1.79;2.214;
                 2.852;3.516;4.215;4.862;9.014;9.911;10.724;12.031;13.278;

13.559;14.979;16.374;18.116;19.149;20.165;21.05;21.824;22.509;
                 23.294;23.961;24.363];


a = 'TAF-4 Exp.';
b = 'Eff. RA-STM';
d = 'SMM-PSFC (Hoffman, 2010)';

end
```

Função para o cálculo das estimativas iniciais (MCTM)

```
function F=MCTM_PLACA (alfaD)

%//////////////////////////////////////////////////////////////////////
% COMPORTAMENTO LINEAR DA PLACA (MTCM) - ESTIMATIVA INICIAL PARA O RA-STM/
%//////////////////////////////////////////////////////////////////////

global roL roT Es Ec eL eT eD sig1 mLT mL mT roLP roTP fpiL fpiT

eL = (mL+mLT*cot(alfaD))/(Es*roL)*0.001*sig1-((roLP*fpiL/(Es*roL))*0.001);
eT = (mT+mLT*tan(alfaD))/(Es*roT)*0.001*sig1-((roTP*fpiT/(Es*roT))*0.001);
eD = -mLT/(Ec*sin(alfaD)*cos(alfaD))*0.001*sig1;

%Equação não-linear de estimativa inicial MCTM
F = (eL-eD)/(eT-eD)-(tan(alfaD))^2;

end
```

Função do RA-STM

```
function COMP_PLACA

%///////////////////////////////////////////////////////////////////////////
% COMPORTAMENTO CARGA-DEFORMÇÃO DA PLACA (RASTM_PLACA)                      /
%///////////////////////////////////////////////////////////////////////////

global roL roT eR eL eT EL ET fL fT FL FT fcm fpT fpL FPT FPL
global ED SIGMAD TAL GAMA ALFAD ER ROLFL_ROTFT ETOTALL ETOTALT EDECL EDECT
SIGMAR
global eD sigmaD edecL edecT etotalL etotalT tal_plot gama_plot sigmaR

%Estimativa inicial com base no MCTM

x(1) = eL*1000;
x(2) = eT*1000;
ed1  = eD*1000;
etotalL = edecL+x(1);
etotalT = edecT+x(2);

%Número máximo de pontos e tamanho do passo

pontos = 1000;
passo  = 4/pontos;

%Cálculo comportamento carga-deformação

for i = 1:pontos

options = optimset('TolX',10^-10,'TolFun',10^-10);
x = lsqnonlin(@(x) RASTM_PLACA (x,ed1-passo*i),x,[0,0],[],options);

%Criar vetores de comportamento:
    ED(i)     = ed1 - passo*i;
    SIGMAD(i)= sigmaD;
    SIGMAR(i)= sigmaR;
    COS       = (x(2)-ED(i))/(eR-ED(i));
    SIN       = (x(1)-ED(i))/(eR-ED(i));
    TAL(i)    = (-SIGMAD(i)+SIGMAR(i))*sqrt(COS*SIN);
    GAMA(i)   = 2*(eR-ED(i))*sqrt(COS*SIN);
    EL(i)     = x(1);%*10^-3;
    ET(i)     = x(2);%*10^-3;
    FL(i)     = fL;
    FT(i)     = fT;
    ALFAD(i) = -atan(sqrt(SIN/COS))*180/pi;
    ER(i)        = EL(i)+ET(i)-ED(i);
    ROLFL_ROTFT (i)  = FL(i)*roL+FT(i)*roT;

    %Relativamente ao pré-esforço

    FPT(i)      = fpT;
    FPL(i)      = fpL;
    ETOTALL(i) = etotalL;
    ETOTALT(i) = etotalT;
    EDECL  (i)  = edecL;
    EDECT  (i)  = edecT;

    %Critérios de paragem (betão de resistência normal ou betão de alta
 % resistência)
    if fcm <= 58
        if - ED(i) >= 3.5;
            break
        end

    else
        if - ED(i) >= 2.8 + 27 * ((98-fcm)/100)^4;
            break
        end
```

```
    end
end

MAXTAL = max(TAL);
MAXGAMAj = GAMA(find(TAL==max(TAL)));
MAXTAL_PLOT = max(tal_plot);
MAXGAMA_PLOT = gama_plot(find(tal_plot==max(tal_plot)));
disp('Valores últimos (máximos) são:');
fprintf('Tau_u,th: %f kN.m\n',MAXTAL);
fprintf('Gama_u,th: %f rad/m\n',MAXGAMAj);
fprintf('Tau_u,exp: %f kN.m\n',MAXTAL_PLOT);
fprintf('Gama_u,exp: %f rad/m\n',MAXGAMA_PLOT);
fprintf('\n')

end
```

```
function F = RASTM_PLACA(x,ed1)

%//////////////////////////////////////////////////////////////////////////
% COMPORTAMENTO NÃO-LINEAR DA PLACA (RA-STM)                              /
%//////////////////////////////////////////////////////////////////////////

global m roL roLP roTP roT eR Es EpsL EpsT ElpsT ElpsL zL zT dEL dET ePiL
global e0 eLy eTy edecL edecT etotalL etotalT
global fL fT fTy fpT fpL fpu fcm fp01 fLy mLT mL mT sigmaD csi Ec sigL sigT
sigmaR
global FF CF

%Cálculos iniciais

%Princípio da Invariância
eR = x(1)+x(2)-ed1;

%Coeficiente de Amolecimento
R = 5.8/(sqrt(fcm));

if   R<= 0.9
    R_linha = R;
else
    R_linha = 0.9;
end

n = ((roL*fLy)+(roLP*fp01)-sigL)/((roT*fTy)+(roTP*fp01)-sigT);

if  n <= 1
    n_linha = n;
else
    n_linha = 1/n;
end

W_f = 1 + 0.2*FF; % Influência das fibras
csi_f = W_f*R_linha/(sqrt(1+((0.4*eR)/n_linha)));


if  csi_f <= 0.9
    csi = csi_f;
else
    csi = 0.9;
end

%Lei constitutiva do betão à compressão com csi corrigido por causa das
%fibras
if abs(ed1)<csi*abs(e0)
    sigmaD = -csi*fcm*(2*(ed1/(csi*e0))-(ed1/(csi*e0))^2);
else
    sigmaD = -csi*fcm*(1-((ed1/(csi*e0)-1)/((4/csi)-1))^2);
end

% Nova Lei constitutiva do betão com fibras à tração
ecy = 0.05; % (1/1000)
ePi = ePiL; % Só existe pré-esforço longitudinal (-)
ecpk = (0.01 - ePi)*1000; % (1/1000)
emax = (0.04 - ePi)*1000; % (1/1000)
fcy = 0.4*FF*CF*(fcm)^0.5; % (MPa)
fcpk = (0.2*FF + 12*roLP)*(fcm)^0.5; % (MPa)
Ec_T1 = fcy/(ecy/1000); % (MPa)
Ec_T2 = (fcpk - fcy)/((ecpk - ecy)/1000); % (MPa)
Ec_T3 = -fcpk/((emax - ecpk)/1000); % (MPa)

if eR <= ecy
    sigmaR  = Ec_T1*eR/1000;
elseif eR > ecy & eR <= ecpk
    sigmaR = fcy + Ec_T2*(eR-ecy)/1000;
else
```

```
    sigmaR = fcpk + Ec_T3*(eR-ecpk)/1000;
end


if  sigmaR >= 0
    sigmaR = sigmaR;
else
    sigmaR = 0;
end

%Relação constitutiva do aço ordinário e de pré-esforço
% corrigida para ter em conta as fibras

%Tensão média de rotura e correspondente extensão do betão à tração

fcr = 0.311*sqrt(fcm);
ecr = 0.08;

%Armadura ordinária longitudinal

BNL  = (1/roL)*(fcr/fLy)^1.5;
enL = eLy*10^-3*(0.93-2*BNL);

if x(1)*10^-3 <= enL
    fL = x(1)*10^-3*Es;
else
    fL = fLy*((1-0.096*FF)*(0.91-
2*BNL)+((0.2*FF+1)*(0.02+0.25*BNL)*(x(1)/eLy)));
end

%Armadura ordinária transversal

BNT  = (1/roT)*(fcr/fTy)^1.5;
enT = eTy*10^-3*(0.93-2*BNT);

if x(2)*10^-3 <= enT
    fT = x(2)*10^-3*Es;
else
    fT = fTy*((1-0.096*FF)*(0.91-
2*BNT)+((0.2*FF+1)*(0.02+0.25*BNT)*(x(2)/eTy)));
end


%Armadura de pré-esforço

etotalL = edecL+x(1)*10^-3;
etotalT = edecT+x(2)*10^-3;

%Armadura de pré-esforço longitudinal

if  edecL ~= 0
        if etotalL > zL
            fpL = ElpsL*(etotalL-dEL)/(1+(ElpsL*(etotalL-dEL)/fpu)^m)^(1/m);
        else
            fpL = EpsL*(etotalL);
        end
    else
        fpL=0;
    end


%Armadura de pré-esforço transversal

if  edecT ~= 0
        if etotalT > zT
            fpT = ElpsT*(etotalT-dET)/(1+(ElpsT*(etotalT-dET)/fpu)^m)^(1/m);
        else
            fpT = EpsT*(etotalT)
```

```
        end
    else
        fpT=0;
    end

%Tensão principal de tração
S = mL*mT-mLT^2;
B = mL*(sigmaR+roT*fT+roTP*fpT)+mT*(sigmaR+roL*fL+roLP*fpL);
C = (sigmaR+roT*fT+roTP*fpT)*(sigmaR+roL*fL+roLP*fpL);
sigma1 = (1/(2*S))*(B-sqrt(B^2-4*S*C));


%Comportamento não linear RA-STM

% Sistema de equações não-linear
F(1) = sigmaD*(x(1)-ed1)/(eR-ed1)-mT*sigma1+roT*fT+roTP*fpT+sigmaR*(x(2)-
ed1)/(eR-ed1);
F(2) = sigmaD*(x(2)-ed1)/(eR-ed1)-mL*sigma1+roL*fL+roLP*fpL+sigmaR*(x(1)-
ed1)/(eR-ed1);

end
```

Função para impressão das curvas de comportamento da placa

```
function PLOT_PLACA

%//////////////////////////////////////////////////////////////////////////
% IMPRESSÃO DAS CURVAS DE COMPORTAMENTO DA PLACA                          /
%//////////////////////////////////////////////////////////////////////////

global a b d
global tal_plot gama_plot tal_smm_plot gama_smm_plot
global FPL FPT ETOTALL ETOTALT ED SIGMAD TAL GAMA EL ET FL FT ER SIGMAR

% Opção:
disp(' ');
disp('PLACAS SÉRIE "TAF" ou PLACA COM DADOS INTRODUZIDOS');
disp(' ');
disp('1 - Curva Tensão de compressão x Deformação de compressão do betão');
disp('2 - Curva Tensão de tração x Deformação de tração do betão');
disp('3 - Curva Tensão de tração x Deformação de tração da armadura
longitudinal ordinária');
disp('4 - Curva Tensão de tração x Deformação de tração da armadura
transversal ordinária');
disp('5 - Curva Tensão de tração x Deformação de tração da armadura
longitudinal de pré-esforço');
disp('6 - Curva Tensão de tração x Deformação de tração da armadura
transversal de pré-esforço');
disp('7 - Curva Tensão de corte x Deformação de corte');
disp(' ');
disp('8 - Voltar ao início');
disp(' ');
disp('0 - Sair');
disp(' ');
IND = input('Escolha uma opção: ');

%Casos de plotagem e impressão das curvas

while IND > 0
    switch IND

% PLACAS SÉRIE "TAF-1" ou PLACA COM DADOS INTRODUZIDOS

        case 1
            % 1 - Curva Tensão de compressão x Deformação de compressão do
betão
            hold on
            plot(-[0 ED],-[0 SIGMAD],'--b','LineWidth',2)

            % Títulos
            xlabel('\epsilon_D (1/1000)');
            ylabel('\sigma_D (MPa)');
            legend(b,'Location','southeast');
            grid on
            hold off


        case 2
            % 2 - Curva Tensão de tração x Deformação de tração do betão
            hold on
            plot([0 ER],[0 SIGMAR],'--b','LineWidth',2)

            % Títulos
            xlabel('\epsilon_R (1/1000)');
            ylabel('\sigma_R (MPa)');
            legend(b,'Location','southeast');
            grid on
            hold off
```

```
 case 3
    % 3 - Curva Tensão de tração x Deformação de tração da armadura
        % longidudinal ordinária
    hold on
    plot([0 EL],[0 FL],'--b','LineWidth',2)

    % Títulos
    xlabel('\epsilon_L (1/1000)');
    ylabel('f_L (MPa)');
    legend(b,'Location','southeast');
    grid on
    hold off


 case 4
    % 4 - Curva Tensão de tração x Deformação de tração da armadura
        % transversal ordinária
    hold on
    plot([0 ET],[0 FT],'--b','LineWidth',2)

    % Títulos
    xlabel('\epsilon_T (1/1000)');
    ylabel('f_T (MPa)');
    legend(b,'Location','southeast');
    grid on
    hold off


 case 5
    % 5 - Curva Tensão de tração x Deformação de tração da armadura
        % longidudinal de pré-esforço
    hold on
    plot([ETOTALL*1000],[FPL],'--b','LineWidth',2)

    % Títulos
    xlabel('\epsilon_p_L (1/1000)');
    ylabel('f_p_L (MPa)');
    legend(b,'Location','southeast');
    grid on
    hold off


 case 6
    % 6 - Curva Tensão de tração x Deformação de traçã da armadura
        % transversal de pré-esforço
    hold on
    plot([ETOTALT*1000],[FPT],'--b','LineWidth',2)

    % Títulos
    xlabel('\epsilon_p_T (1/1000)');
    ylabel('f_p_T (MPa)');
    legend(b,'Location','southeast');
    grid on
    hold off


case 7
    % 7 - Curva Tensão de corte x Deformação de corte
    hold on
    plot(gama_plot,tal_plot,'-rs','LineWidth',2)
    plot(gama_smm_plot,tal_smm_plot,'-g','LineWidth',2,'MarkerSize',7)
    plot([0 GAMA],[0 TAL],'--b','LineWidth',2)

    % Títulos
    xlabel('\gamma_L_T (1/1000)');
    ylabel('\tau_L_T (MPa)');
    legend(a,...
        d,...
```

```
                b,'Location','southeast');
            grid on
            hold off


         case 8
             inicio;
    end

    disp(' ');
    IND = input('Escolha uma opção:');

end
end
```

Anexo VIII. Previsões teóricas do RA-STM PSFC

Placa TAF-1 (Hoffman N.S., 2010)

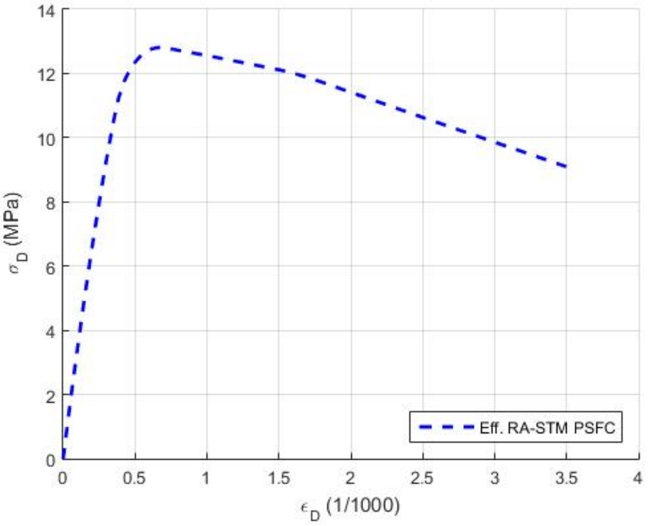

Curva $\sigma_D - \varepsilon_D$

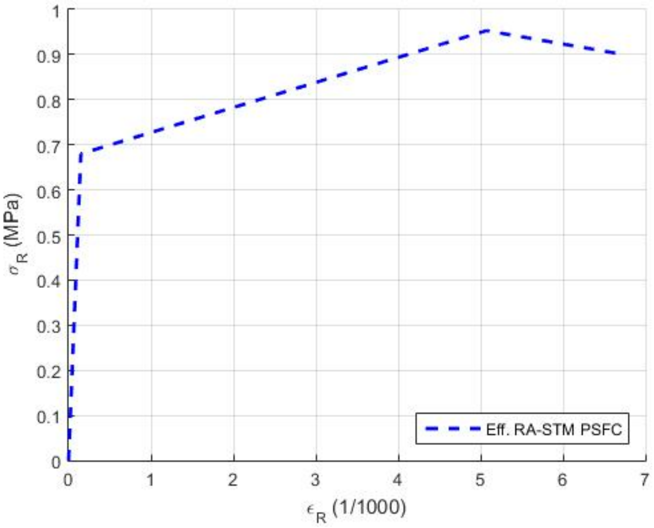

Curva $\sigma_R - \varepsilon_R$

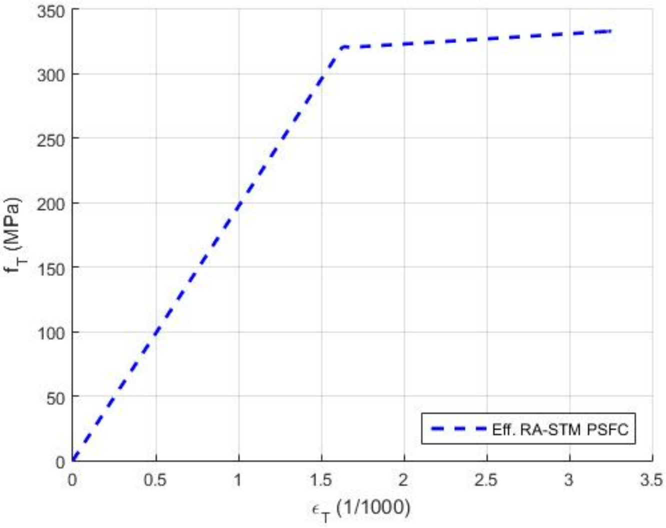

Curva $f_T - \varepsilon_T$

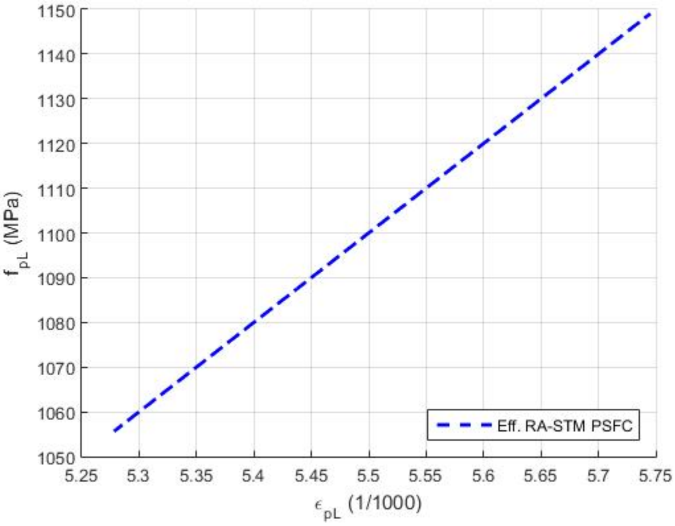

Curva $f_{pL} - \varepsilon_{pL}$

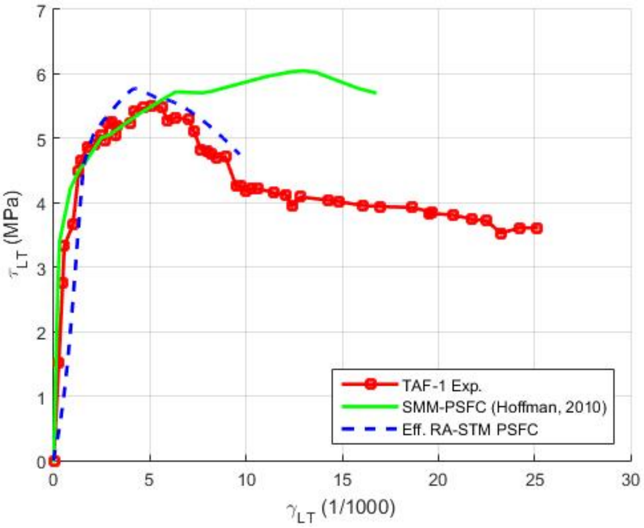

Curva $\tau_{LT} - \gamma_{LT}$

Placa TAF-2 (Hoffman N.S., 2010)

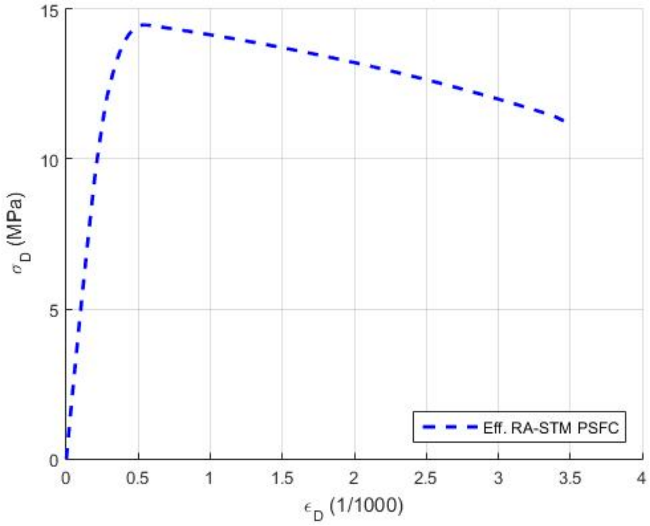

Curva $\sigma_D - \varepsilon_D$

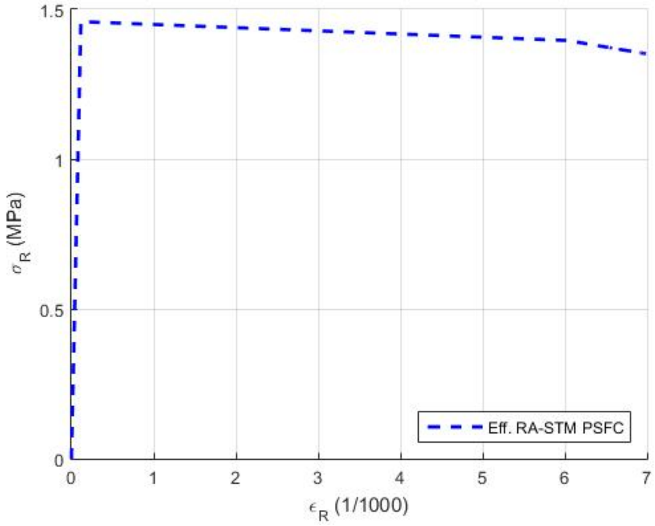

Curva $\sigma_R - \varepsilon_R$

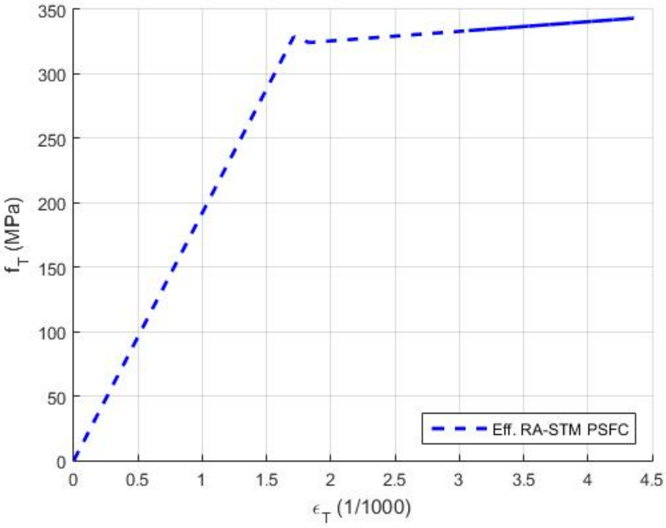

Curva $f_T - \varepsilon_T$

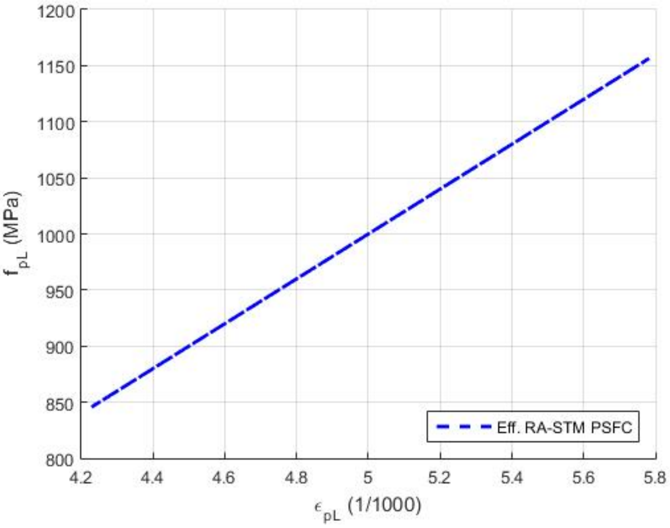

Curva $f_{pL} - \varepsilon_{pL}$

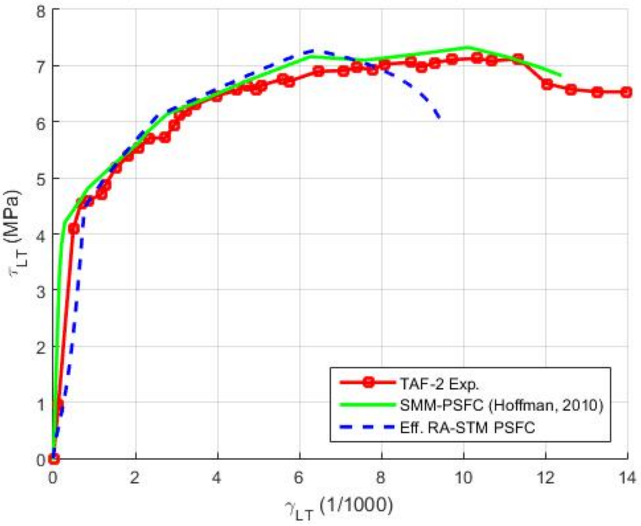

Curva $\tau_{LT} - \gamma_{LT}$

Placa TAF-3 (Hoffman N.S., 2010)

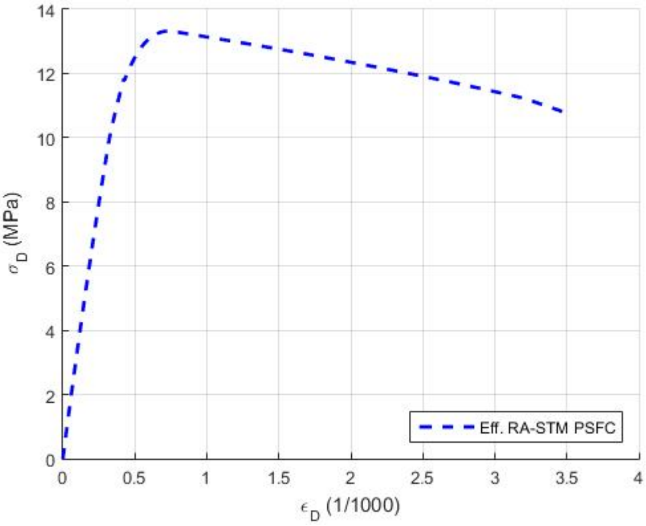

Curva $\sigma_D - \varepsilon_D$

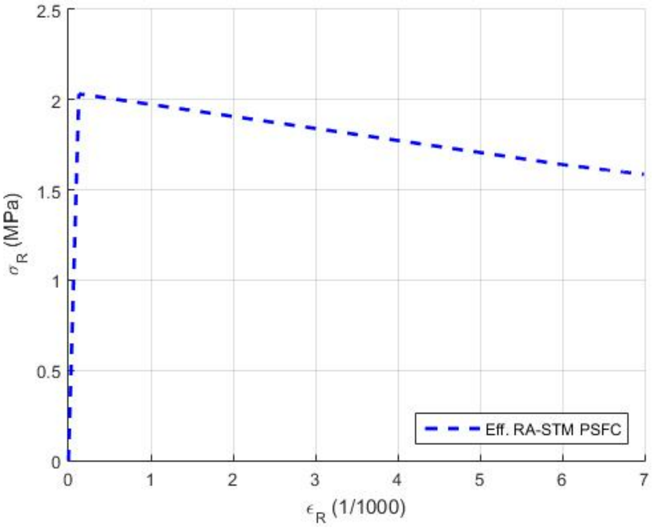

Curva $\sigma_R - \varepsilon_R$

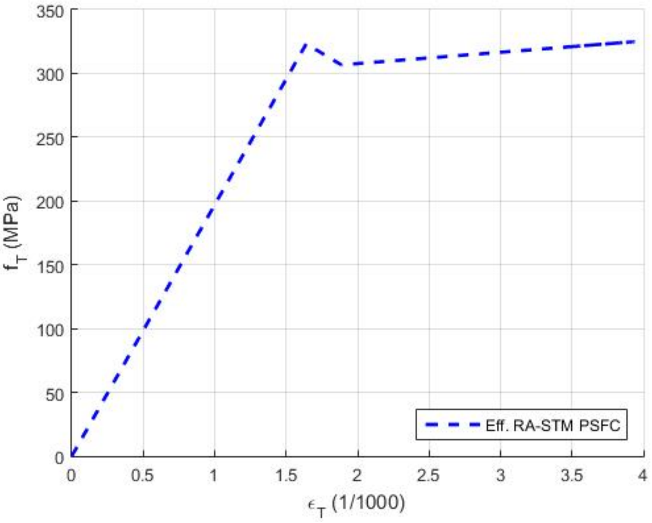

Curva $f_T - \varepsilon_T$

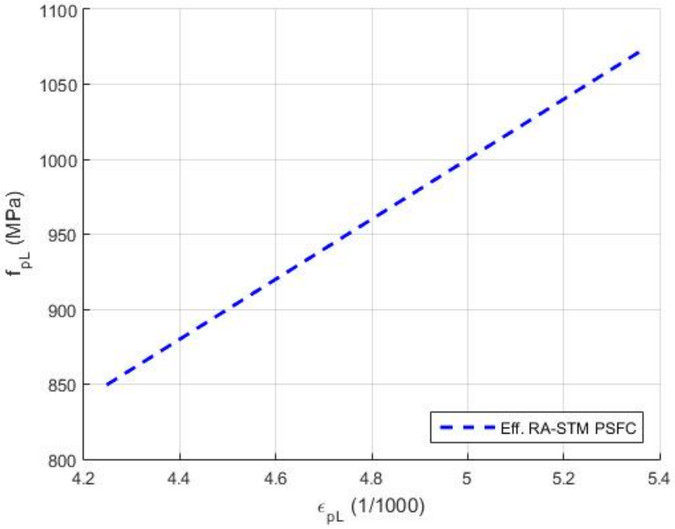

Curva $f_{pL} - \varepsilon_{pL}$

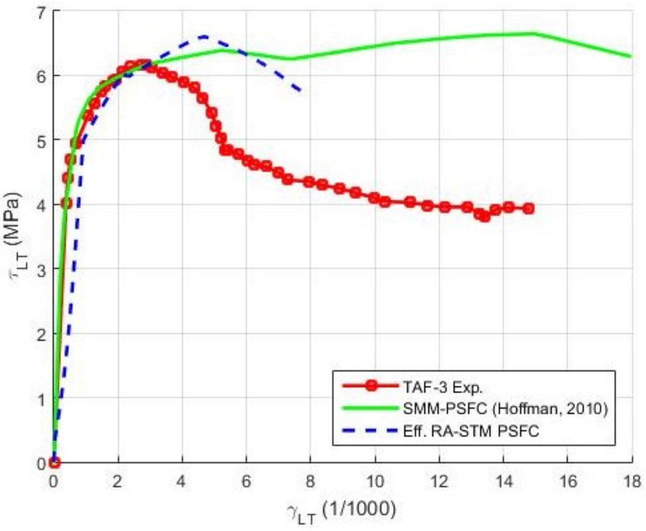

Curva $\tau_{LT} - \gamma_{LT}$

Placa TAF-4 (Hoffman N.S., 2010)

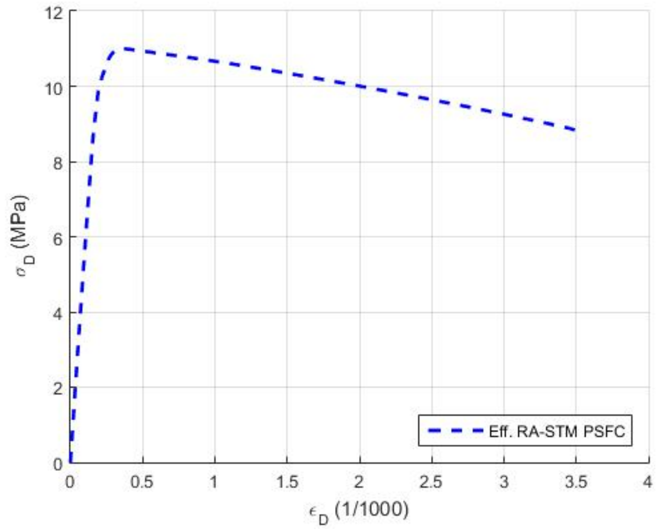

Curva $\sigma_D - \varepsilon_D$

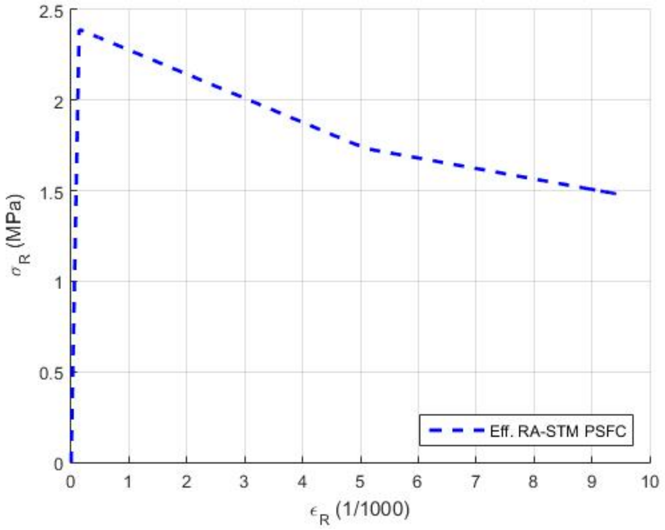

Curva $\sigma_R - \varepsilon_R$

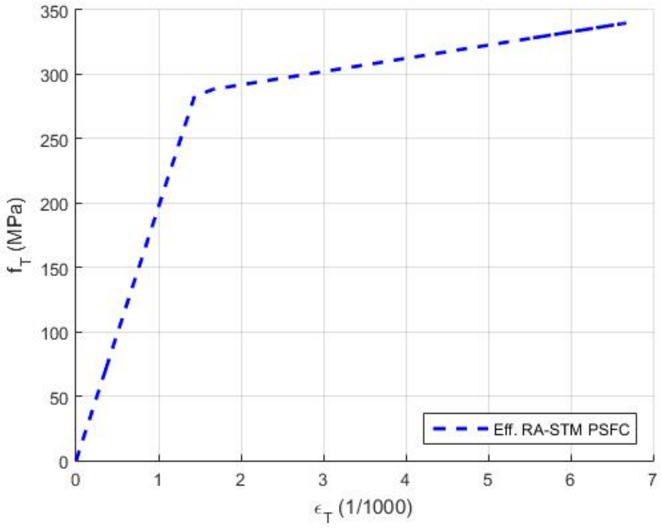

Curva $f_T - \varepsilon_T$

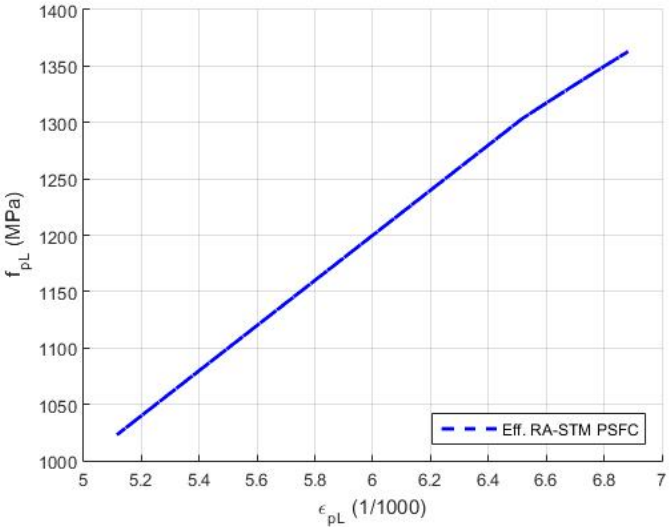

Curva $f_{pL} - \varepsilon_{pL}$

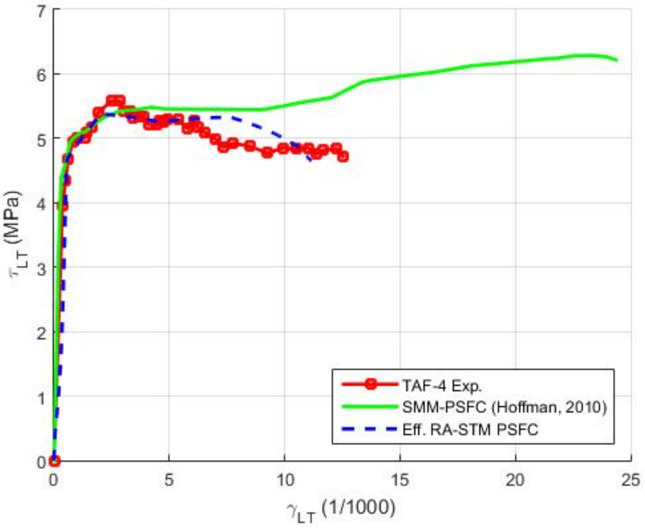

Curva $\tau_{LT} - \gamma_{LT}$

Placa TAF-5 (Hoffman N.S., 2010)

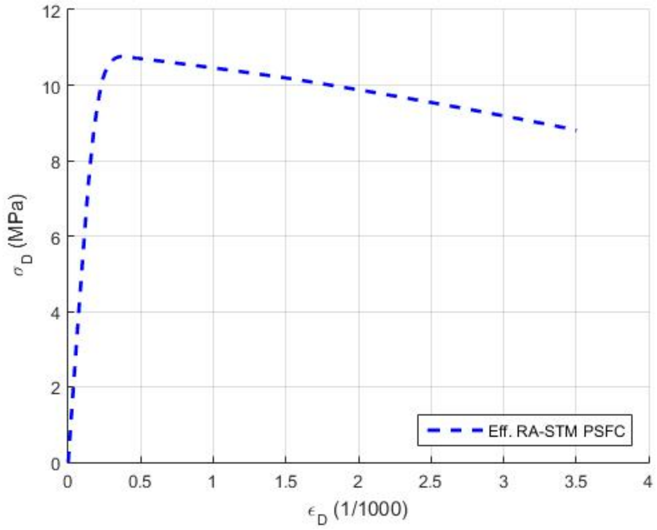

Curva $\sigma_D - \varepsilon_D$

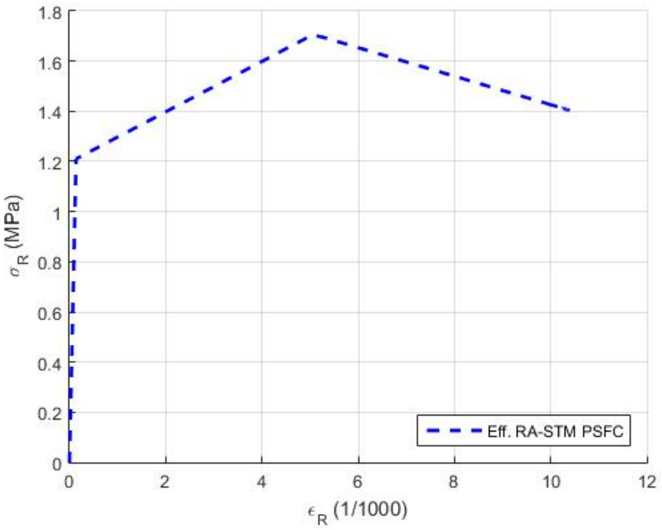

Curva $\sigma_R - \varepsilon_R$

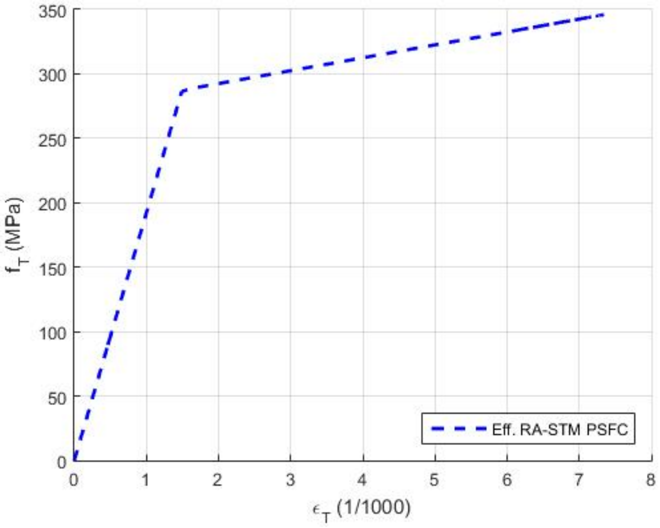

Curva $f_T - \varepsilon_T$

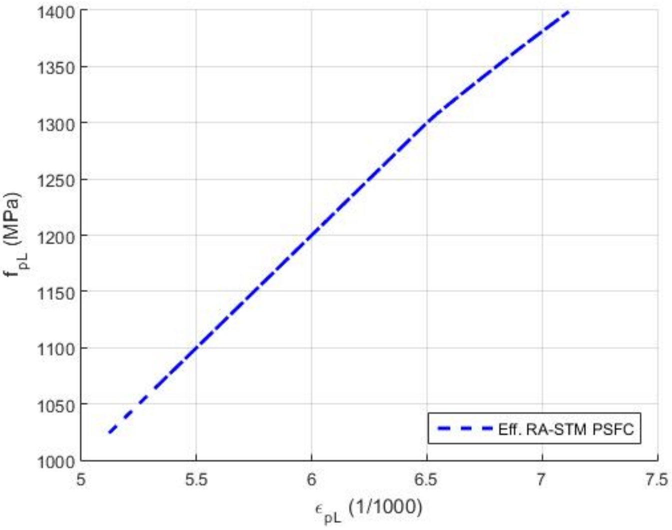

Curva $f_{pL} - \varepsilon_{pL}$

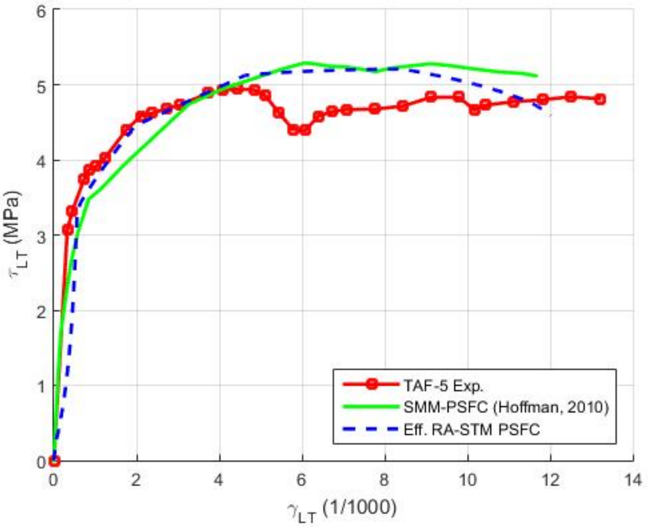

Curva $\tau_{LT} - \gamma_{LT}$